Nanosecond-pulsed pin-to-liquid discharges for the degradation of recalcitrant aqueous organic pollutants

Presented by

María Elena Corella Puertas

Department of Chemical Engineering

McGill University

Montréal, Québec, Canada

February 2021

A thesis submitted to McGill University in partial fulfillment of the requirements of the degree of Doctor of Philosophy

Supervisors:

Dr. Sylvain Coulombe

Dr. Viviane Yargeau

Abstract

In this PhD thesis, a plasma-based reactor was developed for treating water contaminated with persistent organic pollutants. Specifically, the chosen configuration was a pin-to-liquid discharge reactor (gas discharge contacting the liquid surface), powered by repetitively pulsed nanosecond discharges. The initial proof-of-concept was achieved with a preliminary pin-to-liquid discharge configuration by testing the degradation of the methylene blue dye. In the present work, 84 % removal of methylene blue (7 mg/L nominal initial concentration, 1 ml) was achieved after 11 min of treatment without stirring the solution, which is improved until almost complete removal by introducing mixing. The preliminary configuration allowed to study and optimize operating parameters (stirring, voltage, pulse frequency, electrode polarity). Stirring the solution and increasing the voltage and pulse frequency led to more effective dye removal, whereas switching electrode polarity had little effect. Regarding transport of species within not-stirred solutions, an area of convective transport linked to Marangoni flow was observed close to the liquid surface, whereas in the bulk of the liquid mass transport was limited by diffusion. The knowledge gained through the preliminary configuration helped to design and construct a compact, nanosecond-pulsed pin-to-liquid discharge reactor (7.5 ml sample volume), which was used in the remaining part of the present work.

In the process of choosing a suitable material for the high-voltage pin electrode, an extensive literature review revealed that various electrode materials erode in in-liquid discharge configurations, but there was no data available on the erosion of gas-side, high-voltage pin electrodes with above-liquid discharges. Therefore, the compact pin-to-liquid discharge reactor was used to study the erosion of high-voltage pin electrodes, using three different electrode materials (stainless steel, copper and hafnium) with two plasma gases (air, oxygen). Electrode erosion was observed for all studied cases, producing crater-like morphologies on the pin electrode tips and releasing metals in ionic and particle form into the plasma-treated water. The electrode material did not influence the energy deposited per pulse. Based on the results of this study, the preferred material was stainless steel for its low erosion rate in both plasma gases and its

inexpensiveness. Furthermore, the effect of metals introduced through electrode erosion on reactive species in plasma-treated water was investigated over four weeks post-plasma exposure. Three long-lived reactive oxygen and nitrogen species (H_2O_2, NO_2^- and NO_3^-) were detected in plasma-treated water, and their concentration and lifetime were not affected by the electrode material.

The ultimate application of the plasma-based reactor was the degradation of a particularly persistent aqueous pollutant, the pharmaceutical diatrizoate (DTZ). Conventional wastewater treatment plants are not able to remove DTZ, which has been detected in various aqueous environments such as surface waters, groundwaters and wastewater treatment effluents in numerous countries, with concentrations ranging from ng/L to µg/L. Oxygen and air plasmas were used for DTZ removal, with oxygen plasma performing better (e.g. after 20 min treatment of 200 µg/L DTZ in pure water, oxygen led to 90% degradation whereas air achieved 20% degradation). Transformation products (TPs) of DTZ were identified: m/z 486A, 504A, 504B, 628, 630A, 630B (previously described in literature) and m/z 486B, 550, 555, 565, 578 (novel). The residual, acute toxicity of TPs was tested on *Aliivibrio fischeri*. No acute toxicity of TPs was observed. Since DTZ is a particularly recalcitrant aqueous organic pollutant, its successful removal and the lack of formation of toxic TPs indicates that the developed plasma-based technology is promising for treating challenging wastewaters, such as hospital wastewaters.

Abrégé

Dans le cadre de cette thèse de doctorat, un réacteur à plasma a été développé pour traiter l'eau contaminée par des polluants organiques persistants. Plus précisément, la configuration choisie était un réacteur à tige métallique fine au-dessus du liquide alimenté par des décharges de nanosecondes pulsées de manière répétitive. La démonstration de faisabilité a été réalisée avec une configuration préliminaire en évaluant la dégradation du colorant bleu de méthylène. Dans les présents travaux, une élimination de 84 % du bleu de méthylène (concentration initiale nominale de 7 mg/L, 1 ml) a été obtenue après 11 minutes de traitement sans agitation de la solution, qui est améliorée jusqu'à l'élimination presque complète avec agitation du liquide. La configuration préliminaire a permis d'étudier et d'optimiser les paramètres de fonctionnement (agitation, tension, fréquence des impulsions, polarité des électrodes). L'agitation de la solution et l'augmentation de la tension et de la fréquence des impulsions ont permis d'accélérer l'élimination du colorant, tandis que l'échange de la polarité des électrodes a eu peu d'effet. En ce qui concerne le transport du colorant et des espèces réactives dans les solutions non agitées, une zone de transport convectif lié à la force de Marangoni a été observée près de la surface du liquide, alors que sous cette zone, le transfert de masse était limité à la diffusion. Les connaissances acquises grâce à la configuration préliminaire ont permis de concevoir et de construire un réacteur compact à tige métallique fine au-dessus du liquide pulsé à la nanoseconde (volume de solution de 7,5 ml).

Lors du processus de sélection d'un matériau approprié pour l'électrode haute tension à tige, une revue de la littérature approfondie a révélé que divers matériaux d'électrode s'érodent lors de décharges dans le liquide, mais il n'y avait pas de données disponibles sur l'érosion des électrodes haute tension à tige lors de décharges au-dessus de la surface du liquide. En conséquence, le réacteur compact a été utilisé pour étudier l'érosion des électrodes haute tension à tige, en utilisant trois matériaux d'électrode différents (acier inoxydable, cuivre et hafnium) dans deux gaz plasmagènes (air, oxygène). L'érosion des électrodes a été observée dans tous les cas étudiés, produisant des morphologies en forme de cratère sur les extrémités des électrodes à tige et libérant des métaux sous forme d'ions et de particules dans l'eau traitée par plasma. Le matériau de

l'électrode n'a pas influencé l'énergie appliquée par impulsion. Sur la base des résultats de cette étude, le matériau a privilégié était l'acier inoxydable pour son faible taux d'érosion dans les deux gaz porteurs du plasma et son bas prix. En outre, l'effet des métaux introduits par l'érosion des électrodes sur les espèces réactives dans l'eau traitée au plasma a été étudié pendant quatre semaines après l'exposition au plasma. Trois espèces réactives d'oxygène et d'azote à longue durée de vie (H_2O_2, NO_2^- and NO_3^-) ont été détectées dans l'eau traitée au plasma, et leur concentration et leur durée de vie n'ont pas été affectées par le matériau des électrodes.

L'application ultime du réacteur à plasma a été la dégradation d'un polluant aqueux particulièrement persistant, le produit pharmaceutique diatrizoate (DTZ). Les stations d'épuration conventionnelles éliminent peu le DTZ, ce qui explique sa détection dans divers milieux aqueux dans de nombreux pays, et ce à des concentrations allant de ng/L à µg/L. Dans le cadre de cette thèse de doctorat, des plasmas d'oxygène et d'air ont été utilisés pour l'élimination du DTZ, le plasma d'oxygène étant plus performant (par exemple, après 20 minutes de traitement de 200 µg/L de DTZ dans de l'eau pure, l'oxygène atteignait une dégradation de 90% alors que celle de l'air était de 20%). Des produits de transformation (PT) du DTZ ont été identifiés : m/z 486A, 504A, 504B, 628, 630A, 630B (décrits précédemment dans la littérature) et m/z 486B, 550, 555, 565, 578 (nouveaux). La toxicité aiguë résiduelle des PT a été testée sur *l'Aliivibrio fischeri*. Aucune toxicité aiguë des PT n'a été observée. Comme le DTZ est un polluant organique aqueux particulièrement récalcitrant, son élimination réussie et l'absence de formation de PT toxiques indiquent que la technologie développée à base de plasma est prometteuse pour le traitement des eaux usées difficiles à traiter, comme les eaux usées des hôpitaux.

Dedication

To my family, for always being my anchor

Acknowledgements

First of all, I would like to express my gratitude to my supervisors, Prof. Sylvain Coulombe and Prof. Viviane Yargeau. Sylvain, thank you for opening the doors of a PhD at McGill University to me. I truly appreciate your guidance and support, and the freedom you gave me to pursue my research and professional development interests. Viviane, thank you for believing in me and welcoming me to your group at an advanced stage of my PhD. You gave me a new perspective on research and a new research field and environment, which greatly enriched my PhD experience. Thanks to both of you I have grown as a researcher and as a person. Merci beaucoup pour tout!

Second, this research would not have been possible without the financial support from the McGill Engineering Doctoral Award, the Eugenie Ulmer-Lamothe Award, the Natural Sciences and Engineering Research Council of Canada and the Gerald Hatch Faculty Fellowship.

Next, I would like to thank my colleagues. Jennifer and Elmira, I am deeply grateful that we went through our PhD journeys together. Your professional advice, strong friendship and laughter are invaluable, and I would not be where I am today without you. Simon, the end of the PhD would have been a lot harder without your support and sense of humor. Although we were not able to finish and publish our work together due to COVID-19, we gained a friendship for life and I am grateful for that.

I would like to thank the exchange students Eva and Benjamin for being excellent teammates and providing valuable support in the early stages of my PhD studies. I would also like to thank the exchange student Adna for her great support in my first journal article and the beautiful friendship that originated during our fun teamwork. I feel lucky to have worked with Kalyssa, Marco, Marie-Line and Jeong-Ann in the last research project of my PhD studies, and appreciate their dedication, patience and kindness. I would like to thank Audrey for the fruitful interdisciplinary collaboration and the smooth teamwork.

I would like to thank all former PPL lab mates for everything they taught me, and the more recent 3Cs and PPL lab mates for the fun and pleasant environment in the labs. A particular thanks to my office mates over the PhD years – Norma, Evelyne, Valentin, Kseniya, Steven and Simon –

Contents

List of Figures

List of Tables

List of Abbreviations

AOP	Advanced Oxidation Process
CEC	Contaminant of Emerging Concern
DBD	Dielectric Barrier Discharge
DLS	Dynamic Light Scattering
DTZ	Diatrizoate
EDS	Energy Dispersive X-ray Spectroscopy
HPLC-ECD	High-performance liquid chromatography with electrochemical detector
IC	Ion Chromatography
ICM	Iodinated Contrast Media
ICP-OES	Inductively Coupled Plasma with Optical Emission Spectrometry
LC-HRMS	Liquid chromatography with high resolution mass spectrometry
MB	Methylene Blue
PAW	Plasma Activated Water
PTFE	Polytetrafluorethylene
PVC	Polyvinylchloride
RO	Reverse Osmosis
RONS	Reactive Oxygen and Nitrogen Species
SEM	Scanning Electron Microscopy
TEM	Transmission Electron Microscopy
TOP	Total Oxidizing Power
TP	Transformation Product

1

Introduction

1.1   Project motivation

Freshwater is a precious and limited resource available to humans and the environment. Although most of the earth's surface is covered with water (about 71 %), most of it is seawater and only less than 3 % is available as freshwater (nasa.gov/specials/ocean-worlds/). Unfortunately, human activities have caused contamination of this limited resource, leading to biological contamination and/or toxicity from heavy metals or human-made chemicals in most surface waters around the world (Boulay *et al.*, 2011). For this reason, most surface waters need to be treated in order to be safe for human consumption (Boulay *et al.*, 2011). Although wastewater and drinking water treatment plants successfully remove many contaminants (e.g. bacteria, viruses, solids, oils, metals), certain human-made chemicals cannot be adequately removed by conventional treatment plants. Of particular concern are Contaminants of Emerging Concern (CECs), which have been detected in waterbodies in recent decades and whose risk to society and the environment is still largely unknown, as detailed in Chapter 2 (Sauvé and Desrosiers, 2014; Naidu, Jit, *et al.*, 2016; Noguera-Oviedo and Aga, 2016).

Among CECs, iodinated contrast media (ICM) are a family of pharmaceuticals that are particularly recalcitrant to removal by conventional technologies. ICM were first introduced into clinical practice in the 1950s and are currently extensively used in human medicine for radiological and medical diagnostic purposes (Pasternak and Williamson, 2012; Strehl *et al.*, 2019). After the patients leave the medical examinations, ICM are excreted in unmetabolized form in feces and urine, entering hospital and municipal wastewater streams (Weissbrodt *et al.*, 2009; Mendoza *et*

al., 2016; Strehl *et al.*, 2019). Because of their particularly high chemical and biological stability and their low tendency to adsorb to sewage sludge, ICM are not adequately removed in conventional wastewater treatment plants (Kalsch, 1999; Ternes and Hirsch, 2000; Echeverría *et al.*, 2013; Zemann *et al.*, 2014; Hong *et al.*, 2019). As detailed in Chapter 2, ICM have been detected in water bodies in wastewater streams and the environment in numerous locations across the world, with concentrations ranging from ng/L to mg/L. Even advanced oxidation processes (AOPs) such as ozonation, O_3/H_2O_2 or UV have failed to adequately remove ICM, and in some cases they formed toxic TPs (Ternes *et al.*, 2003; Kovalova *et al.*, 2013; Del Moro *et al.*, 2015; Polo *et al.*, 2016; Rivas *et al.*, 2019).

In order to remove the challenging aqueous pollutants such as ICM, innovative and effective technologies are needed. Recently, a technology based on plasma–liquid interactions has shown promising results for the removal of a particularly recalcitrant group of CECs (poly- and perfluorinated compounds), which virtually all other wastewater treatment technologies failed to adequately remove (Singh *et al.*, 2019). This sets a precedent for successful implementation of plasma-based technologies for the treatment of challenging wastewaters. Plasma-based technologies produce reactive oxygen and nitrogen species (RONS) *in situ*, without the need of transporting, handling and storing chemicals. RONS such as the hydroxyl radical (•OH) are powerful oxidants and may break down stable organic bonds. At the current state of the art, plasma-based technologies are usually less energy efficient – in terms of electrical energy needed to degrade a contaminant by one order of magnitude – than other AOPs such as ozonation or UV (Miklos *et al.*, 2018). However, as Chapter 2 will discuss, the recalcitrance of certain CECs to other technologies (requiring above-average energy consumption), together with lowering the energy consumption of plasma technologies through research and innovation, has the potential of reaching a point were plasma technologies become competitive in terms of energy consumption, cost and sustainability.

One innovation that has the potential of lowering the energy consumption of plasma-based treatments is the use of repetitively pulsed nanosecond discharges (vs. traditional AC or DC-powered discharges). These discharges deliver high-voltage pulses in a few nanoseconds, ideally giving enough energy to start plasma-chemical reactions but stopping soon enough to avoid wasting energy. One of the main challenges for the commercialization of the nanosecond-pulsed

plasma technologies is finding inexpensive and reliable nanosecond-pulsed power supplies (Pokryvailo *et al.*, 2006). The Plasma Processing Laboratory (PPL) of McGill University has developed several generations of inexpensive and reliable nanosecond plasma pulsers (Evans *et al.*, 2016; Evans, Bergthorson and Coulombe, 2016; Evans, 2017; Diaz Gomez Maqueo, 2019). They have shown promising results for applications in plasma-assisted combustion and methane reforming (Evans, 2017; Diaz Gomez Maqueo, 2019), but prior to this thesis they had not been tested in plasma–liquid environments.

In this context, this PhD thesis presents a pin-to-liquid discharge technology powered by a nanosecond pulser. The developed pin-to-liquid discharge reactor and process were applied for the successful removal of a model ICM, thus contributing in the quest of finding technologies that enable adequate removal of CECs from freshwaters.

1.2 Objectives

The main objective of this PhD thesis was to develop and optimize a nanosecond-pulsed pin-to-liquid discharge technology for efficient removal of aqueous organic pollutants. To achieve the main objective, following specific steps are addressed:

1) Construction and testing of a preliminary pin-to-liquid discharge configuration to:
    i) Validate the operation of a novel nanosecond-pulsed plasma source over a liquid surface.
    ii) Optimize operating parameters.
    iii) Establish and validate liquid sample analysis approaches.
2) Design and construction of a compact, nanosecond-pulsed pin-to-liquid discharge reactor.
3) Electrical characterization of nanosecond-pulsed pin-to-liquid discharges.
4) Chemical characterization of plasma-treated liquids.
5) Investigation of the erosion of high-voltage electrodes in nanosecond-pulsed pin-to-liquid discharges.
6) Development of an application for the removal of aqueous organic pollutants (dyes and ICM).

7) Identification of TPs of one model aqueous organic pollutant (the ICM DTZ) and testing of their associated residual toxicity, with the goal of ensuring that toxicity is reduced during treatment.

1.3   Organization of the thesis

This manuscript-based thesis is comprised of 7 chapters. Chapter 2, which follows this Introduction, summarizes the literature with regards to the background of this project. This includes an overview of fundamentals of plasma–liquid interactions, with a section on the erosion of high-voltage electrodes, followed by an overview of treatment of CECs with a particular focus on ICM. Chapter 3 presents an outline of the experimental methodology used throughout this thesis, gives details on the two pin-to-liquid discharge configurations developed in the present work, as well as any details pertaining to characterization which were not originally published within the Author's manuscripts (and thus not covered in the subsequent chapters). The body of this work (Chapters 4-6) is composed of manuscripts published, submitted or in preparation for submission for publication in peer-reviewed scientific journals. In Chapter 4, a preliminary nanosecond-pulsed pin-to-liquid discharge configuration is developed and tested on a dye as model organic pollutant. Chapter 5 investigates the erosion of high-voltage electrodes in a compact pin-to-liquid discharge reactor, and its effect on reactive species formed in plasma-treated water. Chapter 6 provides an application of the compact pin-to-liquid discharge reactor for the removal of a recalcitrant aqueous organic pollutant, the ICM DTZ. Finally, Chapter 7 is a closing section that summarizes the overall conclusions and contributions to knowledge that can be drawn from this work, along with recommendations for future work.

2

Background

2.1   Plasma–liquid fundamentals

2.1.1   Introduction to plasma–liquid interactions and their applications

Plasma as a state of matter is a high energy, ionized gas that consists of atoms or molecules with an admixture of charged particles, electrons and ions. They exist in a state of quasi-neutrality, i.e. roughly no overall electric charge (Smirnov, 2012b). Plasmas occur naturally, for example whenever ordinary matter is heated to a temperature greater than about 10,000 °C (lightning, Earth's ionosphere, solar wind and aurora borealis, etc.), or can be human-made both at high (thermal plasma) or low gas temperatures (non-thermal/cold plasma) (National Research Council, 1995; Smirnov, 2012a). While in thermal plasmas all the species in the plasma reach high temperatures, in non-thermal plasmas there is a non-equilibrium state: electrons reach high temperatures while heavier species (ions, atoms) remain at ambient temperature.

Producing electrical discharges in a gas is a relatively simple method to create plasma at laboratory scale (Smirnov, 2012a). In recent years, electrical discharges have also been studied in gas–liquid environments and directly in liquids (mostly water, or in some cases organic liquids) for a wide range of applications including wastewater treatment, medicine, agriculture, nanomaterial synthesis, polymer treatment and analytical chemistry (Locke, Lukeš and Brisset, 2012; Bruggeman *et al.*, 2016; Locke and Lukeš, 2018; Magureanu, Bradu and Parvulescu, 2018; Puač, Gherardi and Shiratani, 2018; Rezaei *et al.*, 2019).

2.1.2 Typical reactor geometries for plasma–liquid interaction

Over the past years, plasma-treated liquids have been produced in a myriad of reactor geometries with different operating principles. These reactors can be sorted into three main categories (Bruggeman *et al.*, 2016):

1) Direct discharges in liquids;
2) Discharges in the gas phase over a liquid, including when a conductive liquid is used as an electrode;
3) Discharges in multiphase environments such as discharges in bubbles inside liquids or discharges contacting liquid sprays or foams.

Note that these discharges can be powered by various types of power inputs such as AC, DC or pulsed (Locke *et al.*, 2006; Bruggeman *et al.*, 2016). The reactors are typically operated at atmospheric pressure (with few exceptions that involve ionic liquids), because low pressure is more costly and risks the evaporation of the liquid (Scholtz *et al.*, 2015; Bruggeman *et al.*, 2016; Rezaei *et al.*, 2019).
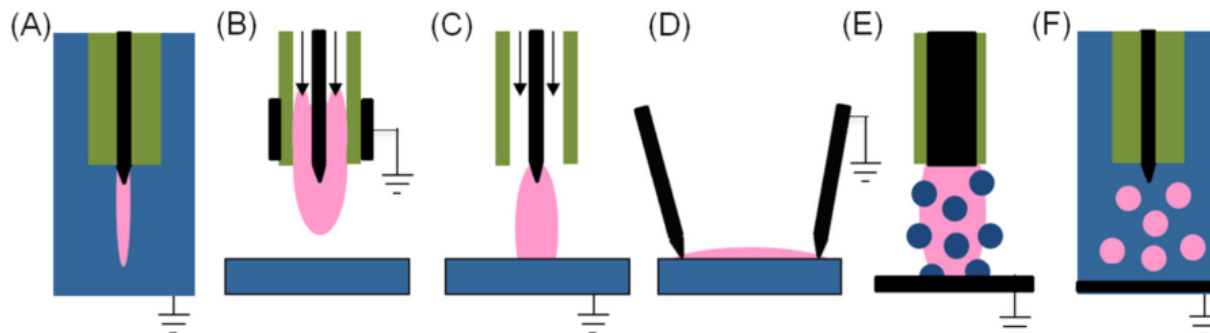
Fig. 2-1 Schematic of different discharges used in plasma–liquid interactions: (A) direct discharge in liquid, (B)–(D) gas phase discharges over a liquid and (E) and (F) multiphase discharges. In more detail: (B) plasma jet without direct contact with liquid, (C) gas phase plasma with liquid electrode, (D) surface discharge, (E) gas phase plasma with dispersed liquid phase (aerosols) and (F) discharges in bubbles. Blue = liquid, pink = plasma, green = dielectric, black = metal electrodes. (Bruggeman *et al.*, 2016).

The mechanism for discharge generation directly in liquids (Fig. 2-1, A) differs significantly from the mechanism in the gas phase, since the liquid density is approx. 1000 times larger than the gas and liquids can have widely varying properties, such as different electrical conductivities and pH (Locke, Lukeš and Brisset, 2012; Adamovich *et al.*, 2017; H. Wang *et al.*, 2019). Whereas the

breakdown strength in atmospheric gas is in the range of tens of kV per centimeter, the one in liquids is generally much higher (e.g. for liquid water it is > 1 MV cm^{-1}) (Locke, Lukeš and Brisset, 2012). Breakdown in the liquid phase is generally associated with an initial formation of bubbles through heating or via cavitation in the liquid, and a subsequent ionization of the gas in the bubbles (Starikovskiy *et al.*, 2011; Locke, Lukeš and Brisset, 2012; Bruggeman *et al.*, 2016). However, Starikovskiy et al. (2011) suggest that breakdown can also occur without a phase change (Starikovskiy *et al.*, 2011). In any case, in-liquid discharges are generally more energy intensive than discharges in gas–liquid environments, which may explain why there has been an increasing focus on discharges in gas–liquid environments in recent years (Malik, 2010; Stratton *et al.*, 2015).

For discharges in the gas phase over a liquid, the electrode system can be completely outside the liquid (Fig. 2-1, B) or a conductive liquid can act as one of the electrodes (Fig. 2-1, C). The first case is typically a plasma jet, in which gas is injected from an electrode tip through a concentric band of ring barrier electrodes forming a stream of active species that extends into the liquid (Fig. 2-1, B) (Locke, Lukeš and Brisset, 2012; Scholtz *et al.*, 2015). Plasma jets are practical for medical applications – particularly when plasma treatment occurs directly on patients' body fluids – since it is preferable to avoid using the patient as electrode. For the second case, a typical configuration is a pin-to-liquid discharge (Fig. 2-1, C), in which discharge channels that originate in the gas phase travel to the surface of the liquid. Once they reach the liquid, discharge channels can propagate along its surface, resembling branched discharge propagation patterns over solid surfaces (Lichtenberg figures) (Belosheev, 1998; Lukes *et al.*, 2014; Stratton *et al.*, 2015). The polarity of the liquid (water anode/cathode) can influence the shape of the discharge patterns (Bruggeman *et al.*, 2008). Another configuration in which the conductive liquid acts as one of the electrodes is the dielectric barrier discharge (DBD) reactor. One plate electrode is placed above the liquid, whereas the other plate electrode is in contact with the conductive liquid. Typically, there is a dielectric barrier between the gas-side electrode and the liquid, interrupting the electron flow and thus preventing the formation of arcs and sparks in the discharge gap (see Fig. 2-2) (Neretti *et al.*, 2016).
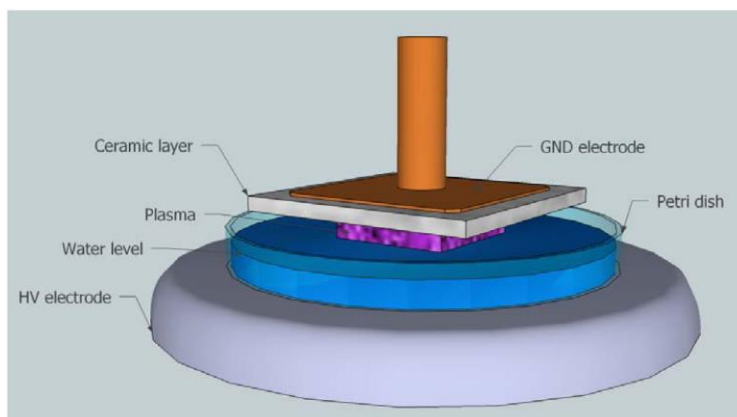
Fig. 2-2 Schematic of a DBD reactor with a ceramic layer acting as dielectric barrier (Neretti *et al.*, 2016).

Compared to discharges over a flat liquid surface, multiphase environments like bubbles or aerosols (examples in Fig. 2-1, E-F) provide a much larger gas–liquid interface area, and thus are expected to favor the mass transfer between species in the two phases. Analogous to the case over a liquid surface, high speed imaging showed that discharges can initiate at bubbles and propagate with a filamentary structure along the gas–liquid interface, on the gas side of the bubble (Locke, Lukeš and Brisset, 2012). Similar observations were made on discharges in contact with aerosols. For the case of air with water droplets, it was observed that streamers propagate on the surface of the droplets (Minamitani and Yamada, 2016). Studies comparing removal of dyes as model organic pollutants showed that multiphase environments have higher energy yields – amount of pollutant decomposed per energy input – than configurations with lower gas–liquid interface areas (e.g. fine droplets in the plasma zone > thin film > deep layer) (Grabowski, Van Veldhuizen and Rutgers, 2005; Malik, 2010; Stratton *et al.*, 2015).

2.1.3 Relevance of studying nanosecond-pulsed pin-to-liquid discharges

As discussed in the previous section, in-liquid discharges are known to be more energy intensive than discharges initiated in the gas phase – the latter have a breakdown voltage that is about two orders of magnitudes smaller. Several studies have confirmed that above-liquid discharges are more energy efficient than in-liquid discharges in terms of producing reactive species and degrading aqueous organic pollutants (Dang *et al.*, 2009; Malik, 2010; Stratton *et al.*, 2015; Kozakova *et al.*, 2018), justifying the relevance of studying discharges in gas–liquid environments.

Within gas–liquid environments, the energy efficiency of electric discharges can be further optimized. Ideally, discharges should provide enough energy to produce relevant reactive species but prevent wasting a significant amount of energy, e.g. heating up the gas and the liquid. Whereas this is very difficult to achieve using traditional continuous DC or AC power, nanosecond pulsed power is an alternative that may minimize energy losses. Studies show that nanosecond pulsers are capable of producing a cold plasma in atmosphere air with large and uniform reacting volumes without spark and arc formation – which may prevent unnecessary heating (Evans, Bergthorson and Coulombe, 2016; Neretti *et al.*, 2016). Indeed, studies comparing different power inputs confirmed that pulsed discharges were more energy efficient than discharges powered by continuous DC or AC in terms of producing reactive species and degrading aqueous organic pollutants (Malik, 2010; Neretti *et al.*, 2016; Yuan *et al.*, 2017; Mahyar *et al.*, 2019). Furthermore, nanosecond pulsed discharges may remove the problem of Taylor cone formation. Taylor cones are liquid instabilities on the gas–liquid interface formed due to electrohydrodynamics, which may limit the homogeneity and stability of the plasma and thereby reduce the reactor efficiency (Bruggeman *et al.*, 2007, 2016; Baroch, Saito and Takai, 2008; P. Bruggeman *et al.*, 2008; Neretti *et al.*, 2016). In nanosecond pulses, the discharge duration is too short for Taylor cones to form (Neretti *et al.*, 2016).

In spite of the advantages of the nanosecond pulsed plasma technologies, one of the main impediments for their commercialization is the lack of suitable, inexpensive nanosecond pulsed power supplies. Over the past years, the Plasma Processing Laboratory (PPL) at McGill University has developed several generations of inexpensive and reliable nanosecond pulsed power supplies (Evans *et al.*, 2016, 2017; Evans, Bergthorson and Coulombe, 2016; Maqueo *et al.*, 2018; Maqueo, Coulombe and Bergthorson, 2019). These nanosecond pulsed power supplies have been tested for combustion enhancement and methane reforming applications, and this work explores their application for plasma-based wastewater treatment for the first time (using the nanosecond pulser version 2017 powered by a diode opening switch generator).

Finally, the choice of a pin-to-liquid discharge configuration (gas discharge contacting the surface of the liquid) will be explained. This configuration is simple enough to be able to study fundamentals of plasma–liquid interactions and test the applicability of plasma technologies for the removal of aqueous organic pollutants on a lab scale. Pin-to-liquid discharges have the

potential of being scaled up, by powering multiple pins or sharp-pointed electrodes in parallel over a water surface. This configuration was recently used in a pilot-scale plasma reactor; it demonstrated rapid removal of persistent aqueous pollutants (poly- and perfluorinated compounds) (Singh *et al.*, 2019). If mass transfer from the plasma to the liquid wants to be further improved in pin-to-liquid discharge configurations, the volume-to-surface ratio of the gas–liquid interface can be increased by treating thin layers of water, or by bubbling gas through the liquid and thus generating a water surface that is not flat (Malik, 2010; Stratton *et al.*, 2015).

2.1.4 Chemical reactions in plasma–liquid environments

This section reviews chemical reactions that occur when a plasma is initiated in a gas phase in contact with water. Although some chemical reactions that occur when the plasma is initiated directly in the liquid phase are similar, they are not reviewed since in-liquid discharges are not the focus of this work.

When plasma is formed from a gas phase, the plasma-generated species can interact with the liquid phase at the gas–liquid interface. Not only the plasma-generated species can chemically 'activate' the liquid water, but species from the liquid phase can, in turn, transfer into the plasma and affect its properties. A schematic diagram of some of the most important species and mechanisms for a (humid) air plasma in contact with water is shown in Fig. 2-3. The most abundant primary species generated under these conditions are hydroxyl ($^\bullet$OH), hydrogen (H$^\bullet$), oxygen (O$^\bullet$) and nitric oxide (NO$^\bullet$) radicals and ions (Lukes, Locke and Brisset, 2012; Bruggeman *et al.*, 2016). These species react with other primary species or with the surrounding gas or liquid molecules, producing oxygen- and nitrogen-based secondary species such as hydrogen peroxide (H_2O_2), nitrogen oxides (N_xO_x), ozone (O_3), nitrous acid (HNO_2), nitric acid (HNO_3), peroxynitrous acid (ONOOH) (Lukes, Locke and Brisset, 2012; Boehm *et al.*, 2016; Bruggeman *et al.*, 2016; Locke and Lukeš, 2018). Note that similar primary and secondary species are formed in discharges in other gases, such as oxygen or noble gases. Since nitrogen is not present in these cases, only oxygen-based species are formed. Where oxygen is not provided by the gas, it can be provided by water that evaporates and enters the plasma zone.
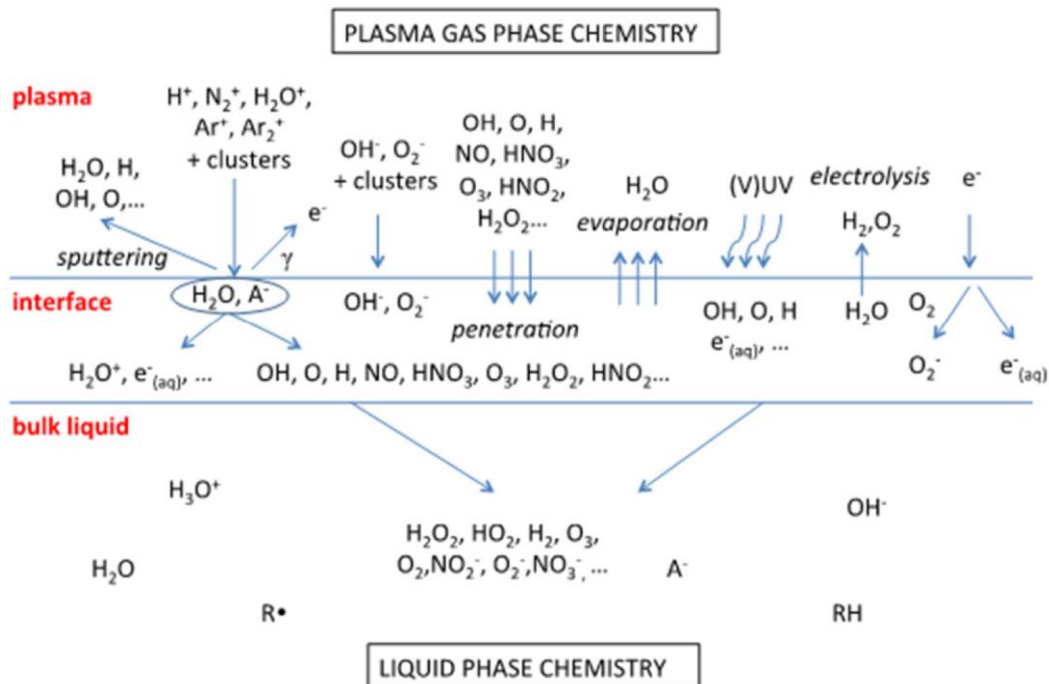
Fig. 2-3 Schematic diagram of some of the most important species and mechanisms for a humid air plasma in contact with water (Bruggeman *et al.*, 2016).

Because of this large number of reactive species, plasma-treated water is a highly reactive and complex medium. This reactive medium is affected by the original chemistry of the gas and liquid phase, the lifetime and interaction of different primary and secondary species (some of them may have post-discharge effects, while others disappear rapidly), transport and kinetic processes, volume-to-surface ratio of the gas–liquid interface and its location with respect to the plasma discharges, and physical discharge characteristics such as discharge duration, voltage, intensity, and electrode configuration. Over the years, experimental and modelling efforts have been studying and unravelling the complexity of plasma–liquid interactions.

Plasma-chemical reactions induced in plasma–liquid interactions can be classified into four main categories (Lukes, Locke and Brisset, 2012):

1) Acid–base reactions due to acidic effects caused in water by the chemical products formed by the plasma (e.g., HNO_2 and HNO_3);

2) Oxidation reactions caused by oxidative effects of RONS produced by the plasma (e.g. $^{\bullet}OH$, H_2O_2, O_3 and $ONOOH$);

3) Reduction reactions caused by reductive species produced by the plasma (e.g. aqueous e⁻, H• and $O_2^{•-}$);

4) Photochemical reactions initiated by UV radiation from the plasma (e.g., photolysis of H_2O_2 and O_3, photocatalysis).

2.1.4.1 Acid–base reactions

There is ample evidence that discharges in (humid) air plasma in contact with liquid water typically lead to strong acidification of the liquid (Lukes, Locke and Brisset, 2012; Aboubakr *et al.*, 2015; Foster and Lai, 2016; Kovačević *et al.*, 2017; Locke and Lukeš, 2018; Bradu *et al.*, 2020). N•, NO• and $NO_2^•$ radicals generated in the gas phase can form nitrous acid (pK_a = +3.35), nitric acid (pK_a = -1.37) and peroxynitrous acid (pK_a = +6.8) either in the gas phase or by interaction with the plasma–liquid interface (Hoeben *et al.*, 2019; Bradu *et al.*, 2020). In both cases, acids can penetrate into the bulk of the liquid and accumulate there as acids and their conjugated bases (NO_2^-, NO_3^-, $ONOO^-$) (Bradu *et al.*, 2020). Because new ions are introduced into the liquid, acidification is typically accompanied by an increase in solution conductivity (Porter *et al.*, 2009; Lukes, Locke and Brisset, 2012; Hoeben *et al.*, 2019). Peroxynitrite is highly unstable and decays to form •OH and $NO_2^•$ radicals, as will be discussed later. NO_2^- and NO_3^- have longer lifetimes (hours to days) (Shen *et al.*, 2016; Liu *et al.*, 2018) and, in the presence of dissolved oxygen, NO_2^- can gradually convert into NO_3^- through the following reactions (Karlsson and Tortensson, 1974; Park and Lee, 1988; Lukes *et al.*, 2005; Lukes, Locke and Brisset, 2012):

$$3NO_2^- + 3H^+ \rightarrow 2NO(aq) + NO_3^- + H_3O^+ \tag{2.1}$$

$$2NO(aq) + O_2(aq) + H_2O \rightarrow 2H^+ + NO_2^- + NO_3^- \tag{2.2}$$
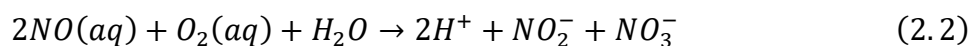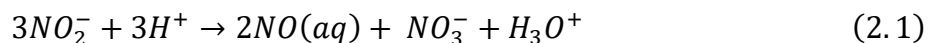
Since the plasma treatment also introduces oxidizing species such as O_3 and H_2O_2, they can also contribute to the oxidation of NO_2^- (Lukes, Locke and Brisset, 2012; Bruggeman *et al.*, 2016):

$$NO_2^- + O_3(aq) \rightarrow NO_3^- + O_2(aq) \tag{2.3}$$

$$NO_2^- + H_2O_2 + H^+ \rightarrow NO_3^- + H_2O + H^+ \tag{2.4}$$
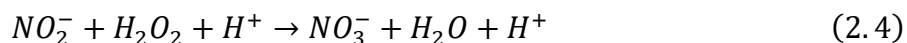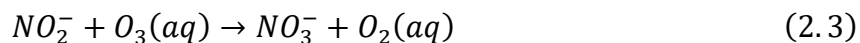
Discharges in gases that do not contain nitrogen may also lead to acidification, although this effect is typically smaller than in discharges in air/nitrogen (Porter *et al.*, 2009; Kovačević *et al.*, 2017; Wang *et al.*, 2017). There have been different approaches to try to explain the acidification induced by discharges in pure oxygen or noble gases. Porter et al. (2009) observed the presence of little amounts of nitrates in liquids treated by discharges in pure oxygen, argon or helium, and attributed

them to the presence of traces of air in the reactor (Porter *et al.*, 2009). Kim et al. (2015) observed no significant change in pH during treatment of distilled water with pure oxygen plasma (Kim, Kam and Mok, 2015). However, in the presence of aqueous organic pollutants (namely sulfonamide antibiotics), they observed an appreciable drop in pH. They attributed this drop to the formation of organic acids (formic, acetic and oxalic acid) and inorganic ions (NO_2^-, NO_3^-, SO_4^{2-}) during the degradation and mineralization of the organic pollutants (Kim, Kam and Mok, 2015). Burlica et al. (2006, 2008) observed a decrease in pH in distilled water induced by discharges in oxygen or argon (Burlica, Kirkpatrick and Locke, 2006; Burlica and Locke, 2008). The explanation they proposed was the formation of to H_3O^+ ions due to the electronic and ionic bombardment in the gas or liquid phase (Burlica, Kirkpatrick and Locke, 2006; Burlica and Locke, 2008):

$$H_2O + e^- \rightarrow H_2O^+ + 2e^- \tag{2.5}$$

$$H_2O^+ \rightarrow {}^\bullet OH + H_3O^+ \tag{2.6}$$

Lukes et al. (2012) and Hoeben et al. (2019) discussed the possible acidification due to accumulation of H_2O_2 in plasma-treated water (Lukes, Locke and Brisset, 2012; Hoeben *et al.*, 2019). As H_2O_2 is a weak acid (pKa = + 11.75) and the final concentrations of H_2O_2 in plasma-treated water are typically in the μmol/L to mmol/L range, both studies concluded that H_2O_2 alone cannot explain the observed drop in pH (Lukes, Locke and Brisset, 2012; Hoeben *et al.*, 2019).

All in all, composition and quantity of reactive species can vary significantly depending on the plasma gas, reactor configuration, power delivery and operating conditions; different cases may involve different causes and levels of acidification. Acidification can affect other plasma-induced chemical reactions, particularly redox reactions. The pH dependency of some oxidation reactions can affect the degradation of aqueous organic pollutants, the inactivation of microorganisms in water as well as biochemical processes in plasma medicine applications (Lukes, Brisset and Locke, 2012; Lukes, Locke and Brisset, 2012; Bradu *et al.*, 2020).

2.1.4.2 Oxidation reactions

Since the discovery of ozone formation in DBDs in air in 1857, ozone generation through plasmas has been extensively studied (Kogelschatz, 2003, 2017). Key steps for ozone generation in plasma

are the dissociation of oxygen molecules, and the collision of the dissociated oxygen with an oxygen molecule, involving a third collision partner (M) (Locke, Lukeš and Brisset, 2012):

$$O_2 + e^- \rightarrow 2O^\bullet + e^- \tag{2.7}$$

$$O^\bullet + O_2 + M \rightarrow O_3 + M \tag{2.8}$$

Factors that affect the formation (and destruction) of O_3 include the type of gas (pure O_2 versus air), gas temperature, plasma treatment time and type of power input (e.g. nanosecond-pulsed discharges versus classical sinusoidal discharges) (Eliasson, Hirth and Kogelschatz, 1987; Kogelschatz, 2003, 2017; Pokryvailo *et al.*, 2006; Neretti *et al.*, 2016). It should be noted that the presence of water vapor can suppress the O_3 generation process and favor the formation of hydrogen peroxide instead (Locke, Lukeš and Brisset, 2012; Lukes, Locke and Brisset, 2012). Although ozone is formed by the gas-phase discharge, it can transfer from the gas phase into the liquid and subsequently oxidize organic compounds present in water. Ozone is a powerful oxidant ($E^0 =2.07$ V), with higher standard redox potential than hydrogen peroxide and other conventional oxidants like chlorine, chlorine dioxide, or permanganate (Lukes, Locke and Brisset, 2012). Molecular ozone reactions with organic compounds are selective and limited to specific functional groups, such as unsaturated and aromatic hydrocarbons with substituents such as hydroxyl, methyl, or amine groups (Khadre, Yousef and Kim, 2001; Lukes, Locke and Brisset, 2012). As ozone is unstable in water at high pH, it decays forming $^\bullet$OH and $HO_2^\bullet$ radicals, which can rapidly react with aqueous organic pollutants (Khadre, Yousef and Kim, 2001; Ignatiev, Pryakhin and Lunin, 2008; Lukes, Locke and Brisset, 2012; Bruggeman *et al.*, 2016). The lifetime of ozone in water is typically in the scale of minutes, and is affected by pH, temperature and presence of impurities in the water (Khadre, Yousef and Kim, 2001; Bruggeman *et al.*, 2016; Neretti *et al.*, 2016). Methods to measure ozone dissolved in water include: the indigo dye method, the UV absorption method, the amperometric-membrane method, and the stripping and gas phase detection method (Majewski, 2012).

There is abundant evidence that gas-phase discharge in contact with liquid water or water vapor leads to the formation of hydroxyl radicals ($^\bullet$OH) (Lukes, Locke and Brisset, 2012; Bruggeman *et al.*, 2016; Locke and Lukeš, 2018). With a very high redox potential ($E^0 = 2.85$ V), it is one of the strongest oxidants that can exist in an aqueous environment (Kogelschatz, 2003; Lukes, Locke and

Brisset, 2012). $^{\bullet}$OH reacts unselectively with most organic and many inorganic compounds (Lukes, Locke and Brisset, 2012). As the radical is highly reactive, its lifetime is very short (about 200 μs in the gas phase, and less in aqueous solution), and it is expected to react at the plasma–liquid interface or after penetration into the liquid by only a few micrometers (Lukes, Locke and Brisset, 2012; Bruggeman $et\ al.$, 2016). The presence of hydroxyl radicals in the gas-phase discharge has been detected by emission spectroscopy with a characteristic OH band at 309 nm or laser-induced fluorescence (Locke, Lukeš and Brisset, 2012; Bruggeman $et\ al.$, 2016). In the liquid phase, $^{\bullet}$OH is often quantified via scavengers that have a high selectivity towards reacting with $^{\bullet}$OH (e.g. tert-BuOH, pCBA or coumarin) to circumvent the challenges of dealing with its short lifetime (Zhao $et\ al.$, 2014; Azerrad $et\ al.$, 2016; Locke and Lukeš, 2018).

Recombination of $^{\bullet}$OH radicals, mainly in the liquid phase, leads to the formation of hydrogen peroxide. In case the recombination reaction happens in the gas phase (less common, since it requires a third reaction partner) or in the gas–liquid interface, hydrogen peroxide diffuses quickly to the liquid phase, since it is highly soluble in water (Lukes, Locke and Brisset, 2012; Wandell and Locke, 2014; Bruggeman $et\ al.$, 2016). Another pathway for hydrogen peroxide generation is by $HO_2^{\bullet}$ radical recombination (Locke, Lukeš and Brisset, 2012). H_2O_2 is considered to be one of the most abundant long-lived plasma-chemical products. It can react with organic matter through direct pathways and indirect pathways. In direct pathways, H_2O_2 participates in redox reactions where it can act as oxidant ($E^0 = 1.77$ V) or reductant ($E^0 = −0.7$ V) (Lukes, Locke and Brisset, 2012). Examples of indirect pathways are (1) the reaction with ozone via formation of $^{\bullet}$OH radicals (Peroxone process), (2) the reaction with nitrites via formation of peroxynitrites, (3) photolysis with UV radiation from plasma via formation of $^{\bullet}$OH and $HO_2^{\bullet}$ radicals or (4) catalysis with iron ions via formation of $^{\bullet}$OH radicals (Fenton process) (Walling, 1975; Lukes, Locke and Brisset, 2012; Lukes $et\ al.$, 2014). The radicals that hydrogen peroxide provides can either recombine to form the same molecule again or attack other molecules, such as the target organic compound. Because of its relatively long lifetime (days to months) (Shen $et\ al.$, 2016; Liu $et\ al.$, 2018), H_2O_2 is one of the most commonly reported reactive species in the plasma–liquid literature and it has been considered a useful, although imperfect, indicator species for $^{\bullet}$OH in several plasma systems (Locke and Shih, 2011; Boehm $et\ al.$, 2016; Bruggeman $et\ al.$, 2016). Chemical analysis of H_2O_2 is usually based on redox reactions, such as colorimetric tests or peroxide analytical strips (Takahashi $et\ al.$, 1999; Wandell and Locke, 2014; Neretti $et\ al.$, 2016; El Shaer $et\ al.$, 2020).

However, these analyses may be affected by the presence of other strong oxidants (Takahashi *et al.*, 1999; Neretti *et al.*, 2016). As plasma-treated water may contain several types of strong oxidants, it can be beneficial to contrast the redox-based tests with direct H_2O_2 measurements such as high-performance liquid chromatography (HPLC) (Takahashi *et al.*, 1999).

Regarding nitrogen-based species, discharges in air generate short-lived radicals such as $N^{\bullet}$, $NO^{\bullet}$ and $NO_2^{\bullet}$ that further react to form peroxynitrite, nitrous and nitric acids in the plasma-treated water (Lukes, Locke and Brisset, 2012). Lukes et al. (2012, 2014) suggests that peroxynitrite ($ONOO^-$) chemistry may play a significant role in the oxidation–degradation processes of organic pollutant abatement in water induced by air discharges (Lukes, Locke and Brisset, 2012; Lukes *et al.*, 2014). The oxidant reactivity of aqueous peroxynitrite is highly pH dependent (Lukes, Locke and Brisset, 2012). Under alkaline conditions, direct oxidation reactions of peroxynitrite ($E^0 = 2.05$ V) with organic compounds are more likely to occur; whereas under acidic conditions, the protonated form of peroxynitrite predominates and it decays into $^{\bullet}OH$ ($E^0 = 2.85$ V) and $NO_2^{\bullet}$ ($E^0 = 0.9$ V) radicals, which subsequently initiate indirect reactions (Lukes, Locke and Brisset, 2012). Because generation of peroxynitrate by air discharges is accompanied by the formation of acids (HNO_2 and HNO_3), indirect reactions are likely to occur in plasma-treated water. Due to the short lifetime of peroxynitrite (typically less than 1 s in acidic solutions), it is very difficult to detect in plasma-treated water, even if it is produced in large quantities during the plasma treatment (Bruggeman *et al.*, 2016; Bradu *et al.*, 2020). Methods that have been used to try to identify peroxynitrite include emission analysis of the plasma/gas phase, chemical analysis of plasma-treated water (e.g. detection of specific products of the reactions of phenol or methyl orange with peroxynitrite) and analysis of antibacterial activity of model solutions mimicking plasma-treated water (Oehmigen *et al.*, 2011; Lukes *et al.*, 2014; Laurita *et al.*, 2015; Bruggeman *et al.*, 2016; Bradu *et al.*, 2020). In spite of the difficulty of detection, there is interest for studying the formation and reactions of peroxynitrite due to its bactericidal and biochemical activity (Naítali *et al.*, 2010; Lukes *et al.*, 2014; Bradu *et al.*, 2020).

2.1.4.3 Reduction reactions

Although plasma–liquid interactions predominantly lead to the formation of oxidizing species, reductive species are also produced. When free electrons from the plasma reach the liquid, they can dissolve into solution due to their negative free energy of hydration $\Delta G_{hyd} = -159$ kJ mol^{-1}

(Rumbach, Bartels and Go, 2018). The presence of solvated electrons in plasma-treated water has been detected by optical absorption techniques (Rumbach *et al.*, 2015b). Because solvated electrons are very powerful reducing agents ($E^0 = -2.89$ V) and reduce almost all other species, they typically have a very short lifetime in the range of ns–µs and are lost within less than 100 nm from the surface (Rumbach *et al.*, 2015a, 2015b; Gopalakrishnan *et al.*, 2016; Rumbach, Bartels and Go, 2018). There is evidence that aqueous electrons introduced by plasma–liquid interactions can initiate electrochemical reactions at the liquid surface, for example (Witzke *et al.*, 2012; Rumbach *et al.*, 2013; Bruggeman *et al.*, 2016):

$$2H^+ + 2e^-(aq) \rightarrow H_2(g) \qquad\qquad (2.9)$$

Another powerful reducing agent found in plasma-treated water is the H$^{\bullet}$ radical ($E^0 = -2.3$ V) (Lukes, Locke and Brisset, 2012). Its presence has been demonstrated using emission spectroscopy (Lukes, Locke and Brisset, 2012). Both aqueous e$^-$ and H$^{\bullet}$ can react with dissolved O_2 to form perhydroxyl radical (HO$_2{}^{\bullet}$) and its conjugate base, the superoxide radical anion (O$_2{}^{\bullet-}$) (Sahni and Locke, 2006; Lukes, Locke and Brisset, 2012; Norberg *et al.*, 2014; Bruggeman *et al.*, 2016). The redox activity of HO$_2{}^{\bullet}$ and O$_2{}^{\bullet-}$ is highly pH dependent, as will be discussed below. The presence of these radicals in plasma-treated water has been confirmed using the chemical probes tetranitromethane and nitroblue tetrazolium chloride (Sahni and Locke, 2006; Lukes, Locke and Brisset, 2012).

The relative importance of reduction reactions depends upon various factors:

1) Electrode configuration: Configurations with a liquid anode typically lead to a higher presence of aqueous e$^-$, since the anode attracts negative charges like e$^-$ (Thagard, Takashima and Mizuno, 2009; Stratton *et al.*, 2017; Rumbach, Bartels and Go, 2018).

2) Plasma gas: In the presence of oxygen, which is a highly electronegative gas, a significant fraction of plasma electrons may be quenched before they reach the water surface. Therefore, discharges in argon or Ar+N$_2$ have shown to produce more solvated electrons than discharges in gas mixtures containing O_2 (Rumbach *et al.*, 2015a, 2015b).

3) Presence of scavengers: Several RONS formed by plasma–liquid interactions can quickly react with reductive species and scavenge them ($^{\bullet}$OH, H_2O_2, NO$_3^-$, NO$_2^-$) (Rumbach *et al.*, 2015a, 2015b; Bruggeman *et al.*, 2016). As an example, $^{\bullet}$OH is produced in large quantities

near the plasma–liquid interface and it can quickly take up an electron, forming OH^- (Bruggeman *et al.*, 2016; Gopalakrishnan *et al.*, 2016).

4) pH: Low pH reduces the amount of solvated e^-, since H^+ acts as electron scavenger (Thagard, Takashima and Mizuno, 2009; Rumbach *et al.*, 2015b). Reduction reactions of $H^•$ are not dependent on the pH (Thagard, Takashima and Mizuno, 2009). Regarding the perhydroxyl radical, it can act as oxidizing or reducing agent depending on the solute. At below about pH 4.5, $HO_2^•$ and oxidation reactions predominate ($E^0 = +1.46$ V); at above about pH 5, its conjugate base $O_2^{•-}$ and reduction reactions predominate ($E^0 = -0.18$ V) (Sahni and Locke, 2006; Lukes, Locke and Brisset, 2012; Armstronga *et al.*, 2013).

5) Reaction location: As reductive species are typically only active near the liquid surface – since they are quickly scavenged by RONS –, redox reactions with surfactants may be particularly relevant (Stratton *et al.*, 2017). It is highly unlikely that a significant concentration of solvated e^- and $H^•$ can penetrate far enough to have a noticeable effect on the bulk of the liquid (Sahni and Locke, 2006; Rumbach, Bartels and Go, 2018).

2.1.4.4 Photochemical reactions

A significant fraction of the power dissipated by plasmas in gas–liquid environments is converted into ultraviolet (UV) light, although the amounts and intensities vary with the type of reactor, gas composition, and other conditions (Lu and Laroussi, 2005; Locke, Lukeš and Brisset, 2012; Lukes, Locke and Brisset, 2012; Foster, Mujovic and Groele, 2018). UV light emission from typical air plasma discharges is mostly at UVA (320 nm–400 nm) and UVB (280 nm–320 nm) wavelengths with intensities below 50 µW cm^{-2} (Moisan *et al.*, 2001; Laroussi and Leipold, 2004; Bruggeman *et al.*, 2016). If water vapor is present, it adds the emission from OH (at 284 and 309 nm) (Laroussi and Leipold, 2004; Bruggeman *et al.*, 2016). UV photons can induce photochemical reactions both in the gas phase (e.g. oxygen dissociation) and in the liquid phase (e.g. dissociation of water or hydrogen peroxide) (Locke, Lukeš and Brisset, 2012). They most likely cross the plasma–liquid interface unhindered other than by the change in index of refraction at the interface, typically penetrating into the bulk of an aqueous solution with wavelengths greater than 185 nm (Bruggeman *et al.*, 2016). UV radiation can interact with organic target compounds in direct or indirect reactions. In the direct way, photons induce photochemical reactions with the organic molecules, possibly dissociating and producing smaller organic compounds. In the indirect way,

photons induce photodissociation of inorganic compounds, which produce secondary species that may further react with the target organic compound. A particularly important reaction for oxidation of pollutants in the liquid phase is the dissociation of hydrogen peroxide by UV at 190–350 nm, as it delivers two highly reactive hydroxyl radicals (Locke, Lukeš and Brisset, 2012):

$$H_2O_2 + hv \rightarrow 2 \ ^\bullet OH \tag{2.10}$$

The research field of AOPs in water purification has already dealt with absorption of UV photons by water and impurities in an extensive way, so there is a large knowledge base that can be transferred to plasma–liquid techniques (Bruggeman *et al.*, 2016).

2.1.5 Erosion of high-voltage electrodes

Electrode erosion is a constraint that should be taken into account when designing the industrial scale-up of plasma–liquid reactors (Holzer and Locke, 2008; Foster, Mujovic and Groele, 2018). Erosion may restrict the operating time of the reactor and affect the stability of the discharge as well as the plasma production efficiency (e.g. due to modification of the electrode tip sharpness) (Blokhin *et al.*, 1999; Holzer and Locke, 2008; Foster, Mujovic and Groele, 2018). Furthermore, erosion may introduce particles and ions into the plasma-treated liquid, which may be seen as detrimental or beneficial depending on the context.

2.1.5.1 Erosion in in-liquid discharges

Over the past 20 years, electrode erosion in in-liquid discharges was extensively studied, showing that metal-based particles and ions are released into the plasma-treated liquid (Blokhin *et al.*, 1999; Efremov *et al.*, 2000; Kolikov *et al.*, 2005; Lukeš *et al.*, 2006; Mededović and Locke, 2006; Mededovic and Locke, 2007; Rutberg *et al.*, 2010; Lukes *et al.*, 2011; Parkansky *et al.*, 2012). This erosion has been linked with physical and/or chemical phenomena including sputtering, melting, evaporation, oxidation and electrochemical-derived processes (Goryachev, Ufimtsev and Khodakovskii, 1997; Kirkpatrick and Locke, 2006; Lukeš *et al.*, 2006; Mededović and Locke, 2006; Holzer and Locke, 2008; Lukes *et al.*, 2011; Lukes, Locke and Brisset, 2012; Liu *et al.*, 2016; Foster, Mujovic and Groele, 2018).

Goryachev et al. (1997) studied the mechanism of electrode erosion in pulsed discharges in water with a pulse energy of around 1 J and a peak voltage of 1 kV (Goryachev, Ufimtsev and

Khodakovskii, 1997). The reactor geometry consisted in a point-to-plane configuration, with the point electrode (anode) being either a 1 mm diameter wire or a 10 mm rod. The materials used for the wire electrode were copper, steel, brass, molybdenum, or tungsten, and for the rod electrode, copper, steel, or alloys containing tungsten and molybdenum. They observed that, for similar materials, the erosion rate of wire electrodes was one order of magnitude higher than the one of rod electrodes. Through scanning electron microscopy (SEM) observations, tests with artificial bubbling, and the use of mathematical models predicting thermal erosion as well as the influence of gas bubbles on the electric field distribution in the liquid, the authors concluded that the erosion of electrodes was determined by two effects: thermal (current heating resembling arc spots) and cavitation (formation of microbubbles at the electrode surface) (Goryachev, Ufimtsev and Khodakovskii, 1997).

Lukes et al. (2006) studied the erosion of high-voltage needle electrodes (2 mm diameter, positive polarity) in an in-liquid needle-to-plate reactor geometry (eq. to point-to-plane) (Lukeš *et al.*, 2006). The pulsed corona discharge had an energy per pulse of 2-3 J and the peak voltage was 20-24 kV. The erosion rates were determined for different electrode materials: tungsten > stainless steel > platinum. They attributed the erosion to a melting effect accompanied by release of anode material by electrolysis. The initially conically shaped electrodes became rounded and covered with crater spots after the discharge (see Fig. 2-4). In the case of tungsten, the surface of the eroded electrode was covered with protrusions that may have affected a distribution of the electric field on the surface and possibly also a distribution of the electrolytic current (Lukeš *et al.*, 2006).

In a similar reactor geometry, Lukes et al. (2011) studied the erosion of tungsten and its associated catalytic effects (Lukes *et al.*, 2011). In this case the energy per pulse was 2.55 J and the peak voltage was 27 kV. Their proposed erosion mechanisms included electrolysis, plasma sputtering, evaporation and oxidation of tungsten by reactive oxygen species formed by the plasma discharge. The formation of spikes on the surface of the tungsten electrode was explained by the high melting point and thermal conductivity of tungsten (T_{mp} = 3410 $^\circ$C, σ_T = 173 Wm^{-1} K^{-1}), which result in very rapid solidification of remains of molten tungsten, shortly after bursting. They observed the release of tungstate ions as well as solid tungsten particles into the plasma-treated water and attributed a catalytic effect to them. They observed that tungstate ions played a dominant role in

the decomposition of H_2O_2, enhancing the degradation of a model contaminant, dimethylsulfoxide (Lukes *et al.*, 2011).
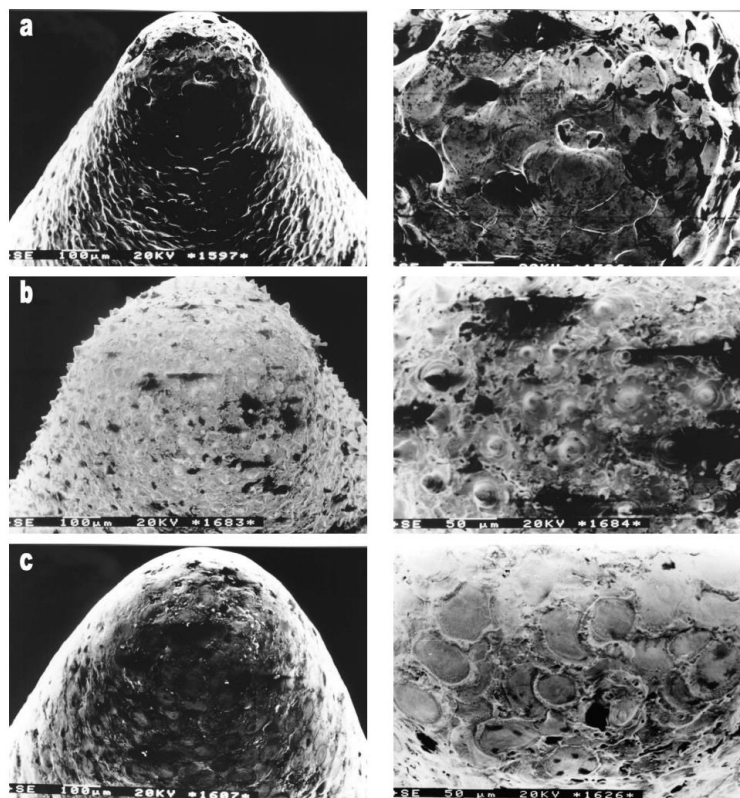
Fig. 2-4 Scanning electron microscopy (SEM) of the tips of needle electrodes (left) and details of electrode surfaces (right) after pulsed corona discharging in water for 60 min (U = 20 kV): a) platinum, b) tungsten, c) stainless–steel (Lukeš *et al.*, 2006).

Mededovic et al. (2006) and Kirkpatrick et al. (2006) observed a similar catalytic effect of eroded metals on H_2O_2 decomposition in an in-liquid pulsed corona discharge (Kirkpatrick and Locke, 2006; Mededović and Locke, 2006). In both cases, platinum high-voltage needle electrodes yielded higher H_2O_2 decomposition rates than nickel-chromium electrodes. The electrode configurations were point-to-plane, with a positive high-voltage point electrode (0.79 mm diameter). The energy per pulse was 1.1 J (Kirkpatrick and Locke, 2006) and the peak voltage was 45 kV (Mededović and Locke, 2006). Kirkpatrick et al. (2006) observed rounding of the electrode tips after the plasma discharge (Kirkpatrick and Locke, 2006), similar to the observations of Lukes et al. (2006) (Lukeš *et al.*, 2006) (see Fig. 2-5). Kirkpatrick et al. (2006) and Mededovic et al. (2006) detected the formation of platinum particles and suggested that they were ejected by sputtering or melting,

based on the observations of electron micrographs of the high-voltage electrodes (Kirkpatrick and Locke, 2006; Mededović and Locke, 2006).
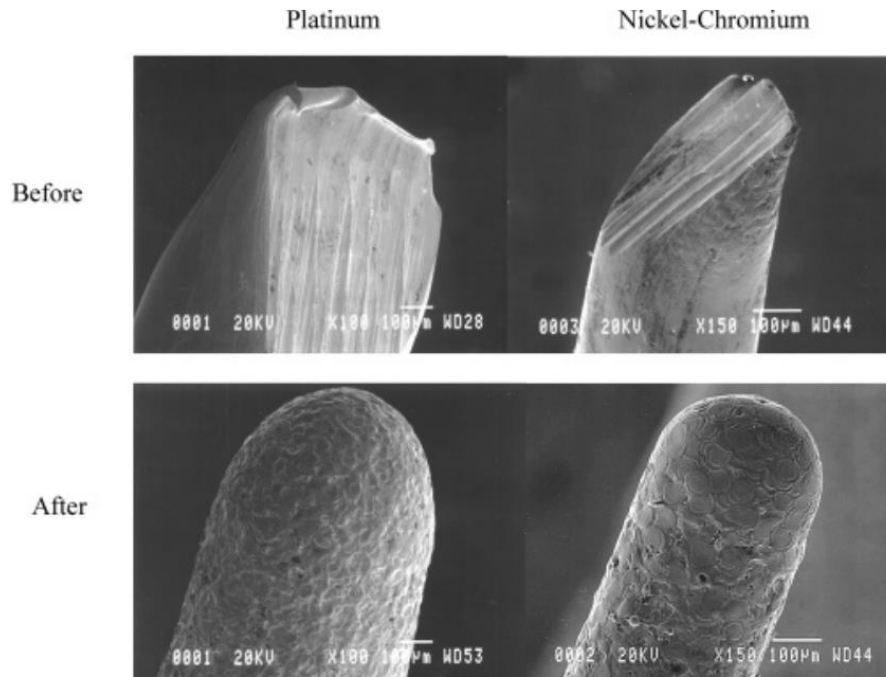
Fig. 2-5 Scanning electron microscopy (SEM) images of platinum and nickel-chromium electrodes both before (top) and after (bottom) their use as high-voltage electrodes. The morphology of the "before" images is caused by the wire cutter, whereas the morphology of the "after" images is caused by the discharge (Kirkpatrick and Locke, 2006).

Although these examples give an idea of the main findings on erosion in in-liquid discharges, this chapter does not intent to be an exhaustive review of the literature on this topic.

2.1.5.2 Erosion in above-liquid discharges

Although erosion in in-liquid discharges was extensively studied, electrode erosion in gas–liquid environments remains largely unexplored. Particularly, the erosion of high-voltage, gas-side electrodes has barely attracted any attention.

Liu et al. (2016) compared the erosion of in-liquid discharges in water and above-liquid discharges in air, in a plate-to-plate reactor geometry (Liu *et al.*, 2016). The peak current was 22 kA and the peak voltage around 17 kV. They observed higher erosion rate for discharges in water and attributed this to the formation of arc spots with high current density and evaporation of the metal. For discharges in air, they explained the erosion by jets of molten metal (Liu *et al.*, 2016). Dai et

al. (2016) used a point-to-plane reactor geometry, with the high-voltage point electrode in an argon atmosphere above the liquid (Dai *et al.*, 2016). They reported the release of iron ions from the submerged electrode, but did not comment on the erosion of the gas-side electrode (Dai *et al.*, 2016).

Since there is an increasing number of studies on plasma discharges in gas–liquid environments (Pokryvailo *et al.*, 2004; Benetoli *et al.*, 2011; Dobrin *et al.*, 2013; Panorel *et al.*, 2013b; Stratton *et al.*, 2015; Kornev and Preis, 2016; Yoon *et al.*, 2018), in many cases with point-to-plane electrode configurations, it is pertinent to look into the erosion of high-voltage, gas-side electrodes. This information will help in the choice of adequate electrode systems and materials.

2.1.5.3 Applications

The introduction of eroded metal particles and ions into plasma-treated liquids can be seen as a challenge or an opportunity for synergistic effects. For water purification, metal-based particles and ions can enhance the removal of contaminants (see 2.1.5.1) and microorganisms. Regarding the removal of microorganisms, silver-based and copper-based ions and nanoparticles introduced by electrode erosion can contribute to the bactericidal and fungicidal properties of plasma-treated water (Kolikov *et al.*, 2007; Rutberg *et al.*, 2010; Vukusic *et al.*, 2016; Su *et al.*, 2019). In spite of these advantages, the presence of metal-based particles and ions in effluents of wastewater treatment plants can be controversial, since they may pose toxicological and environmental challenges (Jeng and Swanson, 2006; Besser and Leib, 2007; Karlsson *et al.*, 2008; Schrand *et al.*, 2010; Simeonidis *et al.*, 2016). Therefore, metals introduced by electrode erosion may need to be removed, which could be particularly challenging for the case of nanoparticles (Simeonidis *et al.*, 2016).

For biomedicine applications, some metal-based nanoparticles and ions can contribute to the disinfecting and antitumoral properties of plasma-treated liquids. The disinfecting properties coincide with the enhanced removal of microorganisms discussed above (Kolikov *et al.*, 2007; Rutberg *et al.*, 2010; Vukusic *et al.*, 2016; Su *et al.*, 2019). Regarding antitumoral properties, Rutberg et al. (2008) obtained an aqueous dispersion of silver oxide nanoparticles by electrode erosion during pulsed electrical discharges in water, and demonstrated that this solution inhibited tumor growth in vivo (Pliss lymphosarcoma cell line) (Rutberg *et al.*, 2008). Preliminary results

of Glory et al. (2020) show that plasma-treated water containing copper-based ions and nanoparticles induces cell death of sarcoma cells (MCA-205 cell line) (Glory *et al.*, 2020).

In nanomaterial synthesis applications, the focus is on producing nanomaterials in controlled sizes, shapes and compositions (Pootawang, Saito and Lee, 2013; Chen, Li and Li, 2015; Rezaei *et al.*, 2019). A well-established method to produce nanomaterials is to use metal ion precursors in liquid (e.g. Ag^+ from $AgNO_3$, Au^{3+} from $HAuCl_4$, or Cu^{2+} from $CuCl_2$), which are reduced to elementary metals by reducing agents introduced by plasma–liquid interactions, nucleating and growing nanomaterials (Thagard, Takashima and Mizuno, 2009; Mariotti *et al.*, 2012; Pootawang, Saito and Lee, 2013; Chen, Li and Li, 2015; Saito and Akiyama, 2015; Rezaei *et al.*, 2019; Shen *et al.*, 2019; Xie *et al.*, 2019; Dzimitrowicz *et al.*, 2020). As an alternative, several studies have explored the use of electrode erosion for the production of nanomaterials. The diverse nanomaterials obtained through electrode erosion in in-liquid discharges include spindle-shaped Au NPs, ZnO nanoflowers, CuO nanofibers, Cu_2O NPs in various geometric shapes, and WO_3 and Pt NPs with irregular shapes (Lo, Tsung and Chen, 2005; Hu, Takai and Saito, 2013; Hu *et al.*, 2014; Sulaimankulova, Mametova and Abdullaeva, 2019; Sirotkin *et al.*, 2020).

2.2 Treatment of aqueous organic contaminants

2.2.1 Contaminants of emerging concern

Contaminants of Emerging Concern (CECs) are contaminants that have been detected in waterbodies in recent decades and whose risk to society and the environment is still largely unknown (Sauvé and Desrosiers, 2014; Naidu, Jit, *et al.*, 2016; Noguera-Oviedo and Aga, 2016). These contaminants may have recently entered waterbodies as a consequence of new technological advances or may have already been in waterbodies for many years, but only raised concerns recently as a result of novel analytical methods and scientific paradigm shifts (Sauvé and Desrosiers, 2014; Naidu, Jit, *et al.*, 2016; Noguera-Oviedo and Aga, 2016). Examples of CECs are pharmaceuticals, personal care products, illicit drugs, engineered nanomaterials, pesticides and household chemicals; as well as their metabolites and TPs (Sauvé and Desrosiers, 2014; Noguera-Oviedo and Aga, 2016; Marshall, 2017; Rodriguez-Narvaez *et al.*, 2017; Kolosov, 2018). Typical routes of entry for these CECs into the environment include incorrect disposal of products in the sewage or landfills (which can leach into the soils and the surrounding groundwater), human

excretion (particularly for pharmaceuticals and illicit drugs), human use (e.g. washing off of personal care products applied on the skin), and agricultural runoff into ground and surface water (particularly for pesticides) (Heberer, 2002; Marshall, 2017; Kolosov, 2018). The term CECs is often interchangeably used with the term "micropollutants", since CECs are typically found in concentrations of ng/L to µg/L (Yang, 2017; Verlicchi, 2018; Sousa *et al.*, 2019). Conventional wastewater treatment processes have not been designed to remove contaminants present in such low concentrations, nor contaminants that are biologically recalcitrant (Verlicchi *et al.*, 2010; Barbosa *et al.*, 2015; Kolosov, 2018). As a consequence, CECs are often not adequately removed in wastewater treatment plants and persist during the water use cycle (Naidu, Arias Espana, *et al.*, 2016; Rodriguez-Narvaez *et al.*, 2017). They have been detected in numerous waterbodies across the world, hence representing a global problem (Naidu, Arias Espana, *et al.*, 2016).

There is limited information on the fate and transport of CECs in the environment and their toxicological impact, due to the large number of different CECs, limited financial resources and the lack of analytical techniques for comprehensively examining the effects of CECs or their mixtures with other CECs or contaminants on ecosystems and human health (Naidu, Arias Espana, *et al.*, 2016; Noguera-Oviedo and Aga, 2016). Even if many CECs have demonstrated low acute toxicity in laboratory studies, this does not exclude them from posing a risk (Noguera-Oviedo and Aga, 2016). In some cases, metabolites and TPs of CECs can have higher toxicity than their parent compounds (Matsushita *et al.*, 2015; Noguera-Oviedo and Aga, 2016; Lee *et al.*, 2018). Furthermore, the effects of chronic exposure to mixtures of CECs is largely unknown (Magureanu, Mandache and Parvulescu, 2015; Naidu, Arias Espana, *et al.*, 2016; Noguera-Oviedo and Aga, 2016). In order to address this knowledge gap, research on CECs has been exponentially increasing since the 1990s (Naidu, Jit, *et al.*, 2016). Toxicological studies on CECs carried out so far have raised various concerns, for instance: estrogens can cause reproductive defects on fish and amphibians (Kidd *et al.*, 2007; Harding *et al.*, 2016; Naidu, Arias Espana, *et al.*, 2016); antibiotics may promote the development of antibiotic resistance genes in bacteria and in the soil environment (Kümmerer, 2009; Gracia-Lor *et al.*, 2012; Noguera-Oviedo and Aga, 2016; Rodriguez-Narvaez *et al.*, 2017); pesticides can have toxic and adverse endocrine disrupting effects on aquatic life, and cause toxic and carcinogenic effects on human health (Marshall, 2017; Kolosov, 2018; Magureanu, Bradu and Parvulescu, 2018). Recently, concerns have been raised that CECs can

enter plants through their water uptake and can bioaccumulate, potentially reaching humans and animals that eat those plants (Keerthanan *et al.*, 2020).

Because of potential risks to ecosystems and human health, some countries have started to develop or implement regulations for CEC monitoring and discharge limits (Naidu, Jit, *et al.*, 2016; Marshall, 2017; Sousa *et al.*, 2019). After pioneering regulations in Europe in recent years, it is expected that countries in North America and Oceania will follow soon (Naidu, Jit, *et al.*, 2016; Marshall, 2017). In Canada's ongoing Chemical Management Plan (CMP), the Canadian government has committed to addressing 4300 chemicals – some of them CECs – by 2020 in terms of risk assessment, risk management, compliance promotion and enforcement, and research and monitoring (Government of Canada, 2014). The upcoming regulations – as well as precautionary principles related to the unknown toxicological impact of many CECs – call for rapid technological development in assessment and removal of CECs (Naidu, Jit, *et al.*, 2016; Noguera-Oviedo and Aga, 2016; Gomes *et al.*, 2017; Marshall, 2017; Kolosov, 2018).

2.2.2 Iodinated contrast media

Iodinated contrast media (ICM) are a family of pharmaceuticals that are among the most prevalent CECs (Lopez-Prieto *et al.*, 2020). ICM were first introduced into clinical practice in the 1950s and are currently extensively used in human medicine for radiological and medical diagnostic purposes (Pasternak and Williamson, 2012; Mendoza *et al.*, 2016; Jeong *et al.*, 2017; Strehl *et al.*, 2019; Nowak, Pacek and Mrozik, 2020). They are given to patients intravascularly or orally and act as radiographic dyes, enhancing the visibility of organs and blood vessels (Pérez and Barceló, 2007; Pasternak and Williamson, 2012).

2.2.2.1 Molecular structure and routes of entry into waterbodies

At present, the most commonly used ICM are diatrizoate, iohexol, iomeprol, iopamidol and iopromide (Nowak, Pacek and Mrozik, 2020). Fig. 2-6 shows their molecular structure, which consists of a tri-iodinated benzene ring with alkyl side chains containing amide, hydroxyl and/or carboxyl functionalities. ICM are often classified as ionic (with a carboxylate-containing benzene substituent) or non-ionic (without a carboxylate-containing benzene substituent) (Nowak, Pacek and Mrozik, 2020). The covalent bonding of iodine to a stable organic functional group (i.e. benzene) reduce the risk of releasing free iodide into the human body (Pasternak and Williamson,

2012; Nowak, Pacek and Mrozik, 2020). The side chains contribute to making the compounds highly soluble in water (Kalsch, 1999; Steger-Hartmann, Länge and Schweinfurth, 1999; Zhao *et al.*, 2014). Although these properties are required for medical treatment purposes, these same properties lead to ICM being excreted in unmetabolized form in feces and urine, typically within one day for healthy patients (Hartwig, Mützel and Taenzer, 1989; Nossen *et al.*, 1995; Pérez and Barceló, 2007; Pasternak and Williamson, 2012; Strehl *et al.*, 2019). Since (1) hospital wastewaters are usually not collected separately and (2) many patients are sent home shortly after the radiographic procedures, excreted ICM typically enter municipal wastewater streams and reach municipal wastewater treatment plants (Weissbrodt *et al.*, 2009; Mendoza *et al.*, 2016; Verlicchi, 2018; Strehl *et al.*, 2019). Because of their particularly high chemical and biological stability and their low tendency to adsorb to sewage sludge, ICM are not adequately removed in conventional wastewater treatment plants (Kalsch, 1999; Steger-Hartmann, Länge and Schweinfurth, 1999; Ternes and Hirsch, 2000; Putschew, Schittko and Jekel, 2001; Echeverría *et al.*, 2013; Zemann *et al.*, 2014; Hong *et al.*, 2019).

2.2.2.2 Environmental presence

ICM have been monitored in several countries in different types of aqueous environments such as hospital effluents, wastewater treatment plant effluents and various waterbodies. Table *2-1* shows mean and maximum monitored ICM concentrations (or alternatively median concentrations where mean concentrations were not available). In hospital effluents the concentrations span from ng/L to mg/L. Both in wastewater treatment plant influents and effluents the concentrations range from ng/L to µg/L, confirming that ICM are generally not adequately removed in the treatment process. In surface waters and groundwaters the concentrations vary between ng/L and µg/L – with ng/L concentration in river estuaries and seawater. In summary, the reviewed studies report appreciable concentrations of ICM in wastewater streams and the environment in numerous locations across the world (Ternes and Hirsch, 2000; Putschew, Schittko and Jekel, 2001; Sacher *et al.*, 2001; Seitz, Weber, *et al.*, 2006; Schulz *et al.*, 2008; Weissbrodt *et al.*, 2009; Boleda, Galceran and Ventura, 2011; Duirk *et al.*, 2011; Wolf, Zwiener and Zemann, 2012; Echeverría *et al.*, 2013; Zemann *et al.*, 2014; Birch *et al.*, 2015; Mendoza *et al.*, 2015, 2016; Kleywegt *et al.*, 2016; Xu *et al.*, 2017; Azuma *et al.*, 2019; Hong *et al.*, 2019; Anim *et al.*, 2020; Zheng *et al.*, 2020).

In an effort to reduce ICM concentrations in the River Ruhr in Germany, a recent pilot study used urine bags to collect contaminated urine of patients that had undergone diagnostic tests in four medical facilities (Strehl *et al.*, 2019). The results showed 20–34% reduction of mean ICM concentrations in the River Ruhr, which according to the authors is promising and encouraging to continue this project on a broader scale (Strehl *et al.*, 2019). However, this may just displace the problem into different waterbodies, since urine bags are treated as non-recyclable domestic waste and later disposed into landfills, where ICM could potentially leach into the soils and the surrounding groundwater.
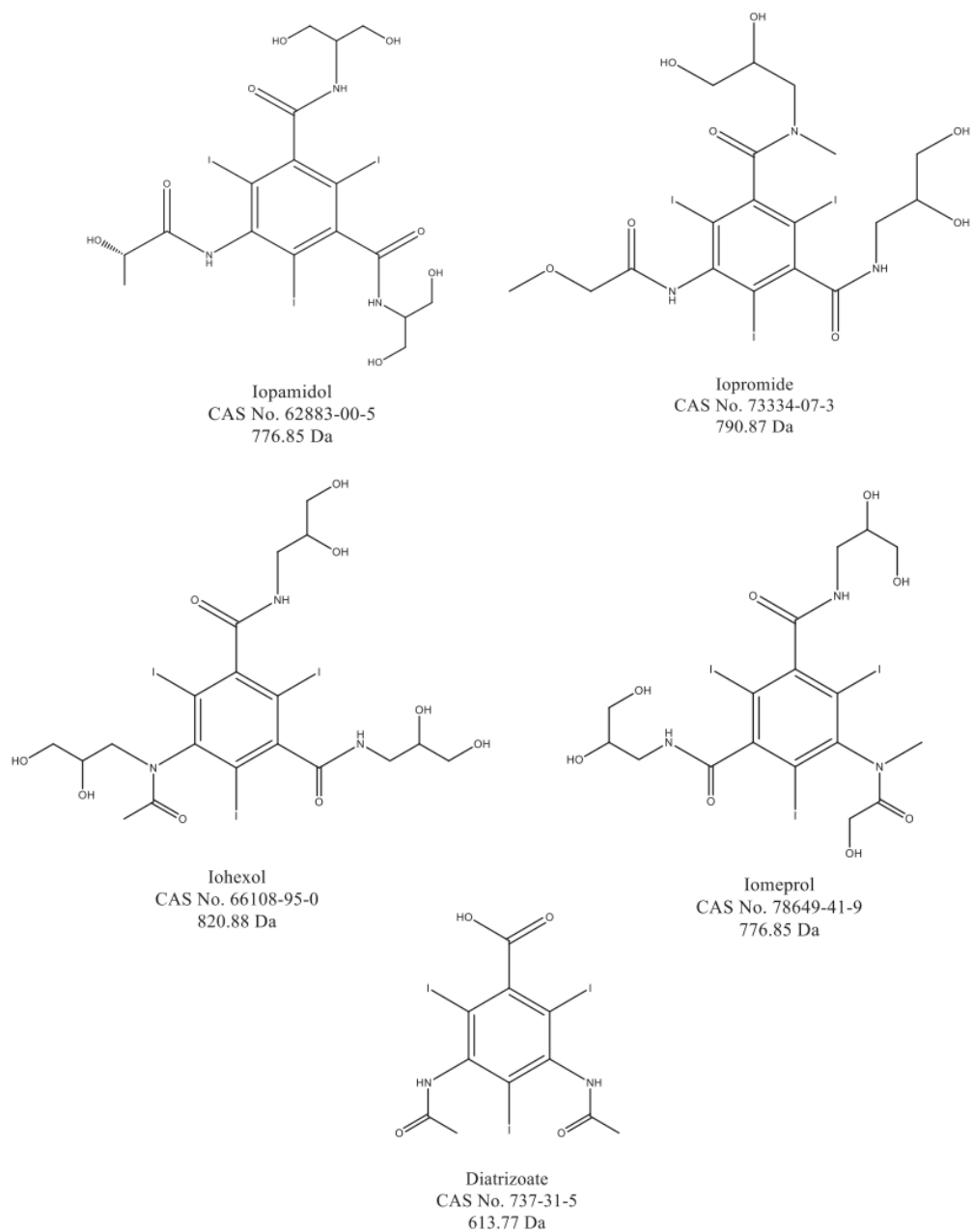
Fig. 2-6 Chemical structures and molecular weights of five common iodinated contrast media (Jeong *et al.*, 2017)

Table 2-1 Review of ICM monitored in various locations across the world (Ternes and Hirsch, 2000; Putschew, Schittko and Jekel, 2001; Sacher *et al.*, 2001; Seitz, Weber, *et al.*, 2006; Schulz *et al.*, 2008; Weissbrodt *et al.*, 2009; Boleda, Galceran and Ventura, 2011; Duirk *et al.*, 2011; Wolf, Zwiener and Zemann, 2012; Echeverría *et al.*, 2013; Zemann *et al.*, 2014; Birch *et al.*, 2015; Mendoza *et al.*, 2015, 2016; Kleywegt *et al.*, 2016; Xu *et al.*, 2017; Azuma *et al.*, 2019; Hong *et al.*, 2019; Anim *et al.*, 2020; Zheng *et al.*, 2020).

Location (country)	Type of ICM	Aqueous environment	Mean (max) concentrations (ng/L)	Additional information	References
Qingdao area (China)	iopromide	rivers	112 (max. 1744)	27 sampling sites across 5 rivers; 14 seawater sampling sites	Zheng 2020
		seawater	37 (max. 244)		
Sydney, Brisbane and Yarra River Estuaries (Australia)	iopromide	river estuary (Sydney)	5 (max. 12)	15 - 31 sampling sites per river estuary	Anim 2020 and Birch 2015
		river estuary (Brisbane)	28 (max. 94)		
		river estuary (Yarra)	7 (max. 13)		
Yodo River basin (Japan)	iohexol	hospital effluents	2074 (max. 3018)	core general hospital with mean 1200 patients/day (mean flow 460m3/day); river water sampled 1 km downstream of STP effluent point of entry	Azuma 2019
		STP influents	10,340 (max. 20,290)		
		STP effluents (chlorination)	8178 (max. 17,325)		
		STP effluents (ozonation)	696 (max. 1255)		
		river	1280 (max. 3041)		
	iomeprol	hospital effluents	11659 (max. 14,657)		
		STP influents	3919 (max. 13,719)		
		STP effluents (chlorination)	2086 (max. 5071)		
		STP effluents (ozonation)	241 (max. 601)		
		river	659 (max. 1717)		
	iopamidol	hospital effluents	20089 (max. 26,336)		
		STP influents	4441 (max. 11,602)		
		STP effluents (chlorination)	3021 (max. 5564)		
		STP effluents (ozonation)	724 (max. 1503)		
		river	1434 (max. 2508)		
	iopromide	hospital effluents	70 (max. 272)		

Location (country)	Type of ICM	Aqueous environment	Mean (max) concentrations (ng/L)	Additional information	References
		STP influents	126 (max. 404)		
		STP effluents (chlorination)	155 (max. 538)		
		STP effluents (ozonation)	31 (max. 72)		
		river	54 (max. 137)		
	ioversol	hospital effluents	11 (max. 23)		
		STP influents	99 (max. 266)		
		STP effluents (chlorination)	815 (max. 3028)		
		STP effluents (ozonation)	42 (max. 124)		
		river	72 (max. 181)		
Seoul area (Korea)	iopromide	STP 1 influents	1167	averages of 7 samples	Hong 2019
		STP 1 effluents	2281		
		river upstream STP 1	1556		
		river downstream STP 1	2248		
		STP 2 influents	1316		
		STP 2 effluents	1913		
		river upstream STP 2	601		
		river downstream STP 2	2160		
Yangtze River Delta (China)	diatrizoate	lake	3 (max. 14)	9 sampling sites on Taihu Lake and 11 on Huangpu River	Xu 2017
		river	14 (max. 14)		
	iohexol	lake	89 (max. 93)		
		river	94 (max. 100)		
	iomeprol	lake	1 (max. 2)		
		river	2 (max. 5)		
	iopamidol	lake	<LOQ		
		river	26 (max. 91)		
	iopromide	lake	4 (max. 28)		

Location (country)	Type of ICM	Aqueous environment	Mean (max) concentrations (ng/L)	Additional information	References
		river	28 (max. 51)		
Toronto area (Canada)	diatrizoate	hospital 1 effluents	1115 (max. 1660)	median concentrations are shown instead of mean concentrations; sewershed includes a total of 3 large urban hospitals (hospitals 1 and 2) and 22 health care facilities; hospital 3 is a large hospital outside the studied sewershed	Kleywegt 2016
		hospital 2 effluents	2360 (max. 3220)		
		hospital 3 effluents	16,400 (max. 50,200)		
		STP influents	205 (max. 538)		
		STP effluents	196 (max. 290)		
	iopamidol	hospital 1 effluents	<LOD		
		hospital 2 effluents	<LOD		
		hospital 3 effluents	32,765 (max. 61,700)		
		STP influents	594 (max. 1110)		
		STP effluents	564 (max. 930)		
Madrid Region (Spain)	diatrizoate	drinking water (Titulcia)	0	median concentrations are shown instead of mean concentrations; sampling in private residences in different cities/towns	Mendoza 2016
		drinking water (Alcorcón)	0		
		drinking water (Madrid city)	0		
		drinking water (Aranjuez)	1 (max. 1)		
	iohexol	drinking water (Titulcia)	2 (max. 4)		
		drinking water (Alcorcón)	1 (max. 2)		
		drinking water (Madrid city)	1 (max. 2)		
		drinking water (Aranjuez)	3 (max. 5)		
	iomeprol	drinking water (Titulcia)	0		
		drinking water (Alcorcón)	0		
		drinking water (Madrid city)	1 (max. 1)		
		drinking water (Aranjuez)	0		
	iopamidol	drinking water (Titulcia)	0		
		drinking water (Alcorcón)	0		

Location (country)	Type of ICM	Aqueous environment	Mean (max) concentrations (ng/L)	Additional information	References
		drinking water (Madrid city)	0		
		drinking water (Aranjuez)	0		
	iopromide	drinking water (Titulcia)	1 (max. 1)		
		drinking water (Alcorcón)	0		
		drinking water (Madrid city)	0		
		drinking water (Aranjuez)	0		
	iodinaxol	drinking water (Titulcia)	0		
		drinking water (Alcorcón)	0		
		drinking water (Madrid city)	0		
		drinking water (Aranjuez)	0		
Valencia Region (Spain)	iomeprol	hospital effluents	1,139,000 (max. 2,093,000)	medium-sized hospital (mean flow 370 m3/day)	Mendoza 2015
Lower Jordan Valley (Jordan)	diatrizoate	groundwater	120 (max. 940)	median concentrations of positives are shown instead of mean concentrations; overall 26 sampling points and 95 samples over 5 years	Zemann 2014
		surface water	140 (max. 850)		
		WWTP effluents	120 (max. 300)		
	iohexol	groundwater	31 (max. 180)		
		surface water	645 (max. 1600)		
		WWTP effluents	270 (max. 9000)		
	iomeprol	groundwater	39 (max.790)		
		surface water	2200 (max. 6900)		
		WWTP effluents	1400 (max. 360,000)		
	iopamidol	groundwater	59 (max. 36,000)		
		surface water	1100 (max. 78,000)		
		WWTP effluents	6600 (max. 680,000)		
	iopromide	groundwater	24 (max. 250)		

Location (country)	Type of ICM	Aqueous environment	Mean (max) concentrations (ng/L)	Additional information	References
		surface water	650 (max. 4500)		
		WWTP effluents	860 (max. 280,000)		
	iotalamic acid	groundwater	10 (max. 10)		
		surface water	21 (max. 23)		
		WWTP effluents	42 (max. 42)		
Tarragona (Spain)	diatrizoate	STP influents	4118 (max. 4672)	3 influent and 3 effluent samples	Echeverría 2013
		STP effluents	2789 (max. 2820)		
	iohexol	STP influents	4969 (max. 5420)		
		STP effluents	3392 (max. 3461)		
	iomeprol	STP influents	4587 (max. 4633)		
		STP effluents	3250 (max. 3521)		
	iopamidol	STP influents	1485 (max. 1627)		
		STP effluents	804 (max. 861)		
	iopromide	STP influents	8091 (max. 8885)		
		STP effluents	6891 (max. 7082)		
Rastatt urban area (Germany)	diatrizoate	groundwater	66 (max. 4240)	60 sampling sites; other ICM were monitored as well, but they selected diatrizoate as focus substance and studied it to a greater extend	Wolf 2012
		surface water	98 (max. 353)		
		wastewater	512 (max. 703)		
Anonymous 10 cities (United States)	diatrizoate	DWTP effluents	(max. 93)	DTP used chlor(amin)ation	Duirk 2011
	iohexol	DWTP effluents	(max. 120)		
	iomeprol	DWTP effluents	<LOQ		
	iopamidol	DWTP effluents	(max. 2700)		
	iopromide	DWTP effluents	(max. 25)		

Location (country)	Type of ICM	Aqueous environment	Mean (max) concentrations (ng/L)	Additional information	References
Llobregat River (Spain)	diatrizoate	DWTP influents	(max. 59)	samples were collected daily during five consecutive days	Boleda 2011
		DWTP effluents (ultrafiltration)	<LOD		
		DWTP effluents (reverse osmosis)	<LOD		
	iohexol	DWTP influents	(max. 71)		
		DWTP effluents (ultrafiltration)	<LOD		
		DWTP effluents (reverse osmosis)	<LOD		
	iopromide	DWTP influents	(max. 505)		
		DWTP effluents (ultrafiltration)	(max. 417)		
		DWTP effluents (reverse osmosis)	(max. 17)		
Anonymous cantonal hospital (Switzerland)	iohexol	hospital effluents	(max. 1,700,000)	medium-sized hospital (mean flow 379 m3/day)	Weissbrodt 2009
	iomeprol	hospital effluents	(max. 2,400,000)		
	iopamidol	hospital effluents	(max. 1,120,000)		
	iopromide	hospital effluents	(max. 1,390,000)		
	ioxitalamic acid	hospital effluents	(max. 550,000)		
Anonymous WWTPs (Germany)	iopromide	WWTP1 influents	3700	3 different WWTPs; 1 week composite samples	Schulz 2008
		WWTP1 effluents	1200		
		WWTP2 influents	31,000		
		WWTP2 effluents	7000		
		WWTP3 influents	5000		
Danube River (Germany)	diatrizoate	river (upstream of STP)	89 (max. 190)	median concentrations are shown instead of mean	Seitz 2006
		river (downstream of STP)	155 (max. 580)		

Location (country)	Type of ICM	Aqueous environment	Mean (max) concentrations (ng/L)	Additional information	References
	iohexol	river (upstream of STP)	40 (max. 125)	concentrations; 2 h-composite samples	
		river (downstream of STP)	86 (max. 360)		
	iomeprol	river (upstream of STP)	100 (max. 210)		
		river (downstream of STP)	160 (max. 480)		
	iopamidol	river (upstream of STP)	210 (max. 470)		
		river (downstream of STP)	210 (max. 520)		
	iopromide	river (upstream of STP)	76 (max.125)		
		river (downstream of STP)	100 (max. 220)		
Baden-Wurttemberg (Germany)	diatrizoate	groundwater	(max. 1100)	105 monitoring wells	Sacher 2001
	iopamidol	groundwater	(max. 300)		
Berlin (Germany)	diatrizoate	STP effluents	13	both channel and lake receive STP effluents	Putschew 2001
		channel	7		
		lake	3		
	iohexol	STP effluents	7		
		channel	2		
		lake	<1		
	iopromide	STP effluents	20		
		channel	11		
		lake	4		
Frankfurt/Main area (Germany)	diatrizoate	STP influents	3300	1 municipal STP (25 STPs in second part of project, values not reported here); 25 rivers and creeks; 1 groundwater sampling site (Hessian Ried)	Ternes 2000
		STP effluents	4100		
		rivers and creeks	(max. 8700)		
		groundwater	(max. 170)		
	iomeprol	STP influents	1600		
		STP effluents	1300		
		rivers and creeks	(max. 890)		

Location (country)	Type of ICM	Aqueous environment	Mean (max) concentrations (ng/L)	Additional information	References
		groundwater	-		
	iopamidol	STP influents	4300		
		STP effluents	4700		
		rivers and creeks	(max. 2700)		
		groundwater	(max. 2400)		
	iopromide	STP influents	7500		
		STP effluents	8100		
		rivers and creeks	(max. 910)		
		groundwater	(max. 210)		
	iothalamic acid	STP influents	180		
		STP effluents	140		
		rivers and creeks	(max. 120)		
		groundwater	(max. 49)		
	ioxithalamic acid	STP influents	170		
		STP effluents	160		
		rivers and creeks	(max. 80)		
		groundwater	(max. 10)		

2.2.2.3 Detrimental effects on ecosystems and human health

ICM have been designed to be well-tolerated by humans during short medical procedures (Steger-Hartmann, Länge and Schweinfurth, 1999; Duirk *et al.*, 2011). Nevertheless, chronic exposure to ICM or their combination with pharmaceuticals found in the aquatic environment may lead to unpredictable effects (Jeong *et al.*, 2010; Magureanu, Mandache and Parvulescu, 2015; Klatte, Schaefer and Hempel, 2017). Recent medical studies showed that some patients react to ICM upon their first contact in a clinical context, and one study suggested that these allergies may have been developed by previous exposure to ICM through drinking water (Böhm, 2018).

Although studying the effects of CECs on ecosystems is a complex task, there have been efforts to investigate possible effects of ICM on the environment. One study reported estrogen activity of iopromide, but later discussions showed that this estrogen activity could not be demonstrated (Krause *et al.*, 2009, 2010; Länge *et al.*, 2010). Short-term toxicity tests with bacteria, algae, crustaceans and fish did not show any toxic effects, even at high ICM doses (10 g/L iopromide) (Steger-Hartmann, Länge and Schweinfurth, 1999). Chronic toxicity tests during 22 days with the crustacean *Daphnia Magna* did not reveal any toxic effects (1 g/L iopromide) (Steger-Hartmann, Länge and Schweinfurth, 1999).

Even if the parent compounds have low toxicity, it cannot be concluded that there is no risk arising from their TPs (Kalsch, 1999). ICM can be subject to aerobic and anaerobic biotransformation in the environment or during wastewater treatment, forming various TPs with largely unknown toxicological significance (Seitz, Weber, *et al.*, 2006; Redeker *et al.*, 2014, 2018). The TPs formed during water disinfection through chlorination or chloramination are particularly concerning: there is evidence that TPs of several ICM can be cytotoxic (iopamidol, iopromide, iohexol, diatrizoate, iomeprol) and genotoxic (iopamidol, iohexol) to mammalian cells (Duirk *et al.*, 2011; Wendel *et al.*, 2014; Jeong *et al.*, 2017). The presence of natural organic matter (NOM) in treated water can significantly enhance the formation of toxic disinfection TPs (Duirk *et al.*, 2011; Ye *et al.*, 2014). Out of precautionary principles, assessing the toxicity of TPs should be a crucial step when selecting a treatment process for wastewater containing ICM.

2.2.2.4 Advanced treatment technologies

As discussed earlier, conventional biological treatments are not able to adequately remove ICM from wastewater, and traditional disinfection by chlor(am)ination leads to the formation of highly toxic TPs. For this reason, the effect of various AOPs on ICM that has been investigated over the last two decades.

Early attempts with AOPs included ozonation and O_3/H_2O_2. Although the latter was more effective, both achieved little to partial ICM degradation (Huber *et al.*, 2003, 2005; Ternes *et al.*, 2003; Snyder *et al.*, 2006; Seitz *et al.*, 2008). Reaction rates with $^{\bullet}$OH (e.g. $k_{^{\bullet}OH,iopromide} = 3.3$ x 10^9 M^{-1} s^{-1}) (Huber *et al.*, 2003) were much higher than with ozone (e.g. $k_{O_3,iopromide} = <0.8$ M^{-1} s^{-1} and $k_{O_3,diatrizoate} = 0.05$ M^{-1} s$^-$) (Huber *et al.*, 2003; Real *et al.*, 2009), and several studies suggested that ICM do not react with ozone directly but rather in indirect reactions via $^{\bullet}$OH (Huber *et al.*, 2003, 2005; Seitz *et al.*, 2008; Real *et al.*, 2009; Wert, Rosario-Ortiz and Snyder, 2009). In general, low to no mineralization was achieved (Huber *et al.*, 2003; Seitz *et al.*, 2008; Matsushita *et al.*, 2016). A study on ozonation of iopamidol identified the formation of several toxic TPs (acute toxicity to *Daphnia Magna*), which decreased with prolonged treatment times (Rivas *et al.*, 2019). Lower removal rates were achieved for ionic vs. non-ionic ICM, with DTZ being particularly recalcitrant (Ternes *et al.*, 2003; Huber *et al.*, 2005; Seitz, Jiang, *et al.*, 2006; Seitz *et al.*, 2008; Hansen *et al.*, 2016). For DTZ, although O_3/H_2O_2 yielded higher removal than ozonation (14 % removal at highest dose of 15 mg/L ozone), removal was still low (25 % removal at highest dose of 10 mg/L O_3/H_2O_2) (Ternes *et al.*, 2003). In both cases, the average initial DTZ concentration was 5.7 µg/L (Ternes *et al.*, 2003). A more recent study with an optimized ozonation pilot system achieved 90 % degradation of DTZ (initial concentration between 10–80 µg/L, not specified in this study) (Hansen *et al.*, 2016). The ozone dose requirement was 4.7 ± 0.6 mg O_3/mg DOC (DOC: dissolved organic carbon), the highest requirement of the 33 studied pharmaceuticals (Hansen *et al.*, 2016).

Numerous studies explored degradation of ICM via photo(cata)lysis, including UV (Real *et al.*, 2009; Kovalova *et al.*, 2013; Giannakis *et al.*, 2017; Azerrad, Isaacs and Dosoretz, 2019), UV or sunlight/O_3 (Ternes *et al.*, 2003; Rivas *et al.*, 2019), UV or sunlight/H_2O_2 (Real *et al.*, 2009; Polo *et al.*, 2016; Giannakis *et al.*, 2017; Nihemaiti *et al.*, 2018; Azerrad, Isaacs and Dosoretz, 2019; X.

Zhao *et al.*, 2019), UV or sunlight/Fenton (Real *et al.*, 2009; Polo *et al.*, 2016; Giannakis *et al.*, 2017), UV/TiO$_2$ (Kovalova *et al.*, 2013; Azerrad, Isaacs and Dosoretz, 2019), sunlight/BN-Bi$_2$MoO$_6$ (He *et al.*, 2020), UV/NaClO (X. Zhao *et al.*, 2019) and gamma radiation (Jeong *et al.*, 2010; Velo-Gala *et al.*, 2012). In general, photo(cata)lysis provided significantly higher ICM removal (and in some cases mineralization) than dark ozonation or dark Fenton (Ternes *et al.*, 2003; Real *et al.*, 2009; Rivas *et al.*, 2019). Real et al. (2009) and Nihemaiti et al. (2018) reported that direct photolysis with UV had a larger contribution to ICM removal than reactions with radicals such as $^\bullet$OH and SO$_4$$^{\bullet-}$ (Real *et al.*, 2009; Nihemaiti *et al.*, 2018). However, particularly recalcitrant ICM such as DTZ or ioxitalamic acid required very high UV doses to achieve substantial removal (95 % removal at 7200 J/m^2 fluence and 180 min recirculation), with remaining ICM concentrations that were still considerably high (20 µg/L) (Kovalova *et al.*, 2013). An *in silico* study on the degradation of DTZ by direct photolysis with UV predicted some photo-TPs to be active for mutagenicity and genotoxicity (Rastogi, Leder and Kümmerer, 2014). Furthermore, *in vitro* acute toxicity tests with *Vibrio Fischeri* showed that solar radiation / H$_2$O$_2$ or Fenton led to the formation of toxic TPs of DTZ, which were still present after 90 min treatment (Polo *et al.*, 2016).

Other technologies that were investigated include activated carbon, reverse osmosis (RO) membranes and electrochemistry. Activated carbon technologies failed to adequately remove ICM, with partial removal of neutral ICM like iopromide and practically no removal of negatively charged ICM like DTZ (Kovalova *et al.*, 2013; Rizzo *et al.*, 2019). RO membranes could be a tool to remove ICM from wastewater streams, but the produced concentrated brine would require treatment (Gur-Reznik *et al.*, 2011; Azerrad *et al.*, 2014) – this does not solve the problem but displaces it to another aqueous solution. Electrochemical processes showed some promising results for the removal of ICM parent compounds (Tissot *et al.*, 2012; Del Moro *et al.*, 2015; Wu *et al.*, 2017; Korshin and Yan, 2018; Turkay *et al.*, 2018; Yan *et al.*, 2018; Moura de Salles Pupo *et al.*, 2020), but there is evidence that both direct electrochemical reduction and indirect electrochemical oxidation (using anodes that produce ROS) can lead to the formation of toxic TPs (Del Moro *et al.*, 2015; Korshin and Yan, 2018; Yan *et al.*, 2018). Even with long treatment times and high current densities (e.g. 150 min at 64 mA/cm^2), complete mineralization was not achieved and toxic TPs remained in the treated water (Del Moro *et al.*, 2015).

Recently, AOPs involving the formation of sulfate radical anions ($SO_4^{\bullet-}$) from peroxymonosulfate (PMS) or peroxydisulfate (PDS) have been applied for the treatment of ICM, e.g. O_3/PMS (Mao *et al.*, 2020), Co^{2+}-activated PMS (H. Zhao *et al.*, 2019; X. Wang *et al.*, 2019), zero-valent Al-activated PDS (Arslan-Alaton *et al.*, 2017; Olmez-Hanci *et al.*, 2017), heat-activated PDS (Wang *et al.*, 2020), UV or sunlight/PDS (Polo *et al.*, 2016; Nihemaiti *et al.*, 2018; X. Zhao *et al.*, 2019). $SO_4^{\bullet-}$ can react with aqueous organic pollutants directly or indirectly via the formation of $^{\bullet}OH$ (H. Zhao *et al.*, 2019; Mao *et al.*, 2020). The reaction rate of $SO_4^{\bullet-}$ with ICM is somewhat lower than the one of $^{\bullet}OH$ (e.g. $k_{SO_4^{\bullet-},iopamidol} = 1.6 \times 10^9$ M^{-1} s^{-1} and $k_{SO_4^{\bullet-},iopromide} = 3.6 \times 10^8$ M^{-1} s^{-1}) (Nihemaiti *et al.*, 2018; Mao *et al.*, 2020). Whereas Mao et al. (2020) showed that contribution of $^{\bullet}OH$ to iopamidol degradation was about 80 % (Mao *et al.*, 2020), Zhao et al. (2019) and Lv et al. (2019) observed that $SO_4^{\bullet-}$ was the dominant radical contributing to the degradation of iohexol (H. Zhao *et al.*, 2019; Lv *et al.*, 2019). There are potential toxicological risks of using $SO_4^{\bullet-}$ for ICM degradation, since there is evidence of formation of toxic TPs of iohexol after treatment with Co^{2+}-activated PMS (H. Zhao *et al.*, 2019) and of DTZ after treatment with sunlight/PDS (Polo *et al.*, 2016).

Nowadays, some of the discussed AOPs are established at full-scale, whereas others are still being investigated at lab- or pilot-scale. Fig. 2-7 shows a general classification of AOPs (not specifically related to ICM research).
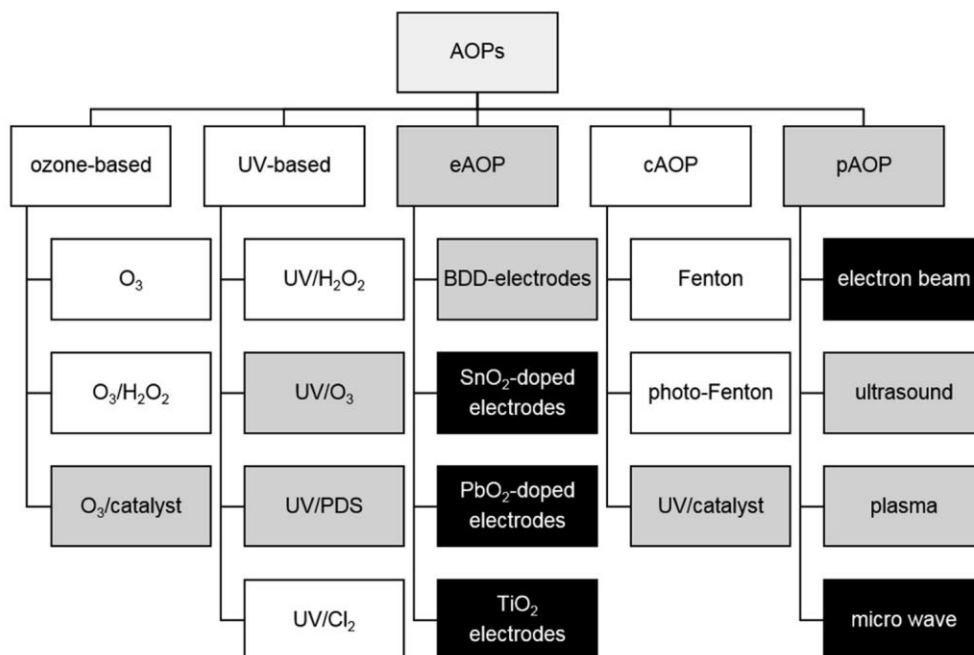
Fig. 2-7 Broad overview and classification of different AOPs. Individual processes are marked as established at full-scale (white), investigated at lab- and pilot-scale (grey) and tested at lab-scale (black), according to data from 2018. eAOP: electrochemical AOP; cAOP: catalytic AOP; pAOP: physical AOP (Miklos *et al.*, 2018)

2.2.3 Relevance of studying plasma technologies for the removal of iodinated contrast media

The previous section discussed numerous efforts to find a treatment technology that ensures adequate removal of ICM. Although high removal rates were achieved by certain technologies, certain ICM required unusually high doses (e.g. ozone or UV radiation) and thus entailed higher energy consumption than the one required to treat other aqueous pollutants (Kovalova *et al.*, 2013; Hansen *et al.*, 2016). Even if high removal rates were achieved for ICM parent compounds, complete mineralization was not reached. This means that TPs remained in the solution, and they were toxic in many cases (e.g. in some ozonation, photo(cata)lytic, electrochemical or $SO_4^{\bullet-}$-based treatments) or their harmfulness is still unknown (Rastogi, Leder and Kümmerer, 2014; Del Moro *et al.*, 2015; Polo *et al.*, 2016; Korshin and Yan, 2018; Yan *et al.*, 2018; H. Zhao *et al.*, 2019; Rivas *et al.*, 2019). Because of these reasons, two decades after research in this field started, the quest to find an effective treatment technology for ICM removal is still relevant. This opens the door for exploring unconventional alternatives, such as plasma technologies.
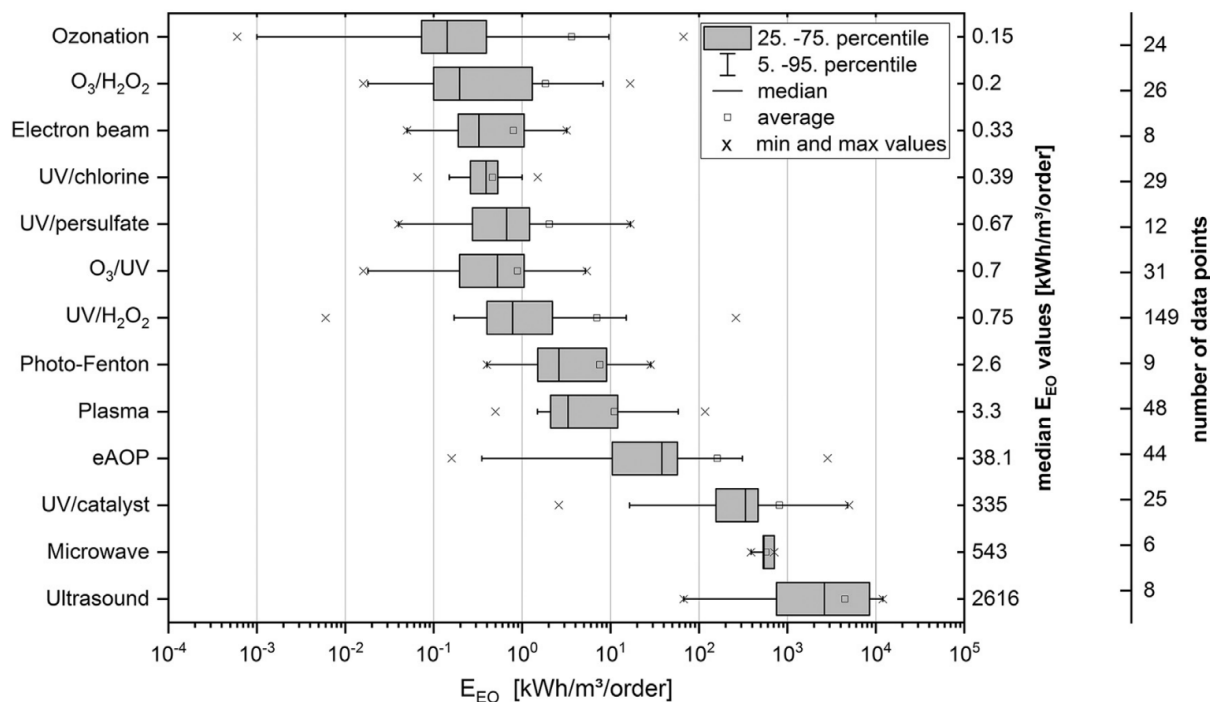
Fig. 2-8 Overview of published E_{EO}-values of different AOPs sorted according to median values. E_{EO} is defined as: "Electrical energy per order is the electrical energy in kWh required to degrade a contaminant C by one order of magnitude in 1 m^3 of contaminated water". For O_3- and UV-based AOP data, only substances resistant to direct ozonation/ photolysis are shown. Median values and number of data points are reported on the second and third y-axis, respectively (Miklos *et al.*, 2018).

Plasma technologies typically require higher energy consumption than several other AOPs, as shown in Fig. 2-8. However, as discussed in detail in 2.1.3, energy efficiency of plasma technologies has been improving over the past years, and the application of nanosecond pulsed discharges looks promising for lowering the energy consumption. The recalcitrance of ICM to other technologies (requiring above-average E_{EO}-values), together with lowering the energy consumption of plasma technologies through research and innovation, has the potential of reaching a point were plasma technologies become competitive in terms of energy consumption, cost and sustainability. Moreover, plasma technologies offer the advantage of producing all reactive species *in situ*, without the need of transporting, handling and storing chemicals (these are required for other technologies, e.g. for chlorination, H_2O_2-based or $SO_4^{\bullet-}$-based treatments).

In a recent success story, a plasma–liquid reactor was scaled up to pilot scale, and achieved rapid removal of particularly recalcitrant CECs (poly- and perfluorinated compounds in investigation-

derived wastewater) that virtually all other wastewater treatment technologies failed to adequately remove (Singh *et al.*, 2019). This sets a precedent for successful implementation of plasma technologies for the treatment of challenging wastewaters.

A few studies have already focused on plasma-based treatment of ICM; they will be reviewed in Chapter 6.

3

Methodology

This chapter provides information on the design and operation of the two pin-to-liquid reactors developed in the present work. Furthermore, it contains details pertaining to characterization which were not originally published within the Author's manuscripts (and thus not covered in the subsequent chapters).

3.1 Pin-to-liquid discharge reactors

3.1.1 Preliminary configuration

3.1.1.1 Reactor description

Fig. 3-1 shows a schematic and pictures of the preliminary pin-to-liquid setup. Disposable BrandTech™ BRAND™ UV-cuvettes (semi-micro or macro size depending on the experiment) were used as vessel. The initial experiments were performed in semi-micro cuvettes filled with 1 mL liquid, whereas the following experiments were run in semi-micro cuvettes filled with 3 mL liquid. As pin-to-liquid configuration, two copper electrodes (0.65 mm diameter) were placed in the cuvette, secured with a 3D-printed cap of acrylonitrile butadiene styrene plastic (ABS). The cap had three holes: two at opposite corners for introducing the electrodes and another one in the center to release gases produced by the plasma. One electrode (negative polarity for most experiments) was located about 1 mm above the liquid surface, whereas the other electrode was immersed in the liquid. The distance between the negative electrode and the liquid surface was fixed by clamping the electrode through another 3D-printed piece screwed on top of the cap. The cuvette was placed in a 3D-printed holder in the middle of a magnetic stirrer and contained a magnetic stir bar with the shape of a cube with the dimensions 8.5 mm x 1.5 mm x 1.5 mm for

continuous stirring. The 3D-printed parts were designed in the software Autodesk Fusion 360 (see schematics in Fig. 3-2).
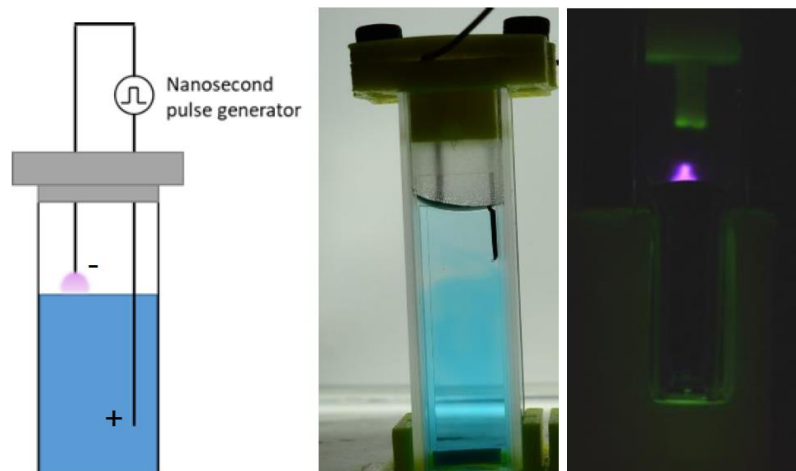
Fig. 3-1 Schematic of the preliminary experimental setup (left), picture of the setup under light (center) and picture of the setup in the dark with generated plasma (right). The electrodes are copper wires.
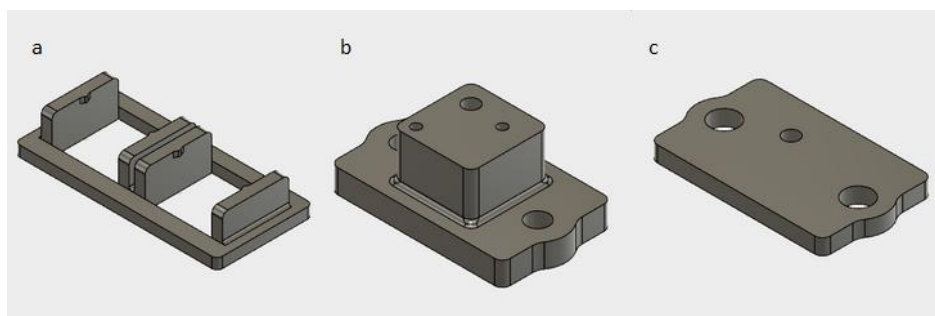
Fig. 3-2 3D printed parts: a – cuvette holder, b – full cuvette cap, c – top of the cuvette cap.

3.1.1.2 Electrical system

The electrodes were powered by a homemade diode opening switch generator, developed at the Plasma Processing Laboratory by Dr. Felipe Aristizábal and Dr. Mathew Evans. The diode opening switch generator supplied two simultaneous nanosecond pulses of equal voltage amplitude (one positive and one negative pulse). Fig. 3-3 shows the electrical system as it was used with the preliminary setup. At that point, the nanosecond pulser was being developed (this is why (4) and (6) were not yet enclosed in a box in Fig. 3-3). To run the nanosecond pulsed plasma a homemade pulse generator, a homemade gate drive, two power supplies (Sorensen 0-600 V and BK precision

0-20 V), a signal generator (Tektronix AFG3102) and an oscilloscope (Siglent SDS 2104X) were used. The discharge voltage signals were measured using two passive high-voltage probes (Tektronix P6015A). Voltage and pulse frequency operating ranges of the nanosecond pulser were tested and reported in 3.1.2.3.
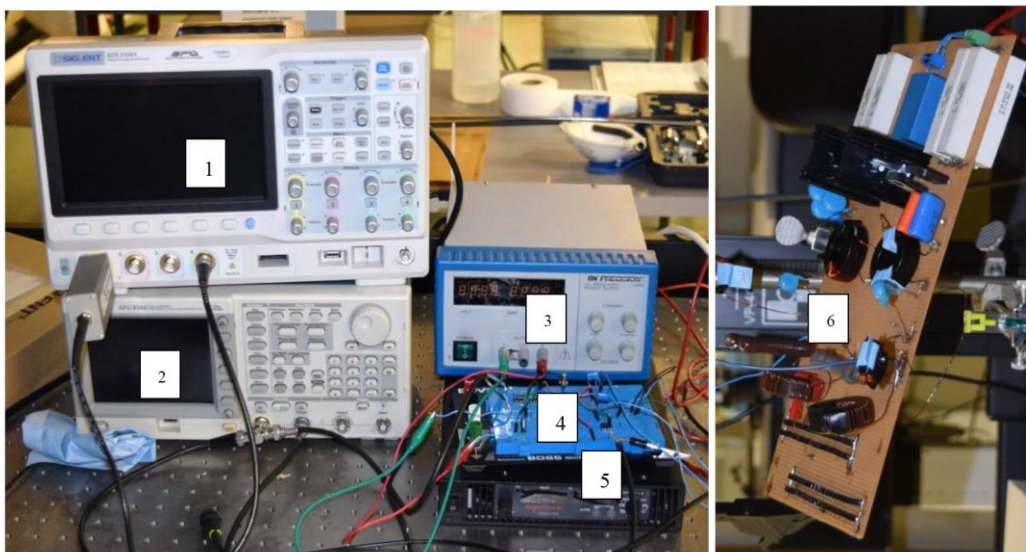
Fig. 3-3 Picture of electrical system with oscilloscope (1), signal generator (2), 0 – 20 V power supply (opens gates of pulse generator) (3), gate drive at 20 V (4), 0 – 600 V power supply (main power supply) (5), and nanosecond pulse generator (6).

3.1.1.3 Preparation of plasma-treated liquid samples

The steps followed for sample preparation can be found in the standard operating procedure in Appendix B.

3.1.2 Principal reactor

3.1.2.1 Reactor design criteria

Following experiments and observations with the preliminary pin-to-liquid discharge configuration described above, the principal reactor of this work was designed according to the following design criteria:

- Easy replacement of the gas-side pin electrode: A homemade reactor top lid allowed for rapid replacing and securing of the pin electrodes (see Fig. 3-4). This was useful for studying the erosion and effect of different electrode materials.

- Modification of the geometry of the submerged electrode: A cylindric, metallic sparger, was placed below the gas-side electrode (see Fig. 3-4), as opposed to the previous thin wire which had been placed in parallel to the gas-side electrode (see Fig. 3-1). According to Stratton et al. (2015), larger diameters of a submerged electrode (placed below the gas-side electrode) lead to longer leaders (plasma channels) propagating along the liquid surface, increasing the plasma–liquid interface (Stratton *et al.*, 2015)**.**

- Variation of gas atmospheres in the reactor chamber: A sealed reactor with a gas inlet (sparger at the bottom of the reactor) and outlet (opening at the top lid) allowed for testing the effect of different plasma carrier gases (see Fig. 3-4).

- Slight upscaling: In order to produce enough plasma-treated sample volume for analytical experiments, the reactor was designed to contain a sample volume of 7.5 mL.

- Mixing: In the previous setup, a magnetic stir bar was used to achieve thorough mixing. However, since one goal was to study metals introduced into the plasma-treated liquid by electrode erosion, a different method of mixing had to be utilized to avoid interactions between the eroded metals and the magnetic stir bar. By bubbling gas through a sparger at the bottom of the liquid, this ensured mixing without the need of a magnetic stir bar. Additionally, bubbling disrupted the liquid surface, potentially increasing the plasma–liquid contact area.

- Temperature control: In the previous setup, some evaporation of the liquid was observed after 20 min plasma treatment time. The temperature of the process liquid should be kept as constant as possible, and evaporation should be prevented in order to maintain a constant distance between the liquid and pin electrode. A circulating cooled water bath was used in the new setup to cool the glass vessel.

3.1.2.2 Reactor description

Fig. 3-4 shows a detailed schematic and picture of the compact pin-to-liquid discharge reactor. A borosilicate glass vessel, open at the top and the bottom, worked as temperature-controlled jacketed reactor. The glass vessel, shown in Fig. 3-5, was custom-made at JRV Scientific Glass Montreal (inner diameter 19.4 mm, height 83.5 mm). The cooling jacket was maintained at 20.5 °C using a circulating water chiller (Marshall Scientific, Thermo Neslab RTE 10 Circulating Chiller). The reactor was secured by a 3D printed plastic laboratory stand designed in Autodesk

Fusion 360 (see Fig. 0-1 in Appendix A) and printed in the Department of Chemical Engineering, McGill University. The stand, which was bolted to the table with 1/4"-screws, enabled to secure or take out the reactor with its lids quickly without needing a clamp that might harm the glass. The top and bottom part of the laboratory stand were connected through nylon threaded rods (10-32 UNF) and secured by nuts (10-32 UNF), all from McMaster-Carr.

The top and bottom of the glass vessel were sealed with lids made from polytetrafluorethylene (PTFE) (manufactured in the machine shop of the Department of Chemical Engineering, McGill University, from a PTFE rod ordered from McMaster-Carr). Fig. 0-2 and Fig. 0-3 (Appendix A) show the technical drawings of both lids. The top lid contained a channel for introducing the pin electrode vertically, as well as an elbow-shaped channel for the gas outlet. Where the pin electrode was introduced at the top, a rubber turnover septum (Fisher Scientific, 9 mm diameter) was used to seal the hole and prevent gas leaks. The pin electrode was secured by a PTFE piece (manufactured in the machine shop of the Department of Chemical Engineering, McGill University, see Fig. 0-4 in Appendix A) with a nylon 4-40 screw (McMaster-Carr). The distance between the pin electrode and the liquid was approximately 2 mm.
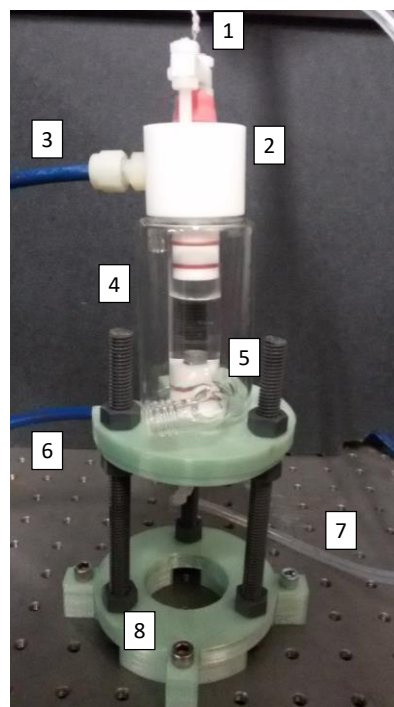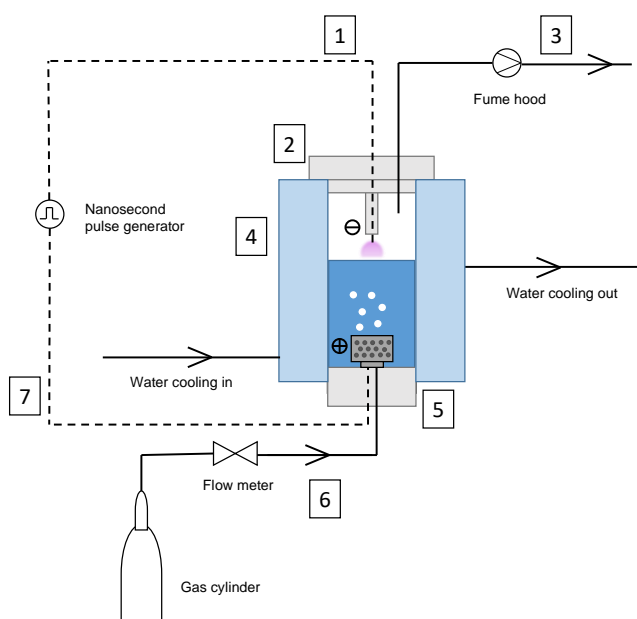
Fig. 3-4 Schematic of the experimental setup (left) and picture of the reactor (right). (1) Negative pin electrode (soldered to a high-voltage cable that is connected to the nanosecond pulse

generator). (2) PTFE top lid (with a red rubber septum to prevent gas leaks where the pin electrode is inserted). (3) Gas outlet. (4) Jacketed glass vessel. (5) PTFE bottom lid with a stainless steel sparger mounted on top (the latter introduces gas and acts as positive electrode). (6) Gas inlet. (7) High-voltage cable that connects the electrode to the nanosecond pulse generator. (8) 3D printed laboratory stand.

On top of the bottom reactor lid, a stainless steel sparger was screwed in. The sparger both supplied gas to the system and acted at positive electrode. Throughout this thesis, two spargers were used:

- Mott sparger: 316L stainless steel, 8 mm diameter, M5 threaded, 5 µm pore size. This sparger was used for the experiments in Chapter 5. Despite regular cleaning, blocking of the pores and irregular bubbling were observed. Preliminary experiments in preparation for Chapter 6 revealed that irregular bubbling was the major contributor to the variability of experimental results.

- Homemade sparger (manufactured in the machine shop of the Department of Chemical Engineering, McGill University): 316L stainless steel, 8 mm diameter, M5 threaded, a single hole with a 0.35 mm diameter. This sparger was used for the experiments in Chapter 6. Regular bubbling was achieved and no pore blocking was observed.

Fig. 3-5 View of the jacketed glass reactor from the top. The opening, where the liquid sample is inserted, is sealed by a top lid (not shown in this picture).

A T-shaped channel connected the gas inlet to the sparger (see Fig. 0-3 in Appendix A). The screw at the bottom of the sparger was soldered to a 302 stainless steel wire (0.25mm diameter, Goodfellow) that extended to the outside of the bottom lid, through an opening at the bottom of the lid. Similar to the electrode opening in the top lid, a rubber turnover septum (Fisher Scientific, 9 mm diameter) was used to seal the hole and prevent gas leaks. Outside the bottom lid, the stainless steel wire was soldered to a high-voltage wire (McMaster-Carr) that was connected to the nanosecond pulser.

Gas entering the reactor through bottom lid was regulated by a Matheson E406 rotameter, calibrated for 5 psi. A volumetric flow rate of 6 cm^3/min was deemed adequate both for air and oxygen flows, because at this rate the bubbling was even and did not produce strong disruptions at the surface of the liquid. As a result, the distance between the liquid level and pin electrode seemed to be constant enough to carry out the experiments. The gas tubing, both at the gas inlet and outlet, were standard hard polyvinylchloride (PVC) tubing with an inner diameter of 0.17" and an outer diameter of 1/4" (McMaster-Carr). The gas oulet was connected to an elephant trunk.

Note that Benjamin Münch (exchange student at the Plasma Processing Laboratory) assisted in the reactor design process and provided the technical drawings presented in this section.

3.1.2.3 Electrical system

The electrodes were powered by a homemade diode opening switch generator, developed at the Plasma Processing Laboratory by Dr. Felipe Aristizábal and Dr. Mathew Evans. Fig. 3-6 shows the complete electrical system. To run the nanosecond pulsed plasma a homemade pulse generator, a homemade gate drive, a main power supply supplying 0-600 V (Sorensen), a secondary power supply supplying 18 V (Lambda) for opening the gates of the pulse generator and a signal generator (Tektronix AFG3102) were used. The discharge voltage signals were measured using two passive high-voltage probes (Tektronix P6015A). The current was measured with a current transformer probe (Pearson 6585). For monitoring of the signals during experiments, a Tektronix TDS2024 oscilloscope was usually used. For more convenient recording of the signals, oscilloscopes from Pico Technology were employed (either PicoScope 2207B or PicoScope 2408B).
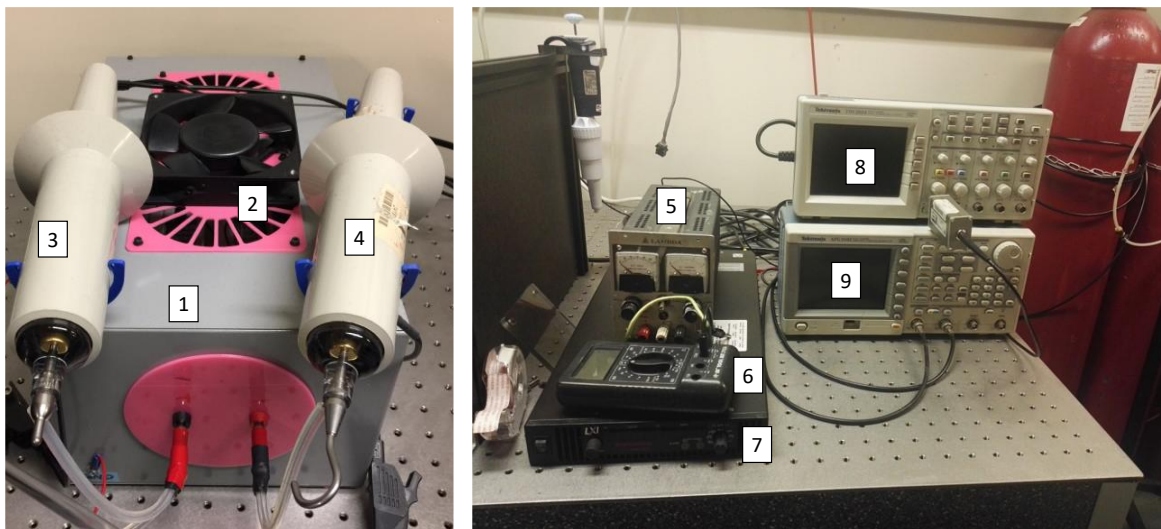
Fig. 3-6 Pictures of electrical system, with enclosed nanosecond pulse generator with gate drive (1), ventilator for cooling the pulse generator (2), high-voltage probe connected to the positive voltage output (3), high-voltage probe connected to the negative voltage output (4), 0 – 20 V power supply (5), multimeter for accurate display of voltage of 0 – 20 V power supply (6), 0 – 600 V power supply (main power supply) (7), oscilloscope (8) and signal generator (9).

The nanosecond pulser supplied two simultaneous nanosecond pulses of equal voltage amplitude (one positive and one negative pulse). In practice, there was a small difference in the voltage amplitudes (e.g. + 5 kV and - 5.9 kV) and a small delay (around 11 ns) between the positive and negative pulse. The delay was adjusted at the signal generator so that the pulses were sent simultaneously. The parameters chosen at the signal generator to generate a pulse were the following: Delay 11 ns, Leading 5 ns, High 5 V, Trailing 5 ns, Low 0 V, Width 1 µs (and variable frequency). During testing of the limits of the homemade nanosecond pulser, a frequency of up to 9 kHz was used. Although this frequency produced pulses as desired, this led to overheating of the power supply after longer consecutive plasma discharge times (after around 30 min). At 3 kHz or lower frequencies no overheating was observed. **Error! Reference source not found.** shows exemplary current and voltage signals produced at a pulse frequency of 3 kHz and a power of 580 V supplied by the main power supply, which generated nanosecond pulses with a total voltage drop of 11 kV across the pin-to-liquid gap of around 2 mm. In the presented example, the Full Width at Half Maximum (FWHM) of the total voltage drop was 44 ns.
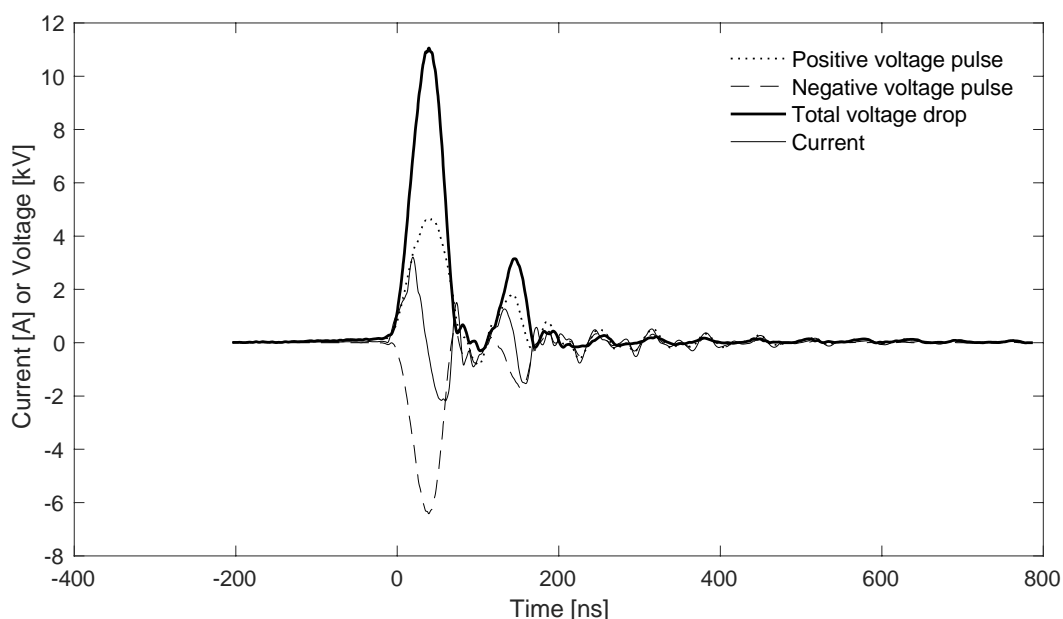
Fig. 3-7 Characteristic voltage and current signals during oxygen plasma treatment at a nanosecond pulse frequency of 3 kHz, averaged for 50 consecutive samples. The measurements were taken 10 min after starting the electric discharges on pure water sample (LC-MS grade) with a conductivity of 1.1 μS/cm.

3.1.2.4 Validation of liquid temperature and mixing

A simple test confirmed the thorough mixing of the liquid sample through bubbling air: 2.5 mg methylene blue powder (M291 of Fisher Scientific) were added to the sample liquid of 7.5 mL, through which a sparger bubbled air. The solution became homogenous with a deep blue color in less than 30 s of bubbling.

To check the temperature inside the reactor, RO water samples (7.5 mL) were plasma-treated for different amounts of time and their temperature was measured with a FISHERbrand[TM] 76 mm Immersion Glass Thermometer. Table 3-1 confirms that the temperature of the samples remained constant.

Table 3-1 Temperatures of a water sample before and after different plasma treatment times, with and without external cooling.

| | Temperature in °C | | | |
| | without cooling | | with cooling | |
Treatment time in min	prior treatment	after treatment	prior treatment	after treatment
5	20.5	28	20.5	20.6
10	20.5	30	20.5	20.6
20	20.5	34	20.5	20.6
30	20.5	34.5	20.5	20.6

3.1.2.5 Preparation of plasma-treated liquid samples

For producing plasma-treated samples, a rigorous method had to be developed to ensure the reproducibility of the results. The developed standard operating procedure can be found in Appendix B.

3.2   Electrical characterization

3.2.1   Energy per pulse calculations

To calculate the energy deposited per nanosecond pulse, a code was developed using the software MATLAB®. The code used the recorded voltage and current signals as input. The calculation was adapted from Rusterholtz's method (Rusterholtz, 2012) and followed the following steps:

1. Finding the capacitance *C:* At low voltage (about 4.5 kV) without plasma ignition, an initial value for the parasitic capacitance of the electrodes and cables was obtained by matching the amplitudes of the derivative of the applied voltage and of the total current (see Eq. 3.1 and Fig. 3-8).

$$I_{measured,no\ plasma} = I_{displacement} = C\frac{dV}{dt} \qquad (3.1)$$

2. Adjusting the delay *d* between voltage and current signals: Because of the different characteristics of voltage and current probes, as well as the different length of the cables that connected the probes to the oscilloscope, there was a delay between the signals. Therefore, the delay was adjusted to match the rise of the main, positive current peak with the rise of the first peak of $C\frac{dV}{dt}$ (see Fig. 3-8).

3. Calculating the conductive current $I_{conductive}$: At the desired voltage for the plasma experiment (typically around 11 kV), the derivative of the applied voltage $\frac{dV}{dt}$ was calculated. For now, the capacitance and delay values obtained in steps 1 and 2 were maintained and used for calculating the displacement current similarly to Eq. 3.1. The displacement current was subtracted from the measured current to obtain the conductive current (see Eq. 3.2 and Fig. 3-9).

$$I_{conductive} = I_{measured,plasma} - I_{displacement} \qquad (3.2)$$

4. Calculating the power P: The power of the pulse was obtained by multiplying the conductive current obtained in step 3 with the signal of the total voltage drop (see Eq. 3.3 and Fig. 3-10).

$$P = I_{conductive}V \qquad (3.3)$$

5. Calculating the energy per pulse E_{plasma}: For the duration of the pulse, the power was integrated to obtain the energy per pulse (see Eq. 3.4 and Fig. 3-10).

$$E_{plasma} = \int_{t_0}^{t_{end}} I_{conductive}V \, dt \qquad (3.4)$$

Note that steps 3-5 were repeated varying the values of C and d to obtain the error associated to the estimation of these parameters (see Chapters 5 and 6). Particularly, it is important to verify whether the change in capacitance at higher voltages has a significant effect on the energy per pulse results. In the present work, varying capacitance values made no significant difference on the energy per pulse results.

Steps 1-5 were carried out with an average of 50 consecutive voltage and current samples to obtain an average energy per pulse (see Fig. 3-10). The process was repeated for the 50 individual samples calculated separately (see Fig. 3-11), and the 50 values of energy per pulse were averaged. The

difference of the individual energy per pulse values (averaged at the end) to the direct averaged energy per pulse value was ≤ 0.3 % for discharges in air and ≤ 3 % for discharges in oxygen.
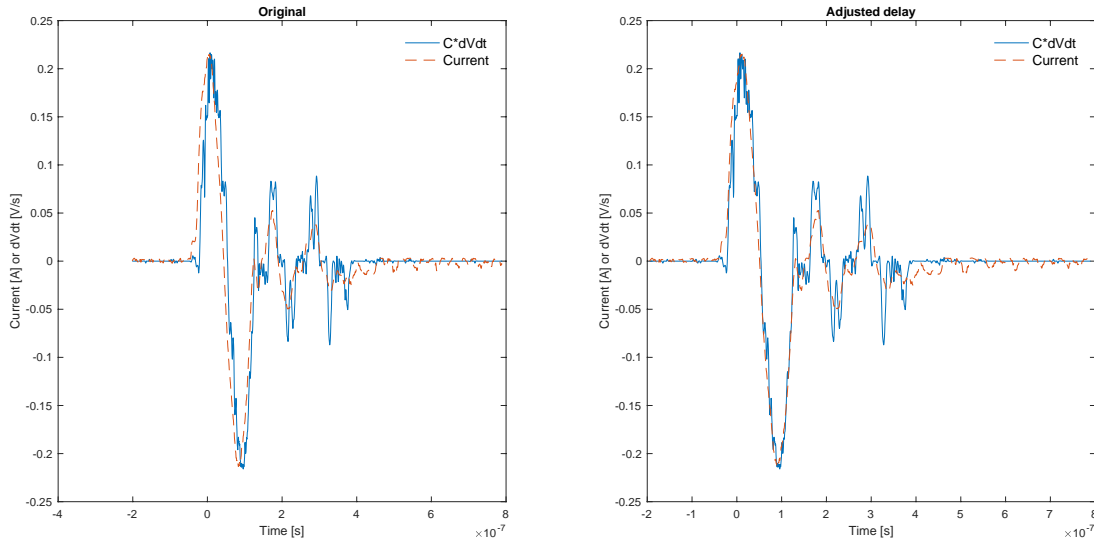
Fig. 3-8 Measured current and calculated derivative of the applied voltage $\frac{dV}{dt}$ averaged for 50 consecutive samples. The nanosecond pulse frequency was 3 kHz and the total voltage drop was 4.5 kV (no plasma ignition). $\frac{dV}{dt}$ was adjusted by a capacitance factor C (2.2 pF) to match the amplitude of the measured current. Left: Original time recording. Right: Delay between the two curves was adjusted by 7 ns.
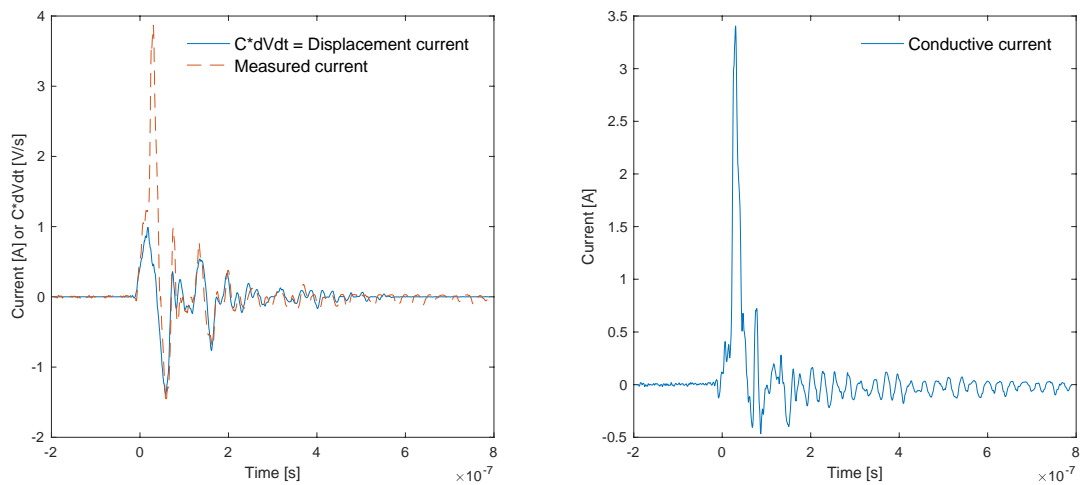
Fig. 3-9 Left: Measured current and calculated displacement current (with adjusted capacitance and delay). Right: Conductive current obtained by subtracting the displacement current from the measured current. Both graphs were obtained from current and voltage signals averaged for 50

consecutive samples, recorded during air plasma treatment of reverse-osmosis water at a pulse frequency of 3 kHz and the total voltage drop was 12 kV (plasma ignited).
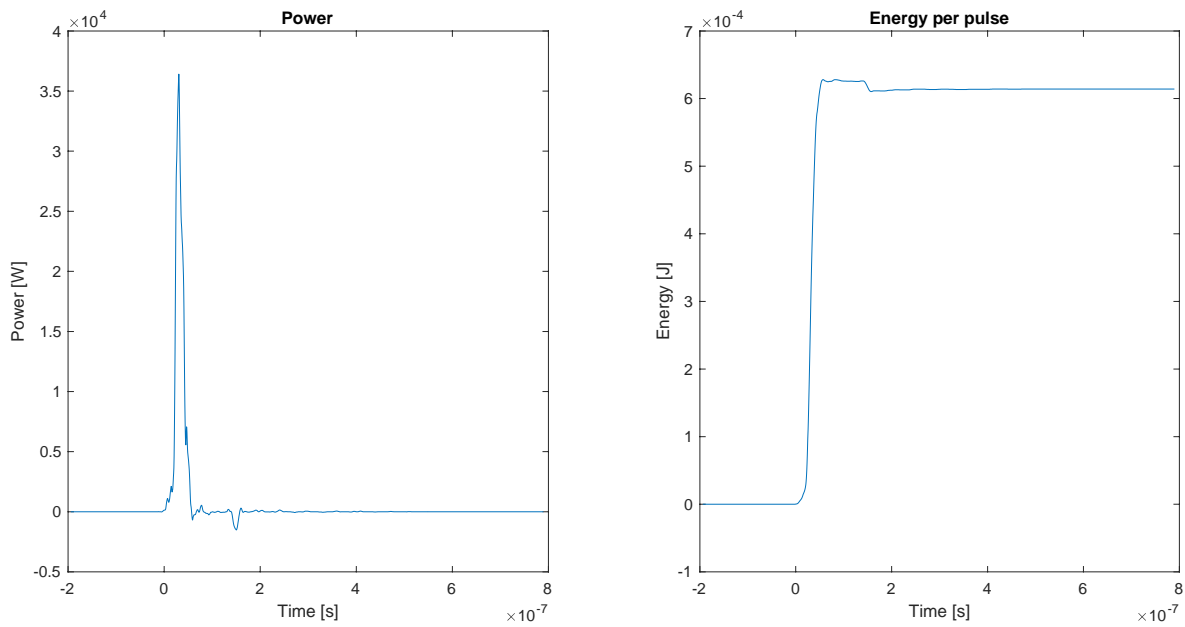
Fig. 3-10 Left: Power curve obtained by multiplying the measured total voltage drop by the calculated conductive current. Right. Energy per pulse obtained by integrating the power curve. Both graphs were obtained from current and voltage signals averaged for 50 consecutive samples, recorded during air plasma treatment of reverse-osmosis water at a pulse frequency of 3 kHz and the total voltage drop was 12 kV.
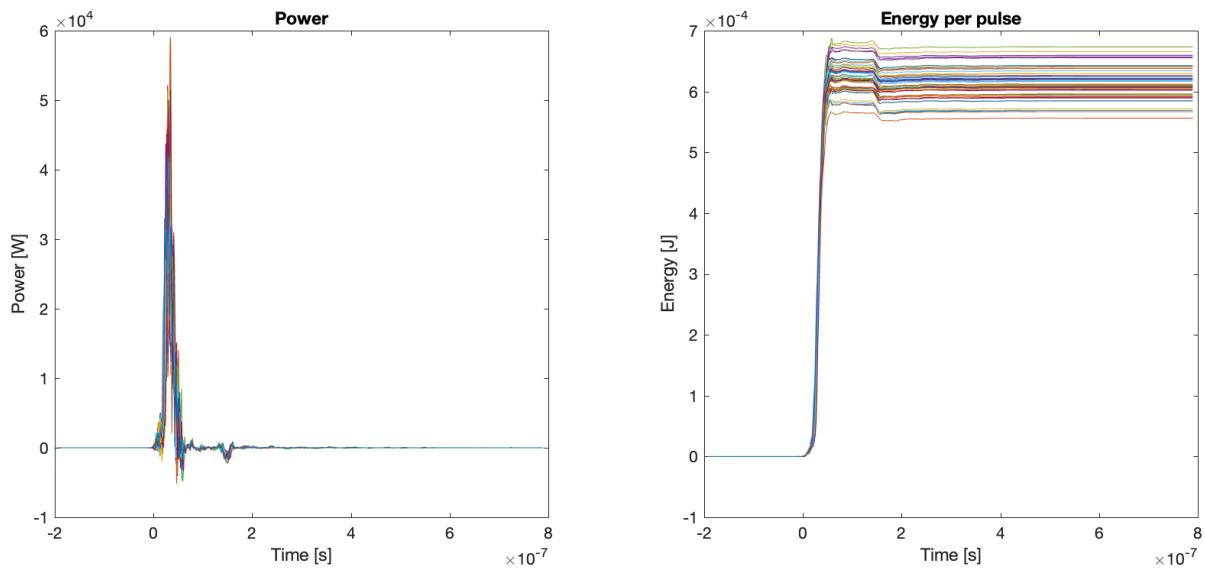
Fig. 3-11 Left: Power curve obtained by multiplying the measured total voltage drop by the calculated conductive current. Right. Energy per pulse obtained by integrating the power curve.

Both graphs show the results of 50 consecutive samples, recorded during air plasma treatment of reverse-osmosis water at a pulse frequency of 3 kHz and the total voltage drop was 12 kV.

3.3   Chemical characterization

3.3.1   Digital imaging

In order to visualize the physical extent of the degradation of methylene blue (MB) in the preliminary setup described in 3.1.1, photos were taken and analyzed. The pulse generator, the cuvette and the magnetic stirrer were enclosed by a black box to prevent contact with the high voltage parts and to take photos in the dark. Information on the LED lantern and the settings of the Nikon D3300 camera can be found in Chapter 4. During the plasma treatment, photos were automatically taken every 10 seconds. Since there was an inevitable light variation due to flickering of the LED lantern, pictures always contained two cuvettes next to each other: the cuvette containing the plasma-treated sample and a reference cuvette containing an untreated sample (representing time t_0).

The largest change in absorbance of the treated MB solution occurs around 660 nm (revealed by UV-vis analysis), which wavelength falls within the spectral response of the red pixel of the digital camera. Therefore, image analysis was performed using the software MATLAB® with a focus on the red pixels of the photos. These are the main steps in the MATLAB® code developed in the present work:

1) Loading the images and labeling them according to the plasma treatment time they represent.
2) Extracting the red pixel light intensities from the images.
3) For each image, extracting the areas of the image containing the plasma-treated sample and the reference sample.
4) For each image, calculating an average red pixel light intensity for the area of the reference sample.
5) For each image, calibrating the red pixel light intensity for the area of the plasma-treated sample (by diving the red pixel light intensity of the plasma-treated sample by the corresponding average red pixel light intensity from the reference sample).
6) Plotting the resulting, calibrated plasma-treated sample images.

3.3.2 UV-vis absorption spectroscopy

Two different spectrophotometers were used for UV-vis absorption measurements in Chapter 4, depending on the experiment:

- USB2000 Ocean Optics spectrophotometer with a USB-ISS-Vis Integrated Sample System (measuring range 390 to 800 nm) and the software SpectraSuite. We chose a scan average of 5 and boxcar width of 5.
- Evolution™ 300 UV-Vis spectrophotometer of Thermo Scientific (measuring range 220 and 900 nm) with the software Thermo Scientific™ VISION pro™. We chose to measure the full wavelength range with a bandwidth of 1 nm.

In the present work, UV-vis spectroscopy measurements were solely used to measure the absorption of aqueous solutions of the MB dye. The measurements were taken in disposable BrandTech™ BRAND™ UV-cuvettes, which also functioned as part of the preliminary reactor presented in 3.1.1. The cuvettes had a pathlength of 1 cm and allowed for UV-vis absorption measurements in the range from 220 to 900 nm. UV-vis spectroscopy measurements were performed at room temperature. A baseline with the reference cell (cuvette containing reversed-osmosis water as base fluid) was taken before every series of measurements. For the USB2000 spectrophotometer, it was also necessary to record a dark spectrum. For this purpose, the light source (tungsten bulb and violet LEDs) is covered by a piece of paper.

The main advantage of the USB2000 Ocean Optics spectrophotometer was that it was transportable, could be placed next to the setup and the measurements were performed quickly with an online method. Measurements with the Evolution™ 300 UV-Vis spectrophotometer were slower because the equipment was located in a different floor than the plasma reactor, but the advantage was that it provided a wider wavelength measuring range. Comparing spectra measured with both spectrometers, a shift of the wavelength was monitored. While the absorption maximum of MB with the Evolution™ 300 UV-Vis spectrophotometer was located at around 660 nm, it was detected at around 665 nm for the USB2000 Ocean Optics spectrophotometer. A calibration of both spectrometers with a special calibration standard cuvette ('Kalibrierstandard Glasfilter Typ 666-F' of Hellma Analytics) showed more precise results for the USB2000 Ocean Optics spectrometer. Its deviation was ± 0.5 nm, whereas the deviation of the Evolution™ 300

spectrophotometer was ± 5 nm around the MB absorbance maximum. The deviation may explain the shift of the absorption maximum. At lower wavelengths the deviation was smaller.

To calculate the concentration of MB by the measured absorbance data, calibration curves were required for both spectrophotometers. A 100 mg/L MB stock (M291 of Fisher Scientific, dissolved in reversed-osmosis water) was prepared and used to obtain dilutions of known concentrations. The maximal absorbance values of these calibration solutions were plotted against their nominal MB concentration. Every calibration solution was measured three times, and the three values were averaged. Fig. 3-12 shows calibration curve for the Evolution™ 300 UV-Vis spectrophotometer and Fig. 3-13 shows the one for the USB2000 Ocean Optics spectrophotometer.
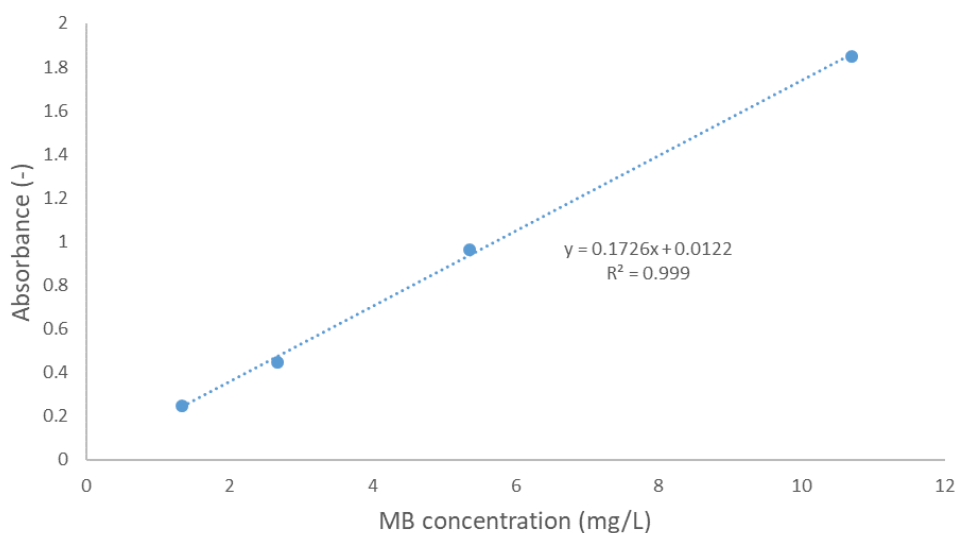
Fig. 3-12 Calibration curve of methylene blue (MB) concentration for the Evolution™ 300 UV-Vis spectrophotometer.
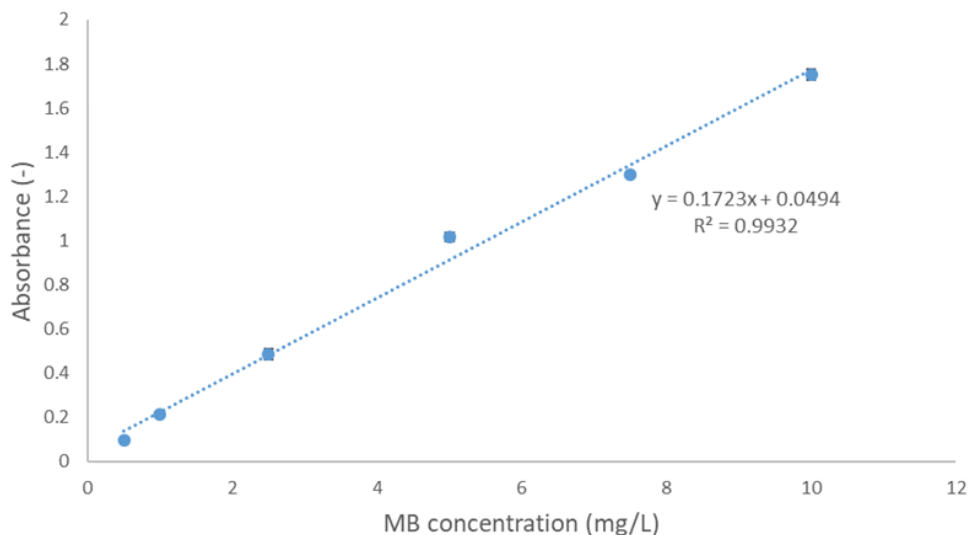
Fig. 3-13 Calibration curve of methylene blue (MB) concentration for the USB2000 Ocean Optics spectrophotometer.

3.3.3 Scanning and transmission electron microscopy

A high-resolution scanning electron microscope (SEM, Hitachi SU-3500) was used in Chapter 5 to investigate the morphology of the tip of high-voltage pin electrodes. The samples were loaded directly into the SEM for observation and did not require any special coating. An Oxford X-Max energy dispersive X-ray spectroscopy (EDS) module attached to the SEM and the software AZtec were used for elemental analysis of the electrode surface. A transmission electron microscope (TEM, Tecnai G2 F20 200 kV Cryo-STEM) was used in a preliminary investigation of nanoparticles introduced into plasma-treated liquids through electrode erosion. A droplet of plasma-treated samples was deposited onto a TEM grid (Ted Pella, lacey formvar stabilized with carbon on copper mesh) and left to dry completely in air before imaging.

3.3.4 Dynamic light scattering

In Chapter 5, dynamic light scattering (DLS) (Malvern Instruments, Zetasizer Nano ZS) was used as to detect nanoparticles in plasma-treated liquid samples, as well as to quantify their size. Intensity and volume-based distributions, Z-average diameters and polydispersity index (PDI) were obtained from the autocorrelation function using the "general purpose mode". The software assumed a spherical particle shape. Whereas intensity-based distributions represent raw data, volume-based distributions are normalized by the particle volume. Blanks with RO water were tested to verify that device was working properly.

3.3.5 Iodometric titrations

Iodometric titrations were performed in Chapters 5 and 6 for obtaining the total oxidizing power (TOP) of plasma-treated water samples. Under the presence of oxidizing species, iodide (colorless) gets immediately oxidized to iodine (yellow) as shown in Eq. 3.5 and 3.7. Through the controlled addition of a reducing solution, the titrant, the iodine gets reduced back to iodide (see Eq. 3.8) which is observed by a slowly fading in color. Adding a starch indicator helps visualize the end point of the titration, as it turns the light-yellow color into a darker violet one. The complete absence of color indicates the end point of the titration. Since the titration was performed in manual mode in the present work (with a Metrohm 888 Titrando equipment), there was human error associated to identifying the end point of the titration. In order to reduce the error, towards the end of the titration the titrant dosage was reduced to 0.1 mL/min, and a white paper was placed behind the beaker containing the sample to facilitate color identification. The quantities and brands of the chemicals used are reported in Chapters 5 and 6. The starch solution was prepared by mixing 2 g of Tyodene™ (indicator for iodometry, Fisher Scientific) into 50 mL of RO water and heating the solution to 50 °C for 60 min to allow for the starch to fully dissolve. When preparing a fresh titrant solution, a quality control of known H_2O_2 concentration (prepared from a Fisher Scientific standard, 30 % ± 1.1, ACS grade) was used to confirm that the nominal titrant concentration was met (less than 2 % error). Blank experiments with RO water (TOP should be 0) were performed regularly to ensure that there was no contamination of the beaker and the chemicals.

Note that iodometric titrations were only reported for samples prepared by oxygen plasma treatment, but not for the ones prepared by air plasma treatment. The reason for this is that air plasma treatment introduces nitrites into the plasma-treated solution (confirmed by ion chromatography in Chapter 5), which are known to go into a cyclic reaction as shown in Eq. 3.5 and 3.6 (Karlsson and Tortensson, 1974; Lukes *et al.*, 2005). This would delay the end point of the titration, and it would not possible to obtain the original TOP.

$$2NO_2^- + 2I^- + 4H^+ \rightarrow 2NO + I_2 + 2H_2O \qquad (3.5)$$

$$2NO + O_2 + H_2O \rightarrow 2H^+ + NO_2^- + NO_3^- \qquad (3.6)$$
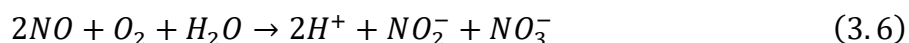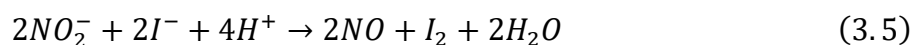
For samples prepared by oxygen plasma treatment, the TOP was calculated represented as H_2O_2 equivalents based on the reactions in Eq. 3.7 and Eq. 3.8 and the corresponding calculation in Eq. 3.9.

$$H_2O_2 + 2\,I^- \rightleftharpoons 2\,OH^- + I_2 \tag{3.7}$$

$$I_2 + 2\,S_2O_3^{2-} \rightleftharpoons 2\,I^- + S_4O_6^{2-} \tag{3.8}$$
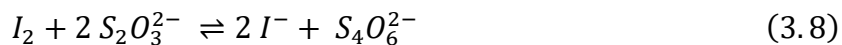
$$c_{m,H2O2} = M_{H2O2} * c_{n,S2O3-} * V_{S2O3-} * 0{,}5 * \frac{1}{V_S} \tag{3.9}$$

The unit of the TOP ($c_{m,H2O2}$) is mg/L H_2O_2 equivalents. The molar mass M_{H2O2} of H_2O_2 is 34.0147 g/mol, the original sample volume V_S is 0.5 mL and the titrant concentration $c_{n,S2O3-}$ is 0.001 mol/L. V_{S2O3-} represents the titrated volume of sodium thiosulfate.

3.3.6 High-performance liquid chromatography

High-performance liquid chromatography (HPLC) was used to measure the concentration of hydrogen peroxide in plasma-treated samples reported in Chapter 5, using a modified version of the method proposed by Takahashi et al (1999) (Takahashi *et al.*, 1999). This method was chosen because there was no potential interference with other RONS present in plasma-treated water. The analytical instrument and sample dilutions are described in Chapter 5. The mobile phase was prepared by dissolving 50 mM of Na_2SO_4 (Fisher Scientific, anhydrous, certified ACS) and 10 µM of EDTA·2Na (Sigma-Aldrich, 90 % titration) in RO water by ultrasonication for 5 min. Prior to introduction into the HPLC system, the solution was filtered via vacuum filtration through a 0.22 µm filter paper (Merck Millipore, Type GV) and degassed for 20 min in an ultrasonic bath. The mobile phase was stored at room temperature and wrapped in aluminum foil for up to two days. When a new mobile phase was introduced, the lines were purged with 5 mL/min, letting the mobile phase go out through a by-pass. For running the analytical experiments, the flow was set to 1 mL/min and the system was equilibrated for about an hour. Preliminary tests revealed that the sensitivity of the detector could change significantly from one day to another (and in some cases within the same day), highlighting the importance of calibrating the instrument regularly. The following calibration solutions were prepared dissolving a H_2O_2 standard solution (Fisher Scientific, 30 % ± 1.1, certified ACS) with RO water: 0, 1, 2 and 4 mg/L. A calibration was performed every day before the start of the experiments (R^2 between 0.996 and 1). At least one quality control with one of the calibration solutions was run by the end of each day, to check whether the calibration curve calculated at the beginning of the experimental day was still accurate (if it was off, the data would be discarded).

3.3.7 Ion chromatography

Ion Chromatography (IC) with an anion-exchange column (Methrom, Metrosep A Supp 7-250) was used in Chapter 5 to analyze the concentration of nitrites and nitrates in plasma-treated water samples. The IC system was described in Chapter 5. The mobile phase, containing 0.318 g/L of Na_2CO_3 (Sigma-Aldrich, ACS grade, anhydrous) dissolved by 10 min ultrasonication in RO water, was filtered via vacuum filtration through a 0.22 μm filter paper (Merck Millipore, Type GV) and degassed for 20 min in an ultrasonic bath prior to use. The mobile phase was stored at room temperature and wrapped in aluminum foil for up to five days. When a new mobile phase was introduced, the lines were purged with 5 mL/min, letting the mobile phase go out through a by-pass. For running the analytical experiments, the flow was set to 0.8 mL/min and the system was equilibrated for about an hour. The calibration solutions were composed of the NO_2^- standard solution (SCP Science, 991 ± 9 mg/L, H_2O based) and NO_3^- standard solution (SCP Science, 999 ± 5 mg/L, H_2O based), their dilutions with RO water to 9.99 mg/L and 0.999 mg/L and a zero point. Since daily quality controls and blanks confirmed that the instrument was very stable, it was not necessary to run the calibration curve daily. The samples were diluted with RO water to 1:5, to a total liquid volume of 2.5 mL.

3.3.8 Inductively coupled plasma

Inductively coupled plasma with optical emission spectrometry (ICP-OES, iCAP 6000 Series) was used for identification and quantification of metals introduced into plasma-treated RO water through the erosion of high-voltage electrodes of different materials (copper, stainless steel and hafnium). Since not all the metal content was present in ionic form – some metal particles were suspected to be present as well, the sample solutions had to be digested before starting the measurements so that all the metal particles got fully oxidized to their last oxidation state. The digestion procedure is described in Chapter 5. Note that once the digestion of the samples was finished, the vials (SCP Science, DIGItube 15 mL A/S Tubes) had to be refilled with RO water to regain the initial sample volume of 5 mL, since water evaporation had occurred during the heating process. For the copper and stainless steel samples, the standard solution RQC-1 (SCP Science, ICP-AES, 5 % HNO_3 matrix), which contains 10 mg/L of different metals (including copper, iron, nickel and chromium) was diluted with a 4 % HNO_3 solution (made from concentrated HNO_3, Fisher Scientific, 63 %, Trace Metal Grade), to seven calibration solutions with concentrations of

0.01, 0.05, 0.1, 0.5, 1, 5 and 10 mg/L. For the hafnium samples, the Hf-standard solution (SCP Science, ICP-AES, 4% HCl matrix) with a concentration of 1000 ± 6 mg/L of hafnium served as the stock solution for the calibration points. The standard was diluted with 4 % HNO_3 to the following eight calibration solutions: 0.005, 0.01, 0.05, 0.1, 0.5, 1, 5 and 10 mg/L. Before starting the measurement of the actual samples, two washes of RO water and one blank (containing 3 mL of RO water with 2 mL of the 4 % HNO_3 solution) were measured.

3.3.9 Liquid chromatography with high resolution mass spectrometry

Liquid chromatography with high resolution mass spectrometry (LC-HRMS) was used for detecting DTZ and its TPs in Chapter 6. Details on the pieces of equipment, software, developed method and optimization of the instrument parameters are reported in Manuscript 3. In order to calibrate the instrument for quantification of DTZ, a daily calibration was run with the following calibration solutions: 0, 5, 10, 25, 50, 100, 200, 300 µg/L DTZ in LC-MS grade water. The calibration solutions were prepared from a 200 mg/L DTZ stock, which was obtained by diluting 10 mg DTZ powder (Toronto Research Chemicals) in 50 mL LC-MS grade water (Fisher Scientific). The stock solution was ultrasonicated until complete dissolution of the DTZ powder, for about 30 min. For plasma-treated samples that had an initial nominal DTZ concentration $C_0 =$ 10 mg/L, samples were diluted by 1:50 for quantification of DTZ and by 1:2 for detection of TPs. For plasma-treated samples that had an initial nominal DTZ concentration $C_0 = 200$ µg/L, samples were not further diluted before injection into the LC-HRMS.

3.4 Biological characterization

3.4.1 Acute toxicity tests

A standard acute Microtox® test was used to determine the toxicity of plasma-treated samples, determined by the decrease in luminescence from *Aliivibrio fischeri*. The methodology is described in Chapter 6. All tests were accompanied by two blanks (diluent) and one positive control (phenol). The blanks ensured that there was nothing wrong with the system (i.e. the luminescence of bacteria behaved as expected for non-toxic environments). Furthermore, blank values were used within the Microtox software to calculate a correction factor that accounted for the natural degradation of light intensity from the bacteria due to the sample diluent and time. The positive control should kill most or all of the bacteria after 10 minutes and ensured that the bacteria were functioning

properly within the testing environment. In order to monitor and determine the toxicity of samples within a large concentration range, 10 serial dilutions with dilution factors of 1.5 or 2 were used. Additionally, screening tests without serial dilutions were performed, as an easy way to test multiple samples to determine if they were toxic. Although there was no quantitative data associated with this type of assay conducted in presence of unknown contaminants at undetermined concentrations, it allowed one to quickly determine if the sample have some level of toxicity and to assess the toxicity relative to the untreated water.

4

Manuscript 1

Methylene blue degradation by a nanosecond-pulsed pin-to-liquid discharge in open air

4.1   Preface

This chapter has not been submitted for journal publication, but parts of its contents were presented at two international conferences:

> E. Corella Puertas, F. Aristizabal, E. Thalhammer and S. Coulombe, *Methylene blue degradation by a nanosecond pulsed pin-to-liquid discharge*, ISPC-23, Montréal (Canada), July 30 – Aug. 4 (2017).

> E. Corella Puertas, E. Thalhammer, F. Aristizabal and S. Coulombe, *Parametric study of methylene blue degradation using a pulsed nanosecond pin-to-liquid discharge in open air*, JSPP 2017, Okinawa (Japan), Dec. 4-7 (2017).

The work was planned, analyzed and written by Elena Corella Puertas (PhD candidate). Dr. Felipe Aristizábal provided support on using the nanosecond pulser, which he had previously developed, as well as guidance on developing the MATLAB code for image analysis of the digital camera. Eva Thalhammer assisted in part of the experimental work and provided support on UV-vis spectroscopy. Dr. Sylvain Coulombe was responsible for supervision and review of the work.

A preliminary pin-to-liquid discharge configuration is used to test the applicability of a novel nanosecond pulser, developed in the Plasma Processing Laboratory, for water purification. Since

the applicability is confirmed, later on the pin-to-liquid discharge configuration is further developed into a compact reactor, which is used for performing the experiments in Chapters 5 and 6. The parametric study of the degradation of a model organic pollutant in this chapter helps to select operating parameters (frequency, voltage, electrode polarity) for the following chapters.

The MB dye, a model organic pollutant, is successfully degraded. Post-discharge degradation of MB implies the presence of residual, long-lived reactive species. This indicates the importance of quenching residual reactive species, in case one wants to separate the degradation of model organic pollutants during the plasma discharge from the post-discharge reactions with residual reactive species. The composition and concentration of residual species are studied in Chapter 5 and this knowledge is applied for choosing appropriate quenchers in Chapter 6.

A simple method is developed to track the degradation and transport of the dye within the aqueous solution. Tracking the degradation of MB by analyzing the red pixel reading of a digital camera has not been previously reported. Combining the image analysis with a scale analysis allows us to infer that, without mixing, a significant convective transport of species takes place near the live electrode, most likely due to the temperature-induced surface tension gradient (Marangoni flow). The mass transport in the bulk of the liquid seems to be limited to diffusion. These results contribute fundamental knowledge on the reaction-mass transport processes, but also reveal the need for external assistance for mixing and contact area enhancement. Due to the knowledge gained in this chapter, the new compact reactor used for the experiments in Chapters 5 and 6 includes bubbling gas from the bottom of the reactor to ensure homogeneous mixing of the plasma-treated solution and an increase in plasma–liquid contact area.

Methylene blue degradation by a nanosecond pulsed pin-to-liquid discharge in open air

Elena Corella Puertas[1], Felipe Aristizabal[1], Eva Thalhammer[1,2], Sylvain Coulombe[1]

[1]Plasma Processing Laboratory, Department of Chemical Engineering, McGill University, Montréal, Canada

[2]Department of Chemistry, Technische Universität München, Munich, Germany

Abstract

A newly developed nanosecond pulser was used to produce plasma discharges in a pin-to-liquid configuration with the ultimate goal of achieving efficient wastewater treatment. An aqueous solution of methylene blue dye was treated as a model organic pollutant (7 mg/L, 1 ml volume). A degradation level of 84 % was achieved after 11 min of treatment without stirring, which is improved until almost complete removal by introducing stirring or optimizing the operating parameters (pulse frequency, voltage). The degradation process continued post-plasma treatment, thus revealing that the plasma–liquid interactions lead to the formation of long-lived species. The extent of the reaction-diffusion zone was imaged by using the red pixel reading of a digital camera. This enabled us to infer that a significant convective transport of species takes place near the live pin electrode, most likely due to the temperature-induced surface tension gradient (Marangoni flow), but that transport in the bulk is limited by diffusion, justifying the need for efficient stirring and enhanced plasma-liquid contact area.

4.2   Introduction

With the increasing world's population and associated growth in industrial and agricultural activities, managing the water resources has become one of the main challenges that humanity is facing. Conventional (mechanical, chemical and biological) wastewater treatment techniques enable the recycling of a large fraction of our potable water resources, but these are not always efficient to degrade hazardous organic pollutants like pesticides, pharmaceuticals, dyes, by-products of water chlorination, halogenated hydrocarbons, aromatic compounds or amines (Foster *et al.*, 2012).

Plasma-based technologies are being explored as alternative wastewater treatment technologies. They have already shown promising results for treating aqueous effluents containing various organic pollutants, without requiring the addition of other chemical agents (Lukes, Locke and Brisset, 2012). Multiple studies have shown that non-thermal plasma discharges in gas–liquid environments produce highly reactive oxidizing species like ozone, hydroxyl radicals and hydrogen peroxide, as well as UV photons (Locke, 2012; Lukes, Locke and Brisset, 2012; Neretti *et al.*, 2016). Among the different plasma reactors employed for water treatment, pulsed corona discharge configurations have shown the highest energy efficiencies for decomposition of toxic organic compounds (Malik, 2010). Short pulsed discharge durations have shown particularly high efficiency, due to the more efficient generation of reactive radicals during the initial phase of the streamer discharge (primary streamer propagation) (Akiyama *et al.*, 2007). If the pulse is short enough (low nanosecond range), the formation of less efficient secondary streamers may be prevented (Starikovskaia, 2006).

In spite of the advantages of the pulsed corona technology for wastewater treatment, one of the main impediments for its commercialization is the lack of suitable, inexpensive nanosecond pulsed power supplies (Pokryvailo *et al.*, 2006). The Plasma Processing Laboratory (PPL) has developed a nanosecond pulsed power supply powered by a diode opening switch generator. The applicability of this nanosecond pulsed power supply to wastewater treatment is tested with a pin-to-liquid discharge configuration. Methylene blue (MB) is chosen as a model organic pollutant to be degraded. The effect of different operating parameters (stirring, pulse frequency, voltage and polarity) on MB degradation is studied.

4.3 Experimental section

4.3.1 Experimental setup

The pin-to-liquid setup consisted of two copper pin electrodes of 0.65 mm diameter placed in a BrandTech^{TM} BRAND^{TM} cuvette (see Fig. 4-1), secured in place and isolated from each other using a 3D-printed piece of acrylonitrile butadiene styrene plastic (ABS). The negative (or positive) electrode was located 1 mm above the liquid surface, whereas the other electrode was immersed in the liquid. The electrodes were powered by a homemade diode opening switch generator, which send two simultaneous voltage pulses of equal amplitude. A full description of the power supply system can be found in Chapter 3. A typical voltage characteristic is shown in Fig. 4-2.
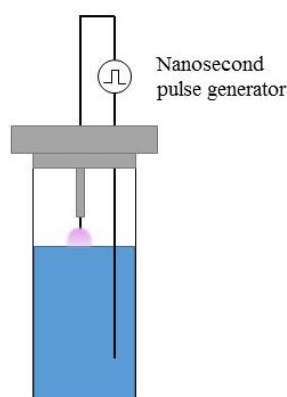
Fig. 4-1 Schematic of the pin-to-liquid setup.
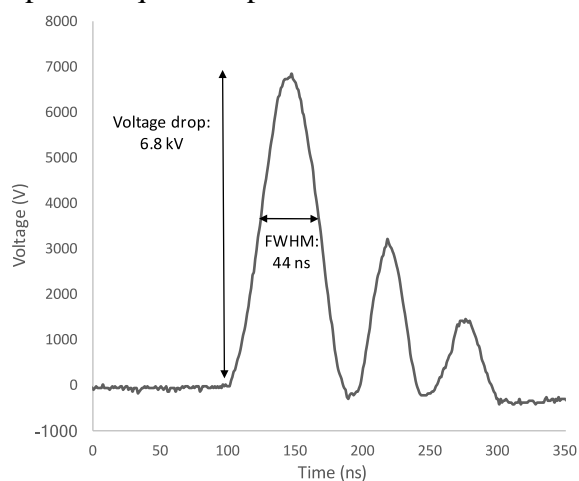
Fig. 4-2 A typical voltage pulse with information on the total voltage drop between the pin electrode and the liquid, and the Full Width at Half Maximum (FWHM) of the principal pulse.

4.3.2 Experimental conditions

For Part 1 of this work, each sample consisted of 1 ml of a 7 mg/L methylene blue solution (M291 of Fisher Scientific, dissolved in reversed-osmosis water) placed in a BrandTech™ BRAND™ semi-micro UV Disposable Cuvette. Pulses were produced at a frequency of 1 kHz and a voltage drop across the electrode gap of 10 kV. The average power was 15 W. All experiments were performed with a negative pin electrode above the liquid, and a positive pin electrode submerged in the liquid. During the plasma treatment, the discharges were interrupted after every minute of treatment to mix the sample by shaking and perform UV-vis spectroscopy measurements (less than 8 min discharge interruption). Five sample repeats were performed to validate reproducibility.

For Part 2 of this work, each sample consisted of 3 ml of a 10 mg/L methylene blue solution (M291 of Fisher Scientific, dissolved in reversed-osmosis water) placed in a BrandTech™ BRAND™ macro UV Disposable Cuvette, and continuously stirred with a magnetic stir bar during the plasma treatment. During the plasma treatment, the discharges were interrupted after every minute of treatment to perform UV-vis spectroscopy measurements (less than 1 min discharge interruption). We used pulse frequencies of 1, 3, 5, and 9 kHz at a constant total voltage drop of 6.8 kV, and total voltage drops of 5.4, 6.8 and 10.8 kV at a constant frequency of 1 kHz. For the experiments studying the effect of stirring, the frequency was 1 kHz and the total voltage drop was 6.8 kV. All experiments were performed with a negative pin electrode above the liquid, except for the one to study the effect of the pin electrode polarity (1 kHz, 6.8 kV). Three sample repeats were performed.

4.3.3 UV-vis spectroscopy

For Part 1 of this work, the UV-vis spectroscopy measurements were performed at room temperature using an Evolution™ 300 UV-Vis spectrophotometer. A baseline with the reference cell (cuvette containing reversed-osmosis water as base fluid) was taken before every series of measurements. Raw spectral absorbance data between the wavelengths 350 and 750 nm at a resolution of 1 nm was recorded and analyzed with the software Thermo Scientific™ VISION pro™.

For measuring the concentration of the dye in Part 2 of this work, its maximal absorbance peak (around 665 nm) was measured by UV-vis spectroscopy measurements (Ocean Optics USB2000 Spectrometer with a USB-ISS-Vis Integrated Sample System) and converted to dye concentration

with a calibration curve. A baseline with the reference cell (cuvette containing reversed-osmosis water as base fluid) as well as a dark spectrum were taken before every series of measurements. Raw spectral absorbance data was recorded and analyzed with the software SpectraSuite.

4.3.4 Digital camera

Pictures were taken with a Nikon D3300 camera at an exposure time of 1/200 s, a F-stop of f/10, an ISO speed of ISO-200 and a focal length of 52 mm. An Energizer® LED folding lantern was placed behind the cuvettes to illuminate the samples from the back. A diffusion paper (by Rosco, model E-Colour #216 White Diffusion) was used to cover the LED lantern surface to make the light more diffuse. Image analysis was performed using MATLAB®.

4.4   Results and discussion

4.4.1   Part 1: Applicability of nanosecond pulser for the removal of an aqueous organic pollutant

4.4.1.1 Methylene blue degradation during plasma treatment

MB aqueous solution samples were treated in the pin-to-liquid discharge configuration for up to 11 min. A characteristic UV-vis spectrum for a treated MB sample is shown in Fig. 4-3. Whereas the two main peaks are attributed to MB, there is a shoulder in the region between 350 and 450 nm that has not been identified yet. This shoulder increases progressively with increasing treatment time. A control experiment of plasma-treated water without MB (not shown here) showed a similar shoulder, implying that the shoulder is probably not due to degradation products of MB but rather other species formed in plasma-treated water.

The maximum absorption peak was found to be at ~660 nm. The maximum absorption peak value of the original and treated samples are plotted in Fig. 4-4. The error bars represent the confidence interval (CI) for a confidence level of 95 % based on the t-Student's statistics for five sample repeats.

The maximal absorbance decreases with increasing plasma treatment time, which confirms that a degradation process is taking place. A calibration curve of MB solutions confirmed a linear correlation between the maximal absorbance peak and the concentration of the dye. Based on this premise, 84% degradation is obtained after 11 min of plasma treatment.
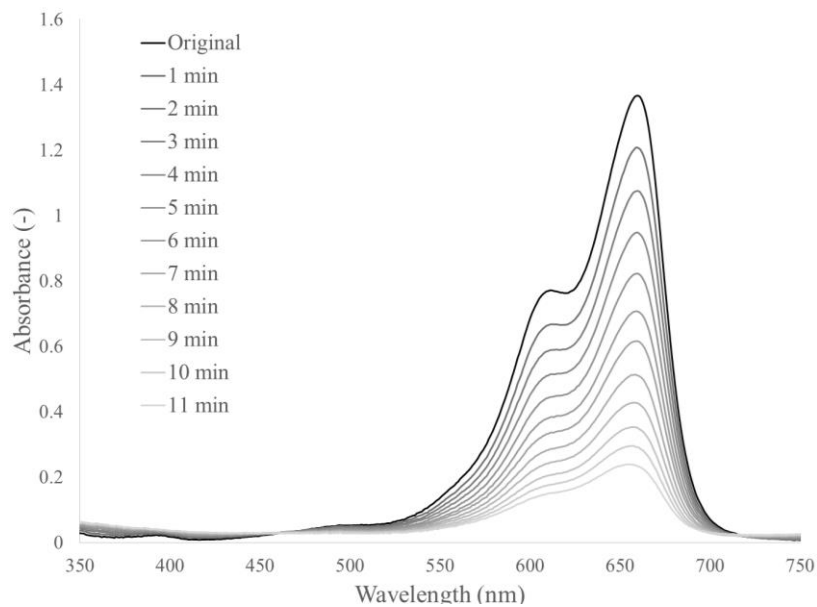
Fig. 4-3 UV-vis absorption spectra for a plasma-treated methylene blue aqueous solution (nominal C_0 = 7 mg/L).
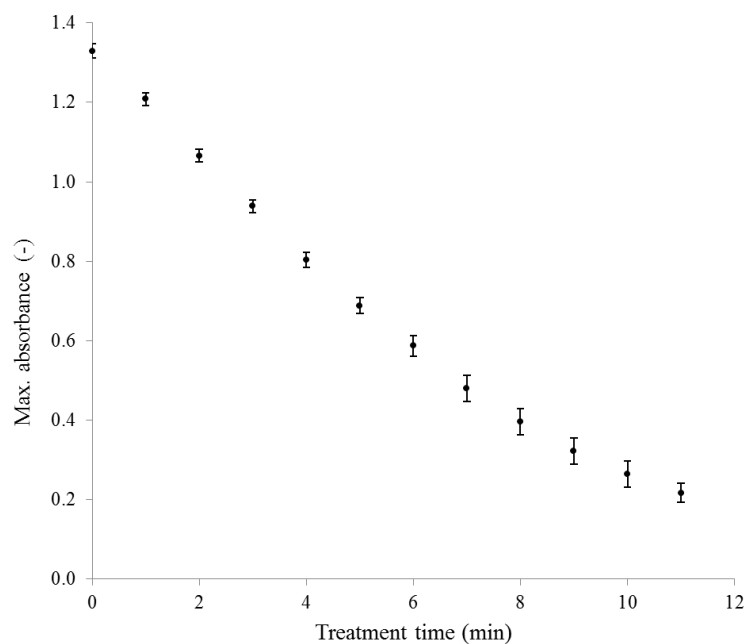
Fig. 4-4 UV-vis absorbance of aqueous methylene blue solutions (nominal C_0 = 7 mg/L) at their maximal absorbance peak (~660 nm) after different plasma treatment times.

4.4.1.2 Post-treatment degradation of methylene blue

After treating the MB solution samples for different amounts of time (3 and 6 min), their post-treatment behavior was studied for three consecutive days. UV-vis absorption measurements revealed that significant degradation had occurred after the first day (see Fig. 4-5): For the samples treated for 3 min, an additional degradation of 22 % was observed, whereas for the samples treated

during 6 min, this additional degradation was 41 %. The degradation eventually plateaued around 2-3 days post-plasma exposure.

The treated samples were compared to untreated samples (named 'original' in Fig. 4-5). The untreated samples showed small oscillations, but no significant degradation behavior. Thus, the degradation observed in the treated samples is attributed to species formed during the plasma treatment, which remain in the solution after the treatment and slowly react with MB. Similar post-discharge temporal reaction phenomena have been reported in literature. For instance, Lukes et al.'s review discusses post-discharge phenomena of bacterial inactivation (Lukes, Brisset and Locke, 2012). Neretti et al. produced so-called 'plasma-activated water' by a dielectric barrier discharge in air in contact with water, which contained long-lived species such as hydrogen peroxide and ozone (lifetimes of minutes to days) (Neretti *et al.*, 2016).
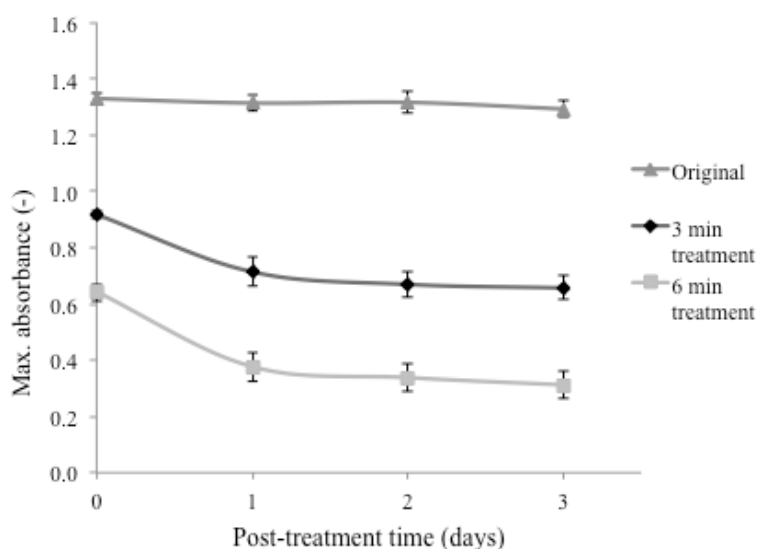
Fig. 4-5 UV-vis absorbance of aqueous methylene blue solutions at their maximal absorbance peak (~660 nm) measured after their plasma treatment. The trendlines are used for guidance.

4.4.1.3 Species transport

Digital images of the solutions were taken at regular intervals during plasma treatment in order to visualize the extent of degradation. In a first experiment, a MB sample was treated for 6 min without mixing. Fig. 4-6 shows the image at the end of the treatment, with the treated sample on the right side and an original solution sample as reference on the left side. A visual observation

reveals a gradual loss in the color of the solution (darker at the bottom and lighter at the top, close to the live electrode).
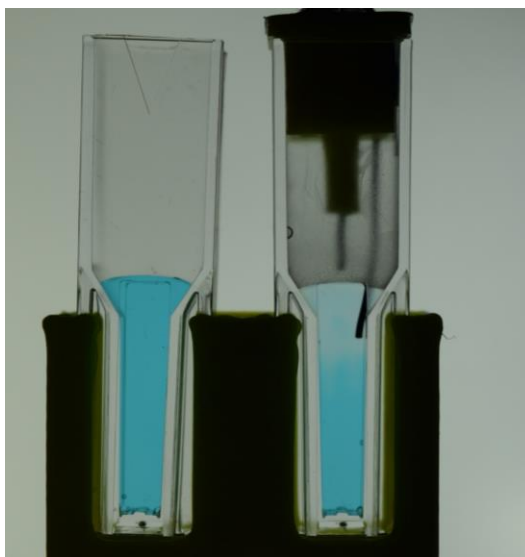
Fig. 4-6 Picture of the pin-to-liquid setup with a treated MB solution sample (right) and an original sample (left).

In a second plasma treatment experiment of MB solution samples, pictures were taken every 10 s (see Fig. 4-7). As the time scale is smaller than in the first experiment, the color gradient that is observed is less pronounced.

Image analysis was performed in order to better visualize the physical extent of the degraded dye zone. The UV-vis analysis revealed that the largest change in absorbance of the treated MB solution occurs around 660 nm (see Fig. 4-3), which wavelength falls within the spectral response of the red pixel of the digital camera. Fig. 4-7 shows the time-evolution of the distribution of red pixel light intensity (right), which is compared to the real images (left).

This analysis clearly reveals the color change in the upper part of the liquid, while this color at the bottom part of the liquid remains unchanged. We infer from the spatial distributions of the red light profile that a recirculating flow sets in near the gas–liquid interface. This circular flow is associated with convective mass transfer in the upper part of the sample. We suspect that a temperature gradient is induced by localized plasma heating. This temperature gradient (radially outward, and axially downward) may cause natural convection (density change) and Marangoni flow (surface tension change).
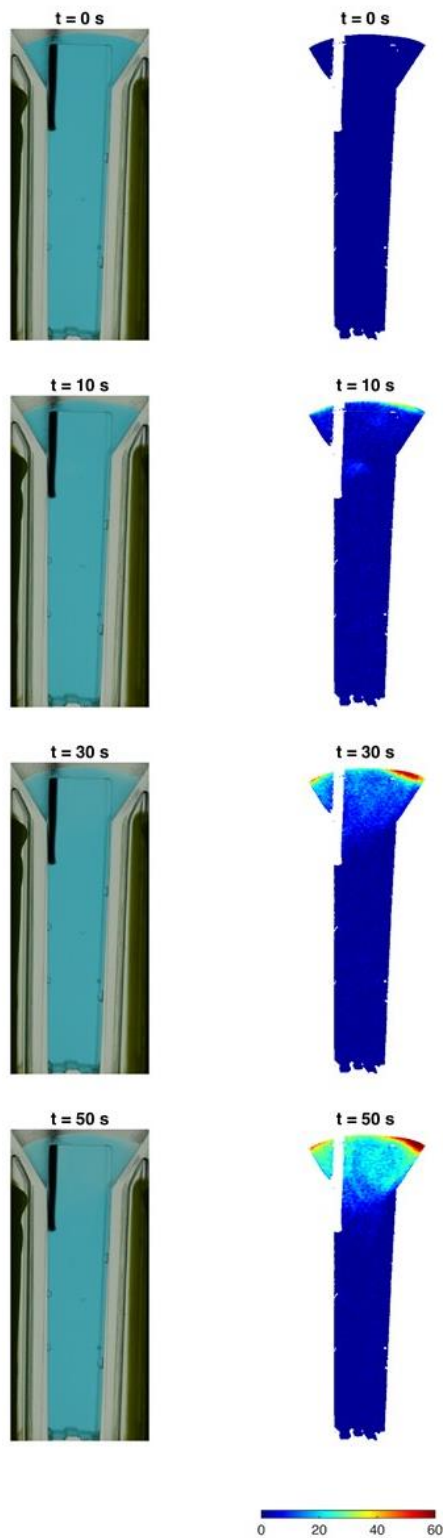
Fig. 4-7 Left: Time-evolution of the aqueous MB sample undergoing plasma treatment. Right: Corresponding image analysis of the samples; the color bar represents the light intensity collected on the red pixel of the digital camera.

In order to estimate which one of the two driving forces is predominant, a simple scale analysis was performed. First, the characteristic viscous dissipation time scale is estimated. Assuming a characteristic distance $L \sim 1$ mm (rough estimate of the flow-affected zone dimension), and that the kinematic viscosity of the MB solution is approximately the same as water at room temperature ($\vartheta_{H2O} = 10^{-6} \, m^2/s$), one obtains:

$$\tau \sim \frac{L^2}{\vartheta} = 1 \, s \qquad (4.1)$$

which value is consistent with observations. This time scale also matches the observations of Mededovic Thagard et al. (2018), who used particle image velocimetry to visualize and quantify plasma-induced flow fields in liquid water (Mededovic Thagard *et al.*, 2018),

Next, the dimensionless Bond number (Bo) which is a measure of the importance of gravitational forces compared to surface tension forces is calculated. Assuming the liquid sample heats at the surface from 20 up to 40 °C, this would give rise to a density difference $\Delta\rho_{H2O} = 6 \, kg/m^3$. With a surface tension between water and air of $\sigma = 0.07 \, N/m$ and $g = 9.81 \, m/s^2$, the Bond number is calculated to be:

$$Bo = \frac{\Delta\rho g L^2}{\sigma} \approx 10^{-3} \qquad (4.2)$$

As the Bo is considerably smaller than 1, the conclusion is that the surface tension effects vastly dominate and are driving the mixing at the top layer of the sample. Since the surface tension of water increases with decreasing temperature, we suspect that the convective flow starts underneath the live electrode and move radially outward along the free surface. Concerning the bottom of the sample (leg of the cuvette), where no significant flow is observed, the mixing is limited to diffusion and becomes inefficient (as revealed with the blue color in Fig. 7).

4.4.2 Part 2: Optimization of operating parameters

4.4.2.1 Stirring

Fig. 4-8 shows the time-evolution of the transparency for a stirred MB solution (top) vs. a not stirred MB solution (bottom). Similar to the previous section, image analysis was performed by studying the distribution of red pixel light intensity of the digital camera, which is equivalent to the transparency of the solution and thus represents the degradation of MB. The stirred solution

has homogeneous transparency except for a small, more transparent layer close to the liquid surface. This indicates that, although the bulk of the solution is homogeneously mixed, reactions at the plasma–liquid contact area occur faster than the stirring. For the solution that is not stirred, the degradation front starts at the plasma–liquid contact area as well. As time progresses, the degradation front travels downwards, with a recirculating flow similar to the one in Fig. 4-7.
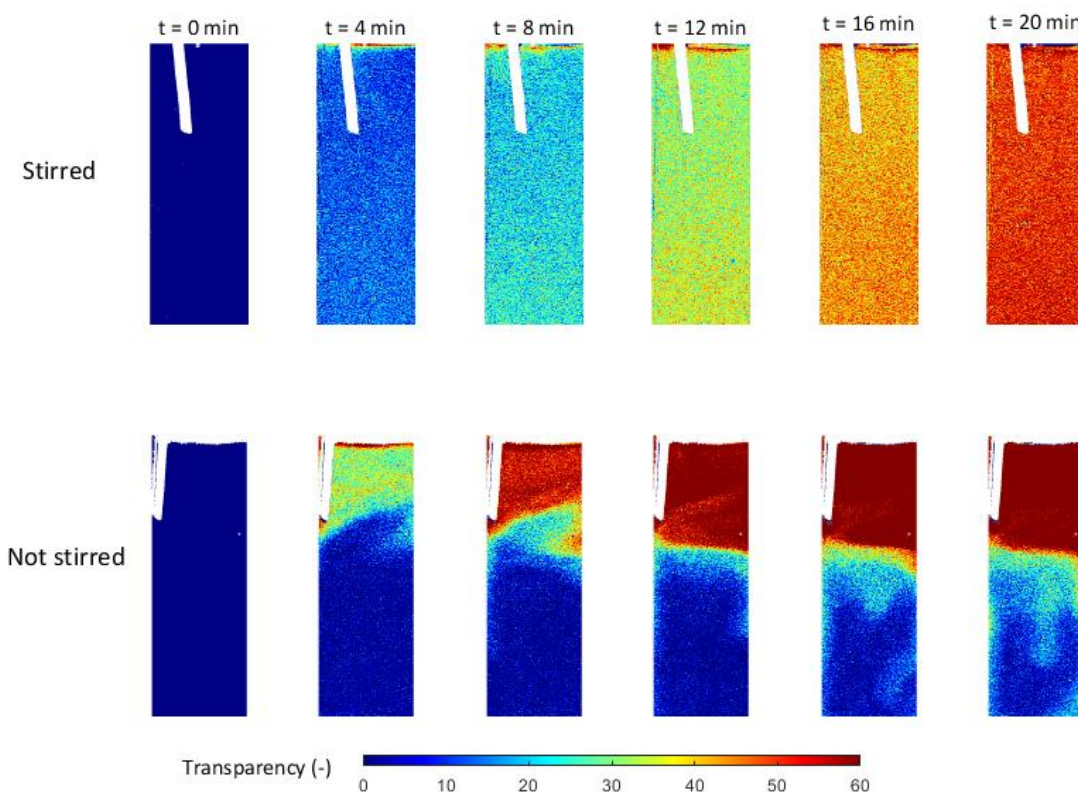
Fig. 4-8 Time-evolution of the transparency of aqueous methylene blue samples undergoing plasma treatment. Digital images of the samples were analyzed, extracting the light intensity collected on the red pixel of the digital camera (red pixel light intensity represented in the color bar).

Fig. 4-9 compares the degradation of MB under stirring vs. no stirring. Note that the 20 and 40 min samples were prepared in separate experiments, and that the "not stirred" samples were shaken before taking UV-vis measurements. After 20 min, stirring achieves 60 % degradation whereas not stirring leads to 34 % degradation. Although convection (observed from image analysis in Fig. 4-7 and Fig. 4-8) already helps mixing the solution, it seems like it is worth introducing additional stirring, since this yields better degradation results.
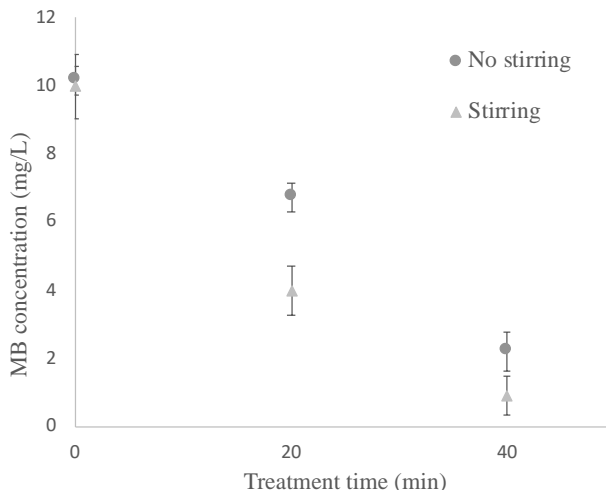
Fig. 4-9 Methylene blue (MB) concentration (nominal C_0 = 10 mg/L) measured at two plasma treatment times. The effect of stirring vs. no stirring is compared.

4.4.2.2 Electrical parameters

Fig. 4-10 shows the effect of varying frequency, voltage and live electrode polarity on MB degradation. Both the increase of the pulse frequency and voltage lead to significantly shorter treatment times required to degrade MB. For the case of the pulse frequency, increasing from 1 to 9 kHz decreases the total time required to degrade MB by 85 % ($\leq$ 0.2 mg/L MB). For the case of the voltage, increasing from 5.4 to 10.8 kV leads to a decrease of the total degradation time by 64 % ($\leq$ 0.2 mg/L MB). These observations can be explained by the fact that these two parameters influence the energy deposited to the liquid, and thus the formation of reactive species that lead to the degradation of the dye. Whereas increasing frequency leads to a higher number of pulses that deposit energy, increasing voltage rises the electrical energy per pulse. The calculation of the energy deposited per pulse will be shown in Chapters 5 and 6.

The different polarities of the electrode above the liquid seem to slightly affect the slope of the degradation process. When low residual dye concentrations are reached, the curves get closer. Inverting the pin-to-liquid polarities can lead to modifying the discharge patterns (Bruggeman *et al.*, 2008), thus possibly affecting the formation of reactive species, which could explain differing degradation behaviors. In any case, the difference between the two polarities on the degradation of MB remains small.
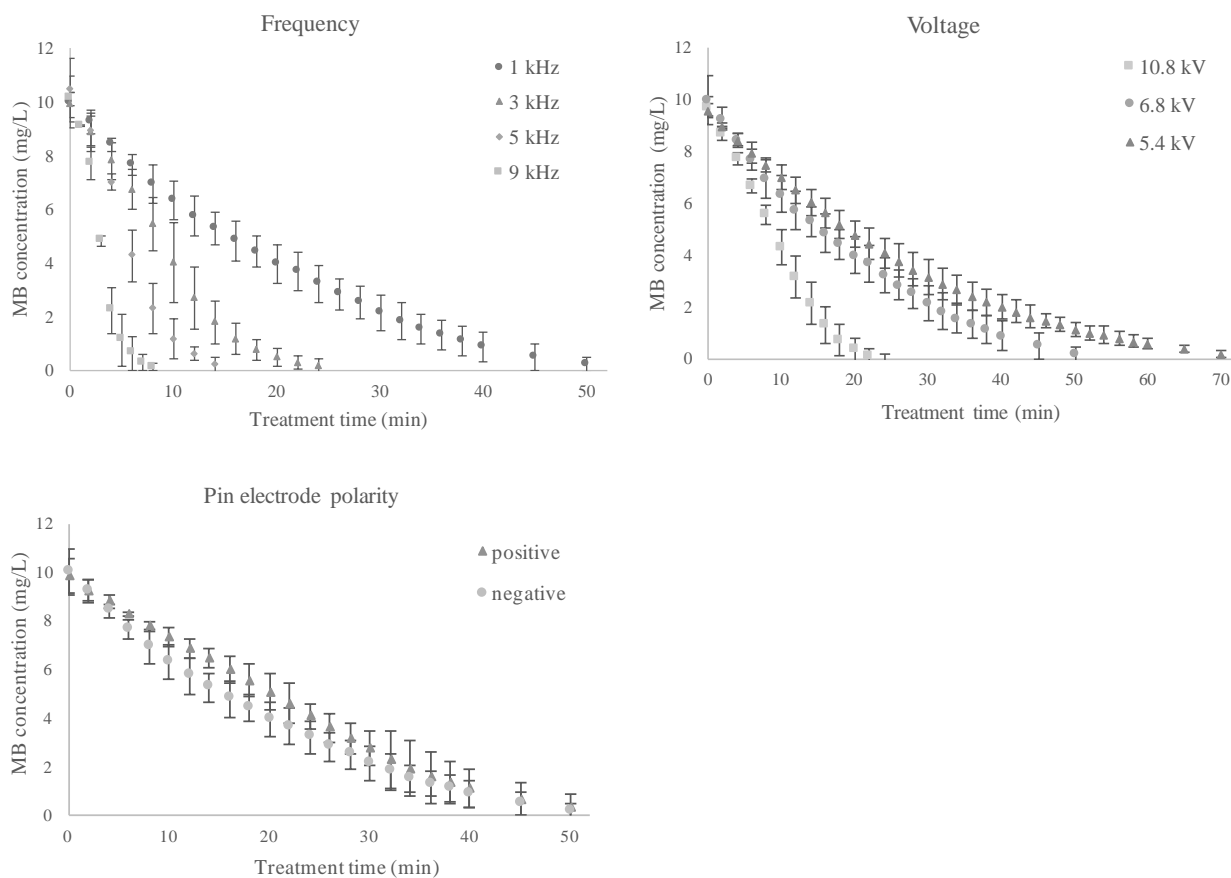
Fig. 4-10 Methylene blue (MB) concentration (nominal $C_0 = 10$ mg/L) measured at different plasma treatment times, each for three sample repeats. All samples were continuously stirred with a magnetic stir bar during the plasma treatment. Top left: Effect of pulse frequency. Top right: Effect of total voltage drop. Bottom left: Effect of pin electrode polarity.

4.5   Conclusions and outlook

Degradation of an aqueous MB solution was achieved by nanosecond pulsed discharges in a pin-to-liquid configuration, confirming the applicability of this newly developed nanosecond pulser to wastewater treatment. After 11 min of treatment, the concentration of the MB dye in a 1 ml cuvette was reduced by 84 %. Post-treatment degradation was observed as well, probably due to the presence of long-lived species produced by the electrical discharges in contact with air and water. The composition and concentration of these long-lived species will be analyzed in future work. In order to isolate the degradation of model organic pollutants during the plasma discharge from the post-discharge reactions with long-lived species, for future work we propose to quench residual reactive species immediately after the plasma treatment.

Pictures taken at different plasma treatment times were analyzed, and a color gradient was observed in the solution. Tracking the degradation of MB by analyzing the red pixel reading of a digital camera has not been previously reported. The image analysis revealed convective mass transport near the free surface. Based on a scale analysis, we deduced that the flow sets in by surface tension effects (Marangoni flow). Below the convective cell, the mass transport in the bulk of the liquid is limited to diffusion. These results contribute fundamental knowledge on the reaction-mass transport processes, but also reveal the need for external assistance for mixing and contact area enhancement. Indeed, introducing forced stirring by a magnetic stir bar yielded better MB degradation results than not stirring the solution.

A parametric study showed that higher voltages and frequencies led to faster removal of the dye, whereas inverting the polarity did not speed up the full removal of the dye. In future work, the effect of different gas atmospheres on the removal of a model organic compound will be studied.

Acknowledgements

5

Manuscript 2

Investigation of the electrode erosion in pin-to-liquid discharges and its influence on reactive oxygen and nitrogen species in plasma-activated water

5.1   Preface

This chapter presents an article published in the journal of "*Plasma Chemistry and Plasma Processing*". The complete citation of the published manuscript is:

> E. Corella Puertas, A. Dzafic and S. Coulombe (2020), *Investigation of the electrode erosion in pin-to-liquid discharges and its influence on reactive oxygen and nitrogen species in plasma-activated water*. Plasma Chemistry and Plasma Processing 40:145–167.

The work was planned, analyzed and written by Elena Corella Puertas (PhD candidate). Adna Dzafic assisted in part of the experimental work and contributed to the particle size analysis. Dr. Sylvain Coulombe was responsible for supervision and review of the work.

The novel, compact pin-to-liquid discharge reactor used in this chapter was designed based on the knowledge obtained in Chapter 4. Since Chapter 4 discussed the potential benefits of mixing the plasma-treated solution and enhancing the plasma–liquid contact area, the new reactor includes bubbling gas from the bottom of the reactor to fulfill both purposes. Chapter 4 reported the presence of residual, long-lived reactive species that reacted with a model organic compound (MB)

post-plasma exposure. In the present chapter, long-lived reactive oxygen and nitrogen species formed in plasma-treated water (hydrogen peroxide, nitrites and nitrates) are studied for four weeks post-plasma exposure. Two gas atmospheres, oxygen and air, are compared.

In the process of designing the pin-to-liquid discharge reactor, a suitable material for the high-voltage pin electrode was searched. The literature review in Chapter 2 revealed that various electrode materials erode in in-liquid discharges, but there was no data available on the erosion of gas-side, high-voltage pin electrodes in above-liquid discharges. To fill this gap, the present chapter studies the erosion of the high-voltage pin electrode for three electrode materials (copper, stainless steel and hafnium). Although all three electrode materials introduce metal-based ions and particles into the plasma-treated liquid, none of them seem to have a significant effect on the formation or lifetime of long-lived reactive species. Since stainless steel is the electrode material with least erosion in both gas atmospheres, this material was chosen for running the experiments in Chapter 6.

Investigation of the electrode erosion in pin-to-liquid discharges and its influence on reactive oxygen and nitrogen species in plasma-activated water

Elena Corella Puertas[1], Adna Dzafic[1,2] and Sylvain Coulombe[1]

[1]*Plasma Processing Laboratory, Department of Chemical Engineering, McGill University, Montréal, Canada*

[2]*Department of Chemistry, Technische Universität München, Munich, Germany*

Abstract

Although the erosion of high-voltage electrodes was extensively studied in in-liquid electrical discharges, to the best of our knowledge, the erosion produced by discharges generated above water has been barely explored. This work studies the erosion of three pin electrode materials (hafnium, copper, stainless steel) in two gas atmospheres (oxygen, air). They are powered by repetitive high-voltage nanosecond pulses, producing pulsed streamer discharges above water. The electrode material does not affect the energy deposited per pulse. The surfaces of all three electrodes erode, releasing metal particles into the water. Stainless steel is the material with least erosion, in both gas atmospheres. Overall, copper in air shows the highest erosion. We also examine how the metals released into the water affect three long-lived reactive oxygen and nitrogen species (RONS), H_2O_2, NO_2^- and NO_3^-, during four weeks post-discharge. After treatment with air plasma, NO_2^- and NO_3^- are measured in the treated water, but H_2O_2 is not detected. NO_2^- is almost completely converted into NO_3^- after two weeks. H_2O_2 is measured for samples prepared with an oxygen plasma. Neither the RONS nor the conductivity of plasma-treated water are significantly affected by the use of different electrode materials.

5.2 Introduction

The study of plasma–liquid interactions is a fast-growing field that is finding applications in various areas such as wastewater treatment, medicine, material synthesis and agriculture (Bruggeman *et al.*, 2016; Locke and Lukeš, 2018; Puač, Gherardi and Shiratani, 2018). Plasma-activated water (PAW) is formed through the interactions of a non-equilibrium plasma with liquid water. In order to produce PAW, electrical discharges can be generated either directly in the liquid, or in a gas atmosphere in contact with liquid water. A number of studies have compared different plasma-liquid configurations in terms of energy yield, which is defined as the amount of pollutant decomposed per energy input (Malik, 2010). The results show that electrical discharges in a gas phase in contact with a liquid are more efficient than in-liquid discharges (Malik, 2010; Stratton *et al.*, 2015; Kozakova *et al.*, 2018). This can explain the increase in the number of studies of discharges in gas-liquid environments in the last years. Furthermore, Malik compared the energy yield of pulsed discharges versus DC discharges (Malik, 2010). According to this study, pulsed corona discharges (PCD) are the most efficient choice, surpassing pulsed dielectric barrier discharges (DBD) and DC discharges (all of them were compared over thin film of water).

In an air plasma in contact with water, the primary species that are generated consist mainly of radicals such as $^\bullet$OH, H$^\bullet$, O$^\bullet$ and NO$^\bullet$, and ions such as H$^+$, N$_2^+$ and H$_2$O$^+$ (Lukes, Locke and Brisset, 2012; Bruggeman *et al.*, 2016). These species react with other primary species or with the surrounding gas or liquid molecules, forming secondary species such as hydrogen peroxide, ozone, nitrous acid, nitric acid and peroxynitrous acid, as well as their ions (NO$_2^-$, NO$_3^-$, ONOO$^-$) (Lukes, Locke and Brisset, 2012; Bruggeman *et al.*, 2016). In an oxygen plasma in contact with water, similar oxygen-based species are formed (Velikonja *et al.*, 2001). Whereas the primary species have short lifetimes of less than a second, some secondary species can be relatively long-lived, for up to weeks (Traylor *et al.*, 2011; Boehm *et al.*, 2016; Shen *et al.*, 2016). Among long-lived species found in PAW, hydrogen peroxide, nitrites and nitrates are commonly reported in the plasma-liquid literature (Boehm *et al.*, 2016; Bruggeman *et al.*, 2016; Locke and Lukeš, 2018). Reactive oxygen and nitrogen species (RONS) in PAW can react with organic molecules in redox reactions and/or acid-base reactions (Lukes, Locke and Brisset, 2012). For instance, in water treatment applications, RONS have been shown to effectively oxidize and degrade various organic pollutants (Malik, 2010; Dobrin *et al.*, 2013; Foster, 2017; Mededovic Thagard *et al.*, 2017; Tampieri *et al.*,

2018). The fact that RONS have bactericidal activity and can trigger various biomolecular mechanisms has been utilized in plasma agriculture and plasma medicine (Oh *et al.*, 2016; Shen *et al.*, 2016; Puač, Gherardi and Shiratani, 2018; Tanaka *et al.*, 2018).

One of the issues associated with various plasma configurations is the erosion of electrodes due to physical and/or chemical phenomena including sputtering, melting, evaporation, oxidation and electrochemical-derived processes (the latter applies if the electrode is in contact with water) (Goryachev, Ufimtsev and Khodakovskii, 1997; Kirkpatrick and Locke, 2006; Lukeš *et al.*, 2006; Mededović and Locke, 2006; Holzer and Locke, 2008; Lukes *et al.*, 2011; Lukes, Locke and Brisset, 2012; Liu *et al.*, 2016; Foster, Mujovic and Groele, 2018). Electrode erosion in in-liquid discharges was extensively studied in the past 20 years, showing that metal ions and particles are released into the PAW (Blokhin *et al.*, 1999; Efremov *et al.*, 2000; Kolikov *et al.*, 2005; Lukeš *et al.*, 2006; Mededović and Locke, 2006; Mededovic and Locke, 2007; Rutberg *et al.*, 2010; Lukes *et al.*, 2011; Parkansky *et al.*, 2012). These metals can show catalytic activity and interact with RONS. In particular, one of the most studied reactions is Fenton's reaction, in which iron ions catalyze the splitting of hydrogen peroxide to form hydroxyl radicals. As hydroxyl radicals are very strong oxidants, Fenton's reaction can enhance the removal of pollutants (Walling, 1975; Mededovic and Locke, 2007; Parkansky *et al.*, 2012; Dai *et al.*, 2016; Cao *et al.*, 2018). Fenton-like reactions can also occur with other ions such as copper or tungsten (Holzer and Locke, 2008; Lukes *et al.*, 2011; Cao *et al.*, 2018). Furthermore, the release of metals can contribute to the disinfecting, cytotoxic and antitumoral properties of PAW (Kolikov *et al.*, 2005; Rutberg *et al.*, 2008, 2010; Vukusic *et al.*, 2016). Depending on the specific application, the release of metals by erosion can be regarded as beneficial or detrimental. An example where electrode erosion can be desirable is the production of nanomaterials (Chen, Li and Li, 2015). For water purification and biomedical applications, electrode erosion can be an opportunity or a challenge. On the positive side, metal particles and ions can enhance the removal of contaminants and microorganisms, as mentioned above. On the negative side, metals in aqueous solutions are expected to pose toxicological and environmental challenges (Besser and Leib, 2007).

As more attention was brought to applications of electrical discharges in gas-liquid environments in the last years, studying electrode erosion was not further pursued in depth. To the best of our knowledge, there are very few studies that have dealt with electrode erosion in high-voltage

discharges in gas-liquid environments. In fact, when reviewing various studies on high-voltage discharges in a gas phase in contact with a liquid, we noticed that most do not report on the erosion of the gas-side electrode, or do not report whether metals released from this gas-side electrode reach the liquid phase (Pokryvailo *et al.*, 2004; Benetoli *et al.*, 2011; Dobrin *et al.*, 2013; Panorel *et al.*, 2013b; Stratton *et al.*, 2015; Kornev and Preis, 2016; Yoon *et al.*, 2018). Dai et al. studied an electrode system with a high-voltage nickel-chromium wire above an aqueous solution, and a grounded stainless or carbon steel electrode in the liquid (Dai *et al.*, 2016). During the plasma treatment, they observed a release of iron ions from the submerged electrode, which initiated Fenton's reaction. However, they did not report whether they observe erosion of the above-liquid, high-voltage electrode (Dai *et al.*, 2016). In Holzer and Locke's study, the grounded electrode was a reticulated vitreous carbon (RVC) disk placed above the liquid, whereas a high-voltage needle electrode was submerged in the liquid. They tried different metals for the needle electrode and observed that erosion occurred in all cases. Furthermore, they found that the H_2O_2 formation rates and efficiencies (amount of H_2O_2 formed per Joule) did not depend on the electrode material (Holzer and Locke, 2008).

This study focuses on electrode erosion and its possible effects on long-lived RONS (hydrogen peroxide, nitrites and nitrates) of the liquid phase, using a pin-to-liquid configuration powered by repetitive high-voltage nanosecond pulses producing pulsed streamer discharges above the liquid. We use hafnium, copper and stainless steel as pin electrode materials, and water as the liquid. We quantify the amounts of metal released into water, and investigate whether these eroded metals have an effect in the post-discharge period.

5.3   Experimental section

5.3.1 Electrode materials

Copper was chosen for its low melting point, which is expected to lead to higher degradation than other metals, and for its toxicity, which can be of interest for disinfection or biomedical applications (Kolikov *et al.*, 2007). Stainless steel was selected because of its resistance to oxidation and corrosion. In case it does erode, it may release iron ions or particles, which could lead to Fenton's reaction. Concerning hafnium, this metal has received little attention from the plasma–liquid community, to the best of our knowledge, though it is used in a different application

context. In plasma arc cutting hafnium is preferred over tungsten and zirconium because it performs better in oxidizing gas environments (Nemchinsky and Severance, 2006). We wanted to check whether it performed better than stainless steel in terms of avoiding electrode erosion and metal deposition into the water.

5.3.2 Experimental setup

Fig. 5-1 shows a schematic of the pin-to-liquid plasma reactor. It consists of a small temperature-controlled jacketed reactor open at both ends, equipped with custom-made lids allowing to mount a pin electrode above the liquid, and a metallic sparger immersed in the liquid which is used to bubble the desired gas through the liquid. The borosilicate glass vessel (JRV Scientific Glass Montreal, inner diameter 19.4 mm, height 83.5 mm) is maintained at 20.5 °C using a circulating water chiller (Marshall Scientific, Thermo Neslab RTE 10 Circulating Chiller). The lids are made of polytetrafluorethylene and provide electrical insulation. The sparger submerged in the liquid is made of 316L stainless steel (Mott, 8.05 mm diameter, 5 µm pore size) and both supplies gas to the system and acts at the anode. We used compressed dry air or oxygen (Praxair, 99.993 % purity) at 6 mL/min at atmospheric pressure. The gas flow was initiated 3 min prior to any experiment to make sure the reactor chamber was sufficiently purged with the desired gas. Fine 0.25 mm-diameter wires of copper (99.99+% purity), 302 stainless steel or hafnium (97% purity) (all by Goodfellow) were used as cathode pin above the liquid. The cathode pin surface was prepared by cutting the metal with a wire cutter with a flush cut profile (McMaster-Carr), and sonicating it in an ethanol bath for 10 min to remove impurities. The cathode was mounted approximately 2 mm above the water surface. Because of the gas bubbles rising to the water surface, the distance between the pin tip and the liquid surface was not constant. Reverse osmosis (RO, 1.2 MΩ·cm, vacuum-filtered through 0.22 µm filter paper Merck Millipore Type GV) was used as the liquid.
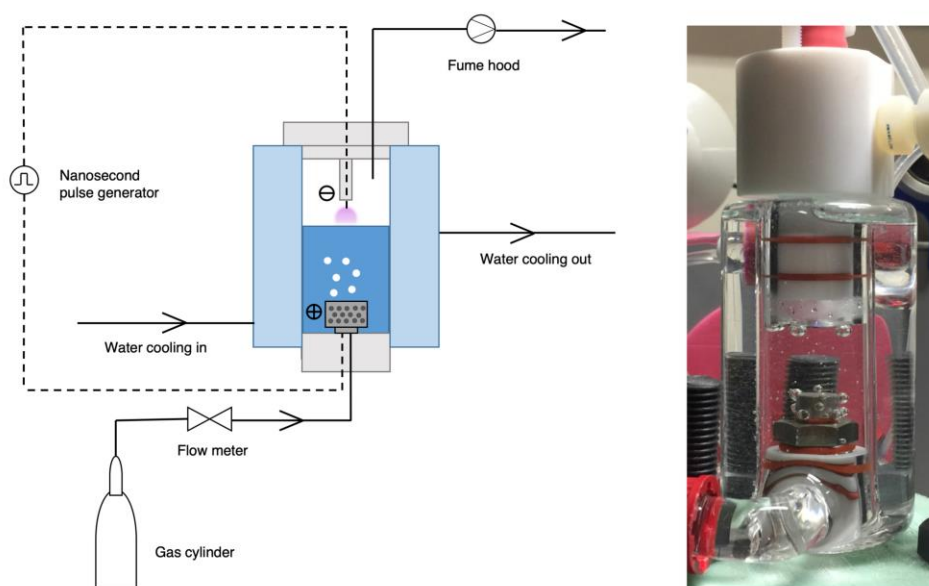
Fig. 5-1 Schematic of the experimental setup (left) and picture of the reactor (right). The cathode is a wire (0.25 mm diameter); the anode is a sparger.

5.3.3 Electrical diagnostics

A homemade diode opening switch generator powered the electrodes, producing two simultaneous pulses. The negative pulse powered the pin electrode; the positive pulse powered the sparger. Nanosecond pulses were produced at a frequency of 3 kHz and a total peak-to-peak voltage drop of 12 kV. The discharge voltage signals were measured using two passive high-voltage probes (Tektronix P6015A), while the current was measured with a current transformer probe (Pearson 6585). The electrical signals were recorded simultaneously using a digital oscilloscope (Pico Technology, PicoScope 2207B). Fig. 5-2 shows characteristic voltage and current signals measured in an air atmosphere for different electrode materials, averaged for 50 sample repeats. Because the oscilloscope only had two channels, we were only able to record two inputs simultaneously. First, we recorded the two voltage pulses simultaneously, and confirmed that they were synchronized and of equal peak amplitude (data not shown here). Second, we recorded the negative voltage pulse and the current simultaneously (see Fig. 5-2).
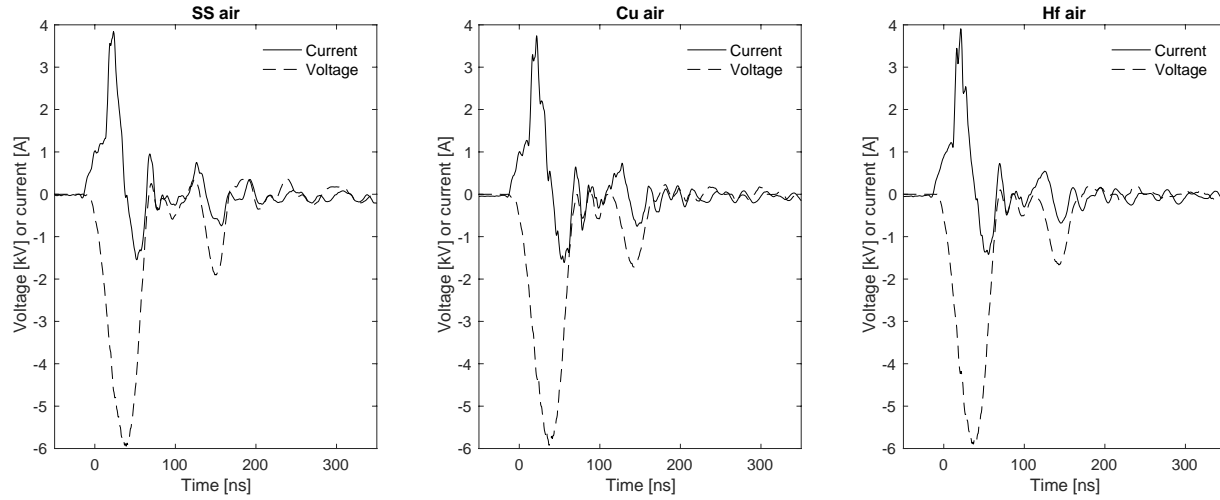
Fig. 5-2 Characteristic voltage and current signals during air plasma treatment at a nanosecond pulse frequency of 3 kHz, averaged for 50 consecutive samples. The voltage signal represents the negative voltage pulse. The simultaneous, positive voltage pulse is not shown here. The material of the electrode was either stainless steel (SS), copper (Cu) or hafnium (Hf).

The calculation of the energy deposited per pulse was based on Rusterholtz's method (Rusterholtz, 2012). First, at low voltages without plasma ignition, the parasitic capacitance of the electrodes and cables was obtained by matching the amplitudes of the derivative of the applied voltage and of the total current (see Eq. 5.1). The capacitance C was 2.17 pF for the stainless steel electrode, 2.40 pF for the hafnium electrode and 2.45 pF for the copper electrode. The delay between the measured current and the displacement current was 7 ns. This delay comes from the different characteristics of the voltage and current probes, as well as from the different cable lengths between the probes and oscilloscope. Second, the conductive current of the plasma was calculated by subtracting the displacement current from the measured current (Eq. 5.2). Finally, the energy deposited per pulse was obtained by integrating the power over the duration of the pulse, using the measured voltage and calculated conductive current (Eq. 5.3).

$$I_{measured,no\ plasma} = I_{displacement} = C\frac{dV}{dt} \tag{5.1}$$

$$I_{measured,plasma} = I_{conductive} + I_{displacement} \tag{5.2}$$

$$E_{plasma} = \int_{t_0}^{t_{end}} I_{conductive} V\, dt \tag{5.3}$$

5.3.4 Chemical analyses

The metal content of the liquid samples was measured by inductively coupled plasma optical emission spectrometry (ICP-OES) (Thermo Scientific, iCAP 6000 Series). The samples were previously digested with acid at 95 °C for 2 hours. For the case of PAW samples produced with copper or stainless steel electrodes, the digestion was done in 4 vol% of HNO_3 (Fisher Scientific, Trace Metal Grade). For the samples produced with a hafnium electrode, the digestion was done in 5 vol% aqua regia, i.e. 4:1 volume ratio of concentrated $HCl:HNO_3$ (Fisher Scientific, Trace Metal Grade, 68% HNO_3, 36% HCl). The data was processed with the software iTEVA (Thermo Fisher Scientific). A multi-ion standard (RQC-1, 10 mg/L, 5% HNO_3) and a Hf standard (1000 mg/L, 4% HCl), both by SPC Science in ICP-AES grade, were diluted in RO water to prepare calibration solutions.

Dynamic light scattering (DLS) (Malvern Instruments, Zetasizer Nano ZS) was used as to confirm the presence of nanoparticles in PAW samples. We analyzed samples that had been plasma-treated for 20 min. For each electrode (Cu, Hf, SS) and gas (air, oxygen) configuration, we measured 4 samples with 3 repeats per sample. Out of the 12 measurements per configuration, we calculated the arithmetic mean of the z-average diameters, as well as the confidence interval for a confidence level of 95 % based on the t-Student's statistics.

The surface of the pin electrode was imaged with a Hitachi SU3500 Scanning Electron Microscope (SEM). Images were taken before (pristine electrode) and after use. The after-use SEM images were obtained after using the electrodes for the ICP-OES experiment, this means their total discharge time was approximately 200 min (in periods of 5, 10, 15 and 20 min).

In order to measure the hydrogen peroxide concentration in PAW samples, we used a modified version of the High-Performance Liquid Chromatography (HPLC) method proposed by Takahashi et al. (Takahashi *et al.*, 1999). The analytical instrument (Hewlett-Packard) was composed of a series 1050 HPLC+UV-Vis system with a 35900E HPLC interface and a 1049A electrochemical detector (ECD). We used an ion exclusion column (Thermo Scientific, Dionex IonPac ICE-AS6). The peaks were integrated with the software (HP ChemStation). The mobile phase contained 50 mM of Na_2SO_4 (Fisher Scientific, ACS grade) and 10 μM of EDTA·2Na (Sigma-Aldrich, 90 % titration), dissolved in RO water. The flow rate of the mobile phase through the HPLC system was

set to 1 ml/min. Before every set of measurements, a calibration curve was measured. A H_2O_2 standard solution (Fisher Scientific, 30 % ± 1.1, ACS grade) was diluted with RO water to prepare the calibration solutions, as well as quality control (QC) samples. The PAW samples were diluted to a volume ratio of 1:15.

Ion Chromatography (IC) was used to analyze the concentration of nitrites and nitrates in PAW samples. The samples were diluted to a volume ratio of 1:5. The IC system was composed of a 820 separation center, 818 IC pump, 833 liquid handling unit, 830 interface, 838 advanced autosampler and 819 IC detector, all by Metrohm. The peaks were integrated with the software (IC Net). We used a mobile phase of 0.318 g/L of Na_2CO_3 (Sigma-Aldrich, ACS grade). NO_2^- standard solution (SCP Science, 991 ± 9 mg/L, H_2O based) and NO_3^- standard solution (SCP Science, 999 ± 5 mg/L, H_2O based) were diluted with RO water to obtain calibration solutions. To confirm the accuracy of the calibration curves, a QC was performed every day before starting the analysis. The solution used for the QC required no further preparation as it was a multi-ion IC standard (SCP Science, H_2O matrix) containing different anions, including nitrate and nitrite at a concentration of 10 mg/L.

Iodometric titrations were performed with the help of a Metrohm 888 Titrando equipment. 0.5 mL of PAW sample was acidified with 2.5 mL of 30% H_2SO_4 (Sigma Aldrich, reagent grade) with 0.18 g/L ammonium molybdate solution (Fisher Scientific, ACS grade). Next, the sample was stirred together with > 0.01 g KI (Fisher Scientific, ACS grade) and five droplets of a 40 g/L starch solution (Fischer Scientific, Tyodene). The titrant was a 0.001 N solution of $Na_2S_2O_3$ (Fisher Scientific, 0.0995 N – 0.1005 N). A H_2O_2 standard solution (Fisher Scientific, 30 % ± 1.1, ACS grade) was diluted with RO water to prepare a control sample with a concentration of 1.1 mmol/L.

The conductivity of the PAW samples was recorded at room temperature with an Oakton Series 510 Benchtop Meter. The equipment was calibrated using Fisherbrand™ Traceable™ Conductivity Calibration Standards. The pH of PAW samples was measured at room temperature with an Orion 420A pH meter. The pH meter was calibrated using three buffer solutions of pH 4, 7 and 10.

5.3.5 Statistical analyses

The error bars shown in the graphs represent the standard deviation of the samples, unless stated otherwise. The ANOVA statistical analysis was performed to check whether the means of two or

more groups were statistically different from each other. The analysis was performed with the Microsoft Excel tool Anova: Single Factor. The significance level was set at $\alpha = 0.05$ for all tests, meaning that there is a 5% risk of concluding that a difference exists when there is no actual difference. When the null hypothesis fails to be rejected (see Table 5-2), it means that there is not enough evidence to state that there is a significant statistical difference between the evaluated means.

5.3.6 Experimental conditions

For all experiments, nanosecond pulses were produced at a frequency of 3 kHz, with a total peak-to-peak voltage drop of 12 kV, a Full Width at Half Maximum (FWHM) of 40 ns and a peak current of 4 A. For the experiments aiming the measurement of the metal content in the plasma-activated water samples, 7.5 mL of water was plasma-treated for 5, 10, 15 or 20 min with 4 repeats. For all other experiments, 7.5 mL of water was plasma-treated for 20 min with 3 repeats. The samples were stored in capped polypropylene tubes (SCP Science, DIGItube 15 ml A/S Tubes) in a 4 °C refrigerator. Because all the analytical measurements had to be taken at room temperature, the samples were taken out of the refrigerator one hour before doing the measurements.

5.4   Results and Discussion

5.4.1 Part 1: Electrical characteristics

Fig. 5-2 shows characteristic voltage and current signals measured in an air atmosphere for stainless steel, hafnium and copper pin electrodes. Both for discharges in oxygen (graphs not shown here) and air, changing the electrode material does not cause any significant effect on the electrical signals. This was confirmed by calculating the energy deposited per pulse. Table 5-1 shows the calculated mean energies with confidence intervals with a confidence level of 99%. For each experimental condition, the energy per pulse is calculated for 50 sample repeats.

In air plasmas, the energy deposited per pulse is around 620 µJ, whereas in oxygen plasmas it is around 350 µJ. Because oxygen is a highly electronegative gas, it attracts and quenches free electrons, forming negative ions (Fridman, Gutsol and Cho, 2007). This electronegative behaviour limits the conductive current that can flow through pure oxygen plasmas, and thus also limits the energy deposited per pulse.

Table 5-1 Mean energy deposited per pulse [µJ] with confidence intervals [µJ] with a 99 % confidence level for 50 sample repeats.

Electrode material	Air plasma	Oxygen plasma
Stainless steel	614 ±10	343 ±6
Hafnium	623 ±9	347 ±6
Copper	618 ±4	357 ±6

There are different sources of uncertainty that can be associated to the energy determination according to on Rusterholtz's method (Rusterholtz, 2012). First, this method assumes that the capacitance of the system does not change with different applied voltages. We verified that this was true for three different voltages (3.9 kV, 4.5 kV, 4.9kV) at which there was no plasma ignition. Furthermore, we checked the sensitivity of the calculations to varying the capacitance C by ± 0.2 pF. This capacitance variation did not have any significant effect on the energy results at the experimental conditions (12 kV). Second, Rusterholtz reports that if the delay between the measured current and the displacement current is not determined correctly, even a mismatch of 0.2-0.3 ns can influence the obtained energy by 50 % (Rusterholtz, 2012). We tested the sensitivity of our calculations to varying the delay by ± 0.5 ns. For the air plasma results, this delay variation led to less than 17 µJ difference from the original value; for the oxygen plasma results, the difference was less than 24 µJ. Therefore, we concluded that the delay only has a small influence on our energy results.

5.4.2 Part 2: Electrode erosion and metal deposition into PAW

5.4.2.1 Electrode tip morphology

Fig. 5-3 shows pin electrode tips imaged by SEM before and after use. The former will be called "pre-treatment" images and the latter "post-treatment" images. Although the electrode tips were cut with a wire cutter with a flush cut profile, in the pre-treatment electrode tip images we see that the surfaces are not completely even. However, we do observe that the surfaces are mostly flat, and some have small pores (especially the stainless steel surface). After the plasma discharges, the surfaces change for all three metals (copper, stainless steel and hafnium) and for both gas atmospheres (air and oxygen).
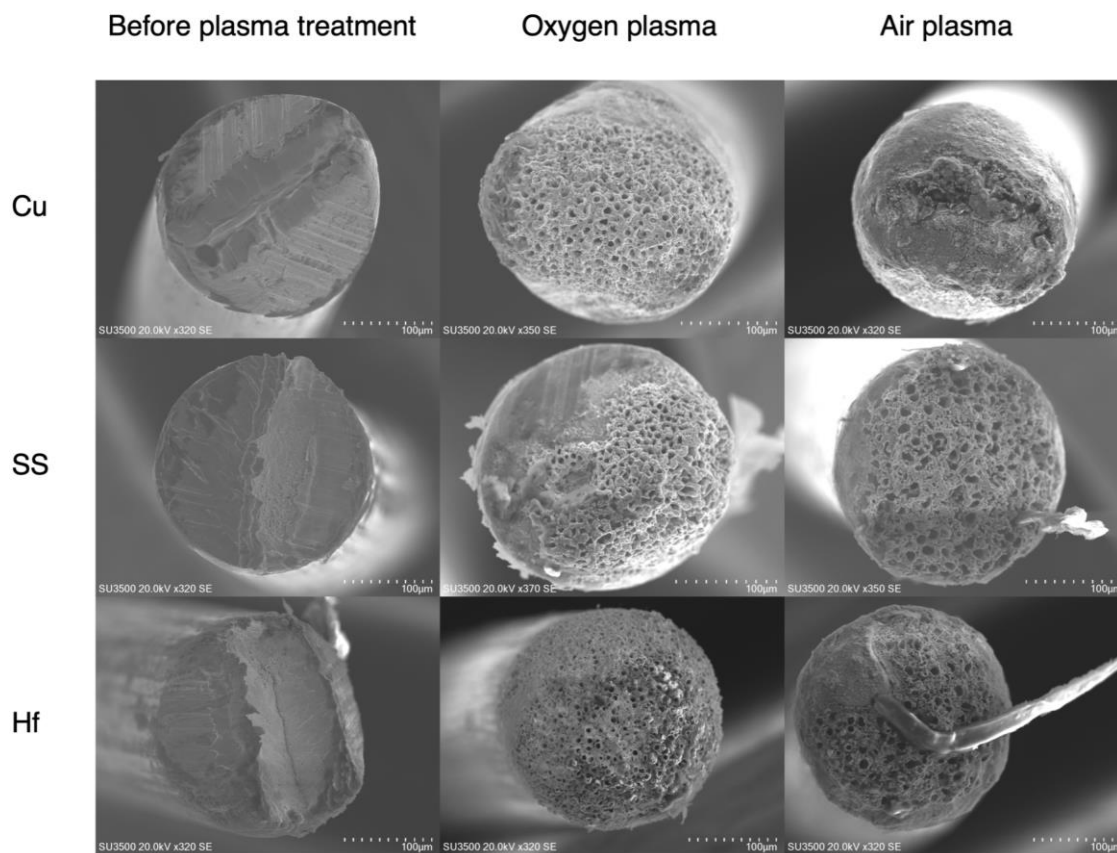
Fig. 5-3 Scanning electron microscope images of the electrode tips. The material of the electrode was either hafnium (Hf), stainless steel (SS) or copper (Cu). The scale on all images is 100 µm.

Hafnium - Both gas atmospheres lead to a crater-like morphology which covers the whole tip surface. The craters formed in an air atmosphere have diameters that range from 3-15 µm, while the oxygen-treated electrodes display craters in the range of 3-8 µm. An elongated piece of dirt, consisting mainly of carbon as confirmed by EDS analysis, contaminated the surface of the air-treated electrode.

Stainless steel - While the air configuration shows a surface fully covered by craters of 3-15 µm-diameter, the morphology of the oxygen-treated electrode exhibits a surface which is partly covered by craters of 3-8 µm diameter and partly flat (upper left area). A possible explanation for this heterogeneous surface is that due to the uneven cut, the surface in the upper left area was significantly behind the other surface area. Discharges typically happen in the area where the distance between the pin and the liquid electrodes is minimal, so they would occur in the most

protruding pin electrode surface. Another possible explanation is that due to the erosion, the surface became brittle and a piece fell off at the upper left area.

Copper – This electrode material leads to a more distinctive difference between the effect of the two gas atmospheres. While the electrode treated in oxygen displays the usual 3-8 μm-diameter craters, smoothly covering the rounded tip surface, the electrode treated in the air environment does not exhibit any crater-like areas. The surface looks quite heterogeneous with areas showing edged, crystal-like structures. Both surfaces are shown in Fig. 5-4. Note that the ICP-OES results will show later that the air-treated copper electrodes lead to the highest metal deposition in the plasma-activated liquid, an order of magnitude higher than all other studied cases. We suspect that copper cannot withstand the discharges in an air atmosphere, and pieces of the surface fall off from time to time.
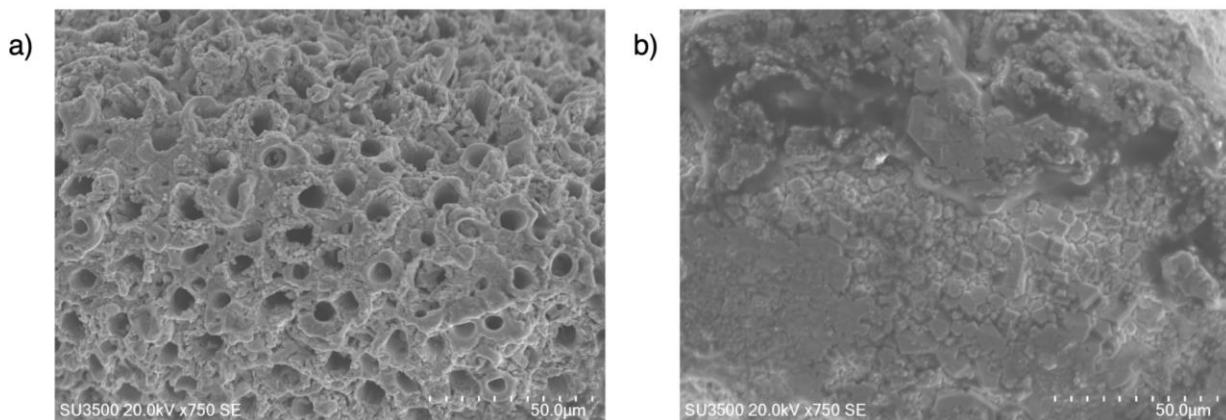
Fig. 5-4 Scanning electron microscope images of the copper electrode tips after an oxygen (a) or air (b) plasma treatment. The scale on the images is 50 μm.

5.4.2.2 Metal content in PAW

Fig. 5-5 shows the metal mass that was deposited from the pin electrode into the liquid, divided by the total energy consumption. The metal concentration in PAW samples was measured by ICP-OES (see metal concentrations in PAW in Fig. 5-11). Note that with the stainless steel electrode, we chose to measure the iron content, as it is its major component. Multiplying the metal concentrations by the known sample volume of 7.5 ml gives the metal mass in the liquid. The energy consumption was calculated multiplying the plasma treatment time by the power supplied from the main power supply to the nanosecond pulser system (61 W). Note that the actual energy

deposited into the plasma is smaller than the energy fed by the main power supply (we did not measure the overall electrical energy efficiency of the nanosecond pulser). The energy efficiency of discharges in air is around 30 %, and of discharges in oxygen is around 20 %.
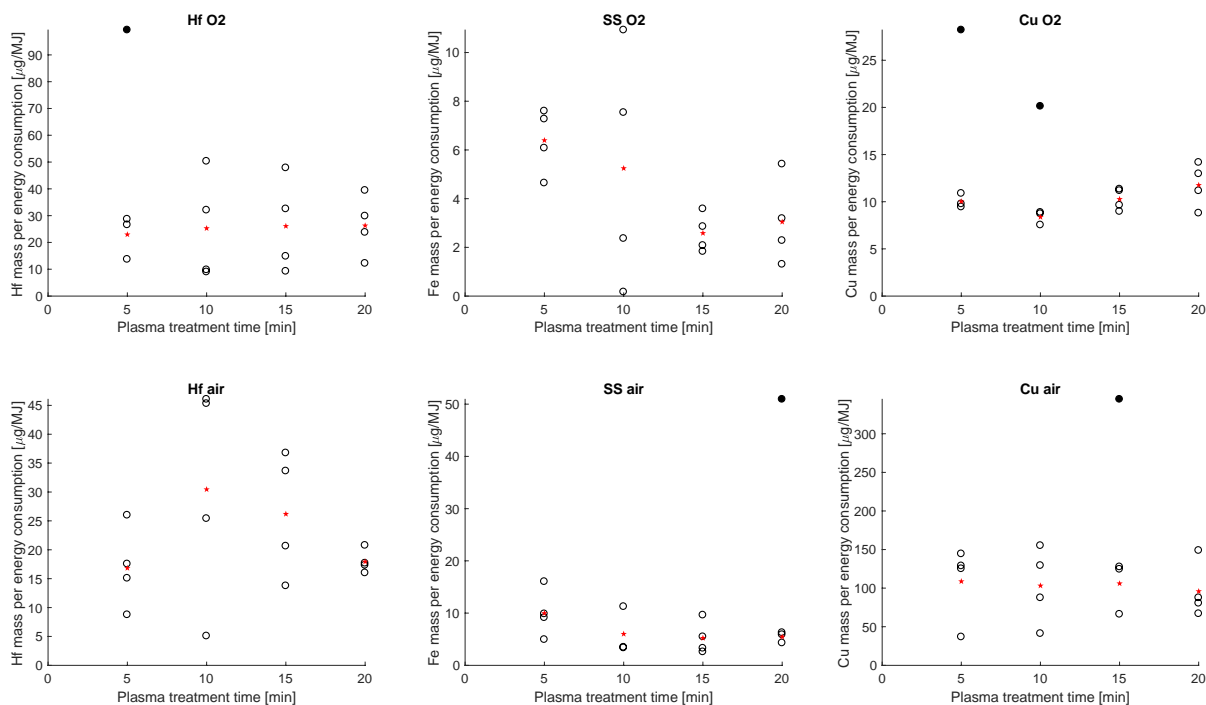
Fig. 5-5 Metal mass that was deposited from the pin electrode into the liquid, divided by the energy consumption of the main power supply. The upper row shows results obtained with an oxygen plasma, and the lower row results obtained with an air plasma. The material of the pin electrode in the gas phase was either hafnium (Hf), stainless steel (SS) or copper (Cu). The circles represent the values obtained for each of the four repeats. The circles filled in black are considered to be outliers. The red stars are the averages of the experimental repeats without the outliers.

When calculating the average metal mass per energy consumption for each time point, we left out some values that we consider to be outliers (represented with a filled black circle in Fig. 5-5). These outliers may be caused by larger metal pieces that are removed from the electrode from time to time during the plasma treatment. This would match the observations we made in the SEM section, where we saw that some of the metal surfaces did not have the usual craters, but rather looked like a larger metal chunk was missing.

For samples obtained under oxygen supply, the hafnium electrode erodes the most, followed by copper and lastly by stainless steel. The metal mass per energy consumption seems to be more or

less constant over the plasma treatment time. It should be noted that in the case of iron in stainless steel, only 45 % of samples are clearly above the quantitation limit (40 % of samples are closely above the quantitation limit and 15 % of samples are below the quantitation limit, but above detection limit). This can explain the large variability of these data points.

Similarly to the case of oxygen plasmas, for air plasmas the metal mass per energy consumption seems to be more or less constant for different plasma treatment times. The results obtained with air plasmas reveal significantly higher erosion of copper and somewhat higher erosion for stainless steel compared to the oxygen plasma results. This could be linked to the fact that air plasmas deposit almost twice as much energy per pulse (see Table 5-1), combined with the different plasma chemistry. The metal mass is around 800 % higher for copper at 20 min and a 60 % higher for stainless steel at 20 min compared to the oxygen plasmas results. For the hafnium electrode, the air environment does not seem to affect the erosion, as the measured metal content is similar to the one obtained with oxygen.

It should be noted that the sparger submerged in the liquid is made of stainless steel. Therefore, we needed to verify whether the measured metal came solely from the stainless steel pin electrode or also from the sparger. In order to do this, we compared the iron content of all PAW samples produced with stainless steel or copper electrodes. To have additional information, we also compared the content of nickel and chromium, two other common components of stainless steel. For the case of samples produced in an oxygen plasma, treatment with the copper pin electrode led to an Fe, Ni and Cr content around the detection limit. The results were similar to values measured in blanks. Therefore, we exclude that the sparger was eroding or leaching ions into the PAW. Samples produced with a stainless steel electrode in oxygen plasma do contain measurable amounts of Fe, Ni and Cr. Thus, we conclude that the erosion comes solely from erosion of the pin electrode.

For the case of air plasmas, the measured Fe, Ni and Cr content is in the same order of magnitude for samples produced with stainless steel or copper electrodes. In this case, we seem to have some erosion or ion leaching from the sparger into the PAW. PAW produced in air contains nitrites and nitrates, which lower the pH compared to PAW produced with oxygen discharges (see Fig. 5-12). The more acidic conditions can perhaps explain this erosion of the sparger. For the longest

treatment time (20 min), the Fe, Ni and Cr content is somewhat higher in samples prepared with a stainless steel electrode versus a copper electrode, by over a factor of 2. Therefore, in the case of a stainless steel electrode with discharges in air, we conclude that both the sparger and the pin electrode are likely to release metals into the PAW.

5.4.2.3 Particle size analysis

The metals in PAW samples that were detected by ICP-OES do not form particles or precipitates that are visible to the naked eye. In order to further investigate these metals in PAW, we used Dynamic Light Scattering (DLS). Per electrode and gas configuration, the particle size distribution was measured 12 times (4 samples with 3 repetitions). The results show the presence of particles of a wide range of sizes, ranging from the scale of 1 nm up to 1000 nm. It should be noted that the polydispersity index (PDI) is very high for all metal cases. All measurements had a PDI above 0.5, and 86% of the measurements had a PDI above 0.7. This indicates that the particles are not monodisperse. A possible explanation for this is that smaller particles agglomerate and build larger particles of a wide range of sizes. In fact, some preliminary transmission electron microscopy (TEM) results indicate that the larger particles consist of agglomerates of very small nanoparticles (images not reported here). For consecutive repeats of the same sample, the particle size distributions vary. This means that the particles are not distributed homogenously, even if the PAW samples were shaken before the measurements. It is even possible that particles have further agglomerated from one measurement to another.

In order to make the results of the different metals and gas atmosphere cases comparable, Fig. 5-6 shows the mean of the z-average diameters (harmonic intensity averaged particle diameter) of the particles. For the copper and stainless steel electrodes, samples produced in an air plasma are larger than the ones produced in an oxygen atmosphere (confirmed by ANOVA statistical analysis, see Table 5-2). This matches the fact that an air plasma led to higher metal deposition in water, as shown previously. If there is more metal present in water, there are more particles that can agglomerate, forming larger agglomerates. Another explanation is that the surface chemistry and electrical charge of the particles may differ depending on the plasma gas, and this would have an influence on the agglomeration of the particles. For the case of hafnium electrodes, there is not enough evidence to state that there is a significant statistical difference between the oxygen and air samples (see see Table 5-2). As the quantity of deposited hafnium is similar for oxygen and air

plasmas, this may match the above-mentioned hypothesis that a similar metal content in PAW would lead to a similar size of agglomerates.
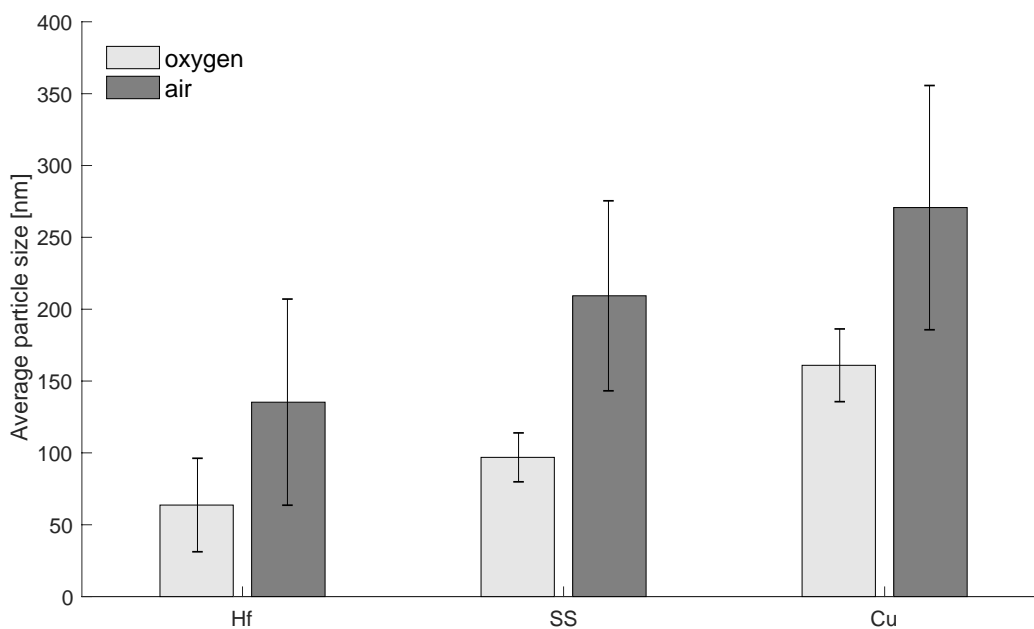
Fig. 5-6 Average size of metal particles found in plasma-activated water, represented by the mean of z-average diameters (12 measurements per electrode and plasma gas configuration). The error bars represent confidence intervals with a confidence level of 95 %. The material of the pin electrode in the gas phase was either hafnium (Hf), stainless steel (SS) or copper (Cu).

5.4.3 Part 3: Effect of eroded metals on reactive oxygen and nitrogen species (RONS)

Having confirmed the presence of eroded metals from different electrodes in the plasma-activated water (PAW), the next step is to study whether and how these metals affect the reactive oxygen and nitrogen species (RONS) in the PAW. We chose to focus on three long-lived RONS that are commonly reported in PAW literature: Hydrogen peroxide (H_2O_2), nitrites (NO_2^-) and nitrates (NO_3^-) (Boehm *et al.*, 2016; Bruggeman *et al.*, 2016; Locke and Lukeš, 2018). Furthermore, we report the conductivity of PAW samples.

5.4.3.1 Nitrite and nitrate

For the PAW produced by discharges in an air atmosphere, we confirmed the presence of nitrites and nitrates in the solution by ion chromatography. In Fig. 5-7, we tracked the content of NO_2^- and NO_3^- from 15 min after plasma treatment to four weeks later. For all three metal electrodes, the

NO_2^- concentration started at about 130 mg/L ($\approx$ 3 mmol/L) and decayed until it almost disappeared after two weeks ($\leq$ 2 mg/L). An ANOVA statistical analysis confirms that the initial NO_2^- concentrations show no significant statistical difference (see Table 5-2). At the same time that the NO_2^- concentration decreased, NO_3^- was formed. Nitrate reached a maximum concentration of 420-460 mg/L ($\approx$ 7 mmol/L) after two weeks and remained constant after that. An ANOVA statistical analysis shows that there is some significant statistical difference for the initial NO_3^- concentrations. This variability may not necessarily be due to the presence of different metals, but perhaps due to rapidly occurring reactions in the initial post-discharge hours, which will be discussed below. In the prolonged post-discharge time (1-4 weeks), we cannot observe a significant statistical difference of the NO_3^- concentrations (see Table 5-2).

There are different pathways in which nitrite can react to form nitrate. Nitrites can disproportionate into nitrates and nitric oxide (NO) under acidic conditions as shown in Eq. 5.4 below (Park and Lee, 1988; Lukes, Locke and Brisset, 2012). NO can in turn react with oxygen dissolved in the water to form NO_2^- and NO_3^- in Eq. 5.5, and the cycle starts again (Karlsson and Tortensson, 1974; Lukes *et al.*, 2005). Furthermore, studies have shown that NO_2^- quickly reacts with reactive oxygen species (ROS) present in the PAW, such as in Eq. 5.6 and Eq. 5.7 (Lukes, Locke and Brisset, 2012; Bruggeman *et al.*, 2016). For the purpose of this post-discharge study, we leave out short-lived radicals produced during the plasma discharge such as $^\bullet OH$, $^\bullet OH_2$, $H^\bullet$, $N^\bullet$, $NO^\bullet$ and $NO_2^\bullet$ because of their extremely short lifetimes. As their lifetimes are less than a second, after their initial effect, we do not expect them to play a role over a long-time scale.

$$3NO_2^- + 3H^+ \rightarrow 2NO(aq) + NO_3^- + H_3O^+ \tag{5.4}$$

$$2NO(aq) + O_2(aq) + H_2O \rightarrow 2H^+ + NO_2^- + NO_3^- \tag{5.5}$$

$$NO_2^- + O_3(aq) \rightarrow NO_3^- + O_2(aq) \tag{5.6}$$

$$NO_2^- + H_2O_2 + H^+ \rightarrow NO_3^- + H_2O + H^+ \tag{5.7}$$
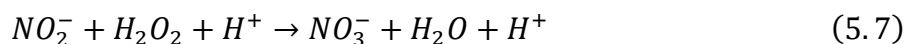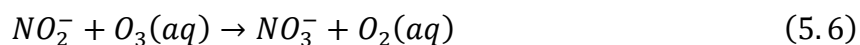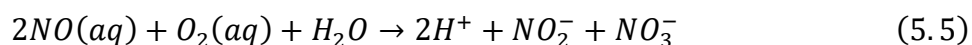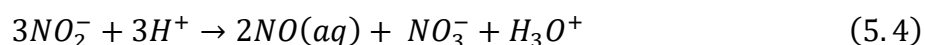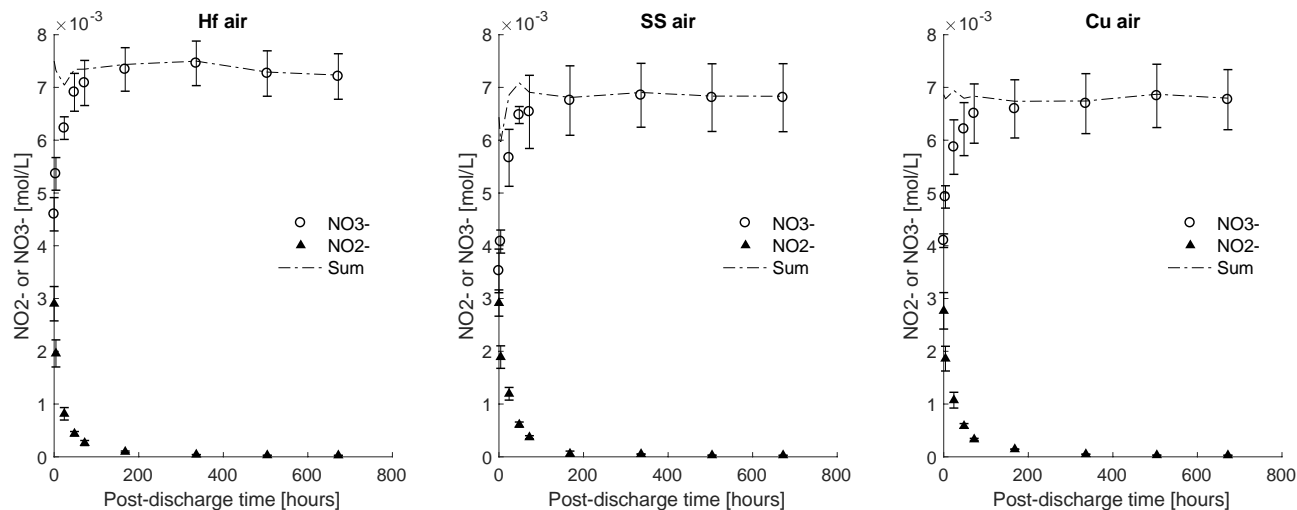
Fig. 5-7 Temporal evolution of the NO_2^- and NO_3^- concentrations in plasma-activated water over the post-discharge time. The samples had been previously plasma-treated in air for 20 min. The dash-dotted line is obtained adding the molar concentrations of NO_2^- and NO_3^-. The material of the pin electrode was either hafnium (Hf), stainless steel (SS) or copper (Cu).

The produced PAW is acidic as observed with the temporal evolution of the pH in the post-discharge period (see Fig. 5-12). For all three metal electrodes, the water had dropped from pH 5 to pH < 3 after plasma treatment, and it remained acidic for all the monitored period. Thus, Reactions Eq. 5.4 and Eq. 5.7 are possible. However, for the PAW produced by discharges in an air atmosphere, we could not detect any H_2O_2 in the post-discharge period. We hypothesize that Reaction Eq. 5.7 occurred so fast that it consumed all the H_2O_2 shortly after plasma treatment was stopped. This may have also been the case for dissolved ozone, although we did not have the means to measure it. We suspect that if present, it reacted rapidly with NO_2^- in solution (Lukes, Locke and Brisset, 2012). Regarding Reaction Eq. 5.5, it can occur because the samples were stored in contact with ambient air, and oxygen could diffuse into the liquid. Therefore, Reactions Eq. 5.4 and Eq. 5.5 probably played a major role in converting NO_2^- to NO_3^- during the monitored post-discharge period.

When adding the molar concentrations of nitrites and nitrates, we observe that their sum remains practically constant (see Fig. 5-7). The constant sum of moles of NO_2^- and NO_3^- suggests that the conversion of NO_2^- to NO_3^- is 1:1. Only in the first post-discharge hours we see small deviations. This can be explained by the fact that other reactive nitrogen species (RNS) can be intermediate species in the process of forming NO_3^- from NO_2^-, such as NO as seen in Reactions Eq. 5.4 and

Eq. 5.5. Furthermore, reactions occur fast in the first post-discharge hours, and it is practically impossible to measure the NO_2^- and NO_3^- concentrations at the exact same time.

In general, the measured NO_2^- and NO_3^- concentrations are practically identical for all three electrode configurations. Therefore, we cannot observe any significant catalytic effect of the different metals on these RONS.

5.4.3.2 Hydrogen peroxide

The hydrogen peroxide concentration of the plasma-activated water samples was analyzed with two techniques: HPLC-ECD and iodometric titration. Whereas the former selectively measures H_2O_2, the latter gives the total oxidizing power (TOP) of any oxidizing species in the solution. By comparing the results of both techniques, we can check if there are any other oxidizing species other than H_2O_2 present in plasma-activated water. Note that H_2O_2 could not be detected in PAW produced by discharges in an air atmosphere. Therefore, this part of the study focuses solely on H_2O_2 that was detected in PAW samples produced in an oxygen atmosphere.

The results of the HPLC-ECD measurements are shown in Fig. 5-8. The initial hydrogen peroxide concentrations are 24 mg/L (0.7 mmol/L) for the case of the hafnium electrode, 31 mg/L (0.9 mmol/L) for the stainless steel electrode and 28 mg/L (0.8 mmol/L) for the copper electrode. Over the monitored post-discharge weeks, hydrogen peroxide remains more or less stable, with some fluctuations that are within the large errors bars.

There are several reasons that can contribute to the large error bars. First, one needs to take into account an equipment error of the HPLC-ECD of 5-9%. This error was determined by quality control samples of known H_2O_2 concentration. Second, one should consider the dilution error, as the PAW samples had to be diluted by a factor of 15 in order to be in the measurement range of the HPLC-ECD (about 2 % error for each pipetting step). Third, there is variability of the H_2O_2 amount produced by the pin-to-liquid discharge. We suspect that the distance between the pin and the liquid may not have been identical in all experiments for two reasons: (1) Although the flow rate of the sparged gas was held constant, we observed that the bubbling was uneven. Sometimes larger bubbles would form, whereas other times the bubbles appeared smaller. The bubbling affected the distance between the pin electrode and the bubbling liquid surface. (2) Because the pin electrodes were very thin (diameter of 0.25 mm) and ductile, it was difficult to keep the tip

completely straight after cleaning the setup between each experiment. This can also lead to small changes in the distance to the liquid surface. Changes in the discharge gap can affect the breakdown voltage, as well as the discharge characteristics and amount of plasma-chemical species produced (Lieberman and Lichtenberg, 2005; Lukes *et al.*, 2005; Lukes, Clupek and Babicky, 2011; Massarczyk *et al.*, 2017; Yoon *et al.*, 2018). Therefore, we hypothesize that the variability of the pin-to-liquid distance contributed to producing variable amounts of H_2O_2. Whereas the first two error sources are specific to the H_2O_2 measurements by HPLC-ECD, the third point discussed applies to any reactive oxygen and nitrogen species produced (such as NO_2^- and NO_3^-).
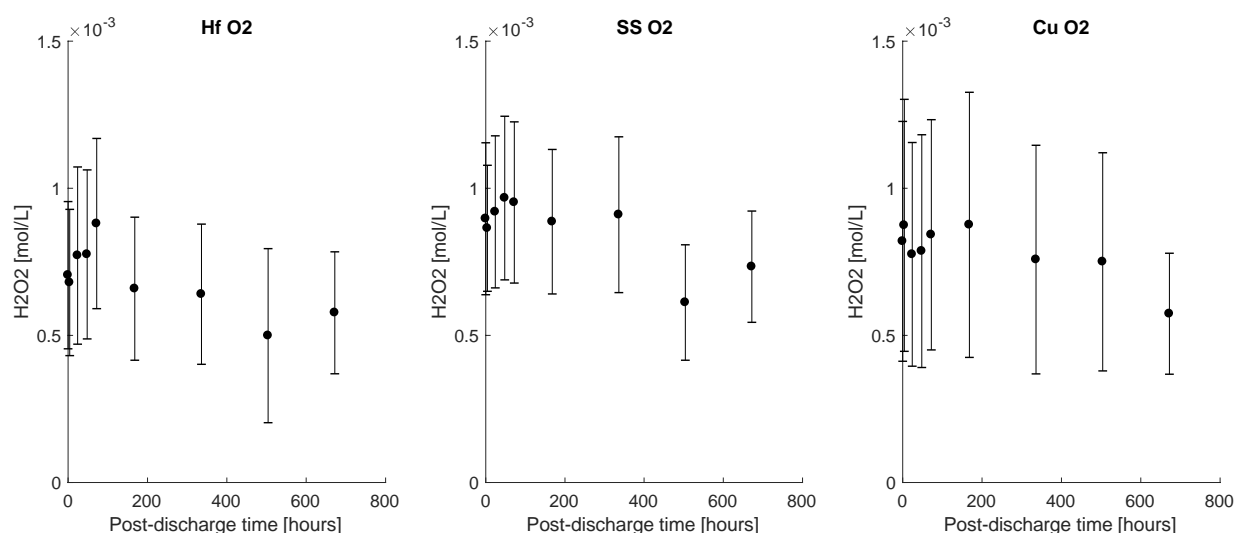
Fig. 5-8 Temporal evolution of the hydrogen peroxide concentration over the post-discharge time, measured by High-Performance Liquid Chromatography (HPLC). The samples had been previously plasma-treated in pure oxygen for 20 min. The material of the pin electrode was either hafnium (Hf), stainless steel (SS) or copper (Cu).

We ran an ANOVA statistical analysis to check (1) whether the means of the different metal electrodes are statistically different from each other and (2) whether the initial values measured at 15 min post-discharge are statistically different from the final ones measured at 4 weeks post-discharge. In all cases, F-values < F-critical and p-value > α (see Table 5-2). This means that we failed to reject the null hypothesis. There is not enough evidence to state that there is a significant statistical difference between (1) the results of different electrode materials and (2) between the initial and the final H_2O_2 concentrations. Because there is no significant statistical difference between the initial and the final H_2O_2 concentrations, it is unclear whether the H_2O_2 concentration changes over the monitored post-discharge time or it stays constant.

Fig. 5-9 shows the results of the iodometric titrations. Iodide can be oxidized by any oxidizing species dissolved in water, such as ozone, hydrogen peroxide or nitrite (Kingzett, 1880; Karlsson and Tortensson, 1974; Lew, 1975). When iodide (I^-, colorless) reacts with oxidizing species, it forms iodine (I_2, yellow). For instance, the oxidation with H_2O_2 under acidic conditions is shown in Eq. 5.8. Thiosulfate ($S_2O_3{}^{2-}$) is used as the titrant and reacts with iodine to revert it to the original iodide form (Eq. 5.9) (Kolthoff, 1921). Using Eq. 5.8 and Eq. 5.9, the titrant volume results can be converted into H_2O_2 concentration equivalents (H_2O_2 eq.). A hydrogen peroxide control with an initial concentration of 1.1 mmol/L was monitored for three weeks, during which the concentration remained constant.

$$H_2O_2 + 2I^- + 2H^+ \rightarrow I_2 + 2H_2O \tag{5.8}$$

$$2S_2O_3^{2-} + I_2 \rightarrow S_4O_6^{2-} + I^- \tag{5.9}$$
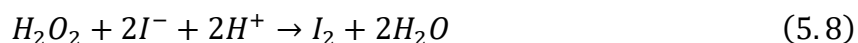
At the beginning of the post-discharge period following plasma treatment in oxygen, H_2O_2 eq. concentrations are 36 mg/L (1.1 mmol/L) with the hafnium electrode, and 31 mg/L (0.9 mmol/L) with the stainless steel and copper electrodes.

Concerning the case of the hafnium electrode, it seems that there are two stages in the graph. In the first stage of 48 h post-discharge, the H_2O_2 eq. concentration average fluctuates between 36 and 40 mg/L. Afterwards, in the second stage, the H_2O_2 eq. concentration average is around 23 to 24 mg/L. This latter range matches the results of H_2O_2 concentrations obtained by HPLC-ECD for the whole post-discharge period (see Fig. 5-8 and Fig. 5-9). However, when we run an analysis of variance between the initial and final hafnium concentrations measured by iodometric titration, we fail to reject the null hypothesis (see Table 5-2). This means that there is no significant statistical difference between the initial and final hafnium values. Therefore, it remains unclear whether the total oxidizing power of hafnium changes over time.

For the stainless steel and copper electrodes, the H_2O_2 eq. concentration stays more or less constant, matching the trend of the H_2O_2 control. In fact, these H_2O_2 eq. results are very similar to the H_2O_2 concentrations measured by HPLC-EDS (see Fig. 5-8 and Fig. 5-9). This indicates that the only reactive oxygen species (ROS) found in these PAW samples in the post-discharge period is H_2O_2. If there were other ROS present, such as dissolved ozone and other shorter-lived ROS, they would react with iodide, and the HPLC-EDS and TOP results would not match.
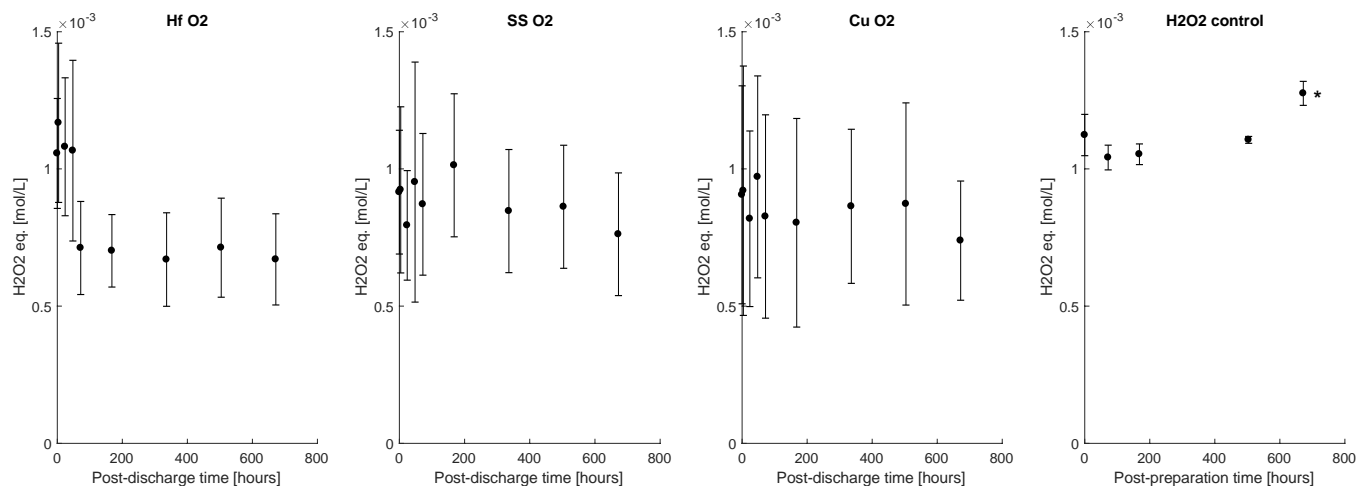
Fig. 5-9 Temporal evolution of the total oxidizing power over the post-discharge time. The titrant results are represented in H2O2 equivalent concentrations. The material of the pin electrode was either hafnium (Hf), stainless steel (SS) or copper (Cu). For the first three graphs, the samples had been previously plasma-treated in pure oxygen for 20 min. The fourth graph represents a control prepared by diluting hydrogen peroxide in reverse-osmosis (RO) water. * We consider that the last point on the hydrogen peroxide control graph is an outlier, because we experienced problems with the titration device during the measurements of this data point.

Both for results obtained by HPLC and the iodometric titration, ANOVA statistical analysis comparing the initial and final H_2O_2 concentrations of all metal electrodes reveals no significant statistical difference between them (see Table 5-2). Therefore, we cannot observe a catalytic effect from these metals on H_2O_2. Alternatively, we could have hypothesized that all metals have a catalytic effect that is identical. However, we consider this to be an unlikely coincidence, especially since the metals are present in different quantities. Holzer and Locke made similar observations for the use of copper and stainless steel electrodes with in-liquid discharges. They did not find any catalytic effect of these metal electrodes on the formation of H_2O_2 (Holzer and Locke, 2008).

5.4.3.3 Conductivity

Fig. 5-10 shows the conductivity of PAW samples that were plasma-treated for 20 min with different electrode materials and gas atmospheres. The initial conductivity of untreated RO water was 1 μS/cm.

107
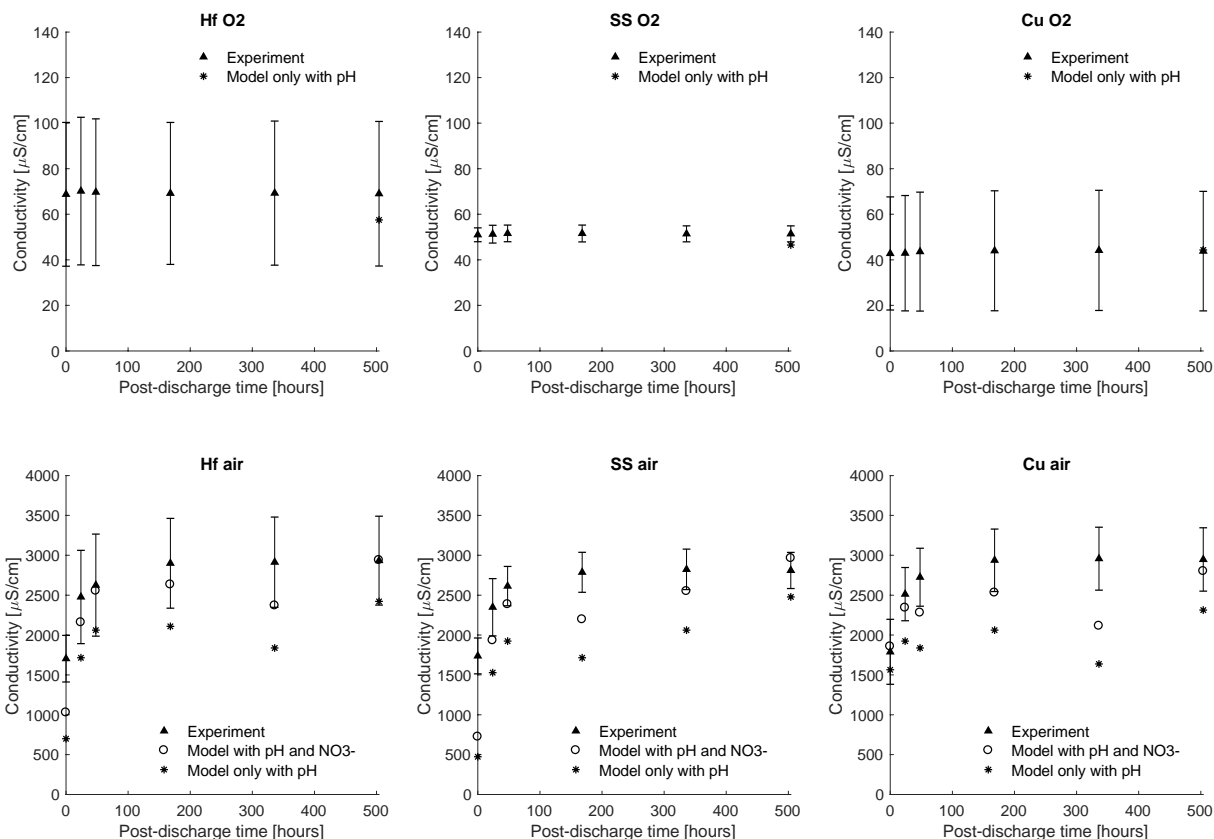
Fig. 5-10 Temporal evolution of the conductivity in plasma-activated water over the post-discharge time. The upper row shows results obtained with an oxygen plasma, and the lower row results obtained with an air plasma. Triangles and error bars: Experimental data for samples that had been previously plasma-treated for 20 min. The material of the pin electrode in the gas phase was either hafnium (Hf), stainless steel (SS) or copper (Cu). Empty circles: Model by Porter et al., calculated using the measured nitrate concentrations, pH and initial conductivity. Stars: Model by Porter et al., calculated using only the measured pH and initial conductivity (Porter *et al.*, 2009).

Concerning the samples produced with air plasma treatment, the conductivity results are almost identical for different electrode materials, starting at an average of 1703 µS/cm for the hafnium samples, 1738 µS/cm for the stainless steel ones and 1789 µS/cm for the copper ones. The conductivity increases over the post-discharge time and after 3 weeks it reaches 2933 µS/cm for the hafnium samples, 2810 µS/cm for the stainless steel ones and 2948 µS/cm for the copper ones. Both for the initial and final conductivity values, there is not enough evidence to state that there is a significant statistical difference between the results of different electrode materials (according to ANOVA in Table 5-2). We suspect that the pH change (which determines the H^+ and OH^- concentrations) and the RONS (NO_2^- and NO_3^-) play a role in the higher conductivity of PAW compared to untreated RO water. Porter et al. proposed a model for estimating the conductivity Λ

of PAW as a function of the initial conductivity Λ_0, H^+, OH^- and optionally NO_3^- concentrations (see Eq. 5.10) (Porter *et al.*, 2009). Lukes et al. later on compared this correlation to experimental data from multiple studies, confirming good agreement between the two (Lukes, Locke and Brisset, 2012).

$$\Lambda = (349.82[H^+] + 198.6[OH^-]) \times 1000 + 71.4[NO_3^-] \times 1000 + \Lambda_0 \qquad \left[\frac{\mu S}{cm}\right] \qquad (5.10)$$

We applied this correlation using our experimental data on initial conductivity, pH and nitrate concentrations over the post-discharge time (see Fig. 5-7 and Fig. 5-12). In order to distinguish the contribution of the pH to conductivity from the contribution of NO_3^-, we used the correlation twice: (1) with all terms as presented in Eq. 5.10; (2) with all terms except for NO_3^-. In Fig. 5-10, we can see that the conductivity modelled with both pH and NO_3^- contributions closely follows the measured conductivity. The modelled values are slightly below the experimental averages, but in most of the cases they are within the experimental error bars. Regarding the conductivity modelled without the NO_3^- contribution, the calculated values are 16-35 % smaller than the model with both pH and NO_3^- contributions. This suggests that H^+ and OH^- play a major role on the conductivity, followed by NO_3^-. This model does not include the effects of NO_2^-, which is present in our PAW during the first post-discharge week. This can explain why the model differs the most from the experimental data in the initial measurement point (15 min post-discharge), when the NO_2^- is at its highest concentration and NO_3^- at its lowest concentration (see Fig. 5-7). Note that the modelled values show some fluctuations. The reason for this is that, in the acidic range, the models are very sensitive to small pH changes. For instance, a fluctuation of pH 2.30 ± 0.05 changes the modelled values by around 12 %.

The conductivity of the samples produced with oxygen plasma treatment is within the same range of order for all three pin electrode materials, with an average of around 70 µS/cm for samples produced with a hafnium pin electrode, 51 µS/cm for the stainless steel ones and 43 µS/cm for the copper ones. The conductivity remains stable for the measured post-discharge period of four weeks (≤ 3 % variation of the results at every time point with respect to the initial results at 15 min post-discharge). Note that the error bars of the three electrode materials overlap, and that stainless steel has the smallest error bars. According to an ANOVA statistical analysis, there is not enough evidence to state that there is a significant statistical difference between the conductivity obtained

with different electrode materials (see Table 5-2). We do not expect the presence of H_2O_2 to have an effect on the conductivity, as the conductivity of a 1 mmol/L H_2O_2 control was the same than the conductivity of untreated RO water. By ion chromatography we detected traces of NO_3^- in PAW that may come from traces of air in the reactor, but they were below the quantitation limit. The presence of traces of NO_3^-, together with the pH change (see Fig. 5-12 and Table 5-3), may explain the increase in conductivity compared to untreated water. We applied the model by Porter et al. presented above in Eq. 5.10, using our experimental data on the pH and initial conductivity. Note that in this case we used the pH values from Table 5-3, which were taken from the same samples that were used to measure the conductivity. In Fig. 5-10, we can see that the modelled values are very close to the experimental results.

To summarize both for air and for oxygen plasmas, it seems that metal ions from electrode erosion do not play a significant role in the conductivity of PAW because (1) there is not enough evidence to state that there is a significant statistical difference between the results of different electrode materials and (2) we compared the experimental data to a model that does not include the effect of metal ions, and nevertheless the model follows the experimental values closely. Note that we have not determined how much of the total metal content in PAW presented in Fig. 5-5 and Fig. 5-11 is in ionic form and how much is in particle form. We plan to study the ratio between the two in future work. If the eroded metals are mostly in particle form, this would explain why we do not see a significant change in conductivity for different electrode materials.

5.5   Conclusions and outlook

We studied the erosion of high-voltage pin electrodes (hafnium, copper and stainless steel) in pin-to-liquid repetitively pulsed nanosecond discharges, as well as how eroded metals affect long-lived RONS. We observed that the electrode material does not influence the energy deposited per pulse. In air plasmas the energy deposited per pulse was around 620 µJ, and in pure oxygen plasmas it was around 350 µJ. Electrode erosion is observed for all studied cases. This erosion produces crater-like morphologies, with slightly smaller crater diameters for the oxygen-treated electrodes compared to the air-treated ones. The erosion releases metal in particle form into the plasma-activated water, with metal amounts that can vary by an order of magnitude depending on the electrode and gas type. Stainless steel stands out as the material that leads to the least erosion both for air and oxygen plasmas. Moreover, only when using an air plasma, we observe that the sparger

submerged in the liquid erodes and/or leaches metal ions. We attribute this to the acidic pH of the plasma-treated liquid. PAW contains polydisperse metal particles that range from nanometer to micrometer size, and that are not evenly distributed in the solution. The size of the particles is larger for samples prepared in an air plasma versus an oxygen plasma. Because preliminary results show that the larger particles are formed from the agglomeration of multiple smaller particles, perhaps stabilizing the solution could lead to a monodisperse solution of nanoparticles.

Furthermore, our results indicate that the studied metals do not have any significant effect neither on long-lived RONS nor on the conductivity of PAW. The PAW produced in air plasma contains NO_2^- and NO_3^-, with almost identical concentrations for all three electrode materials. NO_2^- decays and converts into NO_3^-. For the experiments performed with an oxygen atmosphere, H_2O_2 is the only oxidizing species that remains in the PAW for a long time. The results obtained from HPLC-ECD measurements and iodometric titration are consistent. We cannot observe a significant statistical difference between the samples produced with different electrode materials. Although the type of metal does not have a great effect on the studied RONS, we still consider that the choice of electrode material should be carefully thought through. Toxicological and environmental aspects should be taken into consideration, if we want to design plasma systems that are truly sustainable.

Knowing the lifetime of the long-lived RONS can be useful for various applications. Note that the RONS initial post-discharge concentrations and composition, as well as their storage conditions can have a significant effect on the lifetime of the RONS (Laurita *et al.*, 2015; Shen *et al.*, 2016; Liu *et al.*, 2018). In this study, PAW produced with oxygen plasmas contains around 1 mmol/L H_2O_2, and this concentration is not significantly decreased after 1 month of storage at 4 °C. Regarding air plasmas, practically all NO_2^- is gone after one week of storage at 4 °C, whereas the NO_3^- concentration remains constant from week 1 to 4 after the plasma treatment. Applications like plasma medicine or agriculture could benefit from this knowledge. If one is interested in using H_2O_2 or NO_3^-, there is the possibility to produce large batches of PAW, transport and use them whenever convenient for at least one month. If on the contrary the applications require a certain concentration of NO_2^-, then one has to use the PAW in the first days after the plasma treatment. In this case, producing the PAW close to the application site becomes important. Furthermore, for the application of wastewater treatment, the long lifetime of the RONS has to be taken into

consideration. The persistence of RONS may be detrimental for the environment if the treated water is directly released into waterbodies. For instance, the presence of NO_3^- and the low pH may lead to acidification of the waterbody at the point of emission, potentially causing damage to flora and fauna (Hauschild, Rosenbaum and Olsen, 2017). Regarding the release of H_2O_2 into a waterbody, it can have short-term effects on the resident biota (Schmidt, Gaikowski and Gingerich, 2006). Therefore, it may be necessary to run additional treatment steps to quench the reactive species and neutralize the pH before emission into the environment.

In future work, we want to take a closer look at the physicochemical processes that lead to erosion of the electrode surface. Moreover, we plan to investigate the ratio of metal particles to metal ions in the plasma-treated solutions. Producing nanoparticles in pin-to-liquid discharges can be interesting for nanomaterial applications. In the case one wants to completely avoid metal release, ceramic-coated or carbon electrodes may be suitable alternatives (Šunka, 2001; Holzer and Locke, 2008).

Acknowledgements

5.6   Supplementary Material

Table 5-2 Results of ANOVA statistical analyses. Note that for all calculations, the significance level α was set to $\alpha = 0.05$. The null hypothesis was rejected when the calculated value F was larger than the critical value F-crit and the p-value was smaller than α.

Figure number	Figure description	Description of values tested with ANOVA	F	F-crit	p-value	Null hypothesis rejected
6	Average particle size	Hf O_2 vs air plasma	3.78	4.32	0.07	no
		SS O_2 vs air plasma	13.13	4.32	0.00	yes
		Cu O_2 vs air plasma	8.18	4.32	0.01	yes
		O_2 plasma, all metals	18.62	3.29	0.00	yes
		Air plasma, all metals	4.02	3.30	0.03	yes
7	NO_3^- and NO_2^- measured by IC	NO_2^-, initial points (15 min) of all metals	0.21	5.14	0.82	no
		NO_2^-, final points (4 weeks) of all metals	3.23	5.14	0.11	no
		NO_3^-, initial points (15 min) of all metals	218.07	5.14	0.00	yes
		NO_3^-, intermediate points (1 week) of all metals	1.54	5.14	0.29	no
		NO_3^-, intermediate points (2 weeks) of all metals	1.69	5.14	0.26	no

		NO_3^-, final points (4 weeks) of all metals	1.46	5.14	0.30	no
8	H_2O_2 measured by HPLC	Hf 15 min vs 4 weeks	0.46	7.71	0.53	no
		SS 15 min vs 4 weeks	0.78	7.71	0.43	no
		Cu 15 min vs 4 weeks	0.87	7.71	0.40	no
		Initial points (15 min) of all metals	0.28	5.14	0.76	no
		Final points (4 weeks) of all metals	0.62	5.14	0.57	no
		Initial and final points of all metals	0.72	3.11	0.62	no
9	H_2O_2 measured by iodometric titration	Hf 15 min vs 4 weeks	6.60	7.71	0.06	no
		SS 15 min vs 4 weeks	0.70	7.71	0.45	no
		Cu 15 min vs 4 weeks	0.41	7.71	0.56	no
		Initial points (15 min) of all metals	0.26	5.14	0.78	no
		Final points (4 weeks) of all metals	0.16	5.14	0.85	no
		Initial and final points of all metals	0.98	3.11	0.47	no
10	Conductivity	O2 plasma, initial points (15 min) of all metals	0.98	5.14	0.43	no

Air plasma, initial points (15 min) of all metals	0.06	4.74	0.94		no
Air plasma, final points (3 weeks) of all metals	0.11	4.74	0.90		no
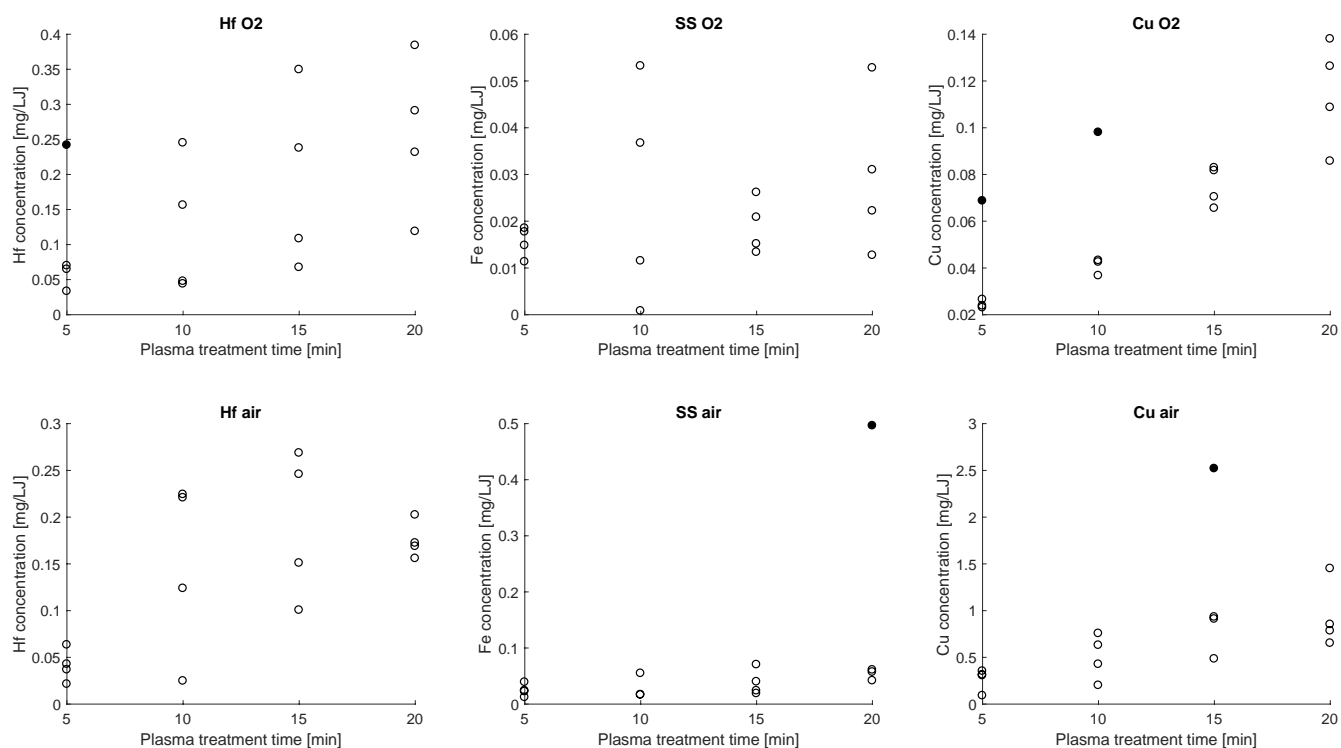
Fig. 5-11 Metal concentration in plasma-activated water at different plasma treatment times, measured by ICP-OES. The upper row shows results obtained with an oxygen plasma, and the lower row results obtained with an air plasma. The material of the pin electrode in the gas phase was either hafnium (Hf), stainless steel (SS) or copper (Cu). The circles represent the values obtained for each of the four repeats. The circles filled in black are considered to be outliers.
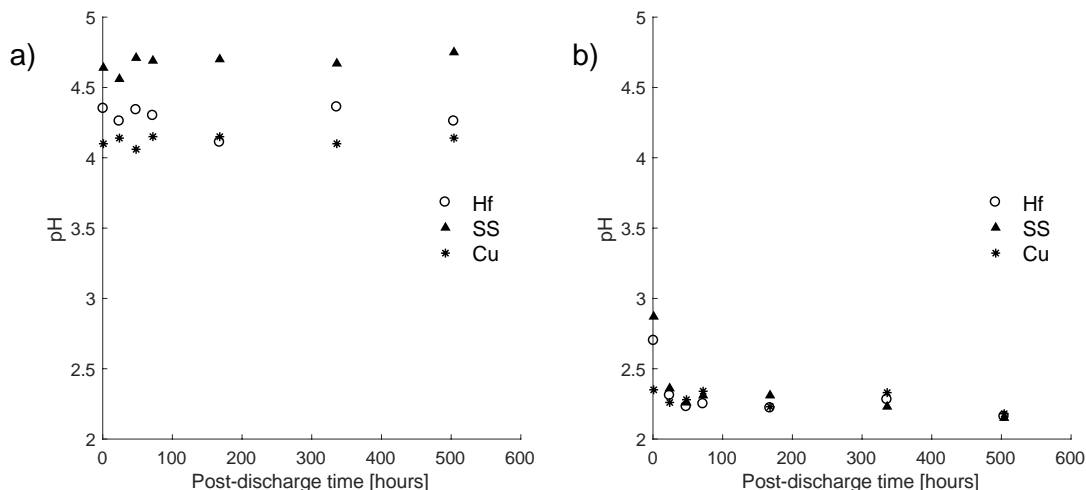
Fig. 5-12 Temporal evolution of the pH of plasma-activated water. The samples had been plasma-treated for 20 min in either oxygen (a) or air (b). The material of the pin electrode was either hafnium (Hf), stainless steel (SS) or copper (Cu). The initial pH of untreated RO water was around pH 5. Note that pH measurements were only performed once, with no repeats.

Table 5-3 pH results of plasma-activated water that had been plasma-treated for 20 min in oxygen. The measurements were taken at 3 weeks post-discharge. These were the same samples that were used to measure the conductivity shown in Fig. 5-10. The pH of untreated RO water was pH 4.87.

	Cu O$_2$	SS O$_2$	Hf O$_2$
	4.06	3.82	3.98
Measurements	3.72	3.95	3.63
	3.94	3.88	3.77
Average	3.91	3.89	3.79
Standard deviation	0.17	0.06	0.18
RSD%	4%	2%	5%

6

Manuscript 3

Degradation of diatrizoate in a pin-to-liquid plasma reactor, its transformation products and their residual toxicity

6.1 Preface

This chapter presents an article submitted to the journal of "*Science of the Total Environment*". The citation of the manuscript is:

E. Corella Puertas, M.-L. Peyot, M. Pineda, K. Volk, S. Coulombe and V. Yargeau (2020), *Degradation of diatrizoate in a pin-to-liquid plasma reactor, its transformation products and their residual toxicity*. Science of the Total Environment.

The work was planned, analyzed and written by Elena Corella Puertas (PhD candidate). Dr. Marie-Line Pejot led the identification of transformation products and proposed their molecular formulas. Dr. Marco Pineda developed the LC-MS methods, ran LC-MS measurements and help with the identification of the transformation products and the elucidation of their molecular formulas. Kalyssa Volk performed Microtox acute toxicity tests. Dr. Viviane Yargeau and Dr. Sylvain Coulombe were responsible for supervision and review of the work.

The compact pin-to-liquid discharge reactor presented in Chapter 5 is also used in this chapter. The only modification that is introduced is the exchange of the commercial multi-holed sparger for a homemade single-holed one. The reason for this change is that irregular bubbling was observed during the work in Chapter 5, and we suspect that this variability in bubbling may have

significantly increased the variability of the results. Out of the three studied electrode materials, Chapter 5 reported the least erosion for stainless steel, and thus this material was chosen for the high-voltage pin electrode in the present chapter.

The present chapter demonstrates the applicability of the pin-to-liquid discharge reactor developed in this PhD thesis for the successful removal of a recalcitrant aqueous organic pollutant, the pharmaceutical DTZ. Similar to Chapter 5, the effect of oxygen and air plasma carrier gases is compared, with oxygen yielding faster DTZ degradation. From the knowledge obtained in Chapter 5 on the composition and concentration of long-lived reactive species, appropriate quenchers are chosen. This allows to study the concentration of DTZ and the formation and toxicity of TPs without the risk of post-discharge effects like the ones observed in Chapter 4. We identify TPs of DTZ and observe no residual toxicity associated to them. However, plasma-treated water controls show some background toxicity. We suspect that this background toxicity is linked to the presence of metal-based particles and ions introduced into the solution through electrode erosion, as reported in Chapter 5. The work presented in Chapter 6 contributes to new knowledge on the nature of TPs formed during plasma treatment.

Degradation of diatrizoate in a pin-to-liquid plasma reactor, its transformation products and their residual toxicity

Elena Corella Puertas[1,2], Marie-Line Peyot[2], Marco Pineda[2], Kalyssa Volk[2], Sylvain Coulombe[1], Viviane Yargeau[2]

[1] *Plasma Processing Laboratory (PPL), Department of Chemical Engineering, McGill University, Montréal, Canada,*

[2] *Controlling Contaminants of Concern Laboratory (3Cs), Department of Chemical Engineering, McGill University, Montréal, Canada*

Abstract

Diatrizoate, a recalcitrant iodinated contrast medium, has been detected in various aqueous environments such as surface waters, groundwaters and wastewater treatment effluents in numerous countries with concentrations ranging from ng/L to µg/L. In the present work, aqueous solutions of diatrizoate were treated in a compact (7.5 mL liquid volume) non-thermal plasma–liquid reactor. The effects of two gas atmospheres, oxygen and air, were compared. Our literature review showed that the use of an oxygen plasma to degrade iodinated contrast media has not been reported before. Our results show that oxygen plasmas are more effective than air plasmas, achieving 66 % higher degradation for an initial concentration of C_0 = 200 µg/L diatrizoate, and 26 % higher degradation for C_0 = 10 mg/L diatrizoate after 20 min of plasma treatment. For the oxygen plasma treatment, the energy efficiency for removing diatrizoate was 0.140 g/kWh for C_0 = 10 mg/L and 0.006 g/kWh for C_0 = 200 µg/L. Transformation products of diatrizoate were identified for the oxygen plasma treatment: m/z 486A, 504A, 504B, 628, 630A, 630B (previously described in literature) and m/z 486B, 550, 555, 565, 578 (novel). Acute toxicity tests on *Aliivibrio fischeri* revealed no residual toxicity associated to transformation products.

Graphical Abstract
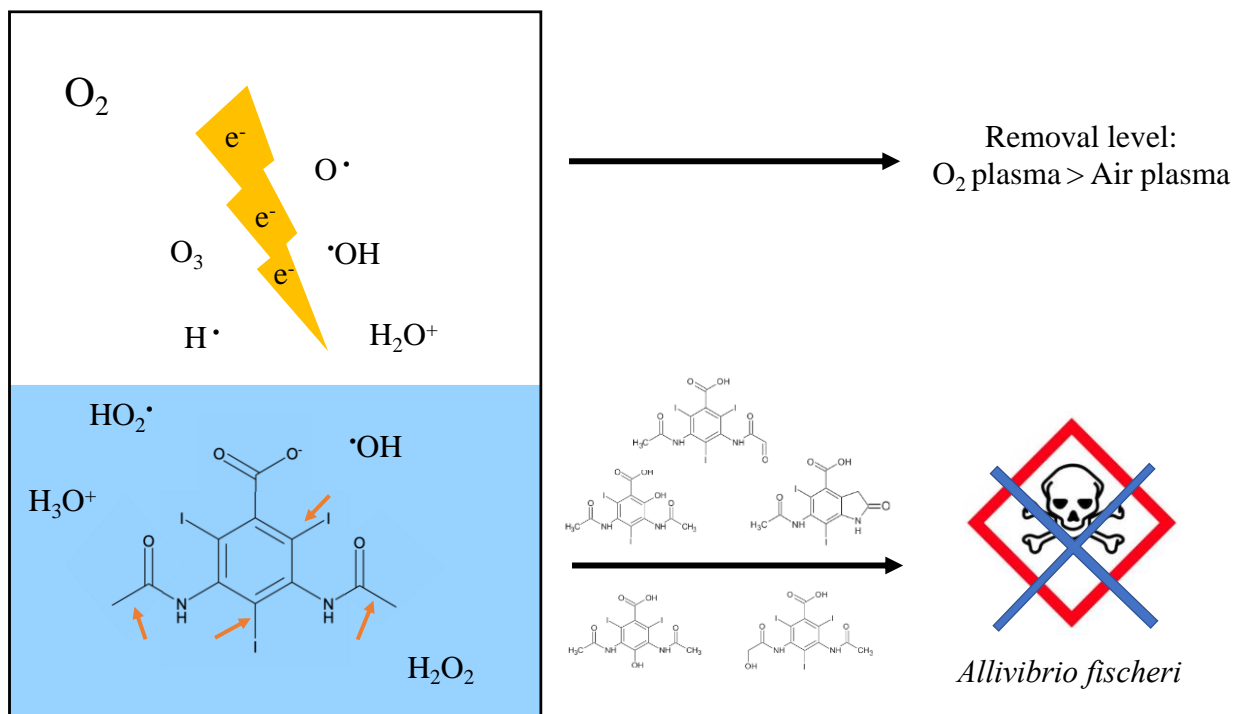
6.2   Introduction

The fate of pharmaceuticals in the environment is a topic of concern since pharmaceuticals are extensively used and may persist in aquatic environments in spite of wastewater treatment processes, and their long-term effects on ecosystems and human health are still largely unknown (Magureanu, Mandache and Parvulescu, 2015; Yang *et al.*, 2017). Toxicological studies on pharmaceuticals in the environment carried out so far have raised various concerns, for instance: estrogens can cause reproductive defects on fish and amphibians (Kidd *et al.*, 2007; Harding *et al.*, 2016; Naidu, Arias Espana, *et al.*, 2016) or antibiotics may promote the development of antibiotic resistance genes in bacteria and in the soil environment (Kümmerer, 2009; Gracia-Lor et al., 2012; Noguera-Oviedo and Aga, 2016; Rodriguez-Narvaez et al., 2017). Iodinated contrast media (ICM) is one family of pharmaceuticals that are particularly stable and that are not adequately removed in conventional wastewater treatment plants (Ternes and Hirsch, 2000; Putschew, Schittko and Jekel, 2001; Echeverría *et al.*, 2013; Zemann *et al.*, 2014). ICM are extensively used in human medicine as radiographic dyes to enhance the visibility of organs and blood vessels during diagnostic tests (Pérez and Barceló, 2007; Pasternak and Williamson, 2012). Although ICM are released in unmetabolized form in feces and urine, typically within 1 day for healthy patients (Hartwig, Mützel and Taenzer, 1989; Nossen *et al.*, 1995; Pérez and Barceló, 2007), patients are typically sent home shortly after the radiographic procedure and the wastewaters containing ICM are not collected separately (Weissbrodt *et al.*, 2009; Verlicchi, 2018). ICM have been detected in various aqueous environments such as surface waters, groundwaters and wastewater treatment effluents in numerous countries, with concentrations ranging from ng/L to µg/L (Ternes and Hirsch, 2000; Seitz, Weber, *et al.*, 2006; Schulz *et al.*, 2008; Duirk *et al.*, 2011; Wolf, Zwiener and Zemann, 2012; Echeverría *et al.*, 2013; Zemann *et al.*, 2014; Mendoza *et al.*, 2016; Xu *et al.*, 2017). In hospital effluents – which were not treated separately and thus discharged into the public sewer system – the concentrations of ICM reached up to mg/L (Weissbrodt *et al.*, 2009; Mendoza *et al.*, 2015; Verlicchi, 2018).

The effects of chronic exposure to ICM on ecosystem and human health are still unclear. Short-term toxicity tests with bacteria, algae, crustaceans and fish did not show any toxic effects, even at high ICM doses (10 g/L iopromide) (Steger-Hartmann, Länge and Schweinfurth, 1999). Chronic toxicity tests during 22 days with the crustacean *Daphnia magna* did not reveal any toxic effects

(1 g/L iopromide) (Steger-Hartmann, Länge and Schweinfurth, 1999). However, the chronic exposure to a combination of pharmaceuticals found in the aquatic environment may lead to unpredictable effects (Magureanu, Mandache and Parvulescu, 2015). Recent medical studies showed that some patients react to ICM upon their first contact in a clinical context, and one study suggested that allergies may have been developed by previous exposure to ICM through drinking water (Böhm, 2018). Furthermore, not only the ICM parent compounds may pose a hazard, but also their transformation products (TPs). There is evidence that disinfection by-products of ICM treated with chlorination or chloramination can be cytotoxic and genotoxic (Duirk *et al.*, 2011; Matsushita *et al.*, 2015; Jeong *et al.*, 2017; Tian *et al.*, 2017). ICM could also be subject to aerobic and anaerobic biotransformation in the environment, forming various TPs (Redeker *et al.*, 2014, 2018). Therefore, there is a need to find a treatment method that efficiently removes ICM and does not produce any hazardous TPs.

Ozonation achieved little to partial success for ICM degradation (Ternes *et al.*, 2003; Huber *et al.*, 2005; Seitz *et al.*, 2008). Other water treatment methods that have been tried so far include O_3/H_2O_2 (Huber *et al.*, 2003; Ternes *et al.*, 2003), biological treatments (Haiß and Kümmerer, 2006; Schulz *et al.*, 2008; Redeker *et al.*, 2018), photodegradation processes (Sugihara *et al.*, 2013; Azerrad *et al.*, 2014; Zhao *et al.*, 2014; Polo *et al.*, 2016; Hu *et al.*, 2019; Rivas *et al.*, 2019), electrochemical processes (Del Moro *et al.*, 2015; Wu *et al.*, 2017; Korshin and Yan, 2018; Yan *et al.*, 2018), $SO_4^{\bullet-}$-based processes (Polo *et al.*, 2016; H. Zhao *et al.*, 2019; Mao *et al.*, 2020) and non-thermal plasma treatments (Krause *et al.*, 2009, 2011; Gur-Reznik *et al.*, 2011; Liu *et al.*, 2013; Azerrad *et al.*, 2016). Although some technologies achieved high removal rates of ICM parent compounds, certain ICM entailed significantly higher energy consumption than the one required to treat other aqueous pollutants (Kovalova *et al.*, 2013; Hansen *et al.*, 2016). The ionic ICM diatrizoate is particularly recalcitrant to degradation by different treatment methods (Ternes *et al.*, 2003; Huber *et al.*, 2005; Seitz, Jiang, *et al.*, 2006; Seitz *et al.*, 2008; Kovalova *et al.*, 2013; Hansen *et al.*, 2016; Rizzo *et al.*, 2019). The methods that are successful at degrading ICM parent compounds typically do not lead to mineralization but to the formation of TPs, which can be toxic in some cases (e.g. in some ozonation, photo(cata)lytic, electrochemical or $SO_4^{\bullet-}$-based treatments) or their harmfulness is still unknown (Rastogi, Leder and Kümmerer, 2014; Del Moro *et al.*, 2015; Polo *et al.*, 2016; Korshin and Yan, 2018; Yan *et al.*, 2018; H. Zhao *et al.*, 2019; Rivas *et al.*, 2019).

In the present work, we focused on the use of non-thermal plasma treatment for ICM degradation. In plasma-based water treatments, electrical discharges are generated either directly in liquid water, or in a gas atmosphere in contact with liquid water (Jiang *et al.*, 2014; Bruggeman *et al.*, 2016). This produces plasma-activated water (PAW), an aqueous solution that contains reactive oxygen and nitrogen species such as $^{\bullet}OH$, O_3, H_2O_2, NO_2^-, NO_3^- and $ONOO^-$ (Lukes, Locke and Brisset, 2012; Bruggeman *et al.*, 2016). Furthermore, during the plasma treatment UV light is produced, which may initiate photochemical reactions (Kogelschatz, 2003; Lukes, Locke and Brisset, 2012; Bruggeman *et al.*, 2016). The composition of PAW can be tuned with the type of discharge and gas used (Kovačević *et al.*, 2017; Vlad and Anghel, 2017; Corella Puertas, Dzafic and Coulombe, 2020). Multiple studies show that this highly reactive environment can degrade recalcitrant contaminants that are not removed with conventional treatment methods (Pokryvailo *et al.*, 2006; Hijosa-Valsero *et al.*, 2013; Magureanu, Mandache and Parvulescu, 2015; Kim, Won and Kim, 2018; Nani *et al.*, 2018; Tampieri *et al.*, 2018). One of the major challenges of plasma reactors is the scale-up (Foster, Mujovic and Groele, 2018). However, plasma reactors may be suitable for treating small-scale, challenging wastewaters at the source – for instance hospital effluents –, due to the effectiveness of the treatment, simplicity of the equipment and operation, and the absence of chemical addition (Lukes, Locke and Brisset, 2012; Magureanu, Mandache and Parvulescu, 2015; Ajo *et al.*, 2018; Kim, Won and Kim, 2018).

Table 6-1 summarizes the results obtained so far using plasma-based methods to degrade ICM (Krause *et al.*, 2009, 2011; Gur-Reznik *et al.*, 2011; Liu *et al.*, 2013; Banaschik *et al.*, 2015; Azerrad *et al.*, 2016). Similar to results reported with other advanced oxidation treatments, diatrizoate seems to be more recalcitrant than iopromide (Gur-Reznik *et al.*, 2011). Several studies reported full removal of ICM parent compounds, but only one study looked into the formation of TPs and proposed degradation pathways (Azerrad *et al.*, 2016). Residual toxicity associated with the TPs was not investigated.

The present work studies the degradation of diatrizoate (DTZ) with a pin-to-liquid plasma reactor, the formation of TPs and their associated residual toxicity. Two DTZ concentrations are examined: 10 mg/L to facilitate the identification of TPs and 200 µg/L, a value in the range expected in hospital wastewater. The effect of two gas atmospheres, oxygen and air, is compared. To our knowledge, the use of an oxygen plasma to degrade ICM has not been reported before. Despite the

higher cost of oxygen over air, oxygen plasma treatments have the advantages of usually being more effective and not introducing major pH changes nor NO_x into the treated water (Malik, 2010; Panorel *et al.*, 2013a; Wang *et al.*, 2017; Singh, Philip and Ramanujam, 2019).

6.3   Materials and methods

6.3.1   Experimental setup

Fig. 6-1 shows a schematic of the pin-to-liquid plasma reactor. It consists of a small temperature-controlled jacketed reactor open at both ends, equipped with custom-made lids allowing to mount a pin electrode above the liquid, and a metallic sparger immersed in the liquid which is used to bubble the desired gas through the liquid. The borosilicate glass vessel (JRV Scientific Glass Montreal, inner diameter 19.4 mm, height 83.5 mm) is maintained at 20.5 °C using a circulating water chiller (Marshall Scientific, Thermo Neslab RTE 10 Circulating Chiller). The lids are made of polytetrafluorethylene and provide electrical insulation. The homemade sparger submerged in the liquid is made of 316L stainless steel and has a single hole with a diameter of 0.35 mm; and supplies gas to the system and acts at the anode. We used compressed dry air or oxygen (Praxair, 99.993 % purity) at 6 mL/min at atmospheric pressure. The gas flow was initiated 4 min prior to any experiment to make sure the reactor chamber was sufficiently purged with the desired gas. A fine 0.25 mm-diameter wire of 302 stainless steel (Goodfellow) was used as cathode pin above the liquid. The cathode pin surface was prepared by cutting the metal with a wire cutter with a flush cut profile (McMaster-Carr). The cathode was mounted approximately 2 mm above the water surface.

Table 6-1 Literature review of plasma technologies used for degradation of iodinated contrast media. *: Values calculated in this study using information provided by the cited articles. Note that the energy efficiencies are calculated for the degradation % reported in the column "Removal and treatment time".

Plasma reactor configuration	Plasma forming gas	Iodinated contrast medium	Initial concentration (mg/L)	Sample volume (L)	Matrix	Removal and treatment time	Energy efficiency (g/kWh)	Kinetics studied	TPs identified	Toxicity of TPs studied	Reference
Continuous corona discharge	Air	Iopromide	79.1*	0.2	Ultra-pure water	99% after 30 min	0.063*	No	No	No	Krause, 2009
Dielectric barrier discharge	Air	Iopromide	79.1*	1	Ultra-pure water	98% after 60 min	0.155*	No	No	No	Krause, 2011
					Ultra-pure water + 0.1M carbamazepine + 0.1M clofibric acid	56% after 60 min	0.089*				
					40% Landfill leachate	19% after 90 min	0.030*				

Plasma reactor configuration	Plasma forming gas	Iodinated contrast medium	Initial concentration (mg/L)	Sample volume (L)	Matrix	Removal and treatment time	Energy efficiency (g/kWh)	Kinetics studied	TPs identified	Toxicity of TPs studied	Reference
Pulsed corona discharge (Aquapure™, pilot scale)	Air with additional ozone injection	Iopromide	0.069	30	Ultra-pure water	100% after <4 h	Not reported, neither enough information provided to calculate it.	First order	No	No	Gur-Reznik, 2011
					Tertiary effluent	98% after 6 h					
					RO brines (1)	90% after 6 h					
					RO brines (2)	>80% after 6 h					
		Diatrizoate	0.065	30	Ultra-pure water	>99% after 6 h					
					Tertiary effluent	70% after 6 h					
					RO brines (1)	40% after 6 h					

Plasma reactor configuration	Plasma forming gas	Iodinated contrast medium	Initial concentration (mg/L)	Sample volume (L)	Matrix	Removal and treatment time	Energy efficiency (g/kWh)	Kinetics studied	TPs identified	Toxicity of TPs studied	Reference
					RO brines (2)	25% after 6 h					
Dielectric barrier discharge	Air	Iopromide	17.0	1	Pure water	99% after 10 min	0.404*	First order	No	No	Liu, 2013
Pulsed corona discharge	None (in-liquid discharge)	Diatrizoate	0.50	0.3	Milli-Q purified water with sodium chloride (30 μS/cm)	45% after 66 min	0.003 (estimated 90% degradation used for calculations)	Assumed first order	No	No	Banaschik 2015
Pulsed corona discharge (Aquapure™, pilot scale)	Air with additional ozone injection	Diatrizoate	20.7*	30	Ultra-pure water	61% after 6 h	Not reported, neither enough information provided to calculate it.	First order	Yes	No	Azerrad, 2016
					RO brines	27% after 6 h		First order	No		

Plasma reactor configuration	Plasma forming gas	Iodinated contrast medium	Initial concentration (mg/L)	Sample volume (L)	Matrix	Removal and treatment time	Energy efficiency (g/kWh)	Kinetics studied	TPs identified	Toxicity of TPs studied	Reference
Pulsed pin-to-liquid discharge	Oxygen	Diatrizoate	10 0.2	0.0075	Pure water (LC-MS grade)	42 % after 20 min 89 % after 20 min	0.140 0.006	No	Yes	Yes	This work
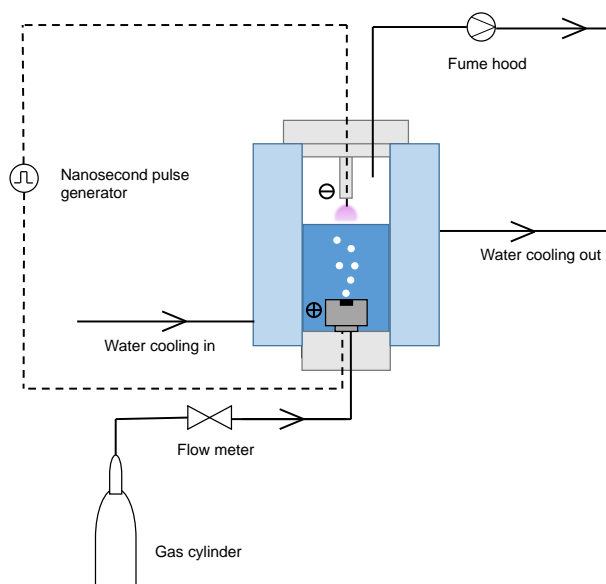
Fig. 6-1 Schematic of the experimental setup.

6.3.2 Experimental conditions

Samples of 7.5 mL containing either 10 mg/L or 200 µg/L diatrizoate (Toronto Research Chemicals) in LC-MS grade water (Fisher Scientific) were plasma-treated for 5-60 min. The higher concentration of diatrizoate (10 mg/L) was used to facilitate the identification of transformation products formed during treatment. Each data point was obtained by starting a new experiment, except for the energy deposited per pulse experiments, in which the plasma was running continuously as measurements were taken every 10 min. For all experiments, nanosecond pulses were produced at a frequency of 3 kHz, with a total peak-to-peak voltage drop of 11 kV and a Full Width at Half Maximum (FWHM) of 40 ns. The peak current varied between 2.9 and 3.4 A. Validation tests confirmed that there is no adsorption of DTZ to the vials (Fisher Scientific, DWK Life Sciences Kimble™ Glass Screw-Thread Sample Vials with PTFE Closure) or reactor walls (see Fig. 6-9 and Fig. 6-10).

6.3.3 Electrical diagnostics

A homemade diode opening switch generator powered the electrodes, producing two simultaneous high-voltage pulses. The negative pulse powered the pin electrode while the positive pulse

powered the sparger. The discharge voltage signals were measured using two passive high-voltage probes (Tektronix P6015A), while the current was measured with a current transformer probe (Pearson 6585). The electrical signals were recorded simultaneously using a digital oscilloscope (Pico Technology, PicoScope 2408B). Fig. 6-2 shows characteristic voltage and current signals measured in an oxygen atmosphere averaged for 50 consecutive sample repeats, which take less than a minute.

The calculation of the energy deposited per pulse was based on Rusterholtz's method (Rusterholtz, 2012). First, the parasitic capacitance of the electrodes and cables was obtained by matching the curves of the derivative of the applied voltage and of the total current (see Eq. 6.1 and Fig. 6-11). The capacitance C was estimated at 5 pF. The delay between the measured current and the displacement current was 2.5 ns. This delay comes from the different characteristics of the voltage and current probes, as well as from the different cable lengths between the probes and oscilloscope. Second, the conductive current of the plasma was calculated by subtracting the displacement current from the measured current (Eq. 6.2). Finally, the energy deposited per pulse was obtained by integrating the power over the duration of the pulse, using the measured voltage and calculated conductive current (Eq. 6.3).

$$I_{displacement} = C\frac{dV}{dt} \tag{6.1}$$

$$I_{measured,plasma} = I_{conductive} + I_{displacement} \tag{6.2}$$

$$E_{plasma} = \int_{t_0}^{t_{end}} I_{conductive} V \, dt \tag{6.3}$$

6.3.4 Energy efficiency calculations

The energy efficiency E_E (in g/kWh) was obtained adapting the calculations used by Malik et al. (Malik, 2010) and Magureanu et al. (Magureanu, Mandache and Parvulescu, 2015):

$$E_E = \frac{C_0 VR}{100Pt} \tag{6.4}$$

C_0 is the initial DTZ concentration (in g/L), V is the solution volume (in L), R is the removal rate (in %), P is the power dissipated in the plasma discharge (in kW) and t is the treatment time (in h). The power P is calculated as:

$$P = E_p f \qquad (6.5)$$

E_p is the energy deposited per pulse and f is the pulse frequency.

6.3.5 Iodometric titrations

Iodometric titrations were performed using a Metrohm 888 Titrando equipment. 0.5 mL of plasma-treated water (LC-MS grade) sample was acidified with 2.5 mL of 30% H_2SO_4 (Sigma Aldrich, reagent grade) with 0.18 g/L ammonium molybdate solution (Fisher Scientific, ACS grade). Next, the sample was stirred together with > 0.01 g KI (Fisher Scientific, ACS grade) and five droplets of a 40 g/L starch solution (Fischer Scientific, Tyodene). The titrant was a 0.001 N solution of $Na_2S_2O_3$ (Fisher Scientific, 0.0995 N – 0.1005 N).

6.3.6 LC-HRMS method

Immediately after each plasma treatment experiment, the samples were quenched with 5% MeOH (Optima™ LC/MS Grade, Fisher Chemical™). Although this does not fully quench residual reactive species (see Fig. 6-15), adding MeOH helped to match the mobile phase of the LC. The quencher combination that fully removes residual reactive species (catalase + $Na_2S_2O_3$) could not be used for LC-HRMS analysis. Regarding catalase, it has a high molecular weight and as it reacts with residual reactive species it might form by-products that could complicate the analysis of DTZ TPs. Concerning $Na_2S_2O_3$, preliminary tests comparing MeOH and NaS_2O_3 showed that MeOH gave better signals (x2) for some TPs. Furthermore, $Na_2S_2O_3$ introduces Na^+ to the system, which may lead to the formation of adducts (salts interacting with some ions produced in the source) and complicate the TP analysis. Since MeOH does not fully quench residual reactive species, LC-HRMS measurements were started as soon as possible, about 15 min after the end of the plasma treatment.

Analysis was performed on an Accela 600 LC System (Thermo Scientific, Waltham MA, USA) in tandem with an LTQ XL Orbitrap mass spectrometer. Both the LC and the MS systems were controlled by the ThermoXcalibur 2.0 software (Thermo Scientific, San Jose CA, USA).

Chromatography was resolved with a 0.2 μm in-line filter unit followed by a security guard cartridge Polar-RP (4 mm x 2 mm ID) connected to the analytical column (100 mm x 2 mm ID; 2.5 μm 100 Å Synergi Polar RP from Phenomenex, Torrance CA, USA). Separation of 25 μL injection was conducted at 30 °C with a binary buffer system composed of Milli-Q water and 0.1 % formic acid (Solvent A) and methanol 0.1 % formic acid (Solvent B). A gradient elution at 0.25 mL/min of A:B was conducted as follows; initial 95:5 (0-1 min), 90:10 (1-3.5 min), ramp to 85:15 (3.5-5.5 min), 80:20 (5.5-11 min), flush with 100% B (11-12.5 min), hold for 2.5 minutes and return to original conditions after 1 min to finally equilibrate for an extra minute for a total running time of 17 min.

Detection of free DTZ and its transformation products was performed using a heated electrospray ionization source (HESI) in positive mode. Optimization of the instrument parameters was performed by direct infusion of a standard solution at 10 μL/min, while source optimization conditions were determined using infusion flow analysis. Nitrogen was used as sheath, auxiliary and sweep gas, while helium was used as the collision gas. Analysis was done on full scan mode at 30000 resolution for the FT-MS Orbitrap detector on a mass range of 50-800 m/z. Quantification of DTZ was achieved by performing a SIM detection simultaneously as the high resolution spectra was collected while the ion trap was used to generate the MS^2 spectra for confirmation of DTZ and its transformation products. The quantification was carried on the Quan Browser module while the post-acquisition data processing for the transformation products was done by applying a mass accuracy windows at ± 5 ppm monoisotopic mass tolerance for the $(M+H^+)$ ion exact mass. Additionally, to the instrument software, Mass Frontier 7.0 and the curetted database mzcloud from Thermo Scientific along MZmine 2.0 software were used on the generation and confirmation of some of the identified TPs.

6.3.7 Acute toxicity tests

A standard acute Microtox® test was used to determine the toxicity of plasma treated samples. The methodology for testing was adapted from the purchased Environmental Bio-Detection Products Inc. (EBPI) kit containing all necessary solutions and reagents to perform the assay. Toxicity was determined by the decrease in luminescence from *Aliivibrio fischeri (V. Fischeri)* and was measured by the Microtox® M500 analyzer as light intensity.

Immediately after each plasma treatment experiment, the samples were quenched with 2 mg/L catalase from bovine liver (Sigma-Aldrich, lyophilized powder, 2,000-5,000 units/mg protein) + 2 mg/L sodium thiosulfate (Sigma-Aldrich, powder, > 98 % purity). Toxicity tests were started about 30 min after the end of the plasma treatment. Before testing, the conductivity and the pH of the sample were adjusted according to Microtox® instructions. The pH of the samples was measured at room temperature with a Fisher Scientific XL60 Accumet® Excel benchtop pH meter. The pH meter was calibrated using three buffer solutions of pH 4, 7 and 10. The conductivity of the samples was recorded at room temperature with an Oakton Series 510 Benchtop Meter. The equipment was calibrated using Fisherbrand™ Traceable™ Conductivity Calibration Standards. It was important to adjust the conductivity before the pH, since the original conductivity of the samples was around 100 µS/cm or lower, and the pH meter was not designed to function at these low conductivities. The 20% effective concentration (EC20) was measured after 15 minutes of incubation time. Toxicity results are represented as percentages of the sample required to obtain a 20% effect.

6.3.8 Statistical Analyses

The error bars shown in the graphs represent one standard deviation of the samples for replicate experiments. An ANOVA statistical analysis was performed to check whether the means of two or more groups were statistically different from each other. The analysis was performed with the Microsoft Excel tool Anova: Single Factor. The significance level was set at $\alpha = 0.05$ for all tests, meaning that there is a 5% risk of concluding that a difference exists when there is no actual difference. When the null hypothesis fails to be rejected, it means that there is not enough evidence to state that there is a significant statistical difference between the evaluated means.

6.4   Results and Discussion

6.4.1 Electrical characteristics

Fig. 6-2 shows characteristic voltage and current signals measured in an oxygen atmosphere. From voltage and current signals measured at different plasma treatment times, the energy deposited per pulse is calculated (see Fig. 6-3). For the energy determination calculations, the capacitance C and the delay between the measured current and the displacement current are estimated parameters. Therefore, it is important to check their associated uncertainty. We checked the sensitivity of the

calculations to varying the capacitance C by $\pm$ 0.5 pF. This capacitance variation did not have any significant effect on the energy results at the experimental conditions. Rusterholtz reports that if the delay between the measured current and the displacement current is not determined correctly, even a mismatch of 0.2-0.3 ns can influence the obtained energy by 50 % (Rusterholtz, 2012). We tested the sensitivity of our calculations to varying the delay by $\pm$ 0.5 ns. This delay variation led to around 20 μJ difference from the original values. Therefore, we concluded that this delay has a small influence on our energy results.

The energy deposited per pulse increases over the plasma treatment time, from around 160 μJ at 1 min to around 250 μJ at 60 min. The increasing energy trend is linked to an increase in measured peak current over the plasma treatment time (the voltage signals remain constant). In turn, the increasing current can be explained by an increase in conductivity in the treated solution, which allows for electric current to flow. For two experimental repeats, we measured the conductivity of the untreated solutions containing C_0 = 10 mg/L DTZ in LC-MS grade water (2.7 and 2.9 μS/cm), as well as solutions after 60 min of plasma treatment (114.2 and 94.8 μS/cm). Note that a similar behaviour of the conductivity and the energy deposited per pulse was observed for two controls of LC-MS water (see Fig. 6-12; initial conductivity 1.1 and 1.1 μS/cm and final conductivities after 60 min treatment of 113.1 and 87.3 μS/cm). During the plasma treatment, ionic reactive species and metal ions from electrode erosion are introduced into the plasma-treated solution, increasing its conductivity (Corella Puertas, Dzafic and Coulombe, 2020).
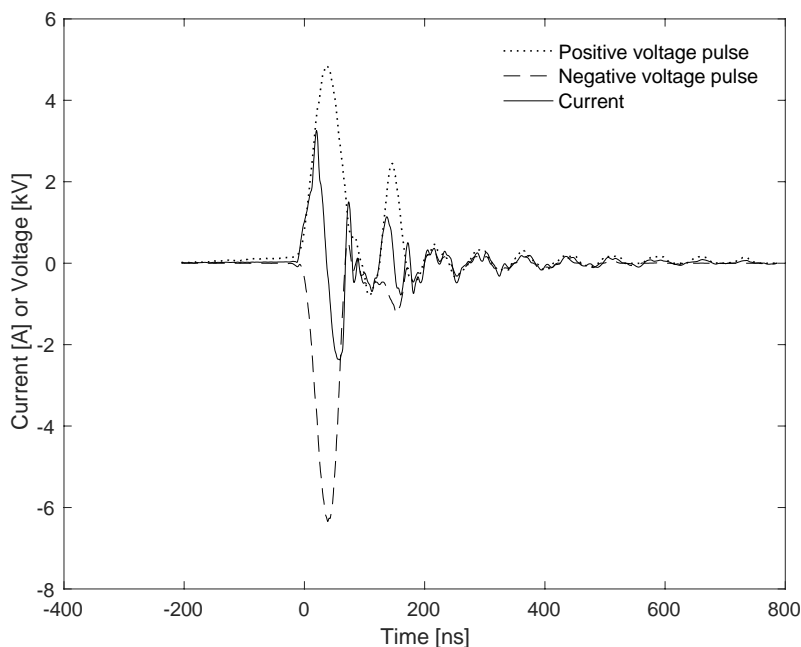
Fig. 6-2 Characteristic voltage and current signals during oxygen plasma treatment at a nanosecond pulse frequency of 3 kHz, averaged for 50 consecutive samples. The measurements were taken 10 min after starting the electric discharges on an aqueous solution containing a nominal initial diatrizoate concentration of C_0 =10 mg/L.
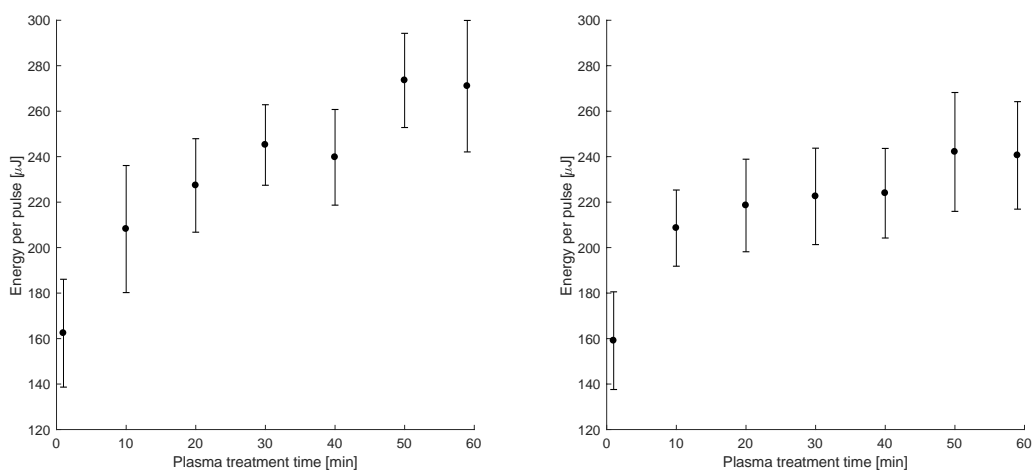
Fig. 6-3 Mean energy deposited per pulse [μJ] with one standard deviation for 50 consecutive sample measurements (2 experimental repeats). The measurements were taken during oxygen plasma treatment at a nanosecond pulse frequency of 3 kHz. The nominal initial concentration of diatrizoate was C_0 =10 mg/L.

135

6.4.2 Diatrizoate removal

Fig. 6-4 compares the effect of air and oxygen plasmas on the temporal evolution of DTZ (nominal C_0 = 10 mg/L) over the plasma treatment time. After 40 min of treatment, the oxygen plasma achieves around 90 % DTZ removal, whereas the air plasma removes around 40 %. For the oxygen plasma, 50 % removal is achieved around 15 to 25 min of treatment. This coincides with the largest variability of the data, which can be explained by the fact that the DTZ degradation reaction is competing with the degradation reactions of TPs. In section 6.4.4 we will see that TPs peak are the most abundant between 15 and 25 min. Note that the increase in energy deposited per pulse over the plasma treatment time discussed in section 6.4.1 does not seem to have a noticeable effect on the degradation trend of DTZ (see Fig. 6-4). A possible explanation is that the degradation reaction is limited by mass transfer from the plasma into the liquid, with a similar amount of reactive oxygen species being transferred into the treated liquid, despite the energy deposited per pulse variations.

In Fig. 6-5, the removal of DTZ in air and oxygen plasmas is studied for two different initial concentrations (nominal C_0 = 200 µg/L or 10 mg/L). Although in both cases oxygen plasma efficiencies higher removal, the difference between the effect of the plasma carrier gases is more pronounced at 200 µg/L. At 200 µg/L, oxygen achieves 66 % more removal than air; at 10 mg/L, oxygen attains 26 % more removal than air. Degrading a higher concentration of DTZ, linked with a higher concentration of TPs, requires more reactive species. Having a limited amount of reactive species available can explain that higher initial DTZ concentrations lead to slower removal in terms of C/C_0.
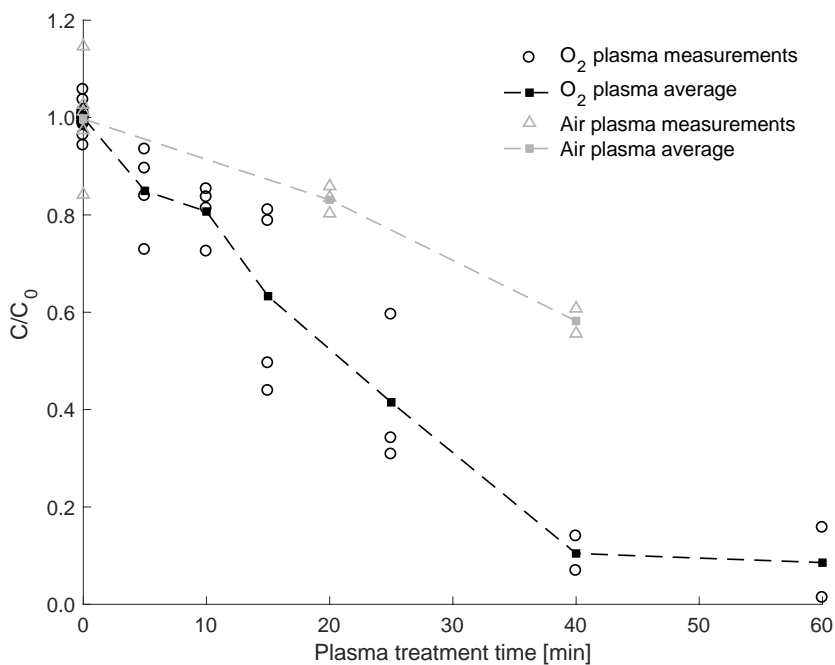
Fig. 6-4 Temporal evolution of diatrizoate over the plasma treatment time, normalized by the measured initial diatrizoate concentration C_0 (nominal $C_0 = 10$ mg/L). The plasma treatment gas was either air or oxygen.
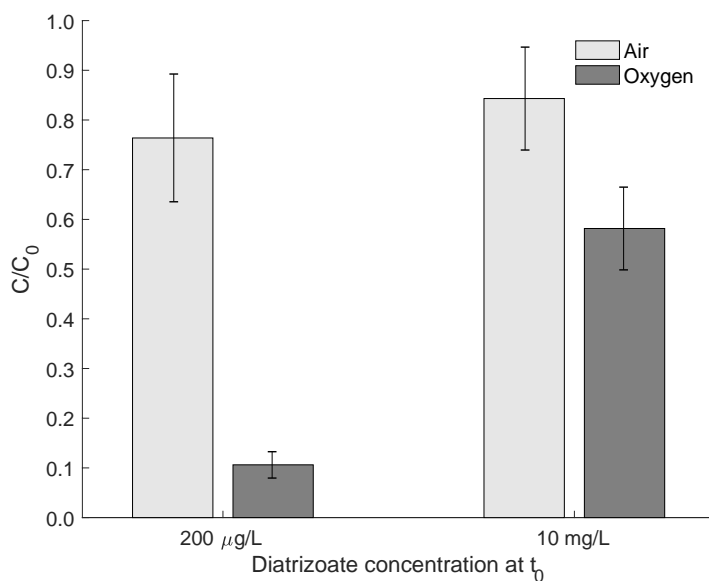
Fig. 6-5 Concentration of diatrizoate after a 20 min plasma treatment, normalized by the measured initial diatrizoate concentration C_0 (nominal $C_0 = 200$ µg/L or 10 mg/L). The error bars represent one standard deviation, n=3-4. The plasma treatment gas was either air or oxygen.

6.4.3 Energy efficiency

The energy efficiency E_E (in g/kWh) is defined as the "amount of compound removed per unit of energy spent in the process". Table 6-1 shows the energy efficiencies calculated for DTZ removal at 20 min of oxygen plasma treatment (corresponding to Fig. 6-5). The energy efficiency calculations required an input of energy deposited per pulse, calculated in section 6.4.1. Since the energy deposited per pulse values obtained at 20 min plasma treatment of 10 mg/L nominal initial DTZ concentration (219 and 227 µJ, see Fig. 6-3) and the values obtained at 20 min plasma treatment of pure water controls (253 and 209 µJ, see Fig. 6-12) were similar, an average of these four energy deposited per pulse values was used for the energy efficiency calculations. The results in Table 6-1 show that the energy efficiency is two orders of magnitude higher at a nominal initial DTZ concentration $C_0 = 10$ mg/L vs. 200 µg/L. This cannot be explained by changes in electrical characteristics, since we used the same energy deposited per pulse for both calculations, and we did not observe significant changes in conductivity for different solution concentrations (see section 6.4.1).

One possible explanation is that higher, homogeneous DTZ concentration implies more DTZ molecules close to the liquid surface. In a general mechanistic model to estimate the treatability of contaminants by plasma-based treatments, the surface concentration of contaminants was found to be the dominant factor determining their removal (Mededovic Thagard *et al.*, 2017). Various reactive species formed in the plasma are very short-lived (< 1 s) and are expected to react at the plasma–liquid interface or after penetration into the liquid by only a few micrometers (Lukes, Locke and Brisset, 2012; Bruggeman *et al.*, 2016). Therefore, having more DTZ molecules at the liquid surface increases the chances of DTZ reacting with short-lived reactive species. Since the liquid is well-mixed – by stirring induced by bubbling as well as by surface tension effects (Marangoni flow) (Corella Puertas *et al.*, 2017) –, the surface is renewed and new DTZ molecules can come in contact with reactive species. This can explain why the amount of DTZ removed per unit of energy spent in the process is higher for higher DTZ concentrations.

Another explanation is the fact that there are various competing reactions occurring: the removal of the parent compound, and the formation and degradation of TPs. For different initial DTZ concentrations, the ratio of reactive species to DTZ molecules will be different, which may favor different reaction pathways. Since the energy efficiency is calculated exclusively for the removal

of the parent compound and does not take into account the energy spent on the degradation of TPs, this can contribute to the disparity between energy efficiencies at different initial DTZ concentrations.

Table 6-1 shows that the energy efficiencies calculated from literature on plasma-based iopromide removal (Krause et al., 2009, 2011; Liu et al., 2013) range from 0.063 to 0.404 g/kWh, for $C_0 = 17$ to 79 mg/L in a pure water matrix. In the present work, the energy efficiency achieved for DTZ removal at $C_0 = 10$ mg/L (0.140 g/kWh) lies within that range. However, removal of DTZ (ionic ICM) is typically more energy intensive than removal on non-ionic ICM such as iopromide, according to literature on plasma-based treatments (Gur-Reznik *et al.*, 2011) and other advanced oxidation treatments (Ternes *et al*., 2003; Huber *et al*., 2005; Seitz, Jiang, *et al.*, 2006; Seitz *et al*., 2008; Kovalova *et al*., 2013; Hansen *et al*., 2016). The only literature value we found on plasma-based DTZ degradation was 0.003 g/kWh at $C_0 = 500$ µg/L (Banaschik *et al.*, 2015). The energy efficiency values obtained in the present work at $C_0 = 200$ µg/L (0.006 g/kWh) and $C_0 = 10$ mg/L (0.140 g/kWh) are higher than Banaschik's. This was to be expected, since in-liquid discharge configurations like the one used by Banaschik are typically less energy efficient than above-liquid discharges (Malik, 2010; Stratton *et al.*, 2015).

6.4.4 Transformation products

We chose to study the TPs of oxygen plasma, since oxygen achieved faster DTZ degradation and higher energy efficiency than air.

The temporal evolution of measured TPs of DTZ was measured over the plasma treatment time. Fig. 6-6 shows six identified TPs that have been previously reported in literature: m/z 486A (deiodination of DTZ and structural rearrangement) (Sugihara *et al.*, 2013; Azerrad *et al.*, 2016), 504A (ipso attacks at iodine moiety) (Jeong *et al.*, 2010; Rastogi, Leder and Kümmerer, 2014; Azerrad *et al.*, 2016), 504B (ipso attacks at iodine moiety) (Jeong *et al.*, 2010; Rastogi, Leder and Kümmerer, 2014; Azerrad *et al.*, 2016), 628 (derived from 630A by oxidation of the hydroxyl moiety) (Azerrad *et al.*, 2016), 630A (hydroxylation of DTZ) (Azerrad *et al.*, 2016) and 630B (hydroxylation of DTZ) (Azerrad *et al.*, 2016). Five TPs shown in Fig. 6-7 are novel: m/z 486B, 550, 555, 565 and 578 and have not been reported before for any oxidative treatment. Note that the TPs are labelled in nominal mass. In general, the TPs peak reach a higher level of abundance

at treatment times between 15 and 25 min. Since the graphs show individual measured data points, the variability of the data is visible. The variability of the data can be linked to various reasons:

- Since the reactor design does not allow for extracting samples during the plasma treatment, every data point is obtained by running a new experiment. Among the variability introduced by new experiments, the system is particularly sensitive to the position of the pin electrode. Because the pin electrode has a small diameter and is ductile, it is difficult to keep the tip completely straight after cleaning the setup between each experiment, which can lead to small changes in the distance to the liquid surface. Changes in the discharge gap can affect the breakdown voltage, discharge characteristics and amount of plasma-chemical species produced, and thus potentially affect the formation and degradation of TPs (Lieberman and Lichtenberg, 2005; Lukes *et al.*, 2005; Lukes, Clupek and Babicky, 2011; Massarczyk *et al.*, 2017; Yoon *et al.*, 2018; Corella Puertas, Dzafic and Coulombe, 2020).

- The small volume of the reactor, as well as possibly small TP concentrations can contribute to the observed variability. Although the initial concentration of the parent compound (10 mg/L DTZ) and its counts measured by mass spectrometry were high ($> 1E+07$), the counts measured for TPs were between 1 and 3 orders of magnitude lower. Detection optimization of the mass spectrometer was based only on a DTZ standard, which might have contributed to the lower detected counts of the TPs. The concentration of TPs was not quantified.

- Around 15 to 25 min plasma treatment time, when the degradation of the parent compound is close to 50 % and the TPs are more abundant, there are many degradation pathways competing. This can explain why both DTZ (see Fig. 6-4) and the TPs (see Fig. 6-6 and Fig. 6-7) show particularly high variability at this plasma treatment time range. The most remarkable variability was observed for TPs 504A, 504B and 578 at 15 min plasma treatment time.
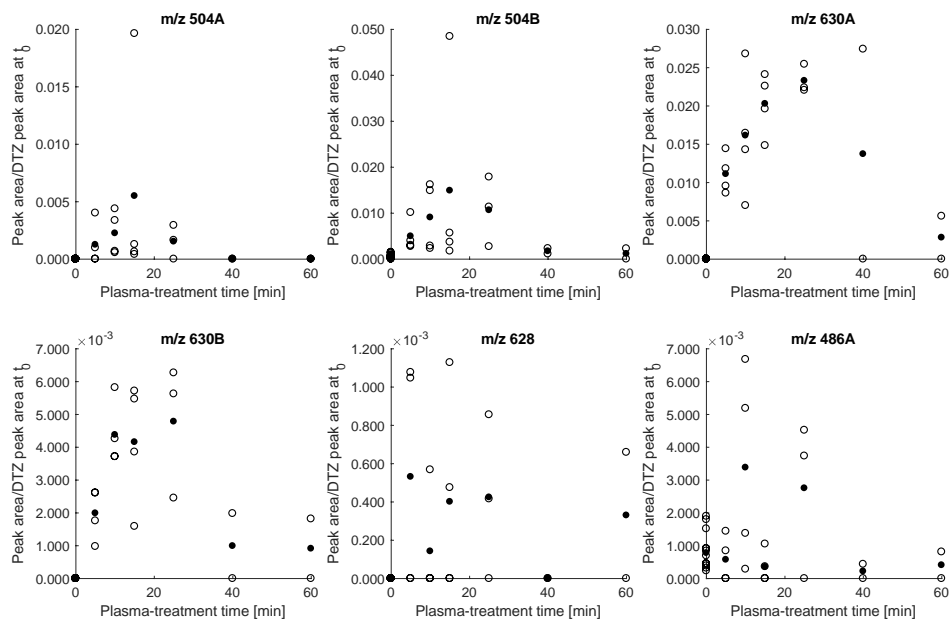
Fig. 6-6 Temporal evolution of measured transformation products of diatrizoate over the plasma treatment time. The presence of these transformation products of diatrizoate has been previously reported in literature. ∘: Measurements. •: Average.
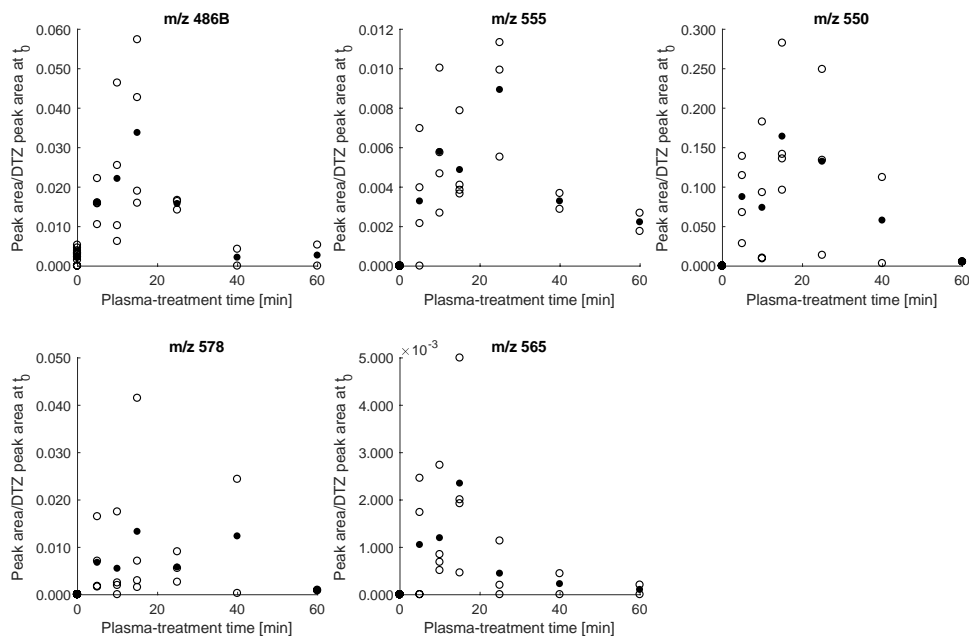
Fig. 6-7 Temporal evolution of measured transformation products of diatrizoate over the plasma treatment time. To the best of our knowledge, these transformation products of diatrizoate have not been previously reported in literature. ∘: Measurements. •: Average.

Some deiodination products of DTZ were detected at t_0: m/z 486A, 486B and 488. This deiodination may have occurred during storage, or perhaps was already present in the DTZ powder. For m/z 486B, it is clear that the concentration increases over time, and thus we categorize it as TP. For m/z 486A, only four of our data points are above the values measured at t_0. Therefore, we are hesitant to categorize m/z 486A as a TP, although it was previously reported in literature, considering its presence before treatment. Regarding m/z 488, it clearly decreases over time (see Fig. 6-13). Therefore, we do not consider m/z 488 to be a TP.

Three m/z were detected at the same retention time as TP550 (m/z 533, 491 and 473). With the MS^2 mass spectrum (see Fig. 6-14), we confirmed that these detected m/z are fragments of TP550 produced by source fragmentation, and thus we do not categorize them as TPs.

Table 6-2 shows retention times and proposed molecular formulas for the TPs of DTZ shown in Fig. 6-6 and Fig. 6-7. Note that for the TPs 578, 550 and 565 the hydrogen content seems very high, given the fact that the parent compound has only 9 H atoms. Further investigation is needed to look at molecular structures and verify whether the proposed molecular formulas can be formed during plasma treatment.

Table 6-2 DTZ transformation products identified for oxygen plasma treatment (C_0 = 10 mg/L).

TP nominal mass	Molecular formula	m/z	RT (min)	Error (ppm)	References
TP-630A	$C_{11}H_9I_3N_2O_5$	630.7719	6.3	1.09	Azerrad, 2016
TP-630B	$C_{11}H_9I_3N_2O_5$	630.7716	4.1	1.10	Azerrad, 2016
TP-628	$C_{11}H_7I_3N_2O_5$	628.7550	2.6	0.48	Azerrad, 2016
TP-504A	$C_{11}H_{10}I_2N_2O_5$	504.8753	3.1	1.79 (Azerrad 2016)	Azerrad, 2016; Jeong, 2010; Rastogi, 2014
TP-504B	$C_{11}H_{10}I_2N_2O_5$	504.8751	6.1	- 3.97 (Azerrad 2016)	Azerrad, 2016; Jeong, 2010; Rastogi, 2014

TP-486A	$C_{11}H_8I_2N_2O_4$	486.8643	5.9	1.40	Azerrad, 2016
TP-486B	$C_{11}H_8I_2N_2O_4$	486.8645	11.1	0.26	This work
TP-578	$C_{12}H_{25}I_3N_2$	578.9229	4.3	- 0.77	This work
TP-550	$C_{10}H_{21}I_3N_2$	550.8915	4.2	- 0.70	This work
TP-565	$C_{11}H_{22}I_3NO$	565.8919	4.2	- 1.87	This work
TP-555	$C_{10}H_9I_2N_2O_9$	555.8470	4.3	0.07	This work

6.4.5 Acute toxicity

Acute toxicity was studied for three plasma treatment times (see Fig. 6-8). At 20 min plasma treatment, 50 % DTZ degradation is achieved and most TPs are at their highest counts. At 40 min, DTZ was removed by one order of magnitude (about 90 % degradation). At 60 min, the TPs were decreased and, in some cases, had disappeared completely. The EC20 (20 % effective concentration) represents the concentration of plasma-treated solution required to cause a 20 % decrease of luminescence of the tested organism, *A. fischeri*. As an example, at 60 min plasma treatment time, about 30 % volume dilution of plasma-treated DTZ caused a 20 % effect on the tested bacteria. Although EC50 (50 % effective concentration) is more commonly used to report toxicity, in this case the toxicity was too low and obtaining EC50 values required extrapolation and had a high associated error. Therefore, reporting the acute toxicity as EC20 was more reliable in this case. ANOVA statistical analysis reveals no significant statistical difference between plasma-treated DTZ solutions and plasma-treated water controls (see Table 6-3). Therefore, we do not observe any residual toxicity associated with the TPs.

Regarding the background toxicity of plasma-treated water, its causes remain unclear. ANOVA statistical analysis showed a significant statistical difference between the 20 and 40 min water controls, indicating an increase in background toxicity over time (see Table 6-3). However, there was no significant statistical difference between 40 and 60 min water controls (see Table 6-3). Since the plasma-treated water is quenched – its total oxidizing power is below quantitation limit

for the chosen quenchers, 2 mg/L $Na_2S_2O_3$ + 2 mg/L catalase (see Fig. 6-15 and Fig. 6-16) – it seems unlikely that residual reactive species are the cause of the measured background toxicity. One possibility is that the background toxicity is linked to metal ions introduced by electrode erosion. In previous work, we proved that high-voltage pin electrodes erode, releasing metal ions and/or metal particles into the plasma-treated solution (Corella Puertas, Dzafic and Coulombe, 2020). Further work is required to confirm whether the eroded metals are inducing toxicity on *A. fischeri*.
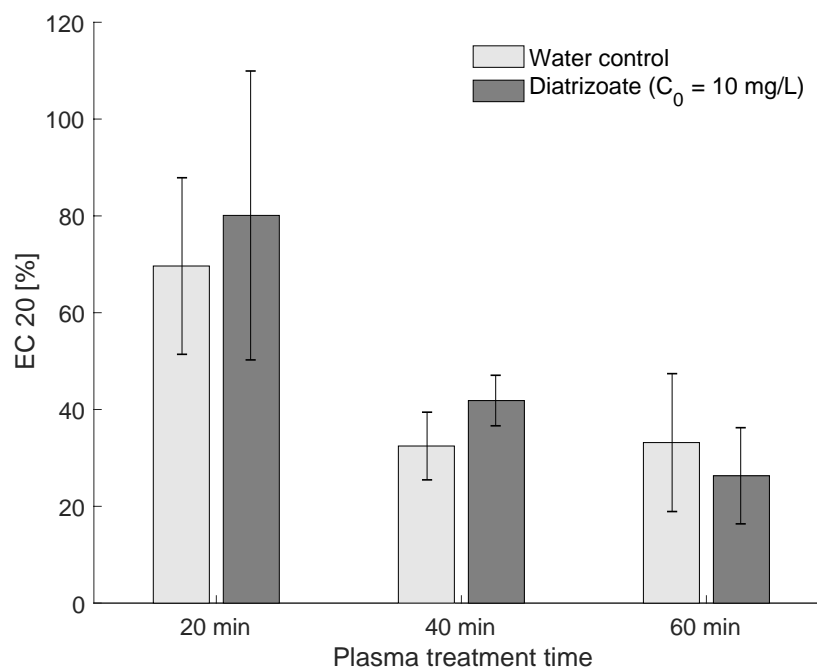
Fig. 6-8 Acute toxicity on *A. fischeri* measured as EC20 values, for plasma-treated LC-MS grade water and plasma-treated diatrizoate (initial nominal $C_0 = 10$ mg/L). The error bars represent one standard deviation, n=3. At t_0, the untreated diatrizoate solution and the untreated water control did not show any toxicity (except for one out of three repeats of the DTZ solution for which the EC20 of diatrizoate could be extrapolated to 273 mg/L).

6.5 Conclusions

We studied the degradation of DTZ, a particularly recalcitrant aqueous pollutant, in a compact non-thermal plasma–liquid reactor. The reactor produced repetitively pulsed nanosecond discharges in a pin-to-liquid configuration. The energy deposited per nanosecond pulse started at around 160 µJ and increased over the plasma treatment time to reach around 250 µJ at 60 min of plasma treatment. This increase in energy deposited per pulse over the plasma treatment time is

linked to an increase in measured current. In turn, the increase in current may be explained by the observed increase in conductivity of the plasma-treated solution over time. We do not expect the change in energy deposited per pulse to pose a problem for wastewater treatment applications. Since wastewaters have significantly higher conductivities than the ones tested in the present work, the change in conductivity and thus in energy deposited per pulse is expected to be negligible. However, this hypothesis would have to be confirmed in future experiments.

Two DTZ concentrations were examined: 10 mg/L to facilitate the identification of TPs and 200 μg/L, which is in the range expected in hospital wastewater. The effects of two plasma carrier gases, oxygen and air, were compared. The use of an oxygen plasma is a novelty in the context of plasma-based degradation of ICM, since previous studies used air plasmas or direct in-liquid discharges. The results show that oxygen plasmas are more effective than air plasmas, achieving 66 % higher degradation for an initial concentration of 200 μg/L DTZ, and 26 % higher degradation for 10 mg/L DTZ after 20 min of plasma treatment. At 20 min oxygen plasma treatment, the energy efficiency for removing DTZ at 10 mg/L initial DTZ concentration (0.140 g/kWh) was two orders of magnitude higher than the one obtained at 200 μg/L initial DTZ concentration (0.006 g/kWh). We attributed this disparity to (1) at higher DTZ concentrations, the presence of more DTZ molecules at the plasma–liquid interface, which may increase the chances of reacting with short-lived reactive species and (2) the fact that the formation and degradation of TPs are not taken into account in the energy efficiency calculations. The energy efficiency of DTZ removal reported in the present work is within the same range than values calculated for plasma-based treatments of iopromide (Krause *et al.*, 2009, 2011; Liu *et al.*, 2013), despite the fact that DTZ removal is typically less efficient than iopromide removal (Ternes *et al.*, 2003; Huber *et al.*, 2005; Seitz, Jiang, *et al.*, 2006; Seitz *et al.*, 2008; Gur-Reznik *et al.*, 2011; Kovalova *et al.*, 2013; Hansen *et al.*, 2016). Furthermore, the energy efficiencies obtained in the present work are higher than the one reported by Banaschik *et al*. for DTZ removal by in-liquid discharges (0.003 g/kWh) (Banaschik *et al.*, 2015). Although these results are promising, the main aim of the present work was not to surpass energy efficiencies reported in literature for DTZ degradation, but rather to test different degradation parameters, study TPs and their associated residual toxicity. In future work, the energy efficiency could be further improved by changing the reactor design to maximize the surface area of the plasma–liquid interface and the surface-to-volume ratio (Malik, 2010; Stratton *et al.*, 2015).

For the oxygen plasma treatment, we identified TPs of DTZ: m/z 486A, 504A, 504B, 628, 630A, 630B (previously described in literature) and m/z 486B, 550, 555, 565, 578 (novel). In general, the TPs peaked between 15 and 25 min of treatment, coinciding with 50 % degradation of DTZ. There was a significant variability in the TP data points, which we attribute to (1) the fact that every data point is obtained by running a new experiment, (2) small reactor volume and small TP concentrations and (3) competing degradation pathways, particularly when TPs are peaking. For the novel TPs, molecular formulas were proposed. Further investigation is needed to identify molecular structures and verify whether the proposed molecular formulas can be formed during plasma treatment.

Acute toxicity was tested on *A. fischeri* for samples with different plasma treatment times (20, 40 and 60 min). We did not observe any residual toxicity which could be associated to the transformation products, since there was no significant statistical difference between plasma-treated DTZ and plasma-treated water controls. The background toxicity of plasma-treated water controls is unlikely to come from residual reactive species, since the samples were quenched. Further work is required to confirm whether the background toxicity of PAW is linked to the presence of metal ions or particles, which are introduced into the solution by erosion of the high-voltage pin electrode (Corella Puertas, Dzafic and Coulombe, 2020). In the case metal release wants to be avoided, ceramic-coated or carbon electrodes may be suitable alternatives (Šunka, 2001; Holzer and Locke, 2008).

Acknowledgements

6.6 Supplementary material
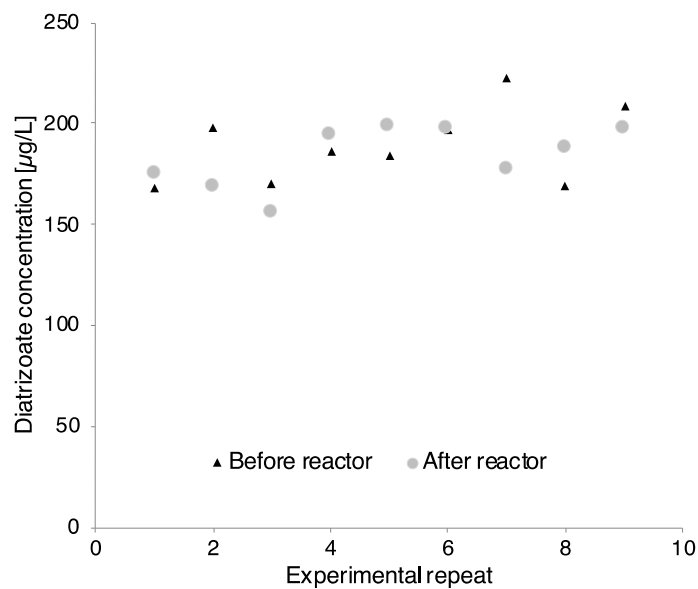
Fig. 6-9 Diatrizoate concentration measured right after solution preparation (nominal C_0 = 200 µg/L), and after transporting the solution using glass vials and keeping the solution in the plasma reactor for 20 min (bubbling air, no plasma treatment).
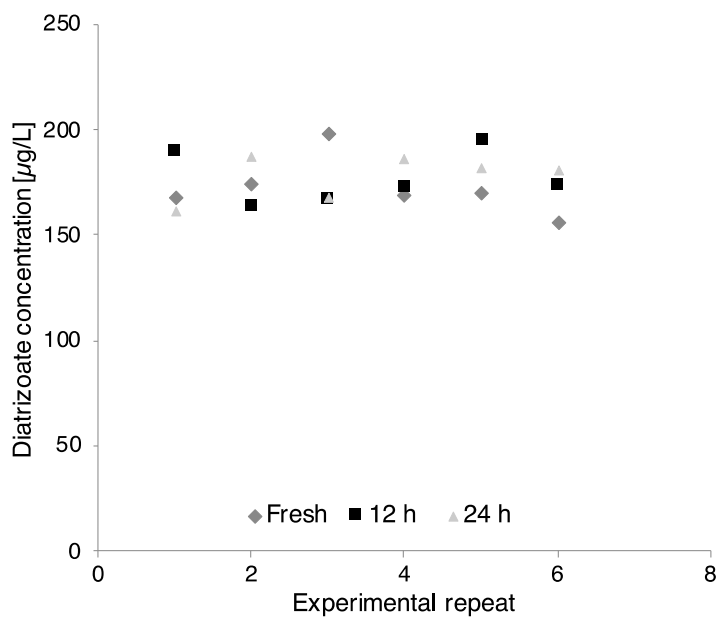
Fig. 6-10 Diatrizoate concentration measured right after solution preparation (nominal C_0 = 200 µg/L) and after storage in glass vials for 12 and 24 hours.
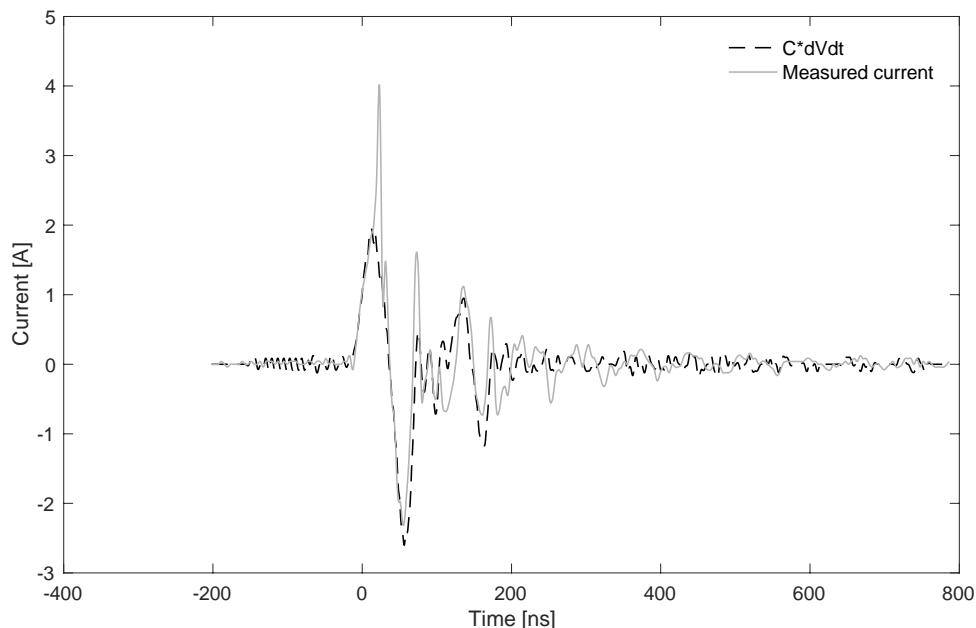
Fig. 6-11 Displacement current (*C*dV/dt*) calculated with *C* = 5 pF and measured current. The voltage and current were measured simultaneously during oxygen plasma treatment at a nanosecond pulse frequency of 3 kHz and were averaged for 50 consecutive samples. The delay between the curves was adjusted by 2.5 ns. The measurements were taken 30 min after starting the electric discharges on an aqueous solution containing a nominal initial diatrizoate concentration of C_0 =10 mg/L.
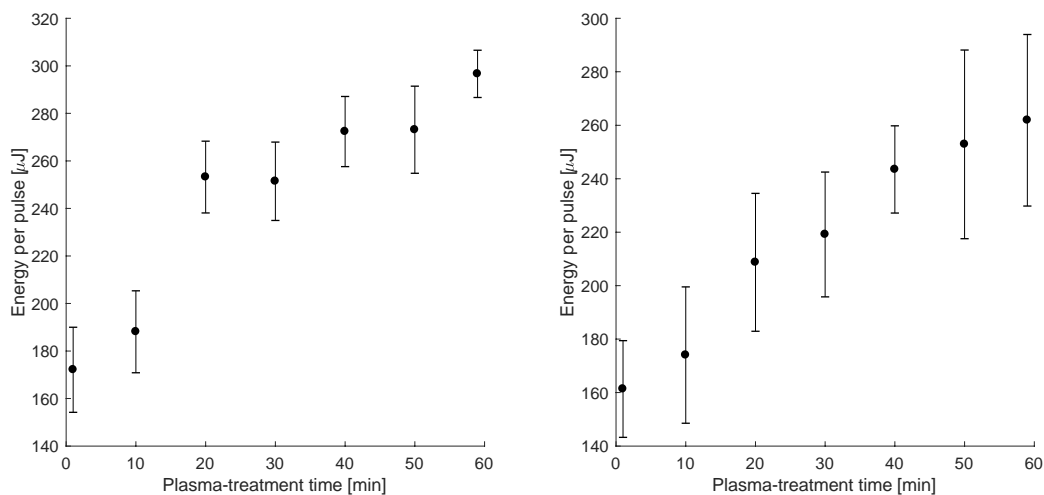
Fig. 6-12 Mean energy deposited per pulse [μJ] with one standard deviation for 50 consecutive sample measurements (2 experimental repeats). The measurements were taken during oxygen

plasma treatment at a nanosecond pulse frequency of 3 kHz. The liquid was LC-MS grade water (no diatrizoate).
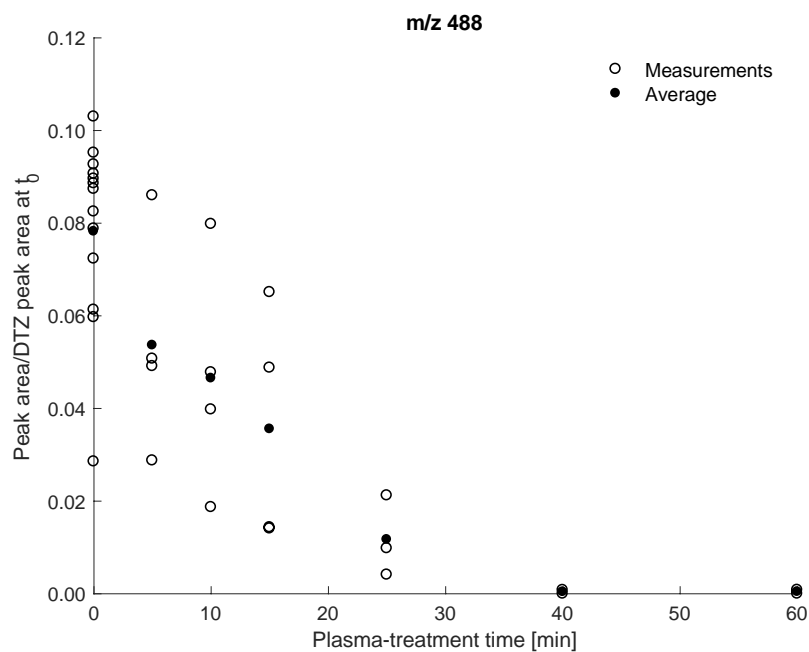
Fig. 6-13 Temporal evaluation of m/z 488 over the plasma treatment, not considered as a transformation product due to the profile of the presence over time.
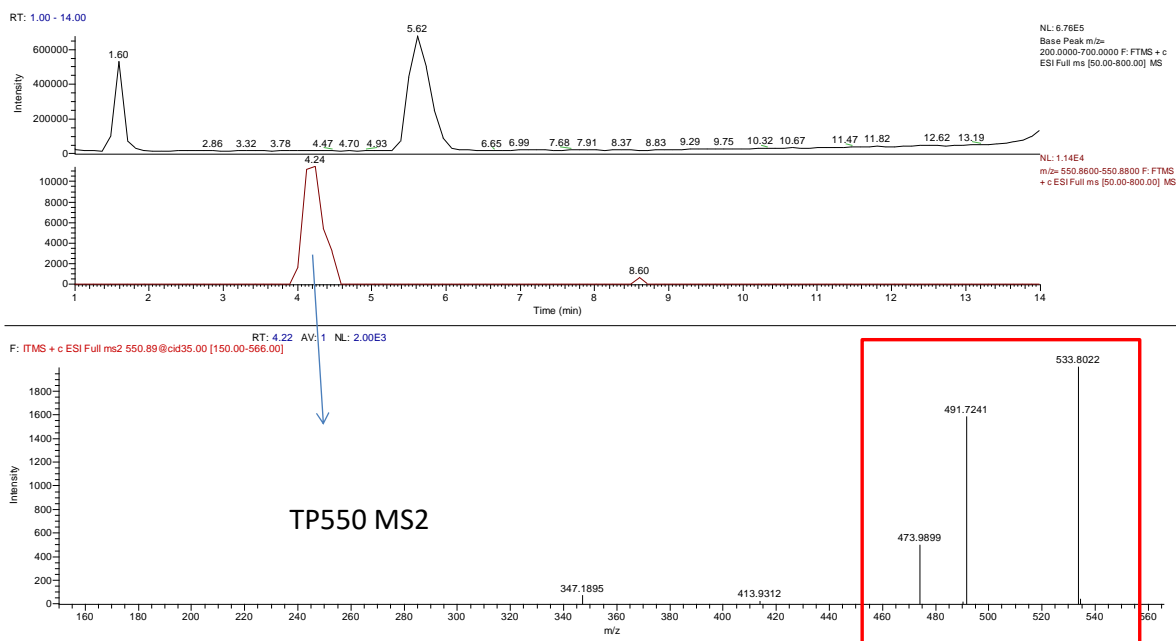
Fig. 6-14 MS^2 of the 550 m/z transformation product, which produces three main fragments: 533, 491 and 473 m/z. Top: Total ion current from 200-700 m/z at 30000 resolution on the FTMS

detector. Middle: Extracted ion chromatogram with a window of 550.86 to 550.88 m/z on the HRMS detector. Bottom: MS^2 mass spectrum detected on the ion trap detector.

Table 6-3 Results of ANOVA statistical analyses for the results shown in Fig. 6-8. Note that for all calculations, the significance level α was set to $\alpha = 0.05$. The null hypothesis was rejected when the calculated value F was larger than the critical value F-crit and the p-value was smaller than α.

Description of values tested with ANOVA	F	F-crit	p-value	Null hypothesis rejected
20 min plasma treatment, DTZ vs water control	0.27	7.71	0.63	no
40 min plasma treatment, DTZ vs water control	3.47	7.71	0.14	no
60 min plasma treatment, DTZ vs water control	0.47	7.71	0.53	no
20 vs 40 min plasma treatment, water control	10.88	7.71	0.03	yes
40 vs 60 min plasma treatment, water control	0.01	7.71	0.94	no
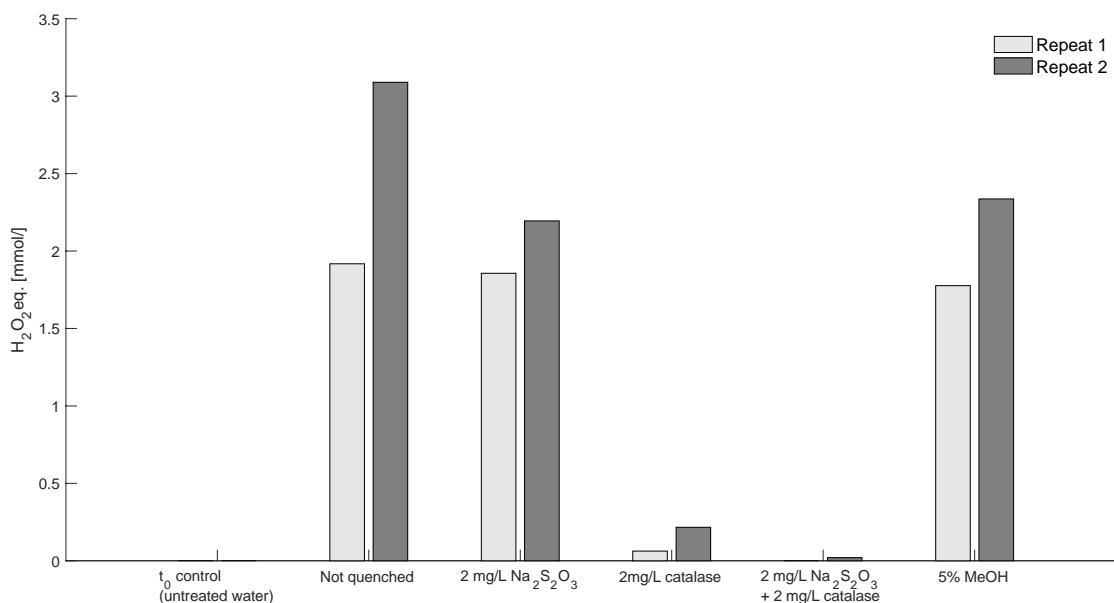
Fig. 6-15 Total oxidizing power of LC-MS grade water samples. The titrant results are represented in H2O2 equivalent concentrations. The samples were plasma-treated for 20 min and subsequently quenched with different quencher types. Note that the results obtained for *2 mg/L Na₂S₂O₃ + 2 mg/L catalase* were below the quantitation limit. On the left, there are two controls (untreated water and 20 min plasma-treated water that was not quenched). The *not quenched* controls were measured within 1.5 hours after the end of the plasma treatment.
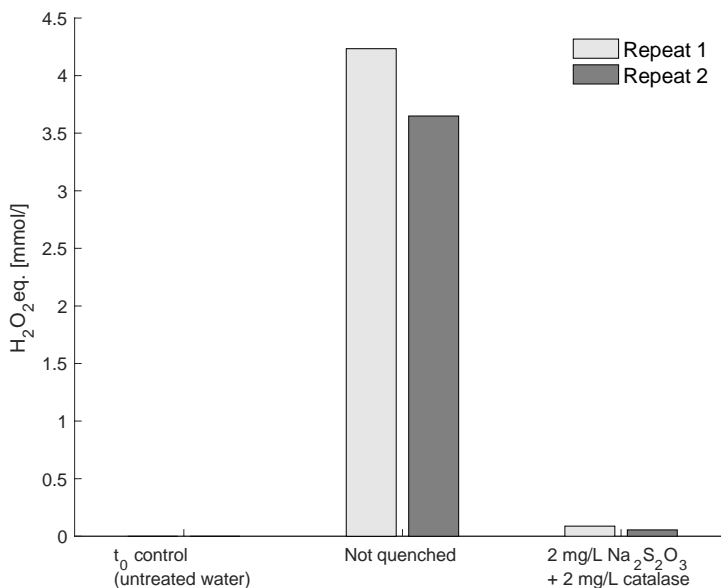
Fig. 6-16 Total oxidizing power of LC-MS grade water samples. The titrant results are represented in H₂O₂ equivalent concentrations. The samples were plasma-treated for 60 min and subsequently quenched with different quencher types. Note that the results obtained for *2 mg/L Na₂S₂O₃ + 2*

mg/L catalase were below the quantitation limit. On the left, there are two controls (untreated water and 60 min plasma-treated water that was not quenched). The *not quenched* controls were measured within 1.5 hours after the end of the plasma treatment.

7

Conclusion

7.1   Summary of conclusions

In this PhD project, a compact pin-to-liquid discharge reactor was developed and used to study the removal of aqueous organic pollutants. In Chapter 4, a preliminary setup demonstrated the applicability of a nanosecond-pulsed pin-to-liquid discharge configuration for removing a model aqueous organic pollutant, the MB dye. Dyes are typically used for testing plasma–liquid reactors, since their degradation can be easily tracked (they fade away as the chromophoric bond is broken during degradation). A novel, simple method was developed for studying the degradation and transport of the dye through image analysis of digital photos. In this method, the key was to track the changes in the red pixels of the images, since the main absorption peak of MB (660 nm) falls into the red spectrum. Image analysis revealed areas of convective mass transport linked to Marangoni flow and areas of diffusion-limited mass transport. It also indicated that the dye removal process could benefit from external assistance for mixing and contact area enhancement. Indeed, introducing forced stirring by a magnetic stir bar yielded higher dye removal than not stirring the solution. A parametric study varying pulse frequency, voltage and polarity helped to choose optimal operating parameters. With the knowledge gained from Chapter 4, the compact nanosecond-pulsed pin-to-liquid discharge reactor was designed and used in Chapters 5 and 6.

Chapter 5 investigated the erosion high-voltage pin electrodes (hafnium, copper and stainless steel) in pin-to-liquid repetitively pulsed nanosecond discharges in air or oxygen. The electrode material did not influence the energy deposited per pulse, which was around 620 µJ for discharges in air and around 350 µJ for discharges in oxygen. Electrode erosion was observed for all studied materials, with stainless steel standing out as the material that led to the least erosion both for air

and oxygen plasmas. Electrode erosion produced crater-like morphologies and released metals in ionic and particle form into the plasma-treated water. Although this study gives initial information on the metal particles introduced by erosion, further work is required to study of their size, shape, composition and how to avoid agglomeration. For wastewater treatment applications, the introduction of eroded metals may want to be avoided, due to toxicological and environmental aspects. Therefore, this work suggests that electrode erosion should be taken into account when designing plasma systems with sustainability in mind. Metals introduced through erosion, combined with the reactive species in plasma-treated water, open opportunities for applications beyond water purification. For instance, in the context plasma medicine, treatment of cancer cells can be enhanced by combining the effect of plasma-formed RONS with the effect of copper ions and nanoparticles introduced through electrode erosion (ongoing collaboration work of the Author with CHUM Research Center in Montréal).

Chapter 5 also showed that the metals introduced by electrode erosion did not affect long-lived RONS. Plasma-treated water formed by discharges in air initially contained nitrites and nitrates, and nitrites complete converted into nitrates after two weeks post-plasma exposure. Regarding plasma-treated water formed by discharges in oxygen, a comparison of results obtained with two different analytical techniques (HPLC-ECD and iodometric titration) led to the conclusion that hydrogen peroxide was the only type of RONS that remained in the solution post-plasma exposure. Knowledge of the type, concentration and lifetime of RONS in plasma-treated water can be useful for applications such as medicine, agriculture and wastewater treatment. For the latter, it may be necessary to run additional treatment steps to quench residual RONS before emission into the environment. For Chapter 6, knowledge on RONS from Chapter 5 was helpful for choosing appropriate quenchers that enabled to study the removal of the model compound without the risk of post-discharge effects like the ones observed in Chapter 4.

In Chapter 6, the compact nanosecond-pulsed pin-to-liquid discharge reactor was successfully used for degrading a model aqueous organic pollutant, the ICM DTZ. An extensive literature review in Chapter 2 showed that DTZ is a particularly recalcitrant CEC, which has been detected in many surface waters and wastewater treatment effluents around world in concentrations ranging between ng/L and µg/L (the latter for certain hospital wastewater effluents). Therefore, the successful removal of this model pollutant is a good indicator that the technology developed in the

154

present work has the potential of successfully removing other aqueous organic pollutants. Oxygen plasma treatment, which was applied for the first time for the removal of DTZ, showed more effective removal than air plasma treatment. In terms of energy consumption, the oxygen plasma treatment required 30 kWh/m^3/order (C_0 = 200 µg/L). Within the range of energy consumption of plasma technologies (see Fig. 2-8), the energy consumption reported in the present work is high. This can be explained by the fact that DTZ is a particularly recalcitrant aqueous pollutant, which requires unusually high energy doses to achieve partial removal in various AOPs (Kovalova *et al.*, 2013; Hansen *et al.*, 2016). TPs were identified and showed no acute toxicity in bacterial tests (*Aliivibrio fischeri*). Plasma-treated water controls showed some residual background toxicity, which is not fully understood at this point and requires further investigation. Nevertheless, since other treatment technologies (such as some ozonation, photocatalytic, electrochemical or $SO_4^{\bullet-}$-based treatments) fail to adequately remove ICM parent compounds and in some cases even produce toxic TPs, the results obtained in the present work are very promising.

7.2   Original contributions

The original contributions of this PhD project are:

1) **Implementation of a novel nanosecond pulser for studying the degradation of model aqueous organic pollutants.** Results show that MB and DTZ are successfully removed by treatment in the nanosecond-pulsed pin-to-liquid discharge configurations developed in the present work.

2) **Insights on the degradation and transport of a model dissolved contaminant, MB, within a non-stirred, plasma-treated aqueous solution**. Results, obtained with a novel method based on image analysis of digital photos, show distinct areas of convective and diffusion-limited transport.

3) **Demonstration that, in a nanosecond-pulsed pin-to-liquid discharge configuration, high-voltage pin electrodes erode releasing metal-based ions and particles into plasma-treated liquids**. Results prove the erosion of three electrode materials (copper, stainless steel and hafnium) in two plasma carrier gases (oxygen and air).

4) **Demonstration that metals introduced through erosion of high-voltage pin electrodes do not have a significant catalytic effect on the formation and lifetime of RONS in plasma-treated water.** Comparison of different metal electrodes (copper, stainless steel and hafnium) shows no significant statistical difference on the formation and lifetime of hydrogen peroxide, nitrite and nitrate.

5) **Demonstration that oxygen plasma treatment yields better results than air plasma treatment for DTZ removal.** Results show that oxygen achieves more effective removal.

6) **Identification of TPs of DTZ treated by oxygen plasma.** Among the identified TPs, 5 are novel and 6 had been previously reported in literature (formed using other plasma carrier gases or other treatment methods).

7) **Investigation of the residual toxicity associated to TPs of plasma-treated DTZ.** Results show that TPs formed by oxygen plasma treatment of DTZ have no associated acute toxicity on *Aliivibrio fischeri*.

7.3   Recommendations for future work

Based on the insights gained from work performed and conclusions drawn in this PhD thesis, as well as the available literature, the following recommendations might be of interest for further investigation of removal of aqueous organic pollutants by plasma-based treatment:

1) This work proves the successful removal of aqueous organic pollutants in a nanosecond-pulsed pin-to-liquid discharge configuration. The fundamental concepts learned from this work could be applied for designing a larger and more energy-efficient pin-to-liquid discharge reactor. In future reactor design, the plasma–liquid contact area could be increased by treating a thinner liquid layer and operating several pin electrodes in parallel. It would also be interesting to compare the removal of MB and DTZ by repetitively pulsed nanosecond discharges to the removal obtained with AC or DC-powered discharges (at same power).

2) Although the removal of a particularly recalcitrant aqueous organic pollutant, the ICM DTZ, foresees that other recalcitrant aqueous organic pollutants could also be successfully removed, this hypothesis would need to be confirmed with further experiments. It would also be interesting to study the treatment of real wastewater samples containing a mixture of pollutants (e.g. hospital wastewaters containing ICM and other pharmaceuticals).

3) Erosion of gas-side, high-voltage electrodes was reported in the present work. Further investigation is required to understand the physicochemical erosion processes occurring at the electrode surface, as well as the shape, size distribution and composition of metal particles formed by this erosion. Furthermore, the presence of metal-based ions and nanoparticles in plasma-treated liquids could be exploited for applications such as plasma-medicine (e.g. copper or silver electrodes could add useful properties to plasma-treated liquids).

4) Studying the toxicity of plasma-treated water revealed that, despite quenching of reactive plasma-chemical species, a residual toxicity remains. Although there is the suspicion that metals introduced by electrode erosion (in this case of stainless steel) may contribute to this residual toxicity, this hypothesis would need to be confirmed with further experiments. For water purification applications, it would be desirable to explore configurations that

completely avoid the introduction of eroded metals into plasma-treated liquids (e.g. with a ceramic coating on high-voltage electrodes).

5) The phenomena occurring when gas is bubbled into the pin-to-liquid reactor were not fully understood. Experimental work revealed that using a sparger that released one bubble at a time (whether the sparger contained a single hole, or it was a multi-holed sparger in which most pores were blocked through contamination) led to significantly higher degradation of aqueous organic pollutants than when multiple, smaller bubbles were introduced. Future work on gas bubbling could provide insights into reaction-mass transport processes.

6) The developed image analysis tool, which tracks the degradation and transport of the MB dye, could provide a simple and quick way of gaining fundamental knowledge on the reaction-mass transport processes in future plasma–liquid reactor configurations (provided that the reactor walls are transparent and enable taking pictures).

References

Aboubakr, H. A. *et al.* (2015) 'Virucidal effect of cold atmospheric gaseous plasma on feline calicivirus, a surrogate for human norovirus', *Applied and Environmental Microbiology*, 81(11), pp. 3612–3622. doi: 10.1128/AEM.00054-15.

Adamovich, I. *et al.* (2017) 'The 2017 Plasma Roadmap: Low temperature plasma science and technology', *Journal of Physics D: Applied Physics*, 50(32), p. 323001. doi: 10.1088/1361-6463/aa76f5.

Ajo, P. *et al.* (2018) 'Hospital wastewater treatment with pilot-scale pulsed corona discharge for removal of pharmaceutical residues', *Journal of Environmental Chemical Engineering*. Elsevier, 6(2), pp. 1569–1577. doi: 10.1016/j.jece.2018.02.007.

Akiyama, H. *et al.* (2007) 'Industrial applications of pulsed power technology', *IEEE Transactions on Dielectrics and Electrical Insulation*, 14(5), pp. 1051–1064. doi: 10.1109/TDEI.2007.4339465.

Anim, A. K. *et al.* (2020) 'Pharmaceuticals, personal care products, food additive and pesticides in surface waters from three Australian east coast estuaries (Sydney, Yarra and Brisbane)', *Marine Pollution Bulletin*. Elsevier, 153(February), p. 111014. doi: 10.1016/j.marpolbul.2020.111014.

Armstronga, D. A. *et al.* (2013) 'Standard electrode potentials involving radicals in aqueous solution: Inorganic radicals', *BioInorganic Reaction Mechanisms*, 9(1–4), pp. 59–61. doi: 10.1515/irm-2013-0005.

Arslan-Alaton, I. *et al.* (2017) 'Removal of iopamidol, an iodinated X-ray contrast medium, by zero-valent aluminum-activated H_2O_2 and $S_2O_8^{2-}$', *Chemical Engineering Journal*. Elsevier B.V., 318, pp. 64–75. doi: 10.1016/j.cej.2016.05.021.

Azerrad, S. P. *et al.* (2014) 'Advanced oxidation of iodinated X-ray contrast media in reverse osmosis brines : The influence of quenching', *Water Research*. Elsevier Ltd, 62, pp. 107–116. doi: 10.1016/j.watres.2014.05.041.

Azerrad, S. P. *et al.* (2016) 'Identification of transformation products during advanced oxidation of diatrizoate : Effect of water matrix and oxidation process', *Water Research*, 103, pp. 424–434. doi: 10.1016/j.watres.2016.07.066.

Azerrad, S. P., Isaacs, M. and Dosoretz, C. G. (2019) 'Integrated treatment of reverse osmosis brines coupling electrocoagulation with advanced oxidation processes', *Chemical Engineering Journal*. Elsevier, 356, pp. 771–780. doi: 10.1016/j.cej.2018.09.068.

Azuma, T. *et al.* (2019) 'Environmental fate of pharmaceutical compounds and antimicrobial-resistant bacteria in hospital effluents, and contributions to pollutant loads in the surface waters in Japan', *Science of the Total Environment*. Elsevier B.V., 657, pp. 476–484. doi: 10.1016/j.scitotenv.2018.11.433.

Banaschik, R. *et al.* (2015) 'Potential of pulsed corona discharges generated in water for the degradation of persistent pharmaceutical residues', *Water Research*. Elsevier Ltd, 84, pp. 127–135. doi: 10.1016/j.watres.2015.07.018.

Barbosa, M. O. *et al.* (2015) 'Pollutants from the EU Watch List : a review of their occurrence and water-treatment options', *European commission -Science for environment Policy*, (August 2013). doi: 10.1016/j.watres.2016.02.047.Contact.

Baroch, P., Saito, N. and Takai, O. (2008) 'Special type of plasma dielectric barrier discharge reactor for direct ozonization of water and degradation of organic pollution', *Journal of Physics D: Applied Physics*, 41(8). doi: 10.1088/0022-3727/41/8/085207.

Belosheev, V. P. (1998) 'Leader discharge over a water surface in a Lichtenberg figure geometry', *Technical Physics*, 43(11), pp. 1329–1332. doi: 10.1134/1.1259193.

Benetoli, L. L. O. de B. *et al.* (2011) 'Effect of temperature on methylene blue decolorization in aqueous medium in electrical discharge plasma reactor', *Journal of the Brazilian Chemical Society*, 22(9), pp. 1669–1678. doi: 10.1590/S0103-50532011000900008.

Besser, B. J. M. and Leib, K. J. (2007) 'Toxicity of Metals in Water and Sediment to Aquatic Biota', in U.S. Department of the Interior (ed.) *Environmental Effects of Historical Mining, Animas River Watershed, Colorado*. Available at: http://pubs.usgs.gov/pp/1651/downloads/Vol2_combinedChapters/vol2_chapE19.pdf.

Birch, G. F. *et al.* (2015) 'Emerging contaminants (pharmaceuticals, personal care products, a food additive and pesticides) in waters of Sydney estuary, Australia', *Marine Pollution Bulletin*. Elsevier Ltd, 97(1–2), pp. 56–66. doi: 10.1016/j.marpolbul.2015.06.038.

Blokhin, V. I. . *et al.* (1999) 'Systems with Different Electrode Materials for Treatment of Water by a Pulsed Electric Discharge', *High Temperature*, 37(6), pp. 998–999.

Boehm, D. *et al.* (2016) 'Cytotoxic and mutagenic potential of solutions exposed to cold atmospheric plasma', *Scientific Reports*, 6(1), p. 21464. doi: 10.1038/srep21464.

Böhm, I. (2018) 'Iodinated X-ray contrast media in aquatic environment in general and in drinking water in particular: A possible source for the primary sensitization of patients', *Chemosphere*, 194, pp. 28–29. doi: 10.1016/j.chemosphere.2017.11.154.

Boleda, M. R., Galceran, M. T. and Ventura, F. (2011) 'Behavior of pharmaceuticals and drugs of abuse in a drinking water treatment plant (DWTP) using combined conventional and ultrafiltration and reverse osmosis (UF/RO) treatments', *Environmental Pollution*. Elsevier Ltd, 159(6), pp. 1584–1591. doi: 10.1016/j.envpol.2011.02.051.

Boulay, A. M. *et al.* (2011) 'Categorizing water for LCA inventory', *International Journal of Life Cycle Assessment*, 16(7), pp. 639–651. doi: 10.1007/s11367-011-0300-z.

Bradu, C. *et al.* (2020) 'Reactive nitrogen species in plasma-activated water: generation, chemistry and application in agriculture', *J. Phys. D: Appl. Phys*, 53, p. 223001. doi: 10.1088/1361-6463/ab795a.

Bruggeman *et al.* (2008) 'Dc excited glow discharges in atmospheric pressure air in pin-to-water electrode systems', *Journal of Physics D: Applied Physics*, 41(21), p. 215201. doi: 10.1088/0022-3727/41/21/215201.

Bruggeman, P. *et al.* (2007) 'Water surface deformation in strong electrical fields and its influence on electrical breakdown in a metal pin-water electrode system', *Journal of Physics D: Applied Physics*, 40(16), pp. 4779–4786. doi: 10.1088/0022-3727/40/16/007.

Bruggeman, P. *et al.* (2008) 'Dc electrical breakdown between a metal electrode and a water surface', *GD 2008 - 17th International Conference on Gas Discharges and Their Applications*, 36(4), pp. 321–324.

Bruggeman, P. J. *et al.* (2016) 'Plasma–liquid interactions: a review and roadmap', *Plasma Sources Science and Technology*, 25(5), p. 053002. doi: 10.1088/0963-0252/25/5/053002.

Burlica, R., Kirkpatrick, M. J. and Locke, B. R. (2006) 'Formation of reactive species in gliding arc discharges with liquid water', *Journal of Electrostatics*, 64(1), pp. 35–43. doi: 10.1016/j.elstat.2004.12.007.

Burlica, R. and Locke, B. R. (2008) 'Pulsed plasma gliding-arc discharges with water spray', *IEEE Transactions on Industry Applications*, 44(2), pp. 482–489. doi: 10.1109/TIA.2008.916603.

Cao, Y. *et al.* (2018) 'Review on reactive species in water treatment using electrical discharge plasma : formation , measurement , mechanisms and mass transfer', *Plasma Sci. Technol.* IOP Publishing, 20, p. 103001. doi: 10.1088/2058-6272/aacff4.

Chen, Q., Li, J. and Li, Y. (2015) 'A review of plasma-liquid interactions for nanomaterial synthesis', *Journal of Physics D: Applied Physics*. IOP Publishing, 48, p. 424005. doi: 10.1088/0022-3727/48/42/424005.

Corella Puertas, E. *et al.* (2017) 'Methylene blue degradation by a nanosecond pulsed pin-to-liquid discharge', in *ISCP23 conference*. Montreal.

Corella Puertas, E., Dzafic, A. and Coulombe, S. (2020) 'Investigation of the Electrode Erosion in Pin-to-Liquid Discharges and Its Influence on Reactive Oxygen and Nitrogen Species in Plasma-Activated Water', *Plasma Chemistry and Plasma Processing*. Springer US, 40, pp. 145–167. doi: 10.1007/s11090-019-10036-3.

Dai, F. *et al.* (2016) 'Experimental and density functional theoretical study of the effects of Fenton's reaction on the degradation of Bisphenol A in a high voltage plasma reactor', *Journal of Hazardous Materials*. Elsevier B.V., 308, pp. 419–429. doi: 10.1016/j.jhazmat.2016.01.068.

Dang, T. H. *et al.* (2009) 'Pulsed electrical discharges in water for removal of organic pollutants: a comparative study', *The European Physical Journal Applied Physics*, 47(2), p. 22818. doi: 10.1051/epjap/2009110.

Diaz Gomez Maqueo, P. (2019) *Non-thermal plasma discharges for methane reforming*. McGill University.

Dobrin, D. *et al.* (2013) 'Degradation of diclofenac in water using a pulsed corona discharge', *Chemical Engineering Journal*. Elsevier B.V., 234, pp. 389–396. doi: 10.1016/j.cej.2013.08.114.

Duirk, S. E. *et al.* (2011) 'Formation of toxic iodinated disinfection by-products from compounds used in medical imaging', *Environmental Science and Technology*, 45(16), pp. 6845–6854. doi: 10.1021/es200983f.

Dzimitrowicz, A. *et al.* (2020) 'Application of Oil-in-Water Nanoemulsion Carrying Size-Defined Gold Nanoparticles Synthesized by Non-thermal Plasma for the Human Breast Cancer Cell Lines Migration and Apoptosis', *Plasma Chemistry and Plasma Processing*. Springer US. doi: 10.1007/s11090-020-10070-6.

Echeverría, S. *et al.* (2013) 'Determination of iodinated X-ray contrast media in sewage by solid-phase extraction and liquid chromatography tandem mass spectrometry', *Talanta*. Elsevier, 116, pp. 931–936. doi: 10.1016/j.talanta.2013.07.080.

Efremov, N. M. *et al.* (2000) 'Experimental investigation of the action of pulsed electrical discharges in liquids on biological objects', *IEEE Transactions on Plasma Science*, 28(1), pp. 224–229. doi: 10.1109/27.842908.

Eliasson, B., Hirth, M. and Kogelschatz, U. (1987) 'Ozone synthesis from oxygen in dielectric barrier discharges', *Journal of Physics D: Applied Physics*, 20(11), pp. 1421–1437. doi: 10.1088/0022-3727/20/11/010.

Evans, M. D. G. *et al.* (2016) 'A 40 kV magnetic pulse compressor for diffuse plasma generation at atmospheric pressure and above', *IEEE Trans. Plasma Sci. (to be submitted).*

Evans, M. D. G. *et al.* (2017) 'Compact Nanosecond Magnetic Pulse Compression Generator for High-Pressure Diffuse Plasma Generation Mathew', *IEEE Transactions on Plasma Science*. IEEE, 45(8), pp. 2358–2365.

Evans, M. D. G. (2017) *Pulsed plasma generator development and low-temperature plasma-assisted combustion at atmospheric pressure*. McGill University.

Evans, M. D. G., Bergthorson, J. M. and Coulombe, S. (2016) 'High-Voltage, High-Frequency Pulse Generator for Nonequilibrium Plasma Generation and Combustion Enhancement', *IEEE Transactions on Plasma Science*, PP(99), pp. 2429–2437. doi: 10.1109/TPS.2016.2606484.

Foster, J. *et al.* (2012) 'Perspectives on the Interaction of Plasmas With Liquid Water for Water Purification', *IEEE Transactions on Plasma Science*, 40(5), pp. 1311–1323.

Foster, J. E. (2017) 'Plasma-based water purification: Challenges and prospects for the future', *Physics of Plasmas*, 24(5), pp. 0–16. doi: 10.1063/1.4977921.

Foster, J. E. and Lai, J. (2016) '2-D Bubble Test Cell for the Study of Interactions at the Plasma-Liquid Interface', *IEEE Transactions on Plasma Science*, 44(7), pp. 1127–1136. doi: 10.1109/TPS.2016.2567322.

Foster, J. E., Mujovic, S. and Groele, J. (2018) 'Towards high throughput plasma based water purifiers: design considerations and the pathway towards practical application', *Journal of Physics D: Applied Physics*. IOP Publishing, 51, p. 293001. doi: 10.1088/1361-6463/aac816.

Fridman, A., Gutsol, A. and Cho, Y. I. (2007) 'Non-thermal atmospheric pressure plasma', *Advances in Heat Transfer*, 40(C), pp. 1–142. doi: 10.1016/S0065-2717(07)40001-6.

Giannakis, S. *et al.* (2017) 'Iohexol degradation in wastewater and urine by UV-based Advanced Oxidation Processes (AOPs): Process modeling and by-products identification', *Journal of Environmental Management*. Elsevier Ltd, 195, pp. 174–185. doi: 10.1016/j.jenvman.2016.07.004.

Glory, A. *et al.* (2020) 'Comparison of the Cytotoxicity of O2-based and Air-based Plasma-treated PBS on Sarcoma Cells', in *IPCM8*. Incheon, Korea.

Gomes, J. *et al.* (2017) 'Application of ozonation for pharmaceuticals and personal care products removal from water', *Science of the Total Environment*. Elsevier B.V., 586, pp. 265–283. doi: 10.1016/j.scitotenv.2017.01.216.

Gopalakrishnan, R. *et al.* (2016) 'Solvated electrons at the atmospheric pressure plasma-water anodic interface', *Journal of Physics D: Applied Physics*. IOP Publishing, 49(29). doi: 10.1088/0022-3727/49/29/295205.

Goryachev, V. L., Ufimtsev, A. A. and Khodakovskii, A. M. (1997) 'Mechanism of electrode erosion in pulsed discharges in water with a pulse energy of ~ 1 J', *Technical Physics Letters*, 23(5), pp. 386–387. doi: 10.1134/1.1261862.

Government of Canada (2014) *Overview of the Chemicals Management Plan*. Available at: https://www.canada.ca/en/health-canada/services/chemical-substances/fact-sheets/overview-chemicals-management-plan.html.

Grabowski, L. R., Van Veldhuizen, E. M. and Rutgers, W. R. (2005) 'Removal of phenol from water: a comparison of energization methods', *Journal of Advanced Oxidation Technologies*, 8(2), pp. 142–149. doi: 10.1515/jaots-2005-0204.

Gracia-Lor, E. *et al.* (2012) 'Occurrence and removal of pharmaceuticals in wastewater treatment plants at the Spanish Mediterranean area of Valencia', *Chemosphere*. Elsevier Ltd, 87(5), pp. 453–462. doi: 10.1016/j.chemosphere.2011.12.025.

Gur-Reznik, S. *et al.* (2011) 'Iodinated contrast media oxidation by nonthermal plasma : The role of iodine as a tracer', *Water Research*. Elsevier Ltd, 45, pp. 5047–5057. doi: 10.1016/j.watres.2011.07.003.

Haiß, A. and Kümmerer, K. (2006) 'Biodegradability of the X-ray contrast compound diatrizoic acid, identification of aerobic degradation products and effects against sewage sludge micro-organisms', *Chemosphere*, 62(2), pp. 294–302. doi: 10.1016/j.chemosphere.2005.05.007.

Hansen, K. M. S. *et al.* (2016) 'Ozonation for source treatment of pharmaceuticals in hospital wastewater - Ozone lifetime and required ozone dose', *Chemical Engineering Journal*. Elsevier B.V., 290, pp. 507–514. doi: 10.1016/j.cej.2016.01.027.

Harding, L. B. *et al.* (2016) 'Wastewater treatment plant effluent alters pituitary gland gonadotropin mRNA levels in juvenile coho salmon (Oncorhynchus kisutch)', *Aquatic Toxicology*. Elsevier B.V., 178, pp. 118–131. doi: 10.1016/j.aquatox.2016.07.013.

Hartwig, P., Mützel, W. and Taenzer, V. (1989) 'Pharmacokinetics of iohexol, iopamidol, iopromide, and iosimide compared with meglumine diatrizoate', *Fortschritte auf dem Gebiete der Rontgenstrahlen und der Nuklearmedizin. Erganzungsban*, 128, pp. 220–223.

Hauschild, M. Z., Rosenbaum, R. K. and Olsen, S. I. (2017) *Life Cycle Assessment: Theory and Practice*, *Life Cycle Assessment: Theory and Practice*. doi: 10.1007/978-3-319-56475-3.

He, H. *et al.* (2020) 'Highly efficient degradation of iohexol on a heterostructured graphene-analogue boron nitride coupled Bi2MoO6 photocatalyst under simulated sunlight', *Science of the*

Total Environment, 730, pp. 1–11. doi: 10.1016/j.scitotenv.2020.139100.

Heberer, T. (2002) 'Tracking persistent pharmaceutical residues from municipal sewage to drinking water', *Journal of Hydrology*, 266(3–4), pp. 175–189. doi: 10.1016/S0022-1694(02)00165-8.

Hijosa-Valsero, M. *et al.* (2013) 'Removal of priority pollutants from water by means of dielectric barrier discharge atmospheric plasma', *Journal of Hazardous Materials*, 262, pp. 664–673. doi: 10.1016/j.jhazmat.2013.09.022.

Hoeben, W. F. L. M. *et al.* (2019) 'On the Possibilities of Straightforward Characterization of Plasma Activated Water', *Plasma Chemistry and Plasma Processing*. Springer US, 39(3), pp. 597–626. doi: 10.1007/s11090-019-09976-7.

Holzer, F. and Locke, B. R. (2008) 'Influence of high voltage needle electrode material on hydrogen peroxide formation and electrode erosion in a hybrid gas-liquid series electrical discharge reactor', *Plasma Chemistry and Plasma Processing*, 28(1), pp. 1–13. doi: 10.1007/s11090-007-9107-x.

Hong, Y. *et al.* (2019) 'Mass-balance-model-based evaluation of sewage treatment plant contribution to residual pharmaceuticals in environmental waters', *Chemosphere*. Elsevier Ltd, 225, pp. 378–387. doi: 10.1016/j.chemosphere.2019.03.046.

Hu, J. *et al.* (2019) 'Degradation of iodinated disinfection byproducts by VUV/UV process based on a mini-fluidic VUV/UV photoreaction system', *Water Research*. Elsevier Ltd, 158, pp. 417–423. doi: 10.1016/j.watres.2019.03.056.

Hu, X. *et al.* (2014) 'Plasma-induced synthesis of CuO nanofibers and ZnO nanoflowers in water', *Plasma Chemistry and Plasma Processing*, 34(5), pp. 1129–1139. doi: 10.1007/s11090-014-9546-0.

Hu, X., Takai, O. and Saito, N. (2013) 'Simple synthesis of platinum nanoparticles by plasma sputtering in water', *Japanese Journal of Applied Physics*, 52(1 PART2). doi: 10.7567/JJAP.52.01AN05.

Huber, M. M. *et al.* (2003) 'Oxidation of pharmaceuticals during ozonation and advanced oxidation processes', *Environmental Science and Technology*, 37(5), pp. 1016–1024. doi:

10.1021/es025896h.

Huber, M. M. *et al.* (2005) 'Oxidation of pharmaceuticals during ozonation of municipal wastewater effluents: A pilot study', *Environmental Science and Technology*, 39(11), pp. 4290–4299. doi: 10.1021/es048396s.

Ignatiev, A. N., Pryakhin, A. N. and Lunin, V. V. (2008) 'Numerical simulation of the kinetics of ozone decomposition in an aqueous solution', *Russian Chemical Bulletin*, 57(6), pp. 1172–1178. doi: 10.1007/s11172-008-0146-0.

Jeng, H. A. and Swanson, J. (2006) 'Toxicity of metal oxide nanoparticles in mammalian cells', *Journal of Environmental Science and Health - Part A Toxic/Hazardous Substances and Environmental Engineering*, 41(12), pp. 2699–2711. doi: 10.1080/10934520600966177.

Jeong, C. H. *et al.* (2017) 'The impact of iodinated X-ray contrast agents on formation and toxicity of disinfection by-products in drinking water', *Journal of Environmental Sciences*. Elsevier B.V., 58, pp. 173–182. doi: 10.1016/j.jes.2017.03.032.

Jeong, J. *et al.* (2010) 'Degradation mechanisms and kinetic studies for the treatment of X-ray contrast media compounds by advanced oxidation / reduction processes', *Water Research*. Elsevier Ltd, 44(15), pp. 4391–4398. doi: 10.1016/j.watres.2010.05.054.

Jiang, B. *et al.* (2014) 'Review on electrical discharge plasma technology for wastewater remediation', *Chemical Engineering Journal*, 236, pp. 348–368. doi: 10.1016/j.cej.2013.09.090.

Kalsch, W. (1999) 'Biodegradation of the iodinated X-ray contrast media diatrizoate and iopromide', *The Science of the Total Environment*, 225, pp. 143–153.

Karlsson, H. L. *et al.* (2008) 'Copper oxide nanoparticles are highly toxic: A comparison between metal oxide nanoparticles and carbon nanotubes', *Chemical Research in Toxicology*, 21(9), pp. 1726–1732. doi: 10.1021/tx800064j.

Karlsson, R. and Tortensson, L.-G. (1974) 'Controlled-potential iodometric titration of nitrite. Application to the determination of nitrite in meat products', *Talanta*, 21(9), pp. 945–950. Available at: https://doi.org/10.1016/0039-9140(74)80047-0.

Keerthanan, S. *et al.* (2020) 'Pharmaceutical and Personal Care Products (PPCPs) in the

environment: Plant uptake, translocation, bioaccumulation, and human health risks', *Critical Reviews in Environmental Science and Technology*. Taylor & Francis, 0(0), pp. 1–38. doi: 10.1080/10643389.2020.1753634.

Khadre, M. A., Yousef, A. E. and Kim, J. G. (2001) 'Microbiological aspects of ozone applications in food: A review', *Journal of Food Science*, 66(9), pp. 1242–1252. doi: 10.1111/j.1365-2621.2001.tb15196.x.

Kidd, K. A. *et al.* (2007) 'Collapse of a fish population after exposure to a synthetic estrogen', *Proceedings of the National Academy of Sciences of the United States of America*, 104(21), pp. 8897–8901. doi: 10.1073/pnas.0609568104.

Kim, Hee-jun, Won, C. and Kim, Hyun-woo (2018) 'Pathogen Deactivation of Glow Discharge Cold Plasma While Treating Organic and Inorganic Pollutants of Slaughterhouse Wastewater', *Water Air Soil Pollut*. Water, Air, & Soil Pollution, 229(237). doi: https://doi.org/10.1007/s11270-018-3895-x Pathogen.

Kim, K. S., Kam, S. K. and Mok, Y. S. (2015) 'Elucidation of the degradation pathways of sulfonamide antibiotics in a dielectric barrier discharge plasma system', *Chemical Engineering Journal*. Elsevier B.V., 271, pp. 31–42. doi: 10.1016/j.cej.2015.02.073.

Kingzett, C. T. (1880) 'Report on the atmospheric oxidation of phosphorus and some reactions of ozone and hydric peroxide', *Journal of the Chemical Society, Transactions*, 37, pp. 792–807. doi: 10.1039/CT8803700792.

Kirkpatrick, M. J. and Locke, B. R. (2006) 'Effects of Platinum Electrode on Hydrogen, Oxygen, and Hydrogen Peroxide Formation in Aqueous Phase Pulsed Corona Electrical Discharge', *Industrial & Engineering Chemistry Research*, 45, pp. 2138–2142. doi: 10.1021/ie0511480.

Klatte, S., Schaefer, H. C. and Hempel, M. (2017) 'Pharmaceuticals in the environment – A short review on options to minimize the exposure of humans, animals and ecosystems', *Sustainable Chemistry and Pharmacy*, 5, pp. 61–66. doi: 10.1016/j.scp.2016.07.001.

Kleywegt, S. *et al.* (2016) 'The contribution of pharmaceutically active compounds from healthcare facilities to a receiving sewage treatment plant in Canada', *Environmental Toxicology and Chemistry*, 35(4), pp. 850–862. doi: 10.1002/etc.3124.

Kogelschatz, U. (2003) 'Dielectric-barrier discharges: Their History, Discharge Physics, and Industrial Applications', *Plasma Chemistry and Plasma Processing*, 23(1), pp. 1–46. doi: 10.1023/A:1022470901385.

Kogelschatz, U. (2017) 'Ozone and beyond: the marvelous development of dielectric barrier discharges', *Journal of Physics D: Applied Physics*. IOP Publishing, 50(5), p. 051001. doi: 10.1088/1361-6463/50/5/051001.

Kolikov, V. a. *et al.* (2007) 'Prolonged microbial resistance of water treated by a pulsed electrical discharge', *Technical Physics*, 52(2), pp. 263–270. doi: 10.1134/S1063784207020193.

Kolikov, V. A. *et al.* (2005) 'Pulse Electric Discharges and Prolonged Microbial Resistance of Water', *Dokl Biol Sci*, 403, pp. 279–281.

Kolosov, P. (2018) *Catalytic Ozonation for the Removal of Contaminants of Emerging Concern and Disinfection of Wastewater*. McGill University.

Kolthoff, J. M. (1921) 'Jodometrische Studien', *Zeitschrift für analytische Chemie*, 60, pp. 338–353.

Kornev, I. and Preis, S. (2016) 'Aqueous Benzene Oxidation in Low-Temperature Plasma of Pulsed Corona Discharge', *J. Adv. Oxid. Technol.*, 19(2), pp. 284–289. doi: https://doi.org/10.1515/jaots-2016-0212.

Korshin, G. and Yan, M. (2018) 'Electrochemical dehalogenation of disinfection by-products and iodine-containing contrast media: A review', *Environmental Engineering Research*, 23(4), pp. 345–353. doi: 10.4491/eer.2018.054.

Kovačević, V. V *et al.* (2017) 'Measurement of reactive species generated by dielectric barrier discharge in direct contact with water in different atmospheres', *Journal of Physics D: Applied Physics*, 50, p. 19pp. doi: https://doi.org/10.1088/1361-6463/aa5fde.

Kovalova, L. *et al.* (2013) 'Elimination of micropollutants during post-treatment of hospital wastewater with powdered activated carbon, ozone, and UV', *Environmental Science and Technology*, 47(14), pp. 7899–7908. doi: 10.1021/es400708w.

Kozakova, Z. *et al.* (2018) 'Comparison of liquid and liquid-gas phase plasma reactors for

discoloration of azo dyes: Analysis of degradation products', *Plasma Processes and Polymers*, p. e1700178. doi: https://doi.org/10.1002/ppap.201700178.

Krause, H. *et al.* (2009) 'Degradation of the endocrine disrupting chemicals (EDCs) carbamazepine, clofibric acid, and iopromide by corona discharge over water', *Chemosphere*. Elsevier Ltd, 75(2), pp. 163–168. doi: 10.1016/j.chemosphere.2008.12.020.

Krause, H. *et al.* (2010) 'Reply to discussion by Reinhard Länge et al. on "Degradation of the endocrine disrupting chemicals (EDCs) carbamazepine, clofibric acid, and iopromide by corona discharge over water" by Krause et al. [Chemosphere 75(2) (2009) 163-168]', *Chemosphere*. Elsevier Ltd, 78, pp. 633–634. doi: 10.1016/j.chemosphere.2009.10.052.

Krause, H. *et al.* (2011) 'Degradation of persistent pharmaceuticals in aqueous solutions by a positive dielectric barrier discharge treatment', *Journal of Electrostatics*. Elsevier Ltd, 69(4), pp. 333–338. doi: 10.1016/j.elstat.2011.04.011.

Kümmerer, K. (2009) 'Antibiotics in the aquatic environment - A review - Part II', *Chemosphere*. Elsevier Ltd, 75(4), pp. 435–441. doi: 10.1016/j.chemosphere.2008.12.006.

Länge, R. *et al.* (2010) 'Discussion by Reinhard Länge et al. on "Degradation of the endocrine disrupting chemicals (EDCs) carbamazepine, clofibric acid, and iopromide by corona discharge over water" by Krause et al. [Chemosphere 75(2) (2009) 163-168]', *Chemosphere*. Elsevier Ltd, 78, pp. 631–632. doi: 10.1016/j.chemosphere.2009.10.052.

Laroussi, M. and Leipold, F. (2004) 'Evaluation of the roles of reactive species, heat, and UV radiation in the inactivation of bacterial cells by air plasmas at atmospheric pressure', *International Journal of Mass Spectrometry*, 233(1–3), pp. 81–86. doi: 10.1016/j.ijms.2003.11.016.

Laurita, R. *et al.* (2015) 'Chemical analysis of reactive species and antimicrobial activity of water treated by nanosecond pulsed DBD air plasma', *Clinical Plasma Medicine*. Elsevier, 3(2), pp. 53–61. doi: 10.1016/j.cpme.2015.10.001.

Lee, D. *et al.* (2018) 'Degradation of sulfonamide antibiotics and their intermediates toxicity in an aeration-assisted non-thermal plasma while treating strong wastewater', *Chemosphere*. Elsevier Ltd, 209, pp. 901–907. doi: 10.1016/j.chemosphere.2018.06.125.

Lew, R. B. (1975) 'Interference of Nitrite in the iodometric Determination of Sulfite', *Journal American Society of Sugar Beet Technologists*.

Lieberman, M. A. and Lichtenberg, A. J. (2005) *Principles of Plasma Discharges and Materials Processing: Second Edition*, *Principles of Plasma Discharges and Materials Processing: Second Edition*. doi: 10.1002/0471724254.

Liu, Y. *et al.* (2013) 'Removal of iopromide from an aqueous solution using dielectric barrier discharge', *Journal of Chemical Technology and Biotechnology*, 88, pp. 468–473. doi: 10.1002/jctb.3851.

Liu, Y. *et al.* (2016) 'Comparison and Evaluation of Electrode Erosion under High-Pulsed Current Discharges in Air and Water Mediums', *IEEE Transactions on Plasma Science*, 44(7), pp. 1169–1177. doi: 10.1109/TPS.2016.2578343.

Liu, Z. C. *et al.* (2018) 'Post-discharge evolution of reactive species in the water activated by a surface air plasma: A modeling study', *Journal of Physics D: Applied Physics*. IOP Publishing, 51(17). doi: 10.1088/1361-6463/aab635.

Lo, C. H., Tsung, T. T. and Chen, L. C. (2005) 'Shape-controlled synthesis of Cu-based nanofluid using submerged arc nanoparticle synthesis system (SANSS)', *Journal of Crystal Growth*, 277(1–4), pp. 636–642. doi: 10.1016/j.jcrysgro.2005.01.067.

Locke, B. R. *et al.* (2006) 'Electrohydraulic discharge and nonthermal plasma for water treatment', *Industrial and Engineering Chemistry Research*, 45(3), pp. 882–905. doi: 10.1021/ie050981u.

Locke, B. R. (2012) 'Environmental Applications of Electrical Discharge Plasma with Liquid Water -- A Mini Review --', *International Journal of Plasma Environmental Science & Technology*, 6(3), pp. 194–203.

Locke, B. R. and Lukeš, P. (2018) 'Special issue: Plasma and Liquids', *Plasma Processes and Polymers*, 15(6), p. 1815062. doi: 10.1002/ppap.201815062.

Locke, B. R., Lukeš, P. and Brisset, J.-L. (2012) 'Elementary Chemical and Physical Phenomena in Electrical Discharge Plasma in Gas – Liquid Environments and in Liquids', in Parvulescu, V. I., Magureanu, M., and Lukes, P. (eds) *Plasma Chemistry and Catalysis in Gases and Liquids*.

1st edn. Wiley-VCH Verlag GmbH & Co. KGaA, pp. 183–242.

Locke, B. R. and Shih, K.-Y. (2011) 'Review of the methods to form hydrogen peroxide in electrical discharge plasma with liquid water', *Plasma Sources Science and Technology*, 20(3), p. 034006. doi: 10.1088/0963-0252/20/3/034006.

Lopez-Prieto, I. J. *et al.* (2020) 'A direct injection liquid chromatography tandem mass spectrometry method for the kinetic study on iodinated contrast media (ICMs) removal in natural water', *Chemosphere*. Elsevier Ltd, 243, p. 125311. doi: 10.1016/j.chemosphere.2019.125311.

Lu, X. and Laroussi, M. (2005) 'Optimization of ultraviolet emission and chemical species generation from a pulsed dielectric barrier discharge at atmospheric pressure', *Journal of Applied Physics*, 98(2), pp. 1–6. doi: 10.1063/1.1980530.

Lukes, P. *et al.* (2005) 'Generation of ozone by pulsed corona discharge over water surface in hybrid gas-liquid electrical discharge reactor', *Journal of Physics D: Applied Physics*, 38(3), pp. 409–416. doi: 10.1088/0022-3727/38/3/010.

Lukes, P. *et al.* (2011) 'The catalytic role of tungsten electrode material in the plasmachemical activity of a pulsed corona discharge in water', *Plasma Sources Science and Technology*, 20(3), p. 034011. doi: 10.1088/0963-0252/20/3/034011.

Lukes, P. *et al.* (2014) 'Aqueous-phase chemistry and bactericidal effects from an air discharge plasma in contact with water: evidence for the formation of peroxynitrite through a pseudo-second-order post-discharge reaction of H_2O_2 and HNO_2', *Plasma Sources Science and Technology*, 23(1), p. 015019. doi: 10.1088/0963-0252/23/1/015019.

Lukeš, P. *et al.* (2006) 'Erosion of needle electrodes in pulsed corona discharge in water', *Czech J Phys*, 56, pp. 916–924. doi: 10.1007/s10582-006-0304-2.

Lukes, P., Brisset, J. and Locke, B. (2012) 'Biological Effects of Electrical Discharge Plasma in Water and in Gas–Liquid Environments', in Parvulescu, V. I., Magureanu, M., and Lukes, P. (eds) *Plasma Chemistry and Catalysis in Gases and Liquids*, pp. 309–352.

Lukes, P., Clupek, M. and Babicky, V. (2011) 'Discharge filamentary patterns produced by pulsed corona discharge at the interface between a water surface and air', *IEEE Transactions on Plasma Science*, 39(11 PART 1), pp. 2644–2645. doi: 10.1109/TPS.2011.2158611.

Lukes, P., Locke, B. R. and Brisset, J. L. (2012) 'Aqueous-Phase Chemistry of Electrical Discharge Plasma in Water and in Gas-Liquid Environments', in Parvulescu, V. I., Magureanu, M., and Lukes, P. (eds) *Plasma Chemistry and Catalysis in Gases and Liquids*. 1st edn. Wiley-VCH Verlag GmbH & Co. KGaA, pp. 243–308. doi: 10.1002/9783527649525.ch7.

Lv, X. D. *et al.* (2019) 'Performance of Cu-cathode/Fe3+/peroxymonosulfate process on iohexol degradation', *Journal of Hazardous Materials*. Elsevier, 366(November 2018), pp. 250–258. doi: 10.1016/j.jhazmat.2018.11.091.

Magureanu, M., Bradu, C. and Parvulescu, V. I. (2018) 'Plasma processes for the treatment of water contaminated with harmful organic compounds', *Journal of Physics D: Applied Physics*. IOP Publishing, 51(31). doi: 10.1088/1361-6463/aacd9c.

Magureanu, M., Mandache, N. B. and Parvulescu, V. I. (2015) 'Degradation of pharmaceutical compounds in water by non-thermal plasma treatment', *Water Research*. Elsevier Ltd, 81, pp. 124–136. doi: 10.1016/j.watres.2015.05.037.

Mahyar, A. *et al.* (2019) 'Development and Application of Different Non-thermal Plasma Reactors for the Removal of Perfluorosurfactants in Water: A Comparative Study', *Plasma Chemistry and Plasma Processing*. Springer US, 39(3), pp. 531–544. doi: 10.1007/s11090-019-09977-6.

Majewski, J. (2012) 'Methods for measuring ozone concentration in ozone-treated water', *Prz Elektrotech (Electr Rev)*, (9), pp. 253–255.

Malik, M. A. (2010) 'Water purification by plasmas: Which reactors are most energy efficient?', *Plasma Chemistry and Plasma Processing*, 30(1), pp. 21–31. doi: 10.1007/s11090-009-9202-2.

Mao, Y. *et al.* (2020) 'Accelerated oxidation of iopamidol by ozone/peroxymonosulfate (O3/PMS) process: Kinetics, mechanism, and simultaneous reduction of iodinated disinfection by-product formation potential', *Water Research*. Elsevier Ltd, 173, p. 115615. doi: 10.1016/j.watres.2020.115615.

Maqueo, P. D. G. *et al.* (2018) 'Regimes of an Atmospheric Pressure Nanosecond Repetitive Pulsed Discharge for Methane Partial Oxidation', *Journal of Physics D: Applied Physics*. IOP Publishing, 51(134005), p. 13pp. doi: 10.1088/1361-6463/aab0cb.

Maqueo, P. D. G., Coulombe, S. and Bergthorson, J. M. (2019) 'Energy efficiency of a nanosecond repetitively pulsed discharge for methane reforming', *Journal of Physics D: Applied Physics*. IOP Publishing, 52(27). doi: 10.1088/1361-6463/ab199b.

Mariotti, D. *et al.* (2012) 'Plasma-liquid interactions at atmospheric pressure for nanomaterials synthesis and surface engineering', *Plasma Processes and Polymers*, 9(11–12), pp. 1074–1085. doi: 10.1002/ppap.201200007.

Marshall, M. (2017) *LuminoTox as a tool to monitor contaminants of emerging concern in municipal secondary effluent and their removal during treatment by ozone*. McGill University.

Massarczyk, R. *et al.* (2017) 'Paschen's law studies in cold gases', *Journal of Instrumentation*, 12, p. P06019. doi: 10.1088/1748-0221/12/06/P06019.

Matsushita, T. *et al.* (2015) 'Changes in mutagenicity and acute toxicity of solutions of iodinated X-ray contrast media during chlorination', *Chemosphere*. Elsevier Ltd, 135, pp. 101–107. doi: 10.1016/j.chemosphere.2015.03.082.

Matsushita, T. *et al.* (2016) 'Use of orbitrap-MS/MS and QSAR analyses to estimate mutagenic transformation products of iopamidol generated during ozonation and chlorination', *Chemosphere*. Elsevier Ltd, 148, pp. 233–240. doi: 10.1016/j.chemosphere.2016.01.037.

Mededovic, S. and Locke, B. R. (2007) 'The role of platinum as the high voltage electrode in the enhancement of Fenton's reaction in liquid phase electrical discharge', *Applied Catalysis B: Environmental*, 72(3–4), pp. 342–350. doi: 10.1016/j.apcatb.2006.11.014.

Mededović, S. and Locke, B. R. (2006) 'Platinum catalysed decomposition of hydrogen peroxide in aqueous-phase pulsed corona electrical discharge', *Applied Catalysis B: Environmental*, 67(3–4), pp. 149–159. doi: 10.1016/j.apcatb.2006.05.001.

Mededovic Thagard, S. *et al.* (2017) 'Plasma-based water treatment: development of a general mechanistic model to estimate the treatability of different types of contaminants', *Journal of Physics D: Applied Physics*. IOP Publishing, 50(1), p. 014003. doi: 10.1088/1361-6463/50/1/014003.

Mededovic Thagard, S. *et al.* (2018) 'An Experimental Investigation of the Liquid Flow Induced by a Pulsed Electrical Discharge Plasma', *Plasma Chemistry and Plasma Processing*. Springer

US, 38(4), pp. 719–741. doi: 10.1007/s11090-018-9905-3.

Mendoza, A. *et al.* (2015) 'Pharmaceuticals and iodinated contrast media in a hospital wastewater: A case study to analyse their presence and characterise their environmental risk and hazard', *Environmental Research*. Elsevier, 140, pp. 225–241. doi: 10.1016/j.envres.2015.04.003.

Mendoza, A. *et al.* (2016) 'Drugs of abuse, cytostatic drugs and iodinated contrast media in tap water from the Madrid region (central Spain): A case study to analyse their occurrence and human health risk characterization', *Environment International*. Elsevier Ltd, 86, pp. 107–118. doi: 10.1016/j.envint.2015.11.001.

Miklos, D. B. *et al.* (2018) 'Evaluation of advanced oxidation processes for water and wastewater treatment – A critical review', *Water Research*, 139, pp. 118–131. doi: 10.1016/j.watres.2018.03.042.

Minamitani, Y. and Yamada, T. (2016) 'Investigation of the Influence of Droplets to Streamer Discharge in Water Treatment by Pulsed Discharge in Air Spraying', 44(10), pp. 1–8.

Moisan, M. *et al.* (2001) 'Low-temperature sterilization using gas plasmas: a review of the experiments and an analysis of the inactivation mechanisms', *International Journal of Pharmaceutics*, 226, pp. 1–21. doi: 10.1016/S0378-5173(01)00752-9.

Del Moro, G. *et al.* (2015) 'Iodinated contrast media electro-degradation: Process performance and degradation pathways', *Science of the Total Environment*. Elsevier B.V., 506–507, pp. 631–643. doi: 10.1016/j.scitotenv.2014.10.115.

Moura de Salles Pupo, M. *et al.* (2020) 'Characterization and comparison of Ti/TiO2-NT/SnO2–SbBi, Ti/SnO2–SbBi and BDD anode for the removal of persistent iodinated contrast media (ICM)', *Chemosphere*, 253. doi: 10.1016/j.chemosphere.2020.126701.

Naidu, R., Jit, J., *et al.* (2016) 'Emerging contaminant uncertainties and policy: The chicken or the egg conundrum', *Chemosphere*. Elsevier Ltd, 154, pp. 385–390. doi: 10.1016/j.chemosphere.2016.03.110.

Naidu, R., Arias Espana, V. A., *et al.* (2016) 'Emerging contaminants in the environment: Risk-based analysis for better management', *Chemosphere*. Elsevier Ltd, 154, pp. 350–357. doi:

10.1016/j.chemosphere.2016.03.068.

Naítali, M. *et al.* (2010) 'Combined effects of long-living chemical species during microbial inactivation using atmospheric plasma-treated water', *Applied and Environmental Microbiology*, 76(22), pp. 7662–7664. doi: 10.1128/AEM.01615-10.

Nani, L. *et al.* (2018) 'ROS production and removal of the herbicide metolachlor by air non-thermal plasma produced by DBD, DC- and DC+ discharges implemented within the same reactor', *Journal of Physics D: Applied Physics*. IOP Publishing, (274002), p. 10pp. doi: 10.1088/1361-6463/aab8b9.

National Research Council (1995) 'Plasma Science: From Fundamental Research to Technological Applications'. Washington, D.C.: National Academies Press. doi: 10.17226/4936.

Nemchinsky, V. A. and Severance, W. S. (2006) 'What we know and what we do not know about plasma arc cutting', *Journal of Physics D: Applied Physics*, 39(22). doi: 10.1088/0022-3727/39/22/R01.

Neretti, G. *et al.* (2016) 'Characterization of a dielectric barrier discharge in contact with liquid and producing a plasma activated water', *Plasma Sources Science and Technology*. IOP Publishing, 26(1), p. 015013. doi: 10.1088/1361-6595/26/1/015013.

Nihemaiti, M. *et al.* (2018) 'Removal of trace organic chemicals in wastewater effluent by UV/H2O2 and UV/PDS', *Water Research*, 145, pp. 487–497. doi: 10.1016/j.watres.2018.08.052.

Noguera-Oviedo, K. and Aga, D. S. (2016) 'Lessons learned from more than two decades of research on emerging contaminants in the environment', *Journal of Hazardous Materials*. Elsevier B.V., 316, pp. 242–251. doi: 10.1016/j.jhazmat.2016.04.058.

Norberg, S. A. *et al.* (2014) 'Atmospheric pressure plasma jets interacting with liquid covered tissue: touching and not-touching the liquid', *Journal of Physics D: Applied Physics*, 47(47), p. 475203. doi: 10.1088/0022-3727/47/47/475203.

Nossen, J. *et al.* (1995) 'Elimination of the non-ionic x-ray contrast media iodixanol and iohexol in patients with severely impaired renal function', *Scandinavian Journal of Clinical and Laboratory Investigation*, 55(4), pp. 341–350. doi: 10.3109/00365519509104972.

Nowak, A., Pacek, G. and Mrozik, A. (2020) 'Transformation and ecotoxicological effects of iodinated X-ray contrast media', *Reviews in Environmental Science and Biotechnology*. Springer Netherlands, 19(2), pp. 337–354. doi: 10.1007/s11157-020-09534-0.

Oehmigen, K. *et al.* (2011) 'Estimation of possible mechanisms of escherichia coli inactivation by plasma treated sodium chloride solution', *Plasma Processes and Polymers*, 8(10), pp. 904–913. doi: 10.1002/ppap.201000099.

Oh, J. S. *et al.* (2016) 'How to assess the plasma delivery of RONS into tissue fluid and tissue', *Journal of Physics D: Applied Physics*. IOP Publishing, 49(30), p. 304005. doi: 10.1088/0022-3727/49/30/304005.

Olmez-Hanci, T. *et al.* (2017) 'Enhanced degradation of micropollutants by zero-valent aluminum activated persulfate: Assessment of toxicity and genotoxic activity', *Water Science and Technology*, 76(12), pp. 3195–3204. doi: 10.2166/wst.2017.489.

Panorel, I. *et al.* (2013a) 'Oxidation of Aqueous Paracetamol by Pulsed Corona Discharge', *Ozone: Science and Engineering*, 35(2), pp. 116–124. doi: 10.1080/01919512.2013.760415.

Panorel, I. *et al.* (2013b) 'Oxidation of aqueous pharmaceuticals by pulsed corona discharge', *Environmental Technology*, 34(7), pp. 923–930. doi: 10.1080/09593330.2012.722691.

Park, J. Y. and Lee, Y. N. (1988) 'Solubility and decomposition kinetics of nitrous acid in aqueous solution', *Journal of Physical Chemistry*, 92(22), pp. 6294–6302. doi: 10.1021/j100333a025.

Parkansky, N. *et al.* (2012) 'Submerged arc breakdown of methylene blue in aqueous solutions', *Plasma Chemistry and Plasma Processing*, 32(5), pp. 933–947. doi: 10.1007/s11090-012-9385-9.

Pasternak, J. J. and Williamson, E. E. (2012) 'Clinical pharmacology, uses, and adverse reactions of iodinated contrast agents: A primer for the non-radiologist', *Mayo Clinic Proceedings*. Elsevier Inc., 87(4), pp. 390–402. doi: 10.1016/j.mayocp.2012.01.012.

Pérez, S. and Barceló, D. (2007) 'Fate and occurrence of X-ray contrast media in the environment', *Analytical and Bioanalytical Chemistry*, 387(4), pp. 1235–1246. doi: 10.1007/s00216-006-0953-9.

Pokryvailo, A. *et al.* (2004) 'A high-power pulsed corona source for pollution control applications', *IEEE Transactions on Plasma Science*, 32(5), pp. 2045–2054. doi: 10.1109/TPS.2004.835952.

Pokryvailo, A. *et al.* (2006) 'High-power pulsed corona source for treatment of pollutants in heterogeneous media', *IEEE Transactions on Plasma Science*, 34(5), pp. 1731–1743. doi: 10.1109/PPC.2005.300550.

Polo, A. M. S. *et al.* (2016) 'Oxidation of diatrizoate in aqueous phase by advanced oxidation processes based on solar radiation', *Journal of Photochemistry and Photobiology A: Chemistry*. Elsevier B.V., 319–320, pp. 87–95. doi: 10.1016/j.jphotochem.2015.12.009.

Pootawang, P., Saito, N. and Lee, S. Y. (2013) 'Discharge time dependence of a solution plasma process for colloidal copper nanoparticle synthesis and particle characteristics', *Nanotechnology*, 24(5). doi: 10.1088/0957-4484/24/5/055604.

Porter, D. *et al.* (2009) 'Formation of hydrogen peroxide, hydrogen, and oxygen in gliding arc electrical discharge reactors with water spray', *IEEE Transactions on Industry Applications*. IEEE, 45(2), pp. 623–629. doi: 10.1109/TIA.2009.2013560.

Puač, N., Gherardi, M. and Shiratani, M. (2018) 'Plasma agriculture: A rapidly emerging field', *Plasma Processes and Polymers*, 15(2), pp. 1–5. doi: 10.1002/ppap.201700174.

Putschew, A., Schittko, S. and Jekel, M. (2001) 'Quantification of triiodinated benzene derivatives and X-ray contrast media in water samples by liquid chromatography-electrospray tandem mass spectrometry', *Journal of Chromatography A*, 930(1–2), pp. 127–134. doi: 10.1016/S0021-9673(01)01186-4.

Rastogi, T., Leder, C. and Kümmerer, K. (2014) 'Qualitative environmental risk assessment of photolytic transformation products of iodinated X-ray contrast agent diatrizoic acid', *Science of the Total Environment*. Elsevier B.V., 482–483(1), pp. 378–388. doi: 10.1016/j.scitotenv.2014.02.139.

Real, F. J. *et al.* (2009) 'Kinetics of the chemical oxidation of the pharmaceuticals primidone, ketoprofen, and diatrizoate in ultrapure and natural waters', *Industrial and Engineering Chemistry Research*, 48(7), pp. 3380–3388. doi: 10.1021/ie801762p.

Redeker, M. *et al.* (2014) 'Removal of the iodinated X-ray contrast medium diatrizoate by anaerobic transformation', *Environmental Science and Technology*, 48(17), pp. 10145–10154. doi: 10.1021/es5014714.

Redeker, M. *et al.* (2018) 'Anaerobic Transformation of the Iodinated X-ray Contrast Medium Iopromide, Its Aerobic Transformation Products, and Transfer to Further Iodinated X-ray Contrast Media', *Environmental Science and Technology*, 52(15), pp. 8309–8320. doi: 10.1021/acs.est.8b01140.

Rezaei, F. *et al.* (2019) 'Applications of plasma-liquid systems: A review', *Materials*, 12(7). doi: 10.3390/ma12172751.

Rivas, F. J. *et al.* (2019) 'Sunlight driven photolytic ozonation as an advanced oxidation process in the oxidation of bezafibrate, cotinine and iopamidol', *Water Research*, 151, pp. 226–242. doi: 10.1016/j.watres.2018.12.013.

Rizzo, L. *et al.* (2019) 'Consolidated vs new advanced treatment methods for the removal of contaminants of emerging concern from urban wastewater', *Science of the Total Environment*, 655(August 2018), pp. 986–1008. doi: 10.1016/j.scitotenv.2018.11.265.

Rodriguez-Narvaez, O. M. *et al.* (2017) 'Treatment technologies for emerging contaminants in water: A review', *Chemical Engineering Journal*. Elsevier B.V., pp. 361–380. doi: 10.1016/j.cej.2017.04.106.

Rumbach, P. *et al.* (2013) 'Decoupling interfacial reactions between plasmas and liquids: Charge transfer vs plasma neutral reactions', *Journal of the American Chemical Society*, 135(44), pp. 16264–16267. doi: 10.1021/ja407149y.

Rumbach, P. *et al.* (2015a) 'The effect of air on solvated electron chemistry at a plasma/liquid interface', *Journal of Physics D: Applied Physics*. IOP Publishing, 48(42). doi: 10.1088/0022-3727/48/42/424001.

Rumbach, P. *et al.* (2015b) 'The solvation of electrons by an atmospheric-pressure plasma', *Nature Communications*. Nature Publishing Group, 6. doi: 10.1038/ncomms8248.

Rumbach, P., Bartels, D. M. and Go, D. B. (2018) 'The penetration and concentration of solvated electrons and hydroxyl radicals at a plasma-liquid interface', *Plasma Sources Science and*

Technology. IOP Publishing, 27(11). doi: 10.1088/1361-6595/aaed07.

Rusterholtz, D. (2012) *Nanosecond Repetitively Pulsed Discharges in Atmospheric Pressure Air*. École Centrale Paris.

Rutberg, F. G. *et al.* (2008) 'Effect of silver oxide nanoparticles on tumor growth in vivo', *Doklady Biochemistry and Biophysics*, 421(1), pp. 191–193. doi: 10.1134/S1607672908040078.

Rutberg, P. G. *et al.* (2010) 'Main results of investigations of pulsed electric discharges in water carried out at IEE RAS', *High Temperature Material Processes*, 14, pp. 175–184.

Sacher, F. *et al.* (2001) 'Pharmaceuticals in groundwaters', *Journal of Chromatography A*, 938(1–2), pp. 199–210. doi: 10.1016/S0021-9673(01)01266-3.

Sahni, M. and Locke, B. R. (2006) 'Quantification of reductive species produced by high voltage electrical discharges in water', *Plasma Processes and Polymers*, 3(4–5), pp. 342–354. doi: 10.1002/ppap.200600006.

Saito, G. and Akiyama, T. (2015) 'Nanomaterial Synthesis Using Plasma Generation in Liquid', *Journal of Nanomaterials*, 2015, pp. 1–21. doi: 10.1155/2015/123696.

Sauvé, S. and Desrosiers, M. (2014) 'A review of what is an emerging contaminant', *Chemistry Central Journal*, 8(1), pp. 1–7. doi: 10.1186/1752-153X-8-15.

Schmidt, L. J., Gaikowski, M. P. and Gingerich, W. H. (2006) *Environmental assessment of hydrogen peroxide for aquaculture use*. La Crosse. Available at: https://animaldrugsatfda.fda.gov/adafda/app/search/public/document/downloadEA/123.

Scholtz, V. *et al.* (2015) 'Nonthermal plasma - A tool for decontamination and disinfection', *Biotechnology Advances*. Elsevier Inc., 33(6), pp. 1108–1119. doi: 10.1016/j.biotechadv.2015.01.002.

Schrand, A. M. *et al.* (2010) 'Metal-based nanoparticles and their toxicity assessment', *Wiley Interdisciplinary Reviews: Nanomedicine and Nanobiotechnology*, 2(5), pp. 544–568. doi: 10.1002/wnan.103.

Schulz, M. *et al.* (2008) 'Transformation of the X-ray contrast medium iopromide in soil and biological wastewater treatment', *Environmental Science and Technology*, 42(19), pp. 7207–

7217. doi: 10.1021/es800789r.

Seitz, W., Weber, W. H., *et al.* (2006) 'Monitoring of iodinated X-ray contrast media in surface water', *Chemosphere*, 64, pp. 1318–1324. doi: 10.1016/j.chemosphere.2005.12.030.

Seitz, W., Jiang, J. Q., *et al.* (2006) 'Removal of iodinated X-ray contrast media during drinking water treatment', *Environmental Chemistry*, 3(1), pp. 35–39. doi: 10.1071/EN05036.

Seitz, W. *et al.* (2008) 'Formation of oxidation by-products of the iodinated X-ray contrast medium iomeprol during ozonation', *Chemosphere*, 70, pp. 1238–1246. doi: 10.1016/j.chemosphere.2007.07.081.

El Shaer, M. *et al.* (2020) 'Antibiotics Degradation and Bacteria Inactivation in Water by Cold Atmospheric Plasma Discharges Above and Below Water Surface', *Plasma Chemistry and Plasma Processing*. Springer US, (0123456789). doi: 10.1007/s11090-020-10076-0.

Shen, J. *et al.* (2016) 'Bactericidal Effects against S. aureus and Physicochemical Properties of Plasma Activated Water stored at different temperatures', *Scientific Reports*. Nature Publishing Group, 6(March). doi: 10.1038/srep28505.

Shen, L. *et al.* (2019) 'Preparation and characterization of amorphous Cr2O3 nanoparticles obtained by solution plasma discharge', *Ceramics International*, 45(17), pp. 23578–23585. doi: 10.1016/j.ceramint.2019.08.068.

Simeonidis, K. *et al.* (2016) 'Inorganic engineered nanoparticles in drinking water treatment: A critical review', *Environmental Science: Water Research and Technology*, 2(1), pp. 43–70. doi: 10.1039/c5ew00152h.

Singh, R. K. *et al.* (2019) 'Rapid Removal of Poly- and Perfluorinated Compounds from Investigation-Derived Waste (IDW) in a Pilot-Scale Plasma Reactor', *Environmental Science and Technology*, 53, p. 11375−11382. doi: 10.1021/acs.est.9b02964.

Singh, R. K., Philip, L. and Ramanujam, S. (2019) 'Continuous flow pulse corona discharge reactor for the tertiary treatment of drinking water: Insights on disinfection and emerging contaminants removal', *Chemical Engineering Journal*. Elsevier, 355(April 2018), pp. 269–278. doi: 10.1016/j.cej.2018.08.109.

Sirotkin, N. A. *et al.* (2020) 'Synthesis and Photocatalytic Activity of WO3 Nanoparticles Prepared by Underwater Impulse Discharge', *Plasma Chemistry and Plasma Processing*. Springer US, 40, pp. 571–587. doi: 10.1007/s11090-019-10048-z.

Smirnov, B. M. (2012a) 'Conclusion – Plasmas in Nature and the Laboratory', in *Fundamentals of Ionized Gases*, pp. 447–458.

Smirnov, B. M. (2012b) 'General Concepts in Physics of Excited and Ionized Gases', in *Fundamentals of Ionized Gases*. 1st edn, pp. 1–52.

Snyder, S. A. *et al.* (2006) 'Ozone oxidation of endocrine disruptors and pharmaceuticals in surface water and wastewater', *Ozone: Science and Engineering*, 28(6), pp. 445–460. doi: 10.1080/01919510601039726.

Sousa, J. C. G. *et al.* (2019) 'Monitoring of the 17 EU Watch List contaminants of emerging concern in the Ave and the Sousa Rivers', *Science of the Total Environment*. Elsevier B.V., 649, pp. 1083–1095. doi: 10.1016/j.scitotenv.2018.08.309.

Starikovskaia, S. M. (2006) 'Plasma assisted ignition and combustion', *Journal of Physics D: Applied Physics*, 39(16), pp. R265–R299. doi: 10.1088/0022-3727/39/16/R01.

Starikovskiy, A. *et al.* (2011) 'Non-equilibrium plasma in liquid water: dynamics of generation and quenching', *Plasma Sources Science and Technology*, 20(2), p. 024003. doi: 10.1088/0963-0252/20/2/024003.

Steger-Hartmann, T., Länge, R. and Schweinfurth, H. (1999) 'Environmental risk assessment for the widely used iodinated X-ray contrast agent iopromide (Ultravist)', *Ecotoxicology and Environmental Safety*, 42(3), pp. 274–281. doi: 10.1006/eesa.1998.1759.

Stratton, G. R. *et al.* (2015) 'Plasma-based water treatment: Conception and application of a new general principle for reactor design', *Chemical Engineering Journal*. Elsevier B.V., 273, pp. 543–550. doi: 10.1016/j.cej.2015.03.059.

Stratton, G. R. *et al.* (2017) 'Plasma-based water treatment: Efficient transformation of perfluoroalkyl substances (PFASs) in prepared solutions and contaminated groundwater', *Environmental Science & Technology*, p. acs.est.6b04215. doi: 10.1021/acs.est.6b04215.

Strehl, C. *et al.* (2019) 'Cost-effective reduction of micro pollutants in the water cycle – Case study on iodinated contrast media', *Science of the Total Environment*. Elsevier B.V., 688, pp. 10–17. doi: 10.1016/j.scitotenv.2019.06.187.

Su, X. *et al.* (2019) 'The Role of High Voltage Electrode Material in the Inactivation of E. coli by Direct-in-Liquid Electrical Discharge Plasma', *Plasma Chemistry and Plasma Processing*. Springer US, (0123456789). doi: 10.1007/s11090-019-09980-x.

Sugihara, M. N. *et al.* (2013) 'TiO2-photocatalyzed transformation of the recalcitrant X-ray contrast agent diatrizoate', *Applied Catalysis B: Environmental*. Elsevier B.V., 129, pp. 114–122. doi: 10.1016/j.apcatb.2012.09.013.

Sulaimankulova, S., Mametova, A. and Abdullaeva, Z. (2019) 'Fusiform gold nanoparticles by pulsed plasma in liquid method', *SN Applied Sciences*. Springer International Publishing, 1(11), pp. 1–8. doi: 10.1007/s42452-019-1345-z.

Šunka, P. (2001) 'Pulse electrical discharges in water and their applications', *Physics of Plasmas*, 8(5 II), pp. 2587–2594. doi: 10.1063/1.1356742.

Takahashi, A. *et al.* (1999) 'Determination of Hydrogen Peroxide by High-Performance Liquid Chromatography with a Cation-Exchange Resin Gel Column and Electrochemical Detector.', *Analytical Sciences*, 15(5), pp. 481–483. doi: 10.2116/analsci.15.481.

Tampieri, F. *et al.* (2018) 'Removal of persistent organic pollutants from water using a newly developed atmospheric plasma reactor', *Plasma Processes and Polymers*, 15(e1700207). doi: 10.1002/ppap.201700207.

Tanaka, H. *et al.* (2018) 'Molecular mechanisms of non-thermal plasma-induced effects in cancer cells', *Biological Chemistry*, 400(1), pp. 87–91. doi: https://doi.org/10.1515/hsz-2018-0199.

Ternes, T. A. *et al.* (2003) 'Ozonation: A tool for removal of pharmaceuticals, contrast media and musk fragrances from wastewater?', *Water Research*, 37(8), pp. 1976–1982. doi: 10.1016/S0043-1354(02)00570-5.

Ternes, T. A. and Hirsch, R. (2000) 'Occurrence and behavior of X-ray contrast media in sewage facilities and the aquatic environment', *Environmental Science and Technology*, 34(13), pp.

2741–2748. doi: 10.1021/es991118m.

Thagard, S. M., Takashima, K. and Mizuno, A. (2009) 'Chemistry of the positive and negative electrical discharges formed in liquid water and above a gas-liquid surface', *Plasma Chemistry and Plasma Processing*, 29(6), pp. 455–473. doi: 10.1007/s11090-009-9195-x.

Tian, F. *et al.* (2017) 'Chlor(am)ination of iopamidol : Kinetics, pathways and disinfection by-products formation', *Chemosphere*. Elsevier Ltd, 184, pp. 489–497. doi: 10.1016/j.chemosphere.2017.06.012.

Tissot, G. B. *et al.* (2012) 'Kinetic experiments of electrochemical oxidation of iohexol on BDD electrodes for wastewater treatment', *Electrochemistry Communications*. Elsevier B.V., 23(1), pp. 48–51. doi: 10.1016/j.elecom.2012.07.006.

Traylor, M. J. *et al.* (2011) 'Long-term antibacterial efficacy of air plasma-activated water', *Journal of Physics D: Applied Physics*, 44(47), p. 472001. doi: 10.1088/0022-3727/44/47/472001.

Turkay, O. *et al.* (2018) 'Electrochemical Reduction of X-ray Contrast Iohexol at Mixed Metal Oxide Electrodes: Process Optimization and By-product Identification', *Water, Air, and Soil Pollution*. Water, Air, & Soil Pollution, 229(6). doi: 10.1007/s11270-018-3823-0.

Velikonja, J. *et al.* (2001) 'Co-generation of ozone and hydrogen peroxide by dielectric barrier AC discharge in humid oxygen', *Ozone: Science and Engineering*, 23(6), pp. 467–478. doi: 10.1080/01919510108962031.

Velo-Gala, I. *et al.* (2012) 'Ionic X-ray contrast media degradation in aqueous solution induced by gamma radiation', *Chemical Engineering Journal*. Elsevier B.V., 195–196, pp. 369–376. doi: 10.1016/j.cej.2012.04.046.

Verlicchi, P. *et al.* (2010) 'Hospital effluents as a source of emerging pollutants: An overview of micropollutants and sustainable treatment options', *Journal of Hydrology*. Elsevier B.V., 389(3–4), pp. 416–428. doi: 10.1016/j.jhydrol.2010.06.005.

Verlicchi, P. (2018) *Hospital Wastewaters: Characteristics, Management, Treatment and Environmental Risks*. doi: 10.1007/978-3-319-62178-4.

Vlad, I. and Anghel, S. D. (2017) 'Time stability of water activated by different on-liquid atmospheric pressure plasmas', *Journal of Electrostatics*. Elsevier B.V, 87, pp. 284–292. doi: 10.1016/j.elstat.2017.06.002.

Vukusic, T. *et al.* (2016) 'Liquid-phase electrical discharge plasmas with a silver electrode for inactivation of a pure culture of Escherichia coli in water', *Innovative Food Science and Emerging Technologies*. Elsevier Ltd, 38, pp. 407–413. doi: 10.1016/j.ifset.2016.07.007.

Walling, C. (1975) 'Fenton's Reagent Revisited', *Accounts of Chemical Research*, 8, pp. 125–131. doi: 10.1021/ar50088a003.

Wandell, R. J. and Locke, B. R. (2014) 'Hydrogen peroxide generation in low power pulsed water spray plasma reactors', *Industrial and Engineering Chemistry Research*, 53(2), pp. 609–618. doi: 10.1021/ie402766t.

Wang, B. *et al.* (2017) 'Degradation of methylene blue using double-chamber dielectric barrier discharge reactor under different carrier gases', *Chemical Engineering Science*. Elsevier Ltd, 168, pp. 90–100. doi: 10.1016/j.ces.2017.04.027.

Wang, H. *et al.* (2019) 'The influence of liquid conductivity on electrical breakdown and hydrogen peroxide production in a nanosecond pulsed plasma discharge generated in a water-film plasma reactor', *Journal of Physics D: Applied Physics*, 52(7). doi: 10.1088/1361-6463/aaf132.

Wang, X. *et al.* (2019) 'Oxidative degradation of iodinated X-ray contrast media (iomeprol and iohexol) with sulfate radical: An experimental and theoretical study', *Chemical Engineering Journal*. Elsevier, 368(February), pp. 999–1012. doi: 10.1016/j.cej.2019.02.194.

Wang, Z. *et al.* (2020) 'Resolving the kinetic and intrinsic constraints of heat-activated peroxydisulfate oxidation of iopromide in aqueous solution', *Journal of Hazardous Materials*. Elsevier, 384(September 2019), p. 121281. doi: 10.1016/j.jhazmat.2019.121281.

Weissbrodt, D. *et al.* (2009) 'Mass Flows of X-ray Contrast Media and Cytostatics in Hospital Wastewater', *Environ. Sci. Technol.*, 43(13), pp. 4810–4817.

Wendel, F. M. *et al.* (2014) 'Transformation of iopamidol during chlorination', *Environmental Science and Technology*, 48(21), pp. 12689–12697. doi: 10.1021/es503609s.

Wert, E. C., Rosario-Ortiz, F. L. and Snyder, S. A. (2009) 'Effect of ozone exposure on the oxidation of trace organic contaminants in wastewater', *Water Research*. Elsevier Ltd, 43(4), pp. 1005–1014. doi: 10.1016/j.watres.2008.11.050.

Witzke, M. *et al.* (2012) 'Evidence for the electrolysis of water by atmospheric-pressure plasmas formed at the surface of aqueous solutions', *Journal of Physics D: Applied Physics*, 45(44), p. 442001. doi: 10.1088/0022-3727/45/44/442001.

Wolf, L., Zwiener, C. and Zemann, M. (2012) 'Tracking artificial sweeteners and pharmaceuticals introduced into urban groundwater by leaking sewer networks', *Science of the Total Environment*. Elsevier B.V., 430, pp. 8–19. doi: 10.1016/j.scitotenv.2012.04.059.

Wu, D. *et al.* (2017) 'Effective degradation of diatrizoate by electro-peroxone process using ferrite / carbon nanotubes based gas diffusion cathode', *Electrochimica Acta*. Elsevier Ltd, 236, pp. 297–306. doi: 10.1016/j.electacta.2017.03.196.

Xie, P. *et al.* (2019) 'Aqueous gold nanoparticles generated by ac and pulse-power-driven plasma jet', *Nanomaterials*, 9(10), pp. 1–17. doi: 10.3390/nano9101488.

Xu, Z. *et al.* (2017) 'Distribution and relevance of iodinated X-ray contrast media and iodinated trihalomethanes in an aquatic environment', *Chemosphere*. Elsevier Ltd, 184, pp. 253–260. doi: 10.1016/j.chemosphere.2017.05.048.

Yan, M. *et al.* (2018) 'Electrochemical reductive dehalogenation of iodine-containing contrast agent pharmaceuticals: Examination of reactions of diatrizoate and iopamidol using the method of rotating ring-disc electrode (RRDE)', *Water Research*, 136, pp. 104–111. doi: 10.1016/j.watres.2018.02.045.

Yang, G. C. C. (2017) 'Global challenges and solutions of emerging contaminants: An editorial overview and beyond', *Chemosphere*, pp. 1222–1229. doi: 10.1016/j.chemosphere.2016.10.076.

Yang, Y. *et al.* (2017) 'Occurrences and removal of pharmaceuticals and personal care products (PPCPs) in drinking water and water/sewage treatment plants: A review', *Science of the Total Environment*. Elsevier B.V., 596–597, pp. 303–320. doi: 10.1016/j.scitotenv.2017.04.102.

Ye, T. *et al.* (2014) 'Comparison of iodinated trihalomethanes formation during aqueous chlor(am)ination of different iodinated X-ray contrast media compounds in the presence of

natural organic matter', *Water Research*. Elsevier Ltd, 66, pp. 390–398. doi: 10.1016/j.watres.2014.08.044.

Yoon, S. *et al.* (2018) 'Mutual Interaction between Plasma Characteristics and Liquid Properties in AC-driven Pin-to-Liquid Discharge', *Scientific Reports*, 8, p. 12037. doi: 10.1038/s41598-018-30540-4.

Yuan, D. *et al.* (2017) 'Comparison of hydroxyl radicals generation during granular activated carbon regeneration in DBD reactor driven by bipolar pulse power and alternating current power', *Vacuum*, 143, pp. 87–94. doi: 10.1016/j.vacuum.2017.06.003.

Zemann, M. *et al.* (2014) 'Sources and processes affecting the spatio-temporal distribution of pharmaceuticals and X-ray contrast media in the water resources of the Lower Jordan Valley, Jordan', *Science of the Total Environment*. Elsevier B.V., 488–489(1), pp. 100–114. doi: 10.1016/j.scitotenv.2014.04.063.

Zhao, C. *et al.* (2014) 'Reductive and oxidative degradation of iopamidol , iodinated X-ray contrast media , by Fe(III)-oxalate under UV and visible light treatment', *Water Research*. Elsevier Ltd, 67, pp. 144–153. doi: 10.1016/j.watres.2014.09.009.

Zhao, H. *et al.* (2019) 'Degradation of iohexol by Co2+ activated peroxymonosulfate oxidation: Kinetics, reaction pathways, and formation of iodinated byproducts', *Chemical Engineering Journal*. Elsevier, 373(May), pp. 1348–1356. doi: 10.1016/j.cej.2019.05.140.

Zhao, X. *et al.* (2019) 'Degradation of iopamidol by three UV-based oxidation processes: Kinetics, pathways, and formation of iodinated disinfection byproducts', *Chemosphere*. Elsevier Ltd, 221, pp. 270–277. doi: 10.1016/j.chemosphere.2018.12.162.

Zheng, Y. *et al.* (2020) 'Source Tracking and Risk Assessment of Pharmaceutical and Personal Care Products in Surface Waters of Qingdao, China, with Emphasis on Influence of Animal Farming in Rural Areas', *Archives of Environmental Contamination and Toxicology*. Springer US, 78(4), pp. 579–588. doi: 10.1007/s00244-020-00725-y.
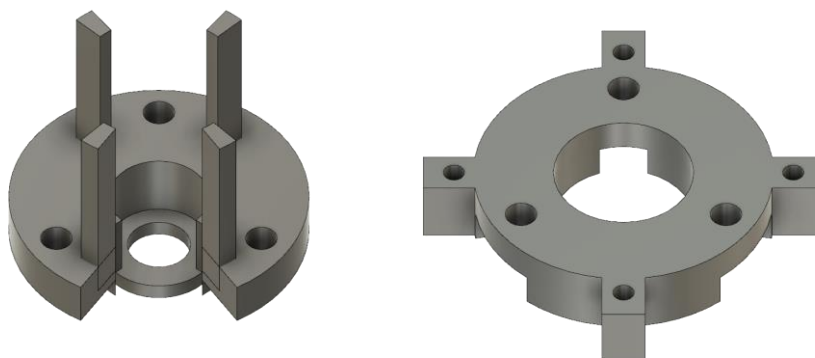
Appendix A

Technical drawings

Fig. 0-1 3D printed parts of the laboratory stand. The top (left) and the bottom (right) parts are connected through threaded rods. Note that the sticks pointing out from the top part were not sturdy, and after some experiments they were removed. With or without sticks, the top part held the reactor securely.
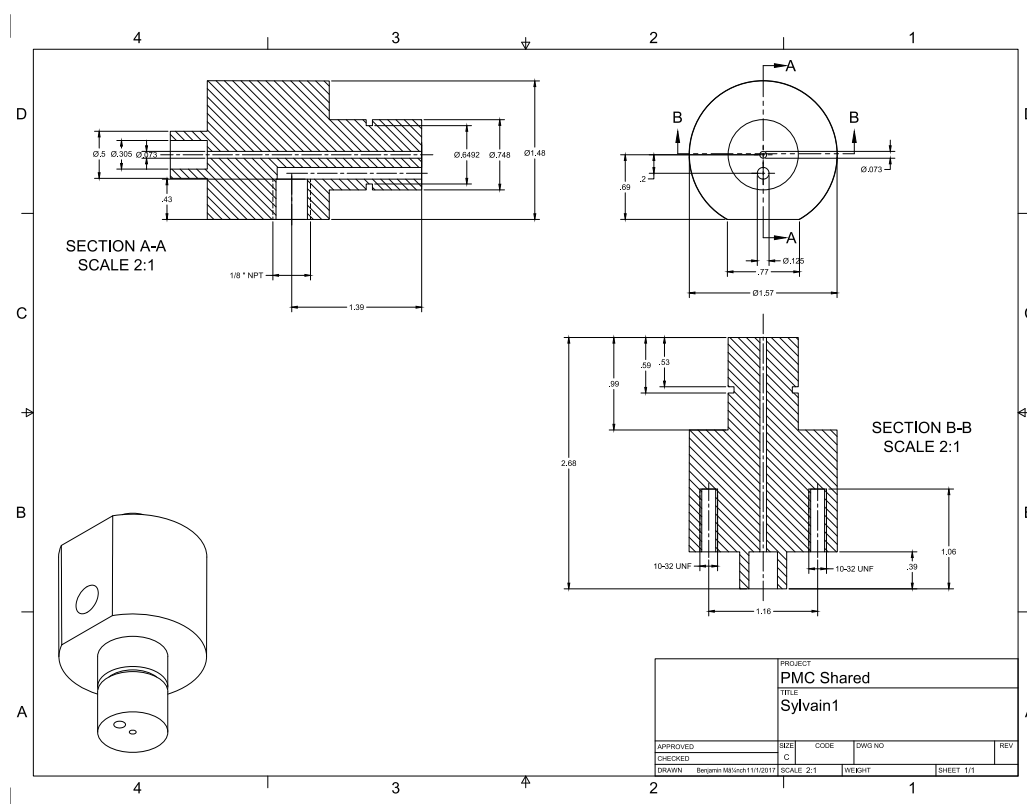

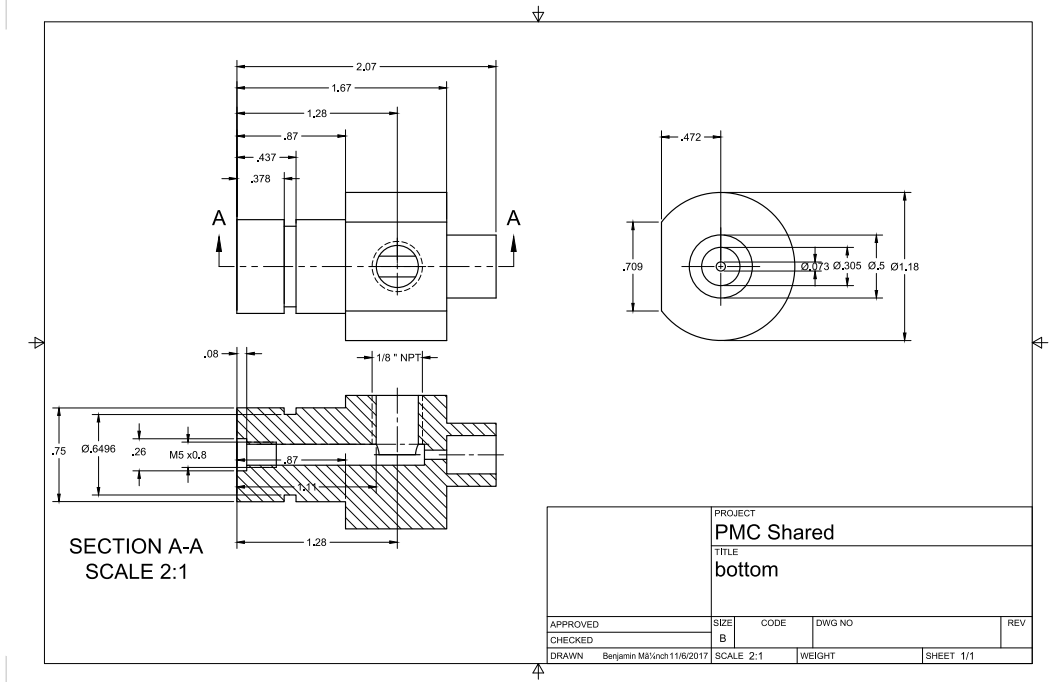Fig. 0-2 Technical drawing depicting the top lid for the glass vessel (imperial units).

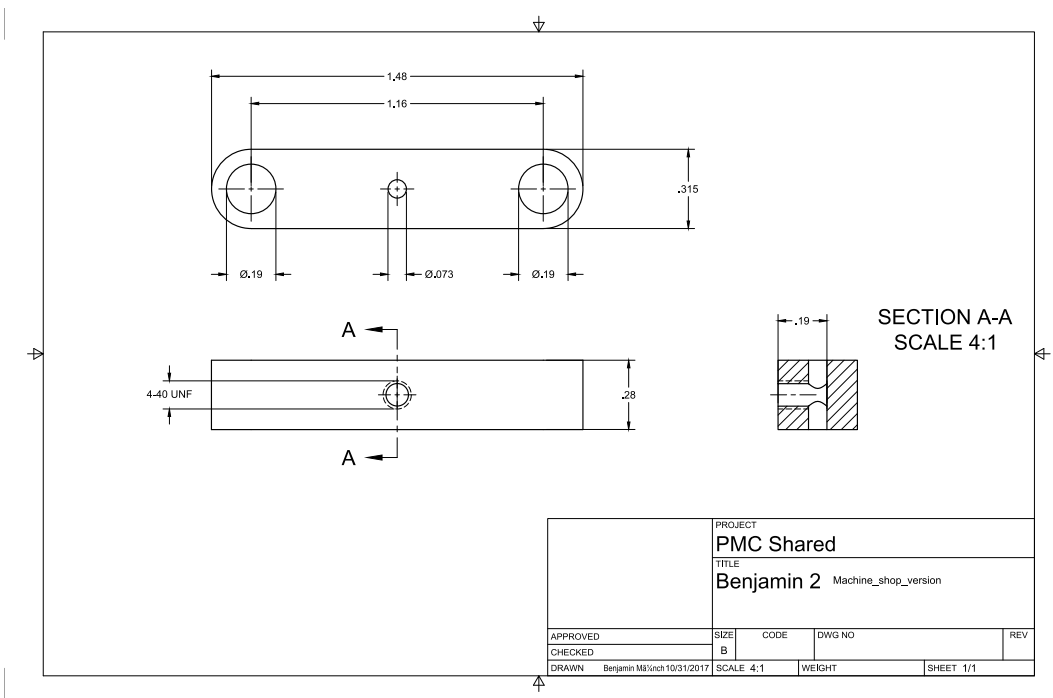Fig. 0-3 Technical drawing depicting the bottom lid for the glass vessel (imperial units).

Fig. 0-4 Technical drawing depicting the piece that secures the pin electrode on top of the reactor (imperial units). The piece is connected to the top lid of the reactor via threaded rods.

Appendix B

Standard operating procedure developed for the preliminary pin-to-liquid discharge reactor

1) Place the cuvette containing the liquid sample in the holder, put the cap with cleaned electrodes in the cuvette and start the magnetic stirrer.
2) Start the power supply.
    a. Turn on the oscilloscope (1), signal generator (2), and both power supplies (3 and 5).
    b. Turn off "main" at the power supply (5).
    c. Adjust the settings to frequency = 1 kHz, high amplitude = 5 V, low amplitude = 0 V and Width = 1 μsec for channel 1 and 2 at the signal generator.
    d. Make sure that frequency for CH1 = CH2 is on so that both pulses are sent at the same time.
    e. Use the signals displayed at the oscilloscope to adjust the delay at the signal generator so that the signals are synchronized.
3) Run and generate the plasma.
    a. Activate pulse signal channel 1 and 2 at the signal generator.
    b. Turn on "main" at the power supply (5) and increase the voltage to 500 V to reach a plasma.
4) Sustain the plasma for a certain time.
5) Turn off the power supply.
    a. Turn off "main" at the power supply (5) and reduce the voltage setting to 0 V.
    b. Turn off both outputs at the signal generator.
    c. Turn off the power supplies, the signal generator and the oscilloscope.
6) Remove the sample.

Standard operating procedure developed for the principal pin-to-liquid discharge reactor

1) Safety glasses and a lab coat are mandatory throughout the entire course of this procedure, and must be worn before entering the laboratory.

2) With nitrile gloves on, use ethanol and Kimwipes to clean the electrodes (pin and sparger; which have a fixed position during the experiment), the lids and the glass vessel. If there is some ethanol waste, it has to be disposed in a properly labeled flammable/ organic/solvent waste container.

3) Fix the bottom lid (with the sparger already screwed in) on the bottom of the glass vessel. Since the sparger is a live electrode, it must be kept away from metallic surfaces (5 cm at least). The sparger is connected to a mass flow meter through the bottom lid and PVC tubing and to the power supply through a high-voltage wire.

4) Add 7.5 mL liquid sample carefully into the glass vessel.

5) Mount the top lid on the top of the glass vessel. The pin electrode should be positioned approximately 2 mm above the liquid surface. Make sure to allow air space between wires/electrodes and the ground (using a plastic stand) for insulation. Then, the gloves can now be removed.

6) Make sure the cooling channel of the glass vessel is properly connected to the water bath. Start water circulation and check for leakage. If constant bubbles are seen through the cooling jacket, this means that there is not enough water in the water bath. Add tap water to the water bath until the production of bubbles halts.

7) Make sure that the setup is grounded everywhere for every electrical device.

8) Make sure that the elephant trunk is working by checking that a light object such as a Kimwipe is affected by the airflow. Make sure that the elephant trunk is located close to the reactor top.

9) Start the gas flow (depending on the experiment: air or oxygen) through the sparger. To do so, open the tank valve and make sure the main valve (valve between the pressure regulator and the flow meter) is closed; then loosen the valve of the pressure regulator setting the pressure to 5 psi and finally opening the main valve. Now the gas inlet has begun followed by an adjustment of the gas flow to a value of 10 in the flow meter. The corresponding

191

volumetric flow rate will be 6 mL/min (ccm). Check for gas leakage with the "snoop" soapy solution.

10) Before starting the power supply system, if doing experiments without air: wait for 4 min after turning on the gas flow to ensure that all the residual air is purged out of the experimental chamber.

11) Start the power supply system.

    a. Turn on the power bar, the oscilloscope, signal generator, and both power supplies.

    b. Turn off "output enable main" at the power supply 1 right after turning on the power supply.

    c. Press the "Recall" button at the signal generator and select setup 1. Make sure that the high amplitude = 5 V, low amplitude = 0 V and width = 1 µs.

    d. Adjust the frequency to a value of 3 kHz for channel 1 and channel 2 (so that both pulses are sent at the same time).

    e. Activate phase/delay at the signal generator and change to nanosecond on channel 2 (since channel 1 is fixed).

12) Plasma ignition.

    a. Activate pulse signal channel 1 and 2 at the signal generator.

    b. Using the multimeter, make sure that the power supply 2 shows 18 V.

    c. Turn on "output enable main" at the power supply 1 and increase the voltage to 580 V (or other desired voltage). The presence of plasma can be confirmed visually (briefly) with the naked eye.

13) At the signal generator, adjust the delay such that both voltage peaks on the oscilloscope align (vertically).

14) Let the system operate while monitoring the electrical signals, flow rates, liquid temperature, and plasma stability (visually) for the desired plasma treatment time.

15) End of plasma treatment.

    a. Turn off "output enable main" at the power supply 1 and reduce the voltage to 0 V.

    b. Turn off the power supplies and turn off the pulse signal of channel 1 and 2 at the signal generator.

    c. Turn off the signal generator, oscilloscope and multimeter.

    d. Turn off the power bar.

16) To avoid any incidental electrical discharge from the electrodes, discharge them to ground by contacting them with a grounded high-voltage cable.

17) Stop the gas flow, put nitrile gloves back on and remove the top lid from the glass vessel.

18) Pipette out the liquid sample from the glass vessel into vials for further analysis.

19) Clean-up of the setup after each run (with gloves on).

   a. Dry the vessel and both lids with Kimwipes.

   b. Clean all three parts with ethanol and Kimwipes.

   c. Let the ethanol evaporate before mounting the lids.

   d. Remove gloves.

20) Turn off the water bath.

21) At the end of each day.

   a. Drain the gas line by first shutting the tank valve and then allowing the remaining gas in the line to drain. Once done, untighten the pressure regulating valve (one left turn) and close the valve between the pressure regulator and flow meter (main valve).

   b. Tidy up the work bench.

   c. Dispose any remaining plasma-treated sample in either the specially labeled waste container or store it in glass vials for further analysis.